Phase Formation and Dielectric Studies of Some BaO-TiO_2-ZrO_2 Based Perovskite System

A Thesis in Physics (Materials Science)

by

Sanjeeb Kumar Rout

Submitted in Partial Fulfillment

of the Requirements for the Degree of

Doctor of Philosophy

April 2006

Department of Physics
National Institute of Technology, Rourkela-769 008
(A Deemed University)
Orissa, India

CERTIFICATE

This is to certify that the thesis entitled, "*Phase Formation and Dielectric Studies of Some BaO-TiO_2-ZrO_2 Based Perovskite System*" being submitted by Sri Sanjeeb Kumar Rout for the award of Ph.D. degree is a record of bonafide research carried out by him under our supervision. In our opinion, the work fulfills the requirements for which it is being submitted.

The work incorporated in this thesis has not been submitted else where earlier, in part or in full, for the award of any other degree or diploma of this or any other institution or university.

Dr. J. Bera		**Dr. S. Panigrahi**
Asst. Professor Department of Ceramic Engg. National Institute of Technology Rourkela-769008 Orissa, India		Professor and Head Department of Physics National Institute of Technology Rourkela-769008 Orissa, India

DEDICATED TO.....

MY BELOVED PARENTS

Abstract

High permittivity barium titanate zirconate (BTZ) is often used for dielectrics in commercial multilayer ceramic capacitors, actuators applications, and is a highly promising material for dynamic random access memory (DRAM) and microelectromechanical system (MEMS) applications due to its very stable, high insulating characteristic against voltage. Especially, the material is promising for environmental friendly application in compared to Lead (Pb) based compositions.

Different solid solutions in the system have been synthesized via solid state reaction route. Detailed phase formation behaviors of the solid solutions were investigated through; (i) phase identification, (ii) phase quantity determination, (iii) change in lattice parameters and crystallite sises, (iv) evolution of phase formation kinetics and reaction mechanism, and (v) structure and microstructure evolution by Rietveld refinement method. The study on reaction mechanism concludes that; titanates form more easily in the system than zirconates. Then titanate inter-diffuses into zirconate, where latter phase acts as diminishing core

Coming to the Rietveld structural refinement on the four-component system, the solid solution system $Ba_{1-x}Sr_x(Ti_{0.5}Zr_{0.5})O_3$ remains cubic up to $x<0.6$ and becomes tetragonal in the range $x>0.6$ to $x=1.0$. Composition with $x=0.6$ contains both the cubic and tetragonal phases. The solid solution system $(Ba_{0.5}Sr_{0.5})(Ti_{1-x}Zr_x)O_3$ remains cubic up to $x\leq0.6$, and the solid solution breaks around $x=0.8$ with the formation of second phase of tetragonal type. Compositions with $x=0.8$ contain both the cubic and tetragonal phases and suggest to have a super-lattice structure due to the presence of two dissimilar structures. The $Ba_{0.5}Sr_{0.5}ZrO_3$ has orthorhombic structure.

Solubility of Ca and Mg in $BaTi_{0.6}Zr_{0.4}O_3$ was also studied by Rietveld method. The Study concludes that Mg forms single phase solid solution with $BaTi_{0.6}Zr_{0.4}O_3$ in the studied composition range and the structure remains cubic at room temperature. But solubility of Ca with $BaTi_{0.6}Zr_{0.4}O_3$ breaks at around 20 atom % of Ca. The composition $Ba_{0.9}C_{0.1}Ti_{0.6}Zr_{0.4}O_3$ remains cubic. With increase in Ca content, a different phase, orthorhombic $CaTiO_3$, grows along with tetragonal $Ba_{0.8}C_{0.2}Ti_{0.6}Zr_{0.4}O_3$.

Detailed composition dependency microstructure and dielectric behavior of the different solid solution in the system has been studied. Temperature dependency dielectric behaviors of some of the selected compositions have been studied.

The substitution of Sr in Ba $(Ti_{0.5}Zr_{0.5})$ O_3 and Zr in $(Ba_{0.5}Sr_{0.5})$ Ti O_3 decreases the grain size, dielectric constant and dielectric loss due to the decrease in charge defects by the substitution. The effect of Ca and Mg on the composition $BaTi_{0.6}Zr_{0.4}O_3$ has been studied in details. Similar dielectric behavior and microstructure are observed with the addition of Ca and Mg at room temperature.

The temperature dependency dielectric study on the composition $BaTi_{0.6}Zr_{0.4}O_3$, $Ba_{0.9}Ca_{0.1}Ti_{0.6}Zr_{0.4}O_3$, $Ba_{0.93}Mg_{0.07}Ti_{0.6}Zr_{0.4}O_3$ and $Ba_{0.86}Mg_{0.14}Ti_{0.6}Zr_{0.4}O_3$ was carried out in the temperature range 130 K to 333 K. The compositions show a diffuse phase transition having its Curie range of temperature much below the room temperature. The Ca-containing composition shows that there is a shift of transition temperature towards room temperature but the Mg containing compositions shows shift of transition temperature further below. A clear deviation from Curie-Weiss law is observed for all the compositions, and degrees of deviations were also calculated. To study the diffuseness, the data were fitted with a modified Curie-Weiss law, and it was found that the degree diffuseness decreases with Ca substitution, but increases with Mg substitution. In order to analyze the relaxation feature, the experimental curves were fitted with Vogel-Fulcher formula and the experimental data were found to be in good agreement with the theoretical fitting.

To get into the realm of physics, relaxor ferroelectric is treated as a close analogy with Ising model of Spin glass system. Further extension of Ising model to spherical random bond–random field model is discussed. Both the models are extensively reviewed and presented towards end of the thesis. Finally, future aspects of theoretical models on present experimental result are proposed. To get more information on the studied materials for practical application, further extension of experimental work are also proposed.

TABLE OF CONTENTS

LIST OF FIGURES

LIST OF TABLES

ACKNOWLEDGEMENTS

I am exceedingly grateful to my parents, Mrs. Santilata Rout and Mr. Siddheswar Rout, for their love, support, and sacrifice from the very first day of my journey of life. If it were not for their vision with respect to my education, I would have been perfecting my farming skills in the small village Bari, I was born in instead of discovering the mysteries of scientific life. A successful journey starts with good preparation. I must acknowledge my brothers, Rajeeb Ku. Rout and Ajeet Ku. Rout. Together with we made a great family, which I believe is the basis for a bright future. As I began my pursuit of higher dreams in NIT (formerly R.E. College), Rourkela, I found a great helper, a source of inspiration, and love which were prerequisites for completion of this dissertation.

It is my strong belief that academic success is closely related to the choice of the right mentors and advisors. I had the privilege and honor to pursue my Ph.D. studies under the guidance and direction of two outstanding teachers, Dr. S. Panigrahi, Professor and Head, department of physics and Dr. J.Bera, Assistant professor, department of ceramic engineering, NIT, Rourkela. I wish to express my reverence and sense of deep gratitude to Dr. S. Panigrahi, for his whole sole guidance not only in this project work but towards a fruitful stay at Rourkela, far away from my village and fatigue less vigil to my day to day life. Without his flawless supervision, wholehearted co-operation and genuine interest this would not have accomplished. I would like to extend my cordial thanks to Dr.J.Bera for his valuable suggestions and timely help without which the work remains incomplete. At the end of this work, I have not only finished my Ph.D. but also become a “perfectionist.” I am deeply thankful for their help, support, and patience in my progress of academic learning and exploration.

I also must acknowledge Professor S. K. Sarangi, Director, National institute of Technology, Rourkela for providing me a platform to carryout this research.

I also would like to express my gratitude to the rest of my doctoral scrutiny committee members: Dr. D. K. Bisoyi, Dr. S. Bhattacharya, Dr. S. Panigrahi, Dr.J. Bera for their invaluable, insightful comments and suggestions that improved the quality of this work.

I also must acknowledge Dr. S. Adak, Head, Ceramic Engineering Department, for his help and extent the experimental facility in his department.

I am extremely thankful to all the supporting and technical staff of the Department of Physics, Department of Ceramic Engineering and Department of Materials and Metallurgical Engineering for their help as and when required without which I have been in troubled waters.

I would like to acknowledge Dr.T.N.Tiwari, Retd. Professor, Department of Physics, NIT, Rourkela for thorough reading the thesis and his valuable suggestion.

I would also like to acknowledge the contribution of my friends and colleagues. Mr. S. K. Naik, Mr. S. K. Swain, Dr. P. C. Mishra, Mr.A.K.Rath and Mr. T. Badapanda, deserve special thanks for their timely help and cooperation during this study.

It will be unforgivable mistake in my life, if I will not acknowledge Miss Ela Sinha, is a friend at present. I was struggling at the Laboratory for many long and sleepless nights. Some times I was frustrated due to lack of experimental facility and for many other regions. But she was always to encourage me towards completion of this work. I must thank in particular for her companionship and constant encouragement.

Last but not least I would like to acknowledge Ministry of Human Resources and Development, Govt. of India, for providing me financial support though a research and development project.

My final words will be for the expression of my hope for the future. I wish I would have the chance to visit NIT, Rourkela very frequently with my family and tell them about my stories as we walk around this beautiful campus. At last another hope is that, Dr. S. Panigrahi will continue research in this particular field and share his valuable thought with many young researchers.

Chapter 1

INTRODUCTION AND BACKGROUND

1.1. Introduction

The discovery of ferroelectricity in barium titanate ($BaTiO_3$) has given birth to a large number of ABO_3 type materials. The diversity of structures exhibited by $BaTiO_3$ based perovskites continues to fascinate in a range of areas including solid state chemistry, physics and the earth science. Ferroelectric oxides with perovskite structure have been currently of great technological interest due to their excellent properties for various related applications in recent years. However it is well known that the ferroelectric materials at present are lead based perovskite that are toxic. Naturally, lead free materials will be of interest because of their obvious health and environmental advantages in future applications.

Barium strontium titanate (BST) is a high-K (dielectric constant) material is commonly used to replace silicon dioxide (SiO_2) as the dielectric in advance memory devices. The high dielectric constant combined with a low dissipation factor makes BST one of the promising candidates for dynamic random access memory (DRAM) applications.

Recently, Ba (Ti_{1-x} Zr_x) O_3 (BTZ) has been chosen as an alternative to BST in the fabrication of ceramic capacitors. The solid solution of Barium titanate ($BaTiO_3$) and barium zirconate ($BaZrO_3$) ie Ba (Ti_{1-x} Zr_x) O_3 shows great similarity to the BST solid solution. Substitution of Ti^{4+} (atomic weight of 47.9, ionic radius of 74.5 pm) with Zr^{4+} (atomic weight of 91.2, atomic radius of 86 pm) exhibits several interesting features in the dielectric behavior of $BaTiO_3$ ceramics. When the Zr content is less than 10 at %, the BZT ceramics show normal ferroelectric behavior and the dielectric anomalies corresponding to the cubic to tetragonal (T_c), tetragonal to orthorhombic (T_2), and orthorhombic to rhombohedral (T_3) phases have been clearly observed. While Zr content is in between 27 to 42 atom %, BZT ceramics exhibit typical relaxor nature. Again with increase of Zr ($\geq$ 0:42 at %) content the BZT materials exhibits like normal ferroelectrics. Ferroelectrics are materials in which spontaneous electric polarisation P_s, can be reversed by application of an electric field for short time. Valasek [1] discovered the polarisation reversal in Rochelle salt. The non linear relationship between the polarisation and the field is one of the main and dominating characteristics of

ferroelectrics [2]. It is the intent of this chapter to provide a brief description of dielectric with an emphasis on ferroelectric and their relaxation behavior.

1.2. Basis for the Ferroelectricity in Crystals

Of the 32 possible crystal classes (i.e. point groups), 11 are Centro symmetric and thus cannot exhibit polar properties. The remaining 21 lack a center of symmetry and thus can posses one or more polar axes. Of these, 20 classes are piezoelectric (the one exception being cubic class) (Fig. 1.1). Piezoelectric crystals have the property that the application of mechanical stress induces polarization, and conversely, the application of an electric field produces mechanical deformation. Of the 20 piezoelectric classes, 10 have a unique polar axis and thus are spontaneously polarized, i.e. polarized in the absence of an electric field. Crystals belonging to these 10 classes are called pyroelectric. The intrinsic polarization of pyroelectric crystals is often difficult to detect experimentally because of the neutralization of the charges on the crystal surfaces by free charges from the atmosphere and by conduction within the crystal. However, because the polarization is a function of temperature, it is often possible to observe the spontaneous moment in these crystals by changing the temperature, hence the name pyroelectrics. Ferroelectric crystals belong to the pyroelectric family, but they also exhibit the additional property that the direction of the spontaneous polarization can be reversed by the application of an electric field. Thus, we have the following simple definition for a ferroelectric crystal: *A ferroelectric crystals is a crystal that possesses reversible spontaneous polarization as exhibited by a dielectric hysteresis loop*. A more detailed discussion on ferroelectric is given in the subsequent sections.

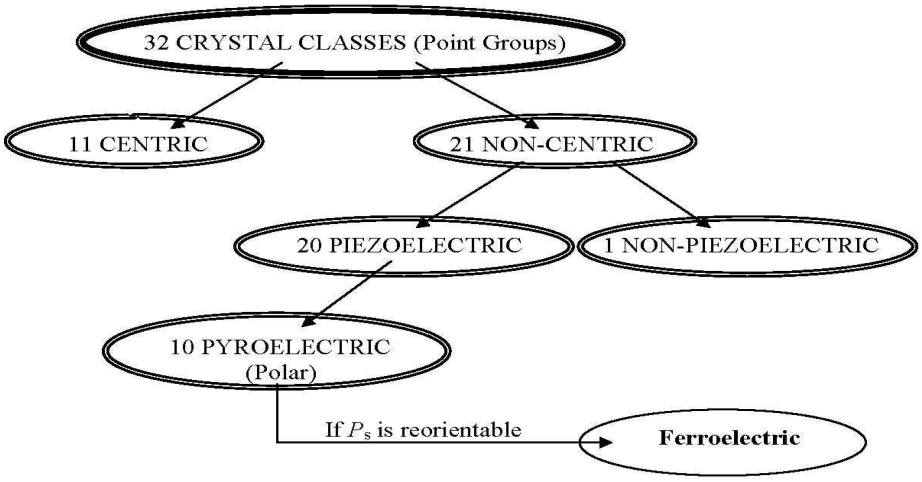

Figure 1.1 A classification scheme for the 32 crystallographic point groups.

1. 3. Dielectric Property

Dielectrics are insulating materials. In dielectrics, all the electrons are bound to their parent molecules and there are no free charges. Even with normal voltage or thermal energy electrons are not released. Dielectrics are nonmetallic materials of high specific resistances and have negative temperature coefficient of resistance.

When a dielectric slab is placed in a static electric field, it acquires a surface charge. The polarization so induced arises from the alignment of electric dipoles (if present) and the displacement of positive and negative charges in the dielectric. For an isotropic, linear dielectric, the polarization vector ***P*** is proportional and parallel to the applied field vector ***E***. The electric flux density, or electric displacement, ***D*** is defined by (in cgs units)

$$\boldsymbol{D} = \boldsymbol{E} + 4\pi\boldsymbol{P} = \varepsilon\boldsymbol{E} \tag{1.1}$$

where ε is the static dielectric constant of the medium. From eq. (1.1) it follows that

$$\varepsilon = 1 + 4\pi\chi \tag{1.2}$$

where χ(= ***P/E***) is the susceptibility. For isotropic dielectrics ε and χ are scalar quantities, which are dependent on the molecular properties of the dielectric. The dielectric constant is determined by the polarizability of the lattice. The polarizability, α, of an atom (or molecule) is defined by

$$\mu = \alpha\boldsymbol{F}, \tag{1.3}$$

where μ is the electric dipole moment and **F** is the local, or effective field acting on the given atom. The polarization ***P*** is defined as the net dipole moment per unit volume and is given by

$$P = \sum_i N_i \mu_i = \sum_i N_i \alpha_i F_i \tag{1.4}$$

where N_i *i*s the number of dipoles per unit volume.

The local field *F* at a given lattice site *i* is generally written as

$$F_i = E + E_{\text{int}} = E + 4\pi \sum_i \phi_{ij} P_j \tag{1.5}$$

where *E* is the applied field, and E_{int} is the internal field acting on the ion *i* due to the other ions *j*. It is usually expressed as a power series in odd powers of the polarization. For small field measurements, however, only the first power term in the polarization need be considered as indicated in Eq. (1.5). ϕ_{ij} is the internal field coefficient, which is a dimensionless quantity that depends on the position of the ion in the lattice. For diagonally cubic lattices, i.e., lattices in which all ions have cubic environment, the Lorentz internal field is applicable and ϕ_{ij} = 1/3. For other lattices the field at each site needs to be computed.

For anisotropic dielectrics,ε, χ and α are tensors, and Eq. (1.1) must be written as

$$\boldsymbol{D} = \varepsilon.\boldsymbol{E} \tag{1.6}$$

with components $$D_j = \sum_{j=1}^{3} \varepsilon_{ij} E_j, \ (i = 1,2,3) \tag{1.7}$$

All other quantities follow similarly. When the dielectric is subjected to an alternating field, both ***D*** and ***P*** will vary periodically with time. In general, however, **D** and **P** cannot follow the field instantaneously. There will always be inertial and energy dissipation effects (losses) and these cause a lag in phase between **E** and the response of the material. Thus, if $$\boldsymbol{E} = \boldsymbol{E_0}\text{Cos } \omega t \tag{1.8}$$

then $$\boldsymbol{D} = \boldsymbol{D_0}\ \text{Cos}(\omega t - \delta) \tag{1.9}$$

where δ is the loss angle. It is independent of E_0 but generally depends on frequency.

In the presence of dielectric losses and relaxation effects, ε and χ are complex quantities composed of charging (real) and loss (imaginary) components. Thus

$$\varepsilon^* = \varepsilon' - i\varepsilon'' \tag{1.10}$$

and $$\chi^* = \chi' - i\chi'' \tag{1.11}$$

The loss angle is given by $$\tan\delta = \varepsilon''/\varepsilon' \tag{1.12}$$

It is simply related to the Q-factor of the dielectric by Q = 1/tanδ, and is obtained rather directly from experiment. ε' and ε'' are related, at any given frequency, by the Kramers-Kronig dispersion relations.

1.4. Frequency Dependence of Polarisation

Polarization occurs due to several atomic mechanisms. For example, let us consider an atom placed inside an electric field. The centre of positive charge is displaced along the applied field direction, while the centre of negative charge is displaced in the opposite direction. Thus a dipole is produced. When a dielectric material is placed inside an electric field such dipoles are created in all the atoms inside. This process of producing electric dipoles which are oriented along the field direction is called polarization in dielectrics.

There are several types of polarisation mechanisms. The basic polarisations mechanisms are; space charge (α_s), orientational or dipolar (α_o), ionic (α_i) and electronic (α_e) (Fig.1.2). The total polarizability of dielectric placed in an alternating field can be written as;

$$\alpha_{Tot} = \alpha_s + \alpha_o + \alpha_i + \alpha_e \qquad (1.13)$$

Space charge polarization is the slowest process, as it involves the diffusion of ions over several interatomic distances. The relaxation time for this process is related to the frequency of successful jumps of ions under the influence of the applied field, a typical value being 10^2 Hz. Correspondingly, space charge polarisation occurs at lower frequencies (50 – 60 Hz). Consider a dielectric medium placed between two electrodes. When no field is applied to the electrode, the positive and negative charges are not separated and there are fixed number of charges. On the other hand, when an electric field is applied, the charges are separated. The positive charges are accumulated near the negative electrode. Therefore, a dipole moment is induced due to displacement of ions. Then, the induced dipole moment per unit volume gives the induced polarisation. This polarisation is also known as interfacial polarisation.

The orientational or dipolar polarisibility arises when the substance is built up of molecules possessing a permanent electronic dipole moment which may be more or less free to change orientation in an applied electronic field. More clearly, according to Debye, this type of polarisation is due to the rotation (orientation) of the molecules of polar dielectrics having a constant dipole moment in the direction of the applied electric field. Orientation polarization is even slower than ionic polarization. The relaxation time for orientation polarization in a liquid is less than that in a solid. For example the relaxation time for orientation polarization is 10^{-10} s in liquid propyl alcohol while it is 3×10^{-6}s in solid ice. Orientation polarization occurs when the frequency of the applied voltage is in the audio range.

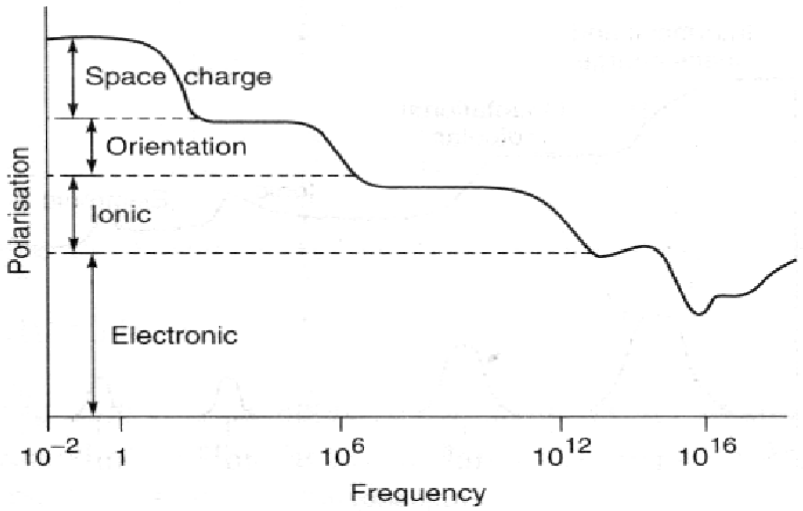

Figure 1.2 *Frequency dependence of the polarisation processes*

The ionic contribution comes from the displacement and deformation of a charged ion with respect to other ions, i.e. Ionic polarization is due to displacement of ions over a small distance due to the applied field. Since ions are heavier than electron cloud, the time taken for displacement is larger. The frequency with which ions are displaced is of the same order as the lattice vibration frequency (~10^{13} Hz). This means that for optical frequency the ions do not respond, as the time required for lattice vibrations is nearly 100 times larger than the period of applied voltage at optical frequency. Hence, at optical frequencies, there is no ionic polarization. If the frequency of the applied voltage is less than 10^{13} Hz, the ions respond. Hence at 10^{13} Hz, we have both electronic polarization and ionic polarization responding.

The electronic contribution arrives from the displacement of electrons in an atom relative to the deformation of the electron shell about a nucleus by the application of external electric field. Electronic polarization is extremely rapid. Even when the frequency of the applied voltage is very high in the optical range (~ 10^{15} Hz), electronic polarization occurs during every cycle of the applied voltage.

In the calculation of total polarization, the space charge polarization is not taken into account, since it occurs as interface and it is very small and hence negligible. In addition to this, the fields are not well defined at interfaces. Therefore, the total polarization vector is given by,

$$\boldsymbol{P} = \boldsymbol{P_e} + \boldsymbol{P_i} + \boldsymbol{P_o} \qquad (1.14)$$

where $\boldsymbol{P_e}$; electronic polarisation, $\boldsymbol{P_i}$; ionic oplarisation and $\boldsymbol{P_0}$; orientational polarisation

1.5. Ferroelectricity and Polarization

Ferroelectricity is a phenomenon which was discovered by Valasek in 1921 [3]. Since then, many essential features of the ferroelectric phenomenon were studied and described. Chronological information is provided for the early ferroelectric crystals in Table 1.1. Now, many excellent books introducing ferroelectric crystals and explaining ferroelectricity (with a number of phenomenological theories) have been published [4-14]. Rochelle salt ($NaKC_4H_4O_64H_2O$) was the first material found to show ferroelectric properties, such as a reorientable spontaneous polarization ***(P_s)***, on cooling below a transition temperature (T_C; Curie point). Many ferroelectrics are low temperature modifications of a high temperature, higher symmetry structure (prototype) which has no spontaneous polarization. This prototypic structure is also called paraelectric. In the ferroelectric phase, modifications to cation and anion positions occur to give relative displacements of ions inside the unit cell, resulting in reversible spontaneous dipole moments. The moment which develops polarization ***(P)*** is equal to qd/V, where q is the electric charge on the displaced ion, d is the relative displacement, and V is the volume of the unit cell. This moment is related to the electric displacement vector as;

$$\boldsymbol{D}=\varepsilon_0 \varepsilon \boldsymbol{E}= \varepsilon \boldsymbol{E}+\boldsymbol{P} \tag{1.15}$$

where ε_0 and ε are the free space and relative permittivity respectively [5,15].

1.6. Piezoelectricity

All ferroelectric materials are potentially piezoelectric (see Fig. 1.1 for a crystal classification). Piezoelectricity is the ability of certain crystalline materials to develop an electrical charge proportional to an applied mechanical stress [9]. This is also called the direct piezoelectric effect. Piezoelectric materials also show a converse effect, where a geometric strain (deformation) is produced on the application of a voltage. The direct and converse piezoelectric effects can be expressed in tensor notation as,

$$P_i = d_{ijk}\sigma_{jk} \text{ (Direct piezoelectric effect)} \tag{1.16}$$

$$\chi_{ij} = d_{kji}E_k \text{ (Converse piezoelectric effect)} \tag{1.17}$$

where P_i is the polarization generated along the i-axis in response to the applied stress σ_{jk}, and d_{ijk} ($=d_{kji}$) is the piezoelectric coefficient. For the converse effect, χ_{ij} is the strain generated in a particular orientation of the crystal on the application of electric field E_k along the k-axis [5].

Table 1.1. A partial list of early ferroelectric crystals [12-14].

Name and Chemical Formula	Curie Temperature, T_C (^oC)	Spontaneous Polarization, P_S ($\mu C/cm^2$)	Year in which reported
Rochelle Salt $NaKC_4H_4O_6 \cdot 4H_2O$	23	0.25	1921
Potassium Dihydrogen Phosphate KH_2PO_4 (KDP)	-150	4	1935
Potassium Dihydrogen Arsenate KH_2AsO_4	-177	5	1938
Potassium Dideuterium Phosphate KD_2PO_4	-60	5.5	1942
Barium Titanate ($BaTiO_3$)	120	26	1945
Lead Titanate ($PbTiO_3$)	490	>50	1950
Potassium Niobate ($KNbO_3$	415	30	1951
Lead Zirconate Titanate* $Pb(Zr_xTi_{1-x})O_3$	~350	>40	1952

*polycrystalline ceramic

1.7. Perovskite Crystal Structure

Most of the useful ferroelectrics, such as barium titanate (BT), lead titanate ($PbTiO_3$), lead zirconate titanate (PZT), lead lanthanum zirconate titanate (PLZT), and potassium niobate ($KNbO_3$), have the perovskite structure. Perovskite is the mineral name of calcium titanate ($CaTiO_3$). Its simplest structure is cubic, which is the high temperature form for many mixed oxides of the ABO_3 type. The simple cubic structure (space symmetry Pm-3m) consists of corner sharing oxygen octahedra (BO_6) arranged in three dimensions with smaller, highly charged cations (B: Ti^{4+}, Zr^{4+}, Sn^{4+}, Nb^{5+}, Ta^{5+}, W^{6+}, etc.) located in the middle of the octahedra, and lower charged, larger cations (A: Na^{+}, K^{+}, Ca^{2+}, Ba^{2+}, Pb^{2+}, etc.) in between the octahedra. The structure is shown in Fig. 1.3. Most perovskite-type ferroelectrics are compounds with either $A^{2+}B^{4+}O_3^{2-}$ or $A^{1+}B^{5+}O_3^{2-}$ type formula [16].

The perovskite structure can be also regarded as a cubic close-packed arrangement of large A and O ions with smaller B ions filling the octahedral interstitial positions. The structure is also very tolerant to cation substitution to both A and B sites of lattice, and hence may lead to more complex compounds, such as $(K_{1/2}Bi_{1/2})TiO_3$, $Pb(Fe_{1/2}Ta_{1/2})O_3$, $Pb(Co_{1/4}Mn_{1/4}W_{1/2})O_3$, $Pb(Mg_{1/3}Nb_{2/3})O_3$, and $Pb(Zn_{1/3}Nb_{2/3})O_3$ [16,17].

The most important member of the tetragonal phosphates is potassium dihydrogen phosphate (KH_2PO_4), commonly abbreviated as KDP [13]. Common characteristics of these early ferroelectrics are that they are colorless, water-soluble substances, and can be grown in large crystals from solution. As will be discussed later, ferroelectricity is mostly observed in certain temperature regions delimited by transition (or Curie) points (T_C), above which the crystals are no longer ferroelectric. In Rochelle salt and KDP, ferroelectricity is present at low temperatures due to their T_C points, +23 and -150 ^{0}C, respectively [13,14]. For study of the ferroelectric effect, these crystals served their purpose. However, from the device application point of view, water solubility, low T_C points, and low polarization values are limiting factors.

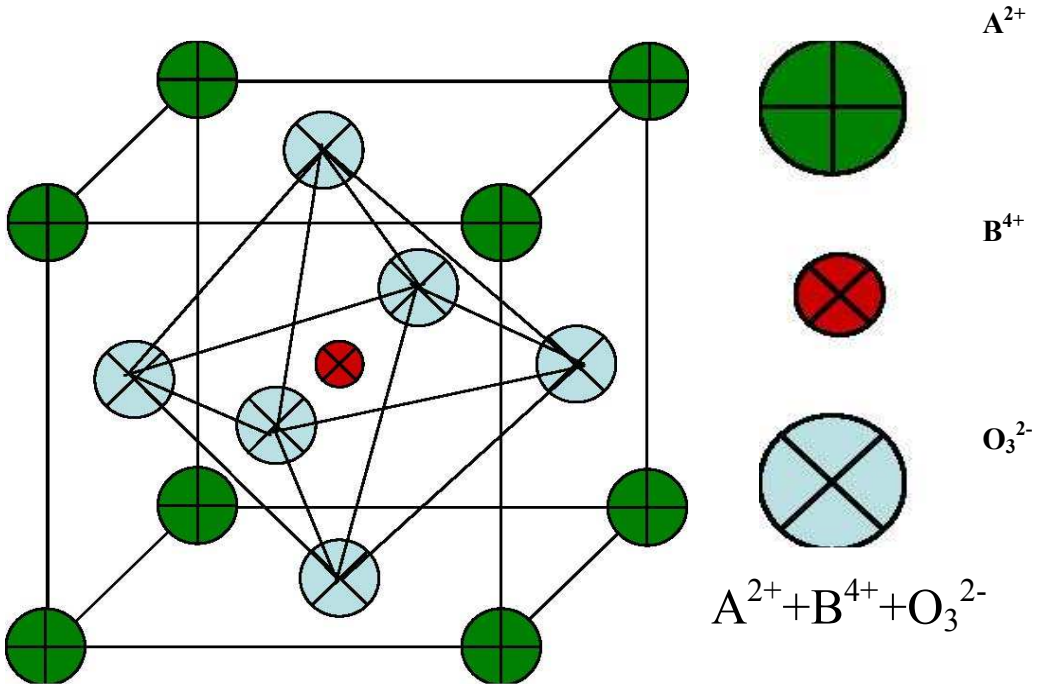

Figure 1.3 A cubic ABO_3 perovskite-type unit cell.

In 1945, barium titanate ($BaTiO_3$), the first ceramic material in which ferroelectric behavior was observed, was reported [18]. With its much simpler structure (perovskite), better ferroelectric properties, chemical and mechanical stability, barium titanate (BT) became one of the most extensively studied ferroelectric materials [12]. $BaTiO_3$ was considered not only as a model system for ferroelectricity, but also for practical applications. Added to the chemical and mechanical stability, it exhibits ferroelectric properties at and above room temperature and can be easily prepared and used in the form of polycrystalline samples [14].

The discovery of ferroelectricity in barium titanate, $BaTiO_3$ [18] has given birth to a large number of ABO_3 type perovskite ferroelectrics, where A= monovalent, divalent or trivalent and B= trivalent, tetravalent or pentavalent. The ideal structure is cubic perovskite, where A and B cations are arranged on a simple cubic lattice and the O ions lie on the face centers nearest the transition metal B cations. Thus the B cations are at the centre of O octahedra, while the A cations lie at larger twelve fold-coordinated sites. This ideal structure displays a wide variety of structural instabilities in the various materials. These may involve rotations and distortions of the O octahedral as well as displacements of the cations from their ideal sites. The interplay of these instabilities accounts for the rich variety of ferroelectric (FE) and antiferroelectric (AFE) behaviors.

By the 1950's the solid solution system $Pb(Ti,Zr)O_3$ (PZT), which also has the perovskite structure, was found to be ferroelectric. PZT compositions are now the most widely exploited of all piezoelectric ceramics both in research and industry. An up to date brief description of BT and PZT systems can be found in ref [19]. As an example of complex perovskites, a relaxor type ferroelectric system will be discussed separately in a later section.

1.8. Ferroelectric Phases and Domains

Ferroelectrics may exhibit one or more ferroelectric (polar) phases (Fig. 1.4) that show a domain structure in which the individual domain states can be reoriented by an applied field. In a ferroelectric crystal usually there are many domains (regions with uniform polarization). Within each individual domain, all the electric dipoles are aligned in the same direction. These domains in a crystal are separated by interfaces called domain walls [16]. Since these walls differ from the perfect crystal, there is a certain amount of energy (W_{dw}; domain wall energy) associated with them, in addition to the elastic energy, W_e. From energy considerations, in real materials, domain patterns depend on many factors, including the existing defect structure and concentration, stress and electric history, boundary conditions, temperature relative to T_C, and even the history of crystal preparation [12, 20]. The ferroelectric domains were first demonstrated in a study of spontaneous birefringence [21, 22]. The explanation for the origin of a ferroelectric domain, from a phenomenological point of view, is that the polydomain system is in a state of minimum free energy. From a microscopic viewpoint, domains were attributed to the change in the electrostatic forces acting on the crystal's faces owing to the spontaneous polarization that occurs as the crystal goes

through the paraelectric-ferroelectric phase transition.

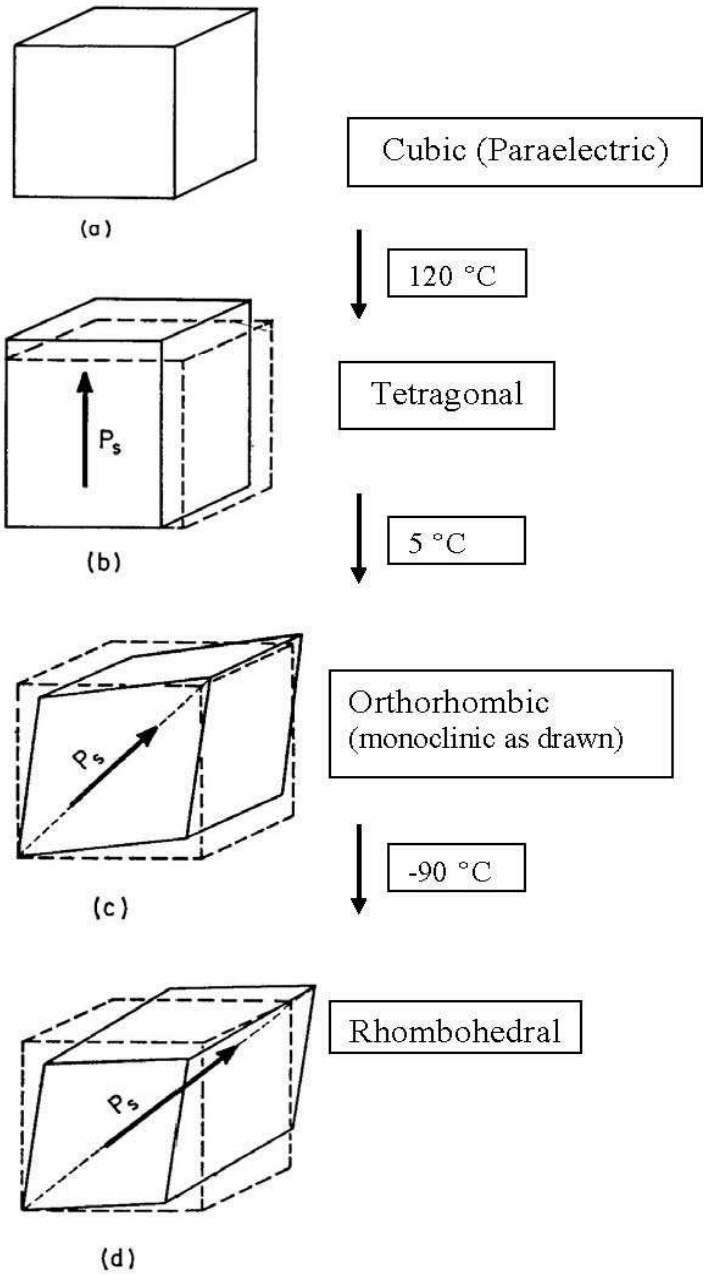

Figure 1.4 Unit cells of the four phases of $BaTiO_3$: a) Cubic, stable above 120 ^{O}C (Tc), b) Tetragonal, stable between 120 ^{O}C and 5 ^{O}C, c) Orthorhombic, stable between 5 ^{O}C and -90 ^{O}C, (monoclinic as drawn) d) Rhombohedral, stable below -90 ^{O}C. (The dotted lines in (b), (c), and (d) delineate the original cubic cell. Arrows indicate the direction of the spontaneous polarization, Ps, in each phase [14].

Fig. 1.5 depicts 180^O domain formation which minimizes the electrostatic energy of the system. Defects and internal stresses must be also considered for a crystal that exhibits piezoelectricity in the paraelectric state [16]. The presence of mechanical stress in a crystal results in the development of non-180^O domain walls configured to minimize the strain. An example is presented in Fig. 1.6 [19]. The structure of a ferroelectric domain depends on the structure of the crystal. In a ferroelectric crystal, the variety of domain patterns and the number of types of domain walls depend on the number of orientations of the dipole moment when the spontaneous polarization occurs from the prototype phase.

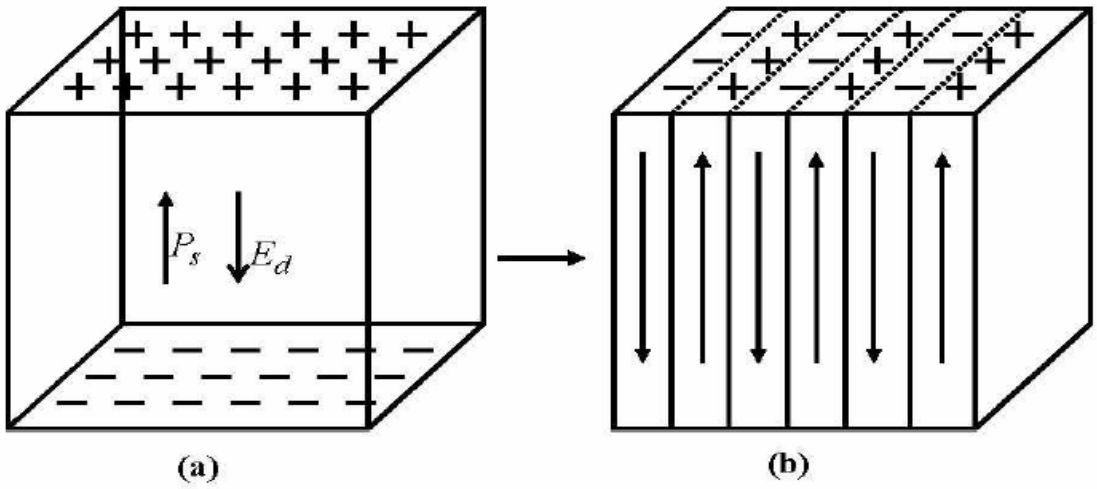

Figure 1.5. (a)Surface charge and depolarizing field (E_d) associated with spontaneous polarisation (P_s); (b) formation of 180^O domains to minimize electrostatic energy [19]

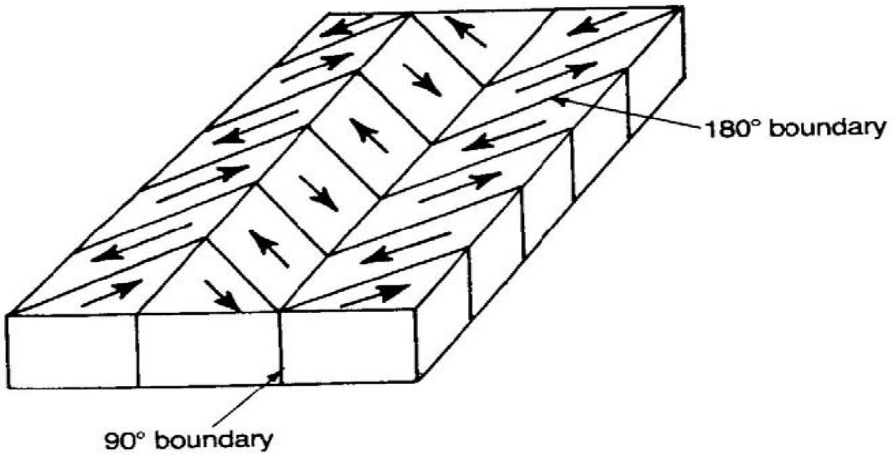

Figure 1.6 Schematic illustrations of 180^O and 90^O domain walls [19].

Ferroelectric domain structures can be observed by various methods:

a) *Optical birefringence*: In optically anisotropic crystals (where the refractive index for light polarized along the polar axis is different from at least one other axis in a crystal), domains can be observed due to the presence of birefringence by using a polarized light microscope.
b) *Second-harmonic generation*: This technique can be used for any crystal which can be phase matched for second harmonic generation with light depends on the optical interaction length with a single domain of either Sign [12]. This technique can be also used to measure the width of extremely small domains with periodic geometry. [23]
c) *Etching and Scanning Electron Microscopy*: For the ferroelectric crystals with sub-micrometer size domain structures, electron microscopy is utilized. Since the information is limited to the surface, very thin crystals are needed. Chemical etching is also commonly used to reveal the domain structures by selective etching of positive and negative ends of domains. Etched samples can be observed by scanning electron microscopes. HCl was commonly used for the early studies in $BaTiO_3$ [6,12].
d) *Powder pattern method*: This technique involves use of a colloidal suspension of charged particles that can preferentially deposit on either positive or negative ends of domains [24].
e) *Liquid crystal method*: This technique can be used to reveal 180^O domain walls [25]. This simple technique is fast and the liquid crystal can respond rapidly to changes of the domain configuration.
f) *X-ray topography*: This technique utilizes anomalous dispersion of X-rays causing a difference between the positive and negative ends of domains [26].
g) *Transmission Electron Microscopy*: A technique using diffraction contrast methods and can be applied to both 180^O and non-180^O domains.

Certainly domain observation techniques are not limited to these techniques mentioned here. The usefulness of each technique varies from one material to another, with the shape, size, transparency of the crystal, and the expected outcome of the observations [12]. Sometimes depending on these criteria, these techniques can be combined for the maximum efficiency. Domain structures are strongly dependent on the symmetry of the ferroelectric phase. As the changes occur in symmetry resulting in

different domain configurations, the other material properties will also be influenced. A brief description on the thermodynamics of ferroelectricity is given in the following section.

1.9. Ferroelectric Phase Transitions and Curie-Weiss Behavior

A typical ferroelectric possesses a spontaneous polarisation $\boldsymbol{P_s}$ that increases with decrease in temperature and appears discontinuously or some time continuously at certain temperature, called Curie temperature or transition temperature T_C. The symmetry of the crystal changes at a phase transition point. All the phase transitions in crystals are due to changes in the force of interaction between the atoms. This change may produce various new properties in crystals. Phase transitions that produce or alter the spontaneous polarisation are called ferroelectric phase transition. By changing temperature or pressure, the atomic arrangements in the crystals may be changed with out any change in chemical compositions. The difference in crystal structures on either side of T_C may be large or small. At this Curie temperature the material undergoes a transition from paraelectric (PE) to a ferroelectric (FE) phase. The ferroelectric structure has a lower symmetry than the corresponding paraelectric structure. At a temperature $T>T_C$ the crystal does not exhibit ferroelectricity, while for $T<T_C$ it is ferroelectric [12-14]. If there are more than one ferroelectric phases as shown in Figure 1.4, the temperature at which the crystal transforms from one ferroelectric phase to another is called the transition temperature. Early research studies on ferroelectric transitions have been summarized by Nettleton [27, 28]. Fig. 1.7 shows the variation of the relative permittivity (ε_r) (or dielectric constant) with temperature as a $BaTiO_3$ ferroelectric crystal is cooled from its non-ferroelectric (or paraelectric) cubic phase to the ferroelectric tetragonal, orthorhombic, and rhombohedral phases. Near the Curie point or phase transition temperatures, thermodynamic properties including dielectric, elastic, optical, and thermal constants show an anomalous behavior. This is due to a distortion in the crystal as the phase changes. The temperature dependence of the dielectric constant above the Curie point $(T>T_C)$ in most ferroelectric crystals is governed by the Curie-Weiss law [29]:

$$\varepsilon' = \varepsilon_0 + \frac{C}{(T - T_0)} \tag{1.18}$$

where ε' is the permittivity of the material, ε_0 is the permittivity of the vacuum, C is the Curie constant and T_0 is the Curie-Weiss temperature.

In case of single crystal ferroelectrics, or other polar materials, the value of ε', P_s and other properties are very sensitive to dopants and defects in the crystal [12]. But in ceramic polar dielectrics these effects are more pronounced and there is an added influence of some parameters such as porosity, grain size, sintering time and sintering temperature etc. [2].

The Curie-Weiss temperature T_0 is, in general, different from the Curie point T_C. For first order transitions $T_0 < T_C$ while for second order phase transitions $T_0 = T_C$ [9, 29]. Transition into a ferroelectric phase occurs differently in different type of ferroelectric materials. These transitions may be of first order or second order in classical proper ferroelectrics [12]. The order of the phase transition is defined by the discontinuity in the partial derivatives of the Gibbs free energy (G) of the ferroelectric at the phase transition temperature [30]. For an n^{th}-order phase transition, the n^{th}-order derivative of G is a discontinuous function at the transition temperature. Thus, spontaneous polarization and strain change continuously at the phase transition for a ferroelectric with the second order phase transition, and are discontinuous at the phase transition temperature for first-order ferroelectrics. Other ferroelectrics show diffuse phase transition behavior. An additional subset in the diffuse ferroelectrics, called "relaxors", will be discussed separately in later section. General property changes with ferroelectric phase transitions are summarized in Fig. 1.8, schematically [30]. *By definition, an applied electric field can reorient the direction of polarization in any ferroelectric crystal, regardless of what type of ferroelectric behavior is exhibited.*

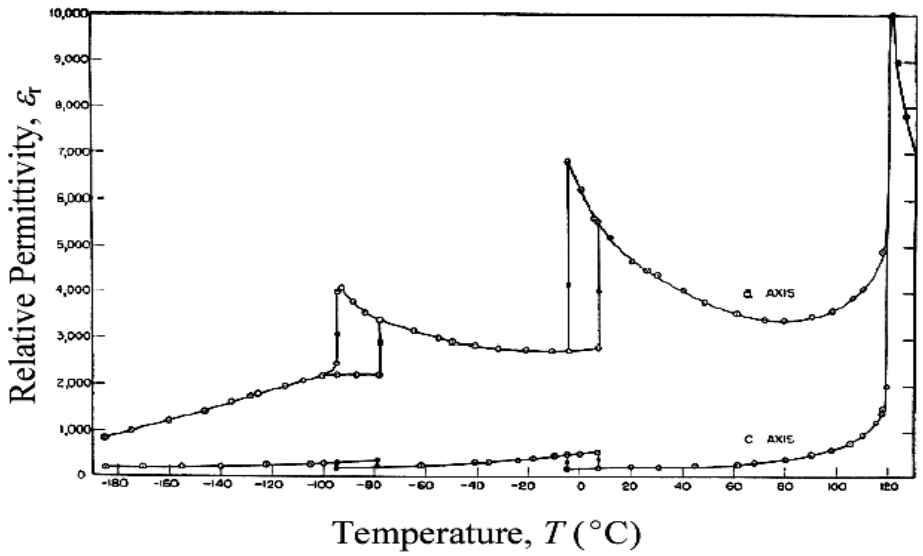

Figure 1.7. Relative permittivities measured along the *a* and *c* directions of a poled tetragonal $BaTiO_3$ crystal versus temperature in a ferroelectric [31]. Note that the samples were not repoled at lower temperatures. It is a residual poling that yields the apparent anisotropy in the rhombohedral phase.

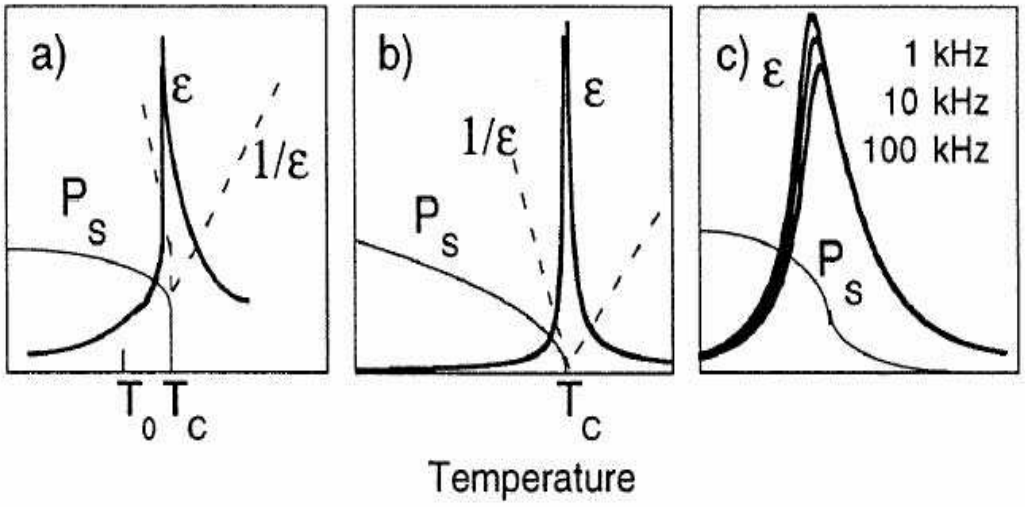

Figure 1.8 Schematic temperature dependence of the dielectric permittivity *(ε)* and spontaneous polarization (***P**s*) for a) a first- and b) a second-order ferroelectric and c) for a relaxor ferroelectric [30].

1.10. Classification of Ferroelectric Crystals

Depending on the temperature variation of dielectric constant or Curie constant C, ferroelectrics can be divided into two groups. In one group, the compounds undergoing order-disorder type transition, have a Curie constant of the order 10^3 while for others which undergoes displacive type transition, it is of the order of 10^5. Initially ferroelectric materials were broadly classified into two categories: (a) soft (KH_2PO_4 -type) and (b) hard ($BaTiO_3$ -type).The phase transition in soft (H-bonded) ferroelectrics is of order disorder type where as in hard ones it is displacive type. The phase transition in soft ferroelectrics involves not only the ordering of the disordered hydrogen atom, but also the deformation of the atomic groups like SO_4^{-2}, Se^{-2}_4 and PO_4^{-3}. In case of displacive type of transition a small atomic displacement of some of the atoms is mainly responsible for phase transition, which has been found in some of the perovskites. However, the difference between displacive and order-disorder type of transition becomes uncertain when the separation of relevant disorder becomes comparable with the mean thermal amplitude of those atoms. The character of ferroelectrics is represented in terms of the dynamics of phase transition

1.11. Diffuse Phase Transition

Many phase transitions in macroscopic homogeneous materials are characterized by the fact that the transition temperature is not sharply defined. In these, so-called diffuse phase transition temperature (DPT), the transition is smeared out over a certain temperature interval, resulting in a gradual change of physical properties in this temperature region. Though this phenomenon is observed in several types of materials [32], however, the most remarkable examples of DPT are found in ferroelectric materials [33]. Ferroelectrics diffuse phase transitions (FDPT) are first mentioned in the literature in the early 1950's [34]. Some characteristics of the DPT are: (a) broadened maxima in the permittivity- temperature curve, (b) gradual decrease of spontaneous and remanent polarisations with rising temperature, (c) transition temperatures obtained by different techniques which do not coincide, (d) relaxation character of the dielectric properties in transition region and (e) no Curie-Weiss behavior in certain temperature intervals above the transition temperature. The diffuseness of the phase transition is assumed to be due to the occurrence of fluctuations in a relatively large temperature interval around the transition. Usually two kinds of fluctuations are considered: (a) compositional fluctuation and (b) polarisation (structural) fluctuation. From the thermodynamic point of view, it is clear that the

compositional fluctuation is present in ferroelectric solids-solutions and polarisation fluctuation is due to the small energy difference between high and low temperature phases around the transition. This small entropy difference between ferroelectric and paraelectric phase will cause a large probability of fluctuation. Kanzing [35] has observed from X-ray diffraction that in a narrow temperature range around the transition $BaTiO_3$ single crystal splits up into FE and PE micro regions. According to Fritsberg [36] substances of less stability are expected to have a more diffuse transition. For relaxor as well as other FDPT the width of the transition region is mainly important for practical applications. Smolensky [37] and Rolov [38] have introduced a model calculation, based on the concept of Gaussian distribution for both the compositional and polarisation fluctuation, from which the diffuseness parameter can be calculated. Complex perovskite type ferroelectrics with distorted cation arrangements show DPT which is characterised by a broad maximum for the temperature dependence of dielectric constant *(ε')* and dielectric dispersion in the transition region [37, 39]. For DPT *ε'* follows modified temperature dependence

$$\frac{1}{\varepsilon'} - \frac{1}{\varepsilon_m} = (T - T_m)^{\gamma} / C' \qquad (1.19)$$

where T_m is the temperature at which *ε'* reaches maximum, ε_m is the value of *ε'* at T_m, *C'* is the modified Curie Weiss like constant and γ is the critical exponent, explains the diffusivity of the materials, which lies in the range $1 < \gamma < 2$ [40]. The smeared out *ε'* vs *T* response has generally been attributed [37, 41, 42] to the presence of microregions with local compositions varying from the average composition over length scale of 100 to 1000 *Å*. Different microregions in a macroscopic sample are assumed [42] to transfer at different temperature, so-called Curie range, leading DPT which is due to compositional fluctuations. The dielectric and mechanical properties of FE system below their T_C are functions of the state of polarisation and stress. So ferroelectrics have major application today because of their characteristic electro-optic, dielectric and hysteresis properties.

For many practical applications, it is desired to use the very large property maxima in the vicinity of the ferroelectric phase transition, to move the transition into the temperature range of interest and to broaden and diffuse the very large sharp peak values. In DPT the dielectric maxima is now much rounder and polarisation persists for a short range of temperature above T_m.

1.12. Relaxor Ferroelectrics

Relaxor ferroelectrics or relaxors, exhibit many properties similar to those of spin and dipolar glasses. Normally relaxor behavior in FE materials results from compositionally induced disorder or frustration. This behavior has been observed and studied most extensively in disordered ABO_3 perovskite ferroelectrics and is also seen in mixed crystals of hydrogen-bonded FEs and AFEs, the so-called protonic glasses. In this section we restrict our comments largely to the ABO_3 oxides.

Relaxor ferroelectrics are characterized by a broad maximum in the temperature dependence of the real part of the dielectric permittivity *(ε'),* a frequency-dependent temperature of the dielectric maximum *(T_m)* and a strong relaxation dispersion of the permittivity at temperatures around and below T_m. They possess local polarisation at temperature above T_m.

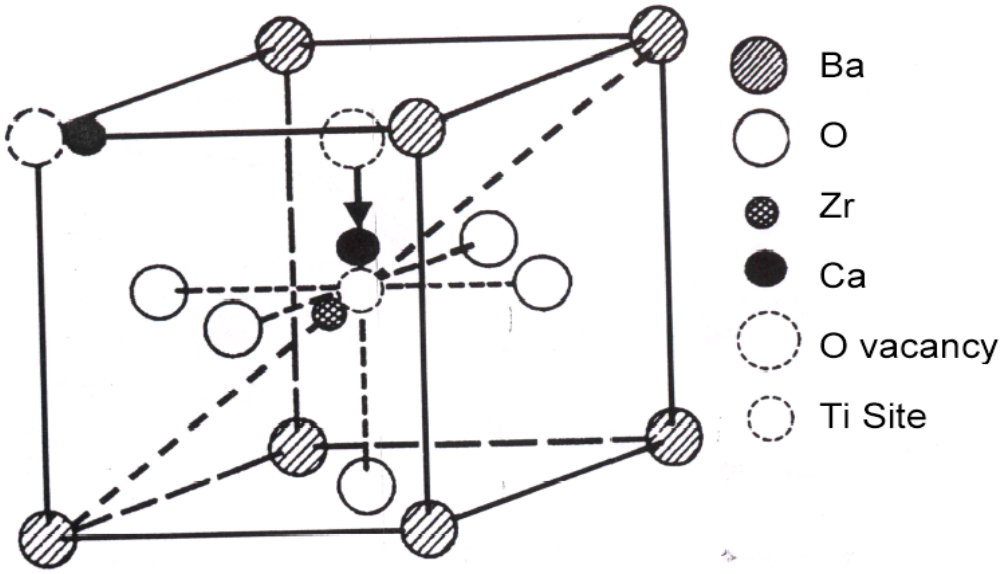

Figure 1.9. The cubic perovskite lattice of $BaTiO_3$ showing the location of various substituents and vacancies.

In the ABO_3 oxides (Fig. 1.9), substituting ions of different sizes, valences, and polarizabilities at both the A and B lattice sites produces dipolar defects and can introduce a sufficiently high degree of disorder so as to break translational symmetry and prevent the formation of a long-range ordered state. Instead, the dipolar motion in such systems freezes into a glass-like state on cooling below a dynamic transition temperature, T_m

In these highly polarizable host lattices, the presence of a dipolar impurity on a given site can induce dipoles in a number of adjacent unit cells within a correlation length of that site. We expect the dipolar motion within this correlation length to be correlated, leading to the formation of polar nanodomains. Indeed, such nanodomains have been observed in many ABO_3 relaxors at temperatures far above the peak in $\varepsilon'(T)$, and their occurrence is now considered to be crucial to the understanding of the properties of relaxors. We picture a distribution of sizes of such nanodomains in which the orientational degrees of freedom are correlated within each domain, but uncorrelated across the various domains. At sufficiently low temperatures, the dipolar motion within each domain freezes, resulting in the formation of an orientational glass (relaxor) state. Such a state is characterized by a distribution of relaxation times related to the sizes of the nanodomains. Two important characteristics of this relaxor state that distinguish it from simple dipolar glasses or spin glasses are the predominant existence of the dipolar nanodomains (vs. largely individual dipoles or spins) and the presence of some degree of cooperative freezing of the orientational degrees of freedom. Evidence of this cooperative effect comes from the observation of some remanent polarization in electric field hysteresis loops. It should be noted, however, that such evidence is also seen in systems of random dipoles in low polarizability hosts for doped alkali halides with sufficiently high concentration of dipoles.

In order to appreciate and understand the properties of relaxors, it is useful to contrast some of their properties with those of normal ferroelectrics. We do so with the help of Fig. 1.10. The contrast is as follows:

- The P-E hysteresis loop (Fig.10 a) is the signature of a ferroelectric in the low-temperature FE phase. The large remanent polarization, $\boldsymbol{P_R}$, is a manifestation of the cooperative nature of the FE phenomenon. A relaxor, on the other hand, exhibits a so-called slim-loop as shown on the righthand side. For sufficiently high electric fields the nanodomains of the relaxor can be oriented with the field leading to large polarization; however, on removing the field most of these domains reacquire their random orientations resulting in a small $\boldsymbol{P_R}$**.** The small $\boldsymbol{P_R}$ is evidence for the presence of some degree of cooperative freezing of dipolar (or nanodomain) orientations.

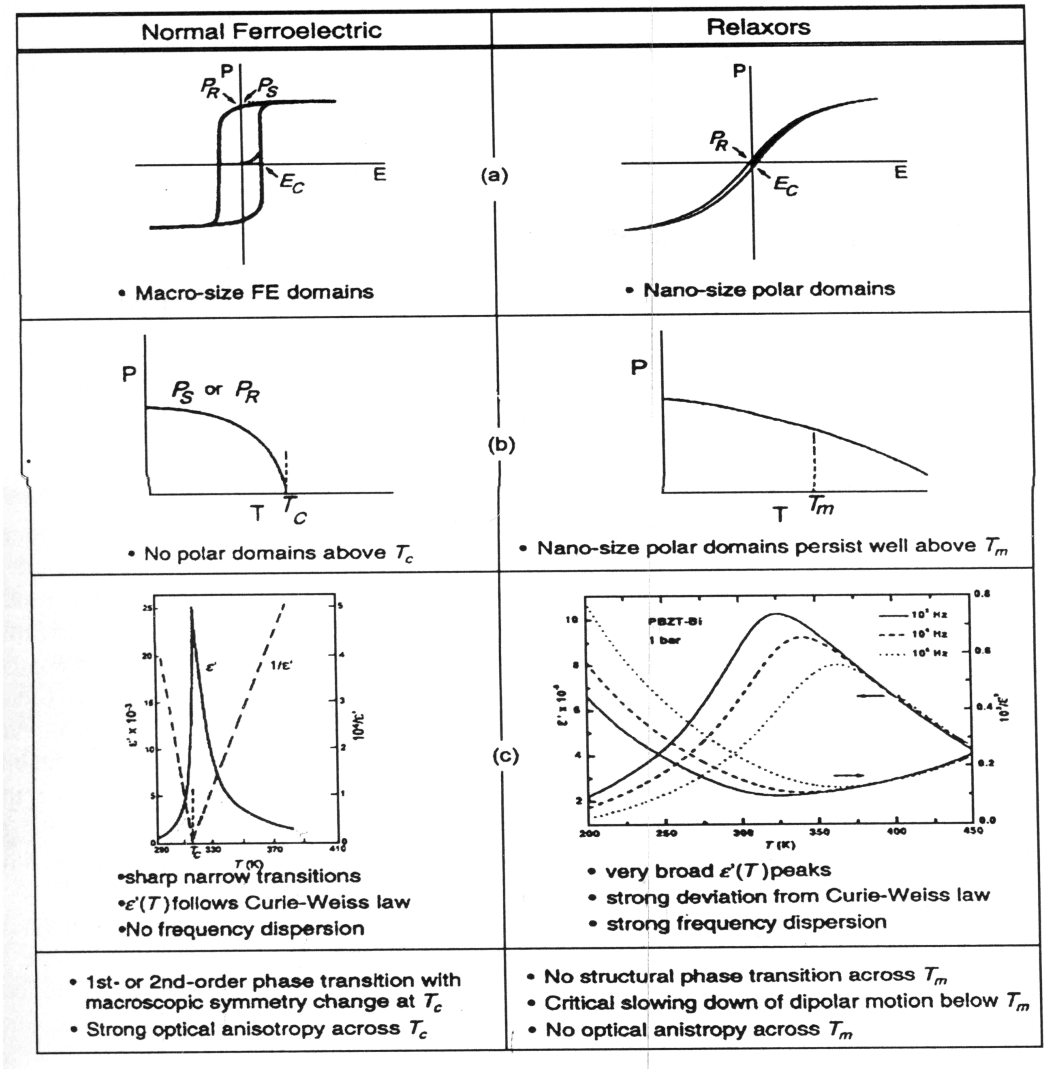

Figure 1.10 Contrast between the properties of normal ferroelectrics and relaxor ferroelectrics, or relaxors.

- The saturation and remanent polarizations of a ferroelectric decrease with increasing temperature and vanish at the FE transition temperature *(T_C).* The vanishing of ***P*** at T_C is continuous for a second-order phase transition (Fig.1.10b) and discontinuous for a first-order transition. No polar domains exist above T_C. By contrast, the field-induced polarization of a relaxor decreases smoothly through the dynamic transition temperature T_m and retains finite values to rather high temperatures due to the fact that nano-size domains persist to well above T_m.
- The static dielectric susceptibility, or dielectric constant *(ε'),* of a ferroelectric exhibits a sharp, narrow peak at T_C (Fig. 1.10c). For a single crystal the peak is very sharp and the width at half max is ~10-20 K. For a mixed oxide FE, e.g., a PZT, the peak is somewhat rounded due to compositional fluctuations, and the width at half

max is typically ~20-40 K. The FE response is frequency independent in the audio frequency range. By contrast, a relaxor exhibits a very broad $\varepsilon'(T)$ peak and strong frequency dispersion in the peak temperature (T_m) and in the magnitude of ε' below T_m. The conventional wisdom has been that the broad $\varepsilon'(T)$ peak, also referred to as a "diffuse phase transition," is associated with compositional fluctuations leading to many micro FE regions with different compositions and T_C' s. The breadth of the peak is simply a manifestation of the dipolar glass-like response of these materials.

- The temperature dependence of ε' of a ferroelectric obeys a Curie-Weiss law, $\varepsilon' = C/(T-T_0)$, above T_C could be shown by the linear $1/\varepsilon'$ vs. T response. By contrast $\varepsilon'(T)$ of a relaxor exhibits strong deviation from this law for temperatures of many 10s to a few 100s degrees above T_m.
- The FE transition can be thermodynamically first or second order and involves a macroscopic symmetry change at T_C. Transparent FEs exhibit strong optical anisotropy across T_m.

The above discussion makes it very clear that the properties and physics of relaxors are very different from those of normal ferroelectrics.

1.13. Physics of Relaxor Ferroelectrics

In this section we shall discuss the properties and physics of relaxor FEs or relaxors, by concentrating on a few prototypical materials. As already noted, in ferroelectrics, relaxor behavior results from either frustration or compositionally induced disorder. This disorder and related random fields are believed to be responsible for the relaxor properties of the mixed ABO_3 perovskite oxides (Fig. 1.9) and of the mixed FE and AFE hydrogen-bonded crystals such as rubidium ammonium dihydrogen phosphate, $Rb_{1-x}(NH_4)_xH_2PO_4$, or RADP. In addition to a broad, frequency-dependent peak in ε' (T) relaxors are characterized by the absence of macroscopic phase (symmetry) change at the transition. However, there is symmetry breaking at the nano-meter scale, leading to the formation of polar nanodomains that exist well above the peak in the susceptibility and strongly affect the properties. Relaxors possess very large dielectric constants, attractive for capacitors; exceptionally large electrostrictive coefficients, important for actuators and micro-positioners; and large electro-optic constants, useful for information storage, shutters, and optical modulators. Because of these remarkable properties and their applications, relaxors are one of the most active current research areas of ferroelectricity.

1.14. ABO_3 Relaxors

The parent compounds of ABO_3 perovskite relaxors (e.e., $PbTiO_3$, $PbZrO_3$, $KTaO_3$) are prototypical soft-mode systems whose dielectric properties and phase transitions are well understood in terms of soft phonon mode theory [12]. A variety of types of disorder in this lattice can produce dipolar defects and induce relaxor behavior. Thus, e.g., (i) in $PbMg_{1/3}Nb_{2/3}O_3$ (or PMN) and related relaxors the disorder is brought by differences in valence (5+ vs. 2+), ionic radii (0.64 Å vs. 0.72 Å), and electronegatives (1.6 vs. 1.2 on the Pauling scale) between Nb^{5+} and Mg^{2+} ions on the B site which introduce charge fluctuations and local ordering ; (ii) in La-substituted $PbZr_{1-x}Ti_xO_3$ (or PLZT) relaxors, the substitution of La^{3+} for Pb^{2+} at the A sites produces randomly distributed Pb^{2+} vacancies (one vacancy for every two La^{2+} ions) that, for high enough concentration, lead to a relaxor state; and (iii) the substitution of Nb^{3+} for Ta^{3+} and Li^{+} for K^{+} in $KTaO_3$ results in off-site dipolar defects that lead to a relaxor state at low concentrations. Clearly, numerous other substitutents in a variety of other FE perovskites can lead to relaxor behavior.

In reflecting on the occurrence of relaxor behavior in perovskites, there appear to be three essential ingredients: (1) the existence of lattice disorder, (2) evidence for the existence of polar nanodomains at temperatures much higher than T_m (3) these domains existing as islands in a highly polarizable (soft-mode) host lattice. The first ingredient can be taken for granted because relaxor behavior in these materials does not occur in the absence of disorder. The third ingredient is also an experimental fact in that relaxor behavior occurs in ABO_3 oxides with very large dielectric constants, i.e., very high polarizabilities. The second ingredient is manifested in many experimental observations common to all perovskite relaxors.

1.15. References

1. J. Valasek, *Phys. Rev*., **15**, 537 (1920).
2. A.R.Von Hippel, *Rev. Mod. Phys*. **22**, 228 (1950).
3. J. Valasek, *Phys. Rev*. **17**, 475 (1921).
4. W. Kanzig, *Ferroelectrics and Antiferroelectrics*, Academic Press,New York (1957).
5. J. F. Nye, *Physical Properties of Crystals*, Oxford University Press, Oxford 1957.
6. E. Fatuzzo and W. J. Merz, *Ferroelectricity,* North-Holland (1967).
7. J. C. Burfoot, *Ferroelectrics*, Van Nostrand, New York 1967.
8. J. B. Grindlay, *An Introduction to Phenomenological Theory of Ferroelectricity*, Pergamon Press, Oxford (1970).
9. B. Jaffe, W.R. Cook and H. Jaffe, *Piezoelectric Ceramics*, London (1971).
10. T. Mitsui, I. Tatsuzaki, and E. Nakamura, *An Introduction to the Physics of*

Ferroelectrics, Gordon and Breach, London (1976).
11. W. G. Cady, *Piezoelectricity*, McGraw – Hill, New York (1946).
12. M. E. Lines and A. M. Glass, *Principles and Applications of Ferroelectrics and Related Materials*, Clarendon Press, Oxford (1977).
13. H. D. Megaw, *Ferroelectricity in Crystals*, Methuen and Co., London (195).
14. F. Jona and G. Shirane, Ferroelectric Crystals, Pergamon Press, Oxford 1962.
15. D. D. Viehland, "*The Glassy Behavior of Relaxor Ferroelectrics*", Ph.D. Thesis, The Pennsylvania State University, University Park, PA (1991).
16. Y. Xu, *Ferroelectric Materials and Their Applications*, North-Holland Elsevier Sci. Publ., Amsterdam (1991).
17. L. E. Cross, *Ferroelectrics*, **151**, 305 (1994).
18. B. Wul and I. M. Goldman, *C. R. Acad. Sci. U. R. S. S*. **46**, 177 (1945).
19. A. J. Moulson and J. M. Herbert, Electroceramics, Chapman and Hall Press, New York (1996).
20. R. Landauer, *J. Appl. Phys*. **28**, 227 (1957).
21. H. Blattner, W. Kanzig, W. J. Merz, and H. Sutter, *Helv. Phys. Acta* **21**, 207 (1948).
22. B. T. Batthias and A. von Hippel, *Phys. Rev*. **73**, 1378 (1948).
23. R. C. Miller, *Phys. Rev*. **134,** A1313 (1964).
24. G. L. Pearson and W. L. Feldmann, *J. Phys. Chem. Solids* **9**, 28 (1958).
25. Y. Furuhata and K. Toriyama, *Appl. Phys. Lett*. **23**, 361 (1973).
26. C. A. Wallace, *J. Appl. Cryst*. **3**, 546 (1970).
27. R. E. Nettleton, *Ferroelectrics* **1**, 3, 87, 93, 111, 121, 127, 207, 221 (1970).
28. R. E. Nettleton, *Ferroelectrics* **2**, 5, 77, 93 (1971).
29. A. Safari, R. K. Panda, and V. F. Janas, *Key Eng. Mater*. **122-124**, 35 (1996).
30. D. Damjanovic, *Rep. Prog. Phys*. **61,** 1267 (1998).
31. W. J. Merz, *Phys. Rev*. **95**, 690 (1954).
32. A.J.Burggraaf, *Proc.9th Int Cong.on Sci of Ceramics*, Noordwijkerhout, Netherland (1977).
33. C.G.F Stenger, A.J.Burggraaf, *J.Phys. Chem.Solids*, **41**, 25 (1980).
34. W. Kanzig, *Helv. Phys. Acta* **24**, 175 (1951).
35. W. Kanzig, *Ferroelectric and Antiferroelectrics*, Academic Press, New york (1957).
36. J. Fritesberg, Proc. 4th Int. Meeting on Ferroelectricity, Leningrad (1977).
37. A.G.Smolensky, *J. Phys.Soc.Japan* **18**, 26 (1970).
38. B.N Rolov, *Soviet Phys. Solid state,* **6**, 1676 (1965).
39. A.G.Smolensky, *J Ferroelectricity,* **53**, 129 (1984).
40. V.S.Tiwari and D.Pandey, *J.Am Ceram Soc.II*, **77,** 1819 (1994).
41. V.V.Kirollov and V.A. Isupov, *Ferroelectrics*, **5**, 3, (1973).
42. L.E.Cross, *Ferroelectrics* **76**, 241 (1987).

Chapter 2

STATEMENT OF THE PROBLEM AND THESIS OBJECTIVES

2.1 Motivation and Objective.

Chapter 1 introduced major characteristics of dielectrics with a special emphasis on relaxor ferroelectrics, which have a wide range of applications. Among the device that utilizes the dielectric properties with a great extent is multilayer ceramic capacitor (MLCC). The concept of utilizing the reversible spontaneous polarisation as a memory state goes back to the early days of ferroelectric research. In this section (Chapter 2) we have discussed our motivation and interest behind the material selection and different characterisations with a brief review on previous work.

S.Gopalan and A.V. Virkar [1] examined the interdiffusion in doped $BaTiO_3$-$BaZrO_3$ sintered couples and a Kirkendall porosity formation was found indicating that transport occurs on all sub-lattices in the system. Solid solution formation mechanism of the system from precursor powder is not available in details.

$SrTiO_3$-$SrZrO_3$ (ST-SZ) solid solution is one of them, which holds promise for application as a proton conductor as well as voltage dependent tunable ceramics [2]. ST-SZ solid solution shows a super lattice structure due to its cell enlargement as a result of tilting of BO_6 (B=Ti, Zr) octahedra [3]. This type of disorder perovskite solid solution offers exciting new possibilities both in the investigation of fundamental physical phenomena and in the exploitation of novel properties for various applications. There is very little literature [2-4] available for this solid solution system.

In addition to the DRAM applications, $Ba_{0.5}Sr_{0.5}TiO_3$ have a variety of other applications which are currently being studied such as hydrogen gas sensors, pyroelectric sensors, as a dielectric layer in electroluminescent display devices and the new class of frequency tunable microwave devices, which include phase shifters, tunable filters, steerable antennas, varacters, frequency triplers, capacitors, oscillators, delay lines and parametric amplifiers etc [5-8]. Due to the above applications phase formation and reaction mechanism of BST is of our interest.

Recently, Kennedy *et al.* [9] conducted a detailed analysis of structural transitions in $SrZrO_3$ due to incorporation of $BaZrO_3$ perovskite due to the tilting of

ZrO_6 octahedra. However, no detailed studies on phase formation and reaction mechanism of $Ba_{0.5}Sr_{0.5}ZrO_3$ are reported in the systems.

Jonker and Kwestroo [10] studied the solid solution formation in the system $BaO\text{-}TiO_2\text{-}ZrO_2$. They observed that the $BaTiO_3\text{-}BaZrO_3$ forms a complete series of solid solution. It is also known that the $BaTiO_3$ forms complete solid solution with $SrTiO_3$ and $MgTiO_3$. However, $BaTiO_3$ and $CaTiO_3$ don't form a continuous series. So it inspires us to study the phase formation and reaction mechanism of all the end compositions and to investigate the solubility of Ca and Mg in the $BaTi_{0.6}Zr_{0.4}O_3$ ceramic. The phase formation and reaction mechanism of compositions $BaTi_{0.5}Zr_{0.5}O_3$, $SrTi_{0.5}Zr_{0.5}O_3$, $Ba_{0.5}Sr_{0.5}TiO_3$, $Ba_{0.5}Sr_{0.5}ZrO_3$, structural effect of Sr substitution on $BaTi_{0.5}Zr_{0.5}O_3$, structural effect of Zr on $Ba_{0.5}Sr_{0.5}TiO_3$ ceramic along with solubility of Ca and Mg in the $BaTi_{0.6}Zr_{0.4}O_3$ composition is discussed in Chapter 4 and Chapter 5. Stoichiometric study was reported in the Chapter 6 using EDXRF.

High permittivity $Ba(TiZr)O_3$ material is often used for dielectrics in commercial capacitor applications [11] and is a highly promising material for dynamic random access memory (DRAM) [12] and microelectromechanical system (MEMS) [13] applications due to its very stable, high insulating characteristic against voltage. It has been reported [11] that at ~15 atom % Zr substitution the three transition temperatures of $BaTiO_3$, rhombohedra to orthorhombic, orthorhombic to tetragonal and tetragonal to cubic, merge near room temperature and the doped material exhibits enhanced dielectric constant. With further increase in Zr contents beyond 15 atoms %, a diffuse dielectric anomaly in ceramic has been observed with the decrease in the transition temperature [14] and the material showed typical relaxor–like behavior in the range 25-42 atom % Zr substitution [15]. Most of the literature in the system $Ba(Ti_{1-x}Zr_x)O_3$ is restricted up to the value of x ~0.4 [12,13,16]. That is the reason, 50 atom% Zr substituted composition $Ba(Ti_{0.5}Zr_{0.5})O_3$ (BTZ) has been taken as a base material for the investigation of the effect of Sr substitution for Ba on its structural and dielectric properties.

In the other hand, barium strontium titanate (BST) ceramics are also popular for DRAM applications [17]. The recent work [18] suggests that $Ba_{1-x}Sr_xTiO_3$ thin films with x=0.5-0.6 are preferred for use at room temperature tunable circuit components. For example, H.M. Cristen *et al* [2] found a strong bias voltage tunability and very low hysteresis in the composition $Ba_{0.5}Sr_{0.5}TiO_3$. Considering all these, the compositions $Ba_{0.5}Sr_{0.5}TiO_3$ has been selected as a base material in the present study to investigate the effect of Zr^{4+} substitution for Ti^{4+} in the material. This substitution was planned as, it is

reported that the substitution of Ti^{4+} with Zr^{4+} ions in barium titanate can reduce the dielectric loss or leakage current in the material [12]. Moreover, the Zr^{4+} ion is chemically more stable than the Ti^{4+} and has a larger ionic size to expand the perovskite lattice. Therefore the conduction by electron hopping between Ti^{4+} and Ti^{3+}, if any, would be depressed by the substitution of Ti with Zr. The BST thin films often have high current emission at low electric field [19]. Therefore, new types of dielectrics with high dielectric constant and low stable leakage current need to be developed. It is expected that Zr-doped $Ba_{0.5}Sr_{0.5}TiO_3$ ceramics should have further improved dielectric losses. A high dielectric constant and low leakage current of $(Ba_{0.65}Sr_{0..35})$ $(Ti_{0.65}Zr_{0..35})$ O_3 thin film has been reported [20] and proposed as a promising material for DRAM applications. A similar type of compositionally graded multilayer $(Ba_{0.8}Sr_{0.2})$ $(Ti_{1-x}Zr_x)O_3$ films have shown an improved dielectric properties and tunability [21]. The tunability of $(Ba_{0.85}Sr_{0.15})$ $(Ti_{0.82}Zr_{0.18})$ O_3 thin films has been reported 57% at an applied voltage of 415 kV/cm [22]. However, no literature is available on phase formation, crystal structure and dielectric properties of typical bulk $(Ba_{0.5}Sr_{0.5})$ $(Ti_{1-x}Zr_x)$ O_3 ceramics. In this work, the phase formation behavior, crystal structure, dielectric properties and conduction characteristic of bulk $(Ba_{0.5}Sr_{0.5})(Ti_{1-x}Zr_x)O_3$ ceramics have been studied. The ultimate aim of this section to reduce the dielectric loss in the ceramic by the substitution of Sr in BTZ and Zr in BST ceramics. The detailed room temperature dielectric study is discussed in the section “composition dependency dielectric study" of Chapter 7.

For composition Ba $(Ti_{1-x}Zr_x)$ O_3, with x in the range $0.26<x<0.42$, the solid solution system showed some interesting relaxor like behaviors in the bulk materials [11, 14, 15]. Decrease in transition temperature and increase in diffusivity with increase in Zr content on the system is observed. This lead free relaxor material presents a great interest both for applications in the field of environmental protection and for fundamental studies. Unfortunately these compositions show the relaxation behavior at their ferroelectric transition temperature much below the room temperature. World wide research is on progress to bring the transition temperature close to room temperature. In theses contest we have substituted Ca and Mg in the Ba site of the $BaTi_{0.6}Zr_{0.4}O_3$ ceramic to shift the transition temperature close to the room temperature. The detailed composition and temperature dependency dielectric study on the ceramic is discussed in the section “temperature dependency dielectric study" of Chapter 7.

The observations on structural and electrical characterization presented in Chapter 4, Chapter 5 and Chapter 7. Some theoretical models like spin glass Ising

model and Spherical random bond random field model on relaxors are extensively reviewer and condencly presented in the chapter 8 which makes the work complete and opens new paths to explore the physics and chemistry of these lead free compounds.

2.2 References

1. S.Gopalan and A.V.Virkir, *J. Am. Cerm. Soc*. **82,** 2887 (1999).
2. H.M.Cristen, L.A. Knauss, and K.S. Harshavardhan, *Materials Science and Engineering B* **56**, 200-203(1998).
3. T.K.Y.Wong, B.J.Kennedy, C.J.Howard, B.A.Hunter, T.Vogt, *J. Solid State Chemistry* **156,** 255-263 (2001).
4. F. Ernst, A. Recnik, P.A. Langjahr, P.D. Nellist and M.Ruhle, *Acta Materialia*, **47**, 1, 183-198 (1998).
5. L.C. Sengupta and S. Sengupta, *IEEE Trans. on Ultrasonics, Ferroelectrics and Frequency Control,* **44,** 792 (1997).
6. F. A. Miranda, R. Romanofsky, F. W. Van Keuls, C. H. Mueller, R. E. Treece and T. E. Rivkin, *Integr. Ferroelectrics* **17,** 231(1998).
7. W. Chang, J. S. Horwitz, A. C. Carter, J. M. Pond, S. W. Kirchoefer, C.M. Jlmore and D. B. Chrisey, *Appl. Phys. Lett*. **72**, 1033 (1999).
8. S. Zafar, R. E. Jones, P. Chu, B. White, B. Jiang, D. Taylor, P. Zurcher and S. Gillepsie, *Appl. Phys. Lett*.**72** (1998) 2820.
9. B.J. Kennedy,C.J. Howard,G.J. Thorogood and J.R. Hester, *J. Solid State Chem*. **161**, 106–112(2002).
10. G.H. Jonker and W. Kwestroo, *Am. Cera.Soc*. **41**, 390-394 (1958).
11. D. Henning, A. Schnell and G Simon, *J Am. Ceram Soc*, **65**, 539 (1982).
12. T. B. Wu, C. M. Wu and M. L. Chen, *Appl Phys Lett,* **69** (18), 2659 (1996).
13. A. Dixit, S.B. Majumder, R.S. Katiyar, and A.S. Bhalla, *Appl. Phys. Lett*, **82,** 2679 (2003).
14. Z .Yu, R. Guo and A.S. Bhalla, *J. Appl. Phys*, **88,** 410 (2000).
15. Z. Yu, C. Ang, R. Guo and A.S. Bhalla, *Appl. Phys. Lett*, **81**, 1285 (2002).
16. C. Hofer, R. Meyer, U. Bottger and R. Waser, *J Euro. Cera. Soc*., **24**, 1473 (2004).
17. K. Abe and S. Komatsu, *J. Appl. Phys*, **77**, 6461 (1995).
18. W.J. Kim, H.D. Wu, W. Chang, S.B. Qadri, J.M. Pond, S.W. Kirchoefer, B.D. Chrisey and J.S. Horwitz, J. *Appl. Phys*, **88**, 5448 (2000).
19. K. Numata, Y. Fukuda, K. Aoki and A. Nishimura, *Jap. J. Appl. Phys*. **34**, 5245-5249 (1995).
20. J-D Byun, J-II Yoon, S.Nahm and J-C Kim, *Materials Research Bulletin* **35** 1755-1761 (2000).
21. C. Wang, B.L. Cheng, S.Y.Wang, H.B.Lu, Y.L.Zhou, Z.N.Chen and G.Z.Yang, *Appl. Phys.lett*. **84**, 765-767(2004).
22. Jiwei Zhai, Xi Yao and Haydn Chen, *Ceramics International* **30,** 1237 (2004).

Chapter 3

EXPERIMENTAL AND CORE MATHEMATICS

The compositions with general formula $Ba_{1-x}Sr_xTi_{1-y}Zr_yO_3$ (with x and/or y=0.0, 0.2, 0.4, 0.5, 0.6, 0.8, 1.0), $Ba_{1-x}Ca_x$ $(Ti_{0.6}Zr_{0.4})$ O_3 (with x =0.0, 0.1, 0.2, 0.4, 0.5) and Ba_{1-x} Mg_x $(Ti_{0.6}Zr_{0.4})O_3$ (with x =0.03, 0.07 and 0.14) were synthesized through conventional solid state reaction route. The conditions and sequences used in the sample preparation, characterization and testing were as follows:

3.1. Precursors

Grade reagents, $BaCO_3$ (S.D. Fine Chem., Mumbai), $SrCO_3$ (S.D. Fine Chem., Mumbai), $CaCO_3$ (E. Merck India Ltd.), $MgCO_3$ (E. Merck India Ltd.), TiO_2 (E. Merck India Ltd.) and ZrO_2 (Loba Chem., Mumbai) were taken as the initial raw materials for the purpose. All the powders were having more than 99% purity.

3.2. Particle Size Analysis

Particle size of all raw powders was analyzed using Malvern Particle size analyzer. There are many theories and models that the modern particle analyst can use. One of the simplest theories used is Fraunhofer model [1]. This model can predict the scattering pattern that is created when a solid, opaque disc of a known size is passed through a laser beam. This model does not describe the scattering exactly as very few particles are disc shaped and a lot of particles are transparent. The Mie theory [2] was developed to predict the way light is scattered by spherical particles and deals with the way light passes through, or is adsorbed by, the particles. The instrument works backwards from the above theories, and captures the actual scattering pattern from a field of particles. Then using the theories mentioned above, it can predict the size of the particles that created that pattern. In Mie theory, as the particles may not have exactly spherical shape, an equivalent spherical model is used. More clearly, the instrument is based on the fundamental principle of optics as “refractive index of the particle is directly dependent on diameter of the particle”. Appropriate amount of powder sample was dispersed in distilled water, pumped to the measurement area where it passed through a measurement unit. The measurement unit contains a Laser source and allows the light to pass through the sample and dispersant. To keep the sample samples

dispersed an ultrasonic probe is used along with the pump and stirrer. The sizes of the particle along with no of particle were measured and statistical averages were calculated using the supplied software.

3.3. Mixing and Milling

The powders were thoroughly mixed in an agate mortar with appropriate amount of Iso Propyl Alcohol (IPA) for 2 to 3 hr. The mixture was then dried under infrared lamps and de-agglomerated by an agate mortar.

3.4. Differential Scanning Calorimetry (DSC) and Thermo Gravimetry (TG) Analysis.

Unlike structural or microscopic methods of materials characterization, DSC can provide information on how a substance "got from here to there" during thermal processing. Thermo Gravimetric Analysis (TGA) is the study of weight changes of the specimen as a function of temperature. The technique is useful strictly for transformations involving the absorption or evolution of gases from a specimen consisting of a condensed phase. Decomposition behavior of some selected raw mixtures and original powders were investigated using a NETZSCH Thermal Analyzer.

The NETZSCH thermal Analyzer is based on the DTA principle, where single heating chamber is used. These devices have a disk (e.g. constantan alloy) on which the sample and reference pans rest on symmetrically placed platforms. Thermocouple were (e.g. chromel alloy) is welded to the underside of each platform. The chromel-constantan junctions make up the differential thermocouple junctions with the constantan disk acting as one leg of the thermocouple pair. A calibration constant within the computer software (determined using standard materials) converts the amplified differential thermocouple voltage to energy per unit time, which is plotted on the y axis of the DSC output.

In a typical TG experiment, specimen powder is placed on a refractory pan (often porcelain or platinum). The pan, in the hot zone of the furnace, is suspended from a high precision balance. A thermocouple is in close proximity to the specimen but not in contact, so as not to interfere with the free float of the balance. The balances are electronically compensated so that the specimen pan does not move when the specimen gains or loses weight.

In all the DSC/TG experiments nearly 10 mg of powder samples were taken for TG analysis and a constant heating rate, $10^{O}C$ per minute was maintained for DSC analysis simultaneously. The effect of particle packing affects both DSC and TG analysis. Therefore, this is also taken into account while doing the experiment.

3.5. Calcinations

After proper mixing, mixed powders were calcined at different temperatures (detailed heat treatments are cited in the text) by an indigenous programmable furnace with intermediate grinding to avoid glamorization of the particles. To study the phase formation behavior and reaction mechanism, the compositions $(Ba_{0.5}Sr_{0.5})TiO3$, $Ba_{0.5}Sr_{0.5}ZrO_3$, $Ba(Ti_{0.5}Zr_{0.5})O_3$ and $Sr(Ti_{0.5}Zr_{0.5})O_3$), were calcined at different temperatures from 700 C to 1600 C for 1 hour in an alumina crucible at heating rate $3^{O}C$ per minute and then cooled in the furnace. The calcined powders were grinded by an agate mortar to avoid aglomarization of the particles and were used for the study of their phase formation as well as their reaction mechanism. The other compositions were calcined at $1300^{0}C$ for 4h, $1400^{0}C$ for 4h and finally $1600^{0}C$ for 1h with intermediate mixing and grinding between each firing.

3.6. X-Ray Diffraction Study

X-ray diffraction (XRD) technique is a powerful tool for material characterization as well as for detailed structural elucidation. As the physical properties of solids (e. g., electrical, optical, magnetic, ferroelectric, etc.) depend on atomic arrangements of materials, determination of the crystal structure is an indispensable part of the characterization of materials, mainly the identification of the chemical species. If a crystalline specimen is visualized as being made up of tiny fragments of completely random arrangement, it is called a fine crystalline powder. XRD patterns are used to establish the atomic arrangement or structure of the materials because the d spacing of diffraction planes is of the order of x-ray wavelength λ, the various orders n of reflection occur only at the precise values of angle θ, which satisfies the Bragg equation given by $\mathbf{n\lambda = 2d\sin\theta}$**.** The powder profile of a substance, even without further interpretation, can be used for identification of materials. The simplicity and advantages of x-ray powder diffraction method can be given as follows: (a) The powder diffraction pattern is the characteristics of a substance, (b) Each substance in a mixture produces its pattern independent to others, (c) It describes the state of chemical combination of

elements in the material, and (d) The method is capable to develop quantitative and qualitative analysis of a substance. The accurate determination of lattice parameters provides an important basis in understanding various properties of the materials. The calculation of lattice constants from the line positions or d spacing can be done from a general formula:

$$\frac{1}{d_{hkl}^2} = V^2\left[h^2b^2c^2\sin^2\alpha + k^2c^2a^2\sin^2\beta + l^2a^2b^2\sin^2\gamma\right] \qquad (3.1)$$

where; V = volume of the unit cell

$$= abc\left(1-\cos^2\alpha-\cos^2\beta-\cos^2\gamma+\cos\alpha\cos\beta\cos\gamma\right)^{1/2} \qquad (3.2)$$

where a, b, c, α, β and γ are lattice parameters and h, k, l are the Miller indices. Using the above formula lattice parameters for all the compositions were found out. The kinematics theory of x-ray diffraction describes that for a perfect cause the spread in the intensity distribution curves, the nature and extent of the intensity spread is an obvious measure of crystal imperfection present in the sample under study. Since the different types of defects may be co-existent in crystalline materials, the problems that arise are of separation of different types of defects and identification and quantitative estimation of the extent and distribution of each type of defects. The different factors affecting the diffraction intensities can be grouped into a single expression for use in calculating the relative intensities of reflections. For powder method, the intensity is

$$I = J\frac{1+\cos^2 2\theta}{4\sin^2\theta\cos\theta}F^2A(\theta) \qquad (3.3)$$

where J is multiplicity factor, and F is structure factor, which can be written as

$$F = \sum_j f_j \exp 2\pi i\left(hx_j + ky_i + lz_j\right) \qquad (3.4)$$

where f_j = atomic scattering factor and A (θ) = absorption coefficient = $\frac{1}{v}\int e^{-\mu x}dx$

where μ is the linear absorption coefficient of the specimen, x is the distance traversed by the beam and V is the volume of the crystal exposed in x-rays. A very important aspect of the intensity distribution among the reflections is to relate the extinction, which is a deciding factor for the symmetry elements involved in the material. The translations involved in these symmetry elements and centered lattices add a new periodicity in the patterns, which shows itself by extinguishing certain classes of x-ray spectra. Each type of extinction is characteristic of a particular space group. Therefore, the absence of such characteristic spectra from the diffraction data is a major criterion for the determination of the lattice type and the space group. The following information

can be obtained from their x-ray powder diffractogram: (i) Quality and confirmation of the prepared samples, (ii) The interplaner spacing d of the reflections, (iii) The intensities of the reflections, and (iv) The unit cell dimensions and lattice type.

In the present case, calcined powders were characterized with respect to phase identification, phase quantity measurement, crystallite size determination and lattice parameter measurement, etc., all by using Cu-K_α XRD (Xpert MPD, Philips, UK). For quantitative estimation of phases, calcined powders were uniformly mixed and the resulting mixture was analyzed using a step size of 0.02^o, 2θ with 10 second/step. The relative weight fractions were quantified from the ratio of peak areas. The phases giving maximum peak area at a particular temperature were considered as 100% formation of those phases at that temperature. Considering that area as 100%, the relative percentages of the respective phases were calculated. On the basis of XRD line broadening at half maxima of the 100% RI peak, crystallite sizes of the phases were estimated using the Scherer equation, as $\mathbf{P=k\lambda/\beta_{1/2}\ Cos\ \theta_p}$, where P; linear particle size, k; 0.89, θ_p; peak position and $\beta_{1/2}$; half peak width.

3.7. Structural and Microstructural Analysis by Rietveld Method

Structural and microstructural parameters were analyzed by using Philips (Netherlands) X-ray diffractometer model PW-1830 with copper $K\alpha_1$ radiation. For Rietveld analysis, the diffraction data were taken at room temperature on step scan mode with step size 0.02 and 5 sec per step. During all the experiments, the X-ray source was supplied a voltage of 35kV and 30 mA current. The peak shape was assumed to be a pseude-Voigt (*pV*) function with asymmetry. The background of each pattern was fitted by a polynomial function of degree four. For a better understanding, the detailed methods of analysis and core mathematics are given in the Chapter 5.

3.8. X-Ray Florescence Study

X-ray fluorescence (XRF) spectrometry provides a non-destructive analytical method capable of analyzing solids from a few parts per million to near 100% for wide range of elements. This versatile technique is ideally suited for analysis of rocks, soils, dust, contaminated land samples, mineral concentration and products, archaeological artifacts, synthetic materials and metals. The nondestructive nature of the technique allows long term storage of samples, which can then be re analyzed any number of times for additional elements as necessary. This approach, therefore, avoids problems of

re-sampling and digestion of separate aliquots. In the present case, the samples were prepared for XRF stufd by pressed powder pellets method. 500 mg of the dried powder sample was crushed and mixed with 500 mg of high purity cellulose powder in 1:1 ratio by weight. The mixture was then crushed thoroughly so as to get a homogenized powder mixture. The corresponding mixtures were then pressed in a KBr press to make pellets of size 25 mm diameters and were taken for XRF study.

3.9. Pellet Preparation

After calcinations, the powders were granulated with an organic binder polyvinyl alcohol (PVA). To get uniform and fined grain, the granules were passed through a 150 μm sieve. The residues after sieving were again crushed in an agate mortar and passed through the sieve. The process was repeated till all the granules became less than 150 μm. To have a pellet of diameter 14mm and thickness 2mm, a cylindrical steal die of 14mm was taken. Initially the die was kept in a highly viscous mobile oil to prevent it from rousting. Taking out from the oil, the die was cleaned with IPA and acetone. Just before putting the granules in the die for pressing, some hydrophobic stearicacid solution was used in the inner surface of the die to avoid sticking of the powder on the inner surface of the die. The granules were put in the die and the piston was slowly inserted into the cylinder. While inserting the piston care was taken so that no powder should come upward in between the gap between piston and inner surface of the cylinder due to the outcome of the air present in the die. Then the die containing the granules were uniaxially pressed with a pressure of 4.5 kiloton per cm in a hydraulic press controlled by an electric motor. Before releasing the presser from the die, minimum 1 minute time was given to minimize the stress on the pellet. After the pellet was formed the green density was measured from its external dimension. Then the pellets were sintered to study the dielectric response of the materials.

3.10. Sintering

Density of the electronic ceramic is a very sensitive parameter and that directly affects their properties. Therefore, proper sintering of the pallets is essential for electrical measurement. The pellets having general compositions $Ba_{1-x}Sr_x(Ti_{0.5}Zr_{0.5})O_3$, $(Ba_{0.5}Sr_{0.5})Ti_{1-x}Zr_xO_3$ and $(Ba_{1-x}Sr_x)Ti_{0.6}Zr_{0.4}O_3$ were taken on an alumina plate and sintered at 1400^OC for 2 hours in a programmable furnace at a heating rate of 3^0C per minute with an intermediate shocking of 4 hours at 500^OC for organic removal. The

pellets were furnace cooled and taken out of the furnace for initial density measurement (the detailed procedure adopted for calculation of density is described in the next section). The initial density measurement shows that all the pellets are having greater than 30 % porosity. Again the pellets were sintered at $1450^{O}C$ for 10 hours and finally at $1500^{O}C$ for 4 hours at a heating rate of $3^{0}C$ per minute with an intermediate cooling. After final sintering at $1500^{O}C$ for 4 hours, the porosity was found to be within permissible range. The exact values of the porosity of different compositions are cites in the text of this Chapter. As CaO and MgO have lower melting point than BaO and SrO the sintering temperature for the compositions $Ba_{1-x}(Sr/Mg)_xTi_{0.6}Zr_{0.4}O_3$ is reduced from the above sintering temperature. The Ca and Mg containing compositions were sintered in the same programmable furnace at $1400^{O}C$ for 2 hours and $1450^{O}C$ for 6 hours with an intermediate cooling. Like the previous process, these compositions were also allowed for shocking at $500^{O}C$ for 4 hours for organic binder removal in the initial heat treatment.

3.11. Density Determination

After the above heat treatment on the samples, the dry weights of the pellets were measured by a digital electronic balance. Then the samples were given different identification to avoid any confusion and kept together in a glass beaker. The samples-containing beaker was kept in a vacuum oven and heated at $100^{O}C$. At this temperature water starts boiling and simultaneously vacuum was also created by the use of a suction pump. Heating the samples in the vacuum for 30 minutes, the pores present in the pellets were completely filled with water. The heater of the oven was switched off and the vacuum was slowly released. Now the beaker was taken out of the oven. The weight of the pellets were taken, in a digital electronic balance and interpreted as shocked weight. After the shocked weights were taken the samples were suspended in water with the help of a speciall designed hanger to hang the pellets inside water and the measured weight is interpreted as suspended weight.

The experimental bulk density and apparent porosity were measured by using Archimedes principle;

$$B.D = D/(W-I) \quad (3.5)$$

$$A.P = (W-D)/(W-I) \quad (3.6)$$

where: *D*; Dry weight, *W*; Shocked weight and *I;* suspended weight.

X-ray densities were calculated as suggested by B.D. Cullity [3]

$$\rho = \frac{\sum A}{NV}$$

$$= \frac{1.66042 \sum A}{V} \tag{3.7}$$

where: ρ; X-ray density (g/cc), $\sum A$: Sum of the atomic weights of all the atoms in the unit cell, N; Avogadro's number, V; Volume of a unit cell. If the composition is of atomic weight A, then

$$\sum A = n_1 M \tag{3.8}$$

where n_1; number of molecules per unit cell and M; molecular weight

The macroscopic density or the experimental bulk density of a particular specimen, determined from Archimedes principle is usually less and that can't be exceeded the X- ray density, because the macroscopic specimen usually contains some cracks and pores.

3.12. Microstructure Study

In modern material science research, microstructural study is widely used as a powerful tool for prediction of many inheriting properties of the materials. It produces micrographs by scanning the surface of a specimen with a small electron probe (a beam of electron) synchronous with an electron beam from a source. The discs were polished in an automatic polish machine and thermal etching was done at $1300^{O}C$ for 2 hours. The microstructure was studied by an optical microscope connected with a PC. The soft ware used here was Video Master. Using this software, while measuring the grain size, some lines of known length were drawn on the micrograph. The number of grains cut by the lines was counted. Then the average grain sizes were calculated by dividing the length of the line by the no of grain coming under that line. Minimum 10 lines, each having the length not less than 200 micrometers were drawn on the different places of a single micrograph and average grain sizes were calculated to minimize the error. To minimize the error and for a detailed insight study of the micrograph, SEM is always preferred, which is beyond the scope of the present laboratory.

3.13. Electroding

The selection of suitable electrode for the test materials is important. In our case the contacting, conducting thin film electrode method is adopted because (i) It causes

minimum error caused by air gap between the electrode and surface of the test material, which is more in case of contacting rigid metal electrode method, and (ii) Procedure to measure and equation to obtain dielectric constant are simple, which are relatively complex in non contacting electrode method. In our case, thin silver electrodes were printed on to opposite faces of the ceramic disk by screen printing technique. For organic removal printed disks were kept on an alumina plate and fired at 700^0C for 15 minutes. This procedure is repeated twice for better electroding

3.14. Electrical Measurements

There are several types of polarizations, each of which can be explained by its intrinsic physical mechanism. The three basic types of polarizations are electronic, ionic and orientational. When an insulator is placed in an external electric field, electrons of the atoms are displaced slightly with respect to the nuclei, so induced dipole moments result and cause the electronic polarization. When the atoms of a molecule do not share their electrons symmetrically, the electron-clouds will be displaced eccentrically towards the stronger binding one. Thus the ions acquire charges of opposite polarity. These net charges will tend to change the equilibrium positions of the ions themselves under the action of an external electric field. This displacement of charged ions or groups of ions with respect to each other creates a second type of induced dipole moment. It represents the ionic polarisation of the unlike partners of molecule giving rise, in addition, to permanent dipole moments, which exist even in the absence of an external electric field. Such dipoles experience a torque in an electric field that tends to orient them in the direction of the field. Consequently an orientation (or dipole) polarisation can arise. These three mechanisms of polarisation are due to charges locally bound in atoms, molecules or in the structure of solids. In addition to all these, there usually exist charge carriers that can migrate for some distance through the dielectric. Generally carriers are impeded in motion because of being trapped in the materials interfaces. Hence they cannot freely discharge at the electrodes and space charges result. Such distortion appears as an increase in the capacitance of the sample and may be distinguishable from a rise of the dielectric constant. Thus a fourth polarisation, called the space charge (or interfacial) comes into play. For electronic and ionic polarisations, the frequency effect is negligible upto about 10^{10} Hz. As the optical range of frequencies is reached, electronic contribution becomes sole contributor. The effect of temperature on both electronic and ionic polarisations is small. At higher temperatures, polarisation increases due to ionic and crystal imperfection mobility. The

combined effect produces a sharp rise in the dielectric constant at low frequency with increasing temperature corresponding to both dipole orientation effects and space charge effects. The total polarisation is a sum of these four polarisations (assuming that they act independently) [4].

When the dielectric is placed in alternating fields, these polarisations are set up and give rise to the dielectric constant. A temporal phase shift is found to occur between the driving field and the resulting polarisation and a loss current component appears giving rise to the dielectric loss of the sample. Here this polarisation, **P**, as well as the electric displacement, **D** varies periodically with time. In general, however, **P** and **D** may lag behind in phase relative to electric field **E**, so that

$$\mathbf{D} = \mathbf{D}_0 \cos(\omega t - \delta) = \mathbf{D}_1 \cos\omega t + \mathbf{D}_2 \sin\omega t \tag{3.9}$$

where δ is the phase angle and slightly less than 90°,

$$\mathbf{D}_1 = \mathbf{D}_0 \cos\delta$$

and

$$\mathbf{D}_2 = \mathbf{D}_0 \sin\delta$$

The ratio of displacement vector to electric field ($\mathbf{D}_0$ / $\mathbf{E}_0$) is in general frequency dependent for most of the dielectrics. Hence, we can introduce two frequency dependent dielectric constants:

$$\varepsilon'(\omega) = (\mathbf{D}_0 / \mathbf{E}_0) \cos\delta \tag{3.10}$$

$$\varepsilon''(\omega) = (\mathbf{D}_0 / \mathbf{E}_0) \sin\delta \tag{3.11}$$

These two constants can be expressed in terms of a single complex dielectric constant, $\varepsilon^* = \varepsilon' - j\varepsilon''$. As the applied voltage (V) varies periodically with time as:

$$V = V_0 e^{i\omega t}$$

The total current, $$I = \frac{dQ}{dt} = \frac{d(CV)}{dt} = jC\omega V = j\omega\varepsilon C_0 V \tag{3.12}$$

Where, C and C_0 are the capacitance in a dielectric medium and vacuum respectively. Therefore,

$$I = j\omega C_0 V\left(\varepsilon' - j\varepsilon''\right) = \omega\varepsilon'' C_0 V + j\omega C_0 V\varepsilon' = I_l + I_c \tag{3.13}$$

The tangent loss is given by,

$$\tan\delta = \frac{I_l}{I_c} = \frac{\varepsilon''}{\varepsilon'} \tag{3.14}$$

The total current I through the capacitor can be resolved into two components, a charging current (I_c) in quadrature with voltage and conduction current I_l in phase with the voltage. The vector resolution of current is shown in Fig. 3.1.

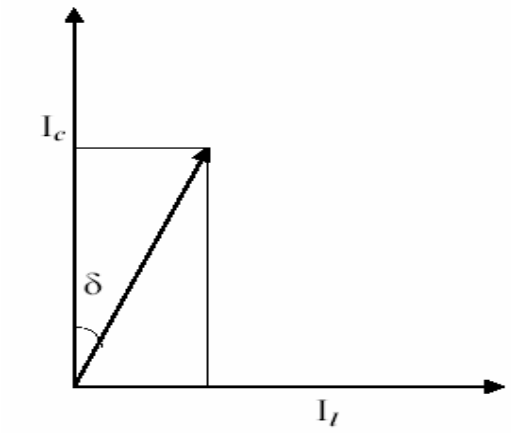

Figure 3.1: The vector resolution of ac current in a capacitor

For a parallel plate capacitor with sinusoidal applied voltage, loss current density is given by

$$J_1 = \omega \varepsilon_0 \varepsilon'' V = \sigma V \tag{3.15}$$

where $$\sigma = \omega \varepsilon' \varepsilon_0 \tan \delta \tag{3.16}$$

is the dielectric conductivity. The effective conductivity defined in this manner depends upon frequency and is always greater than dc conductivity. The loss factor is the primary criterion for the usefulness of a dielectric as an insulator. So for application purposes where high capacitance in the smallest physical space in required, materials with high dielectric constant and low tangent loss (tanδ) must be used. The dielectric properties of ferroelectrics depend on the field strength at which they are measured. This is a consequence of non-linear relation between polarisation and electric field.

Room temperature dielectric measurements were carried out by the contacting thin electrode method. After electroding the cylindrical samples, pallets are in Metal (silver)-Insulator (sample)-Metal (silver) form. The samples in MIM form were kept in a calibrated Agilent 16451B dielectric test fixture and connected to HP-4192A LF Impedance Analyzer. Room temperature dielectric measurements were carried out over the range 10Hz to 13MHz using pure sinusoidal wave. The Impedance Analyzer is connected with a PC for data acquisition. The sinusoidal a.c frequencies were applied along the axis of the cylinder keeping the d.c. bias voltage disabled. The capacitance and loss tangent of the materials were measured as a function of ac frequency. The

dielectric constant or permittivities of the materials at different frequencies were calculated using the relation $\varepsilon_r = \frac{tC_p}{A\varepsilon_0}$, where t is the thickness, A is the area of the electrode, t is the thickness of the material, C_p is the capacitance measured in parallel mode and ε_0 is the permittivity of the free space which is 8.854×10^{-12} [F/m]. The a.c conductivity of the samples was calculated using capacitance and tan δ.

The temperature dependency of dielectric constant was carried out with a self designed programmable temperature controller oven. The temperature was reduced using liquid nitrogen. The sample was kept in side an indigenous tube furnace having tube diameter 18 mm with a self-designed fixture. The tube furnace temperature sensor along with the sample was kept in vacuum to avoid the effect of moisture on the dielectric properties. When the temperature of the sample chamber became stable (130^{O}K), the furnace was turned on and temperature was increased upto 333^{O}K with a heating rate of 0.5°C min^{-1}. (In the present case liquid nitrogen temperature was not achieved due to radiation losses). While heating, the dielectric data were taken with in 4 or 5 degree interval and found to be reproducible.

3.15. References

1. F.M. Etzler, R. Deanne, Principle and Particle Systems Characterizations, 14 (6) 278-282 (2004) and http://www.microtrac.com/laserdiffraction.cfm
2. A.J.Preetham, P. Shirley and B. Smith, A practical analysis model for day light. In proceedinds of the 26th annual conference on computer graphics and interactive technique, pp. 91-100, ACM press/Addison Weslay publishing Co., (1999) and V.I.Tatarskii, IEEE transaction on Antenas and Propagations, 51(10), 2808 (2003)
3. B.D.Cullity "*Elements of x-ray Diffraction*", 2nd Edition, Addison- Wesley Publishing Company, Inc. (1978).
4. M. E. Lines and A. M. Glass, *Principles and Applications of Ferroelectrics and Related Materials*, Clarendon Press, Oxford (1977).

Chapter 4

PHASE FORMATION AND REACTION MECHANISM.

4.1. Introduction

Understanding solid state transformations and associated changes in crystal chemistry is a crucial endeavor in materials science and mineralogy. Out of the various means to study transformation kinetics, e.g. thermal analysis, various spectroscopic, and magnetic measurement techniques, only diffraction studies provide the details of the lattice parameters and atomic positions necessary to fully characterize the crystalline phase.

Perovskites such as $BaTiO_3$, $SrTiO_3$, $BaZrO_3$, $SrZrO_3$, $CaTiO_3$, $CaZrO_3$ are important technological materials with applications as dielectrics, piezoelectrics, electro-optical materials, catalysts and proton conductors [1-4]. Many recent studies of such oxide systems have focused on the phase equilibria and dielectric properties of perovskite-related solid solutions having $CaTiO_3$, $SrTiO_3$ or $BaTiO_3$ -all of which exhibit large permittivities as one of the end-compounds [5-6]. In contrast, $AZrO_3$-based perovskites (A; divalent metallic cation), which exhibit much lower permittivities than their titanate analogs, have received less attention. Solid solution compositions in $BaTiO_3$ (BT)-$BaZrO_3$ (BZ) or BTZ-system have been established as one of the most important compositions for dielectrics in multilayer ceramic capacitors [7].

The room-temperature crystal structures of all the end-compounds have been reported in the literature: $BaZrO_3$ crystallizes with an ideal cubic perovskite structure [8], while $SrZrO_3$ [9] exhibits orthorhombic symmetry. $BaTiO_3$ exhibits cubic as well as tetragonal symmetry where as $SrTiO_3$ exhibits cubic symmetry. $CaTiO_3$ and $CaZrO_3$, both exhibits orthorhombic symmetry.

Diffusion of ions in perovskites is a fundamental rate controlling process for numerous phenomena. The simultaneous diffusion of the various species within the crystal is a complex process. Interdiffusion is a solid-state phenomenon, which governs diffusional phase transformation kinetics. There have been numerous studies on interdiffusion in metallic systems [10], although such studies are relatively rare in ionic system. Lindstrom [11] theoretically examined the interdiffusion in AY-BY where A and B are cations and Y is an anion. The lattice velocity “v” was shown to be zero, i.e.,

an absence of a Kirkendall effect, when either Y is immobile or the self diffusivities of A and B are equal.

Despite numerous practical applications of these individual compounds and their solid solutions, phase formation of these compounds and reaction mechanism during phase formation were not studied in details. Thus the study on interdiffusion in these materials is of interest. The fabrications of these materials usually involve a high temperature processing step. It has been reported by Pask and Templeton [12] that during the growth of $BaTiO_3$ in the TiO_2-BaO reaction, an intermediate phase Ba_2TiO_4 was observed but Ubaldini *et al* [13] did not observed such phase in the BaO-ZrO_2 system during processing of $BaZrO_3$. During high temperature processing, two fast transport processes can be considered: surface diffusion and gas phase diffusion. Surface diffusion coefficients in oxides are typically 4-8 orders of magnitude larger than lattice diffusion coefficients [14]. Moreover, it is well known that the presence of water vapor has a noticeable effect on sintering, structural rearrangement, and crystal coarsening of MgO and other oxides [15]. All the above observations suggest that surface diffusion is the mass transport mechanism operating in most cases of powder reactions. It was also reported by Ubaldini *et al*, [13] in surface diffusion reaction that reaction rate constant is very much dependent on size of the particle, irrelevant of their shape. i.e smaller the particle size, lower will be the required temperature for phase formation reaction and vice versa. The perovskite phases grows as a more or less uniform concentric layer with gradual consumption of central particle and reaction can be considered as diminishing core mechanism. The resulting temperature dependency of kinetics constant follows Arrhenious law. A detailed literature survey on activation energy reveals that, Lewis et al [16] predict activation energy of 15.1 eV for diffusion of Ti vacancies in $BaTiO_3$ and 11.59 eV in $SrTiO_3$. By contrast, Rhodes and Kingery [17] found that the activation energies for diffusion of both Sr and Ti were about 4.92 eV. Similarly, Werniek [18] deduced from conductivity relaxation studies activation energies of 2.05 and 2.76 eV for diffusion of oxygen and Ba vacancies respectively. Gopalan and Virkar [9] reported that the Ti diffusivity in $BaTiO_3$ and $SrTiO_3$ is greater than either Ba or Sr. On the other hand, during formation of zirconate, Ubaldini *et al*, [13] reported that the formation of $BaZrO_3$ requires activation energy of 3.047 eV and 2.290 eV in dry and humid air respectively. Again Gopalan and Virkar [19] also reported the activation energy of 3.66 eV for interdiffusion of $BaTiO_3$-$BaZrO_3$.

Butler *et al* [20] investigated interdiffusion in $SrTiO_3$-$CaTiO_3$ and concluded that interdiffusion of these alkaline- earth cation in their titanates occurs via a vacancy

mechanism. In their work, Ti and O were a priori assumed to be immobile because their concentrations are spatially invariant. Samples in their work were made by embedding powder compacts of $SrTiO_3$ inside powder compact of $CaTiO_3$ and simultaneously densifying and annealing at elevated temperatures.

Recently, Kennedy *et al*. [21] conducted a detailed analysis of structural transitions in $SrZrO_3$ due to incorporation of $BaZrO_3$ perovskite due to the tilting of ZrO_6 octahedra. However, no detailed studies on its reaction mechanism are reported in the systems. In last few years, perovskite solid solutions having super lattice structure had received great attention as a better proton conductor material [22]. $SrTiO_3$-$SrZrO_3$ (ST-SZ) solid solution is one of them, which holds promise for application as a proton conductor as well as voltage-dependent tunable ceramic [23]. ST-SZ solid solution shows a super lattice structure due to its cell enlargement as a result of tilting of BO_6 (B=Ti, Zr) octahedra [24]. This type of disorder perovskite solid solution offers exciting new possibilities both in the investigation of fundamental physical phenomena and in the exploitation of novel properties for various applications.

In most cases of oxide compounds, the formation of solid solution consists of the replacement of certain ions by analogous ion (same valence and size). If this is the case with neighbor compounds, the stability relations between these compounds may be changed by different energies involved in the formation of the solid solution. As a result some compounds disappear from a phase diagram or appear with higher stability. Jonker and Kwestroo [25] studied the solid solution formation in the system BaO-TiO_2-ZrO_2. They observed that the $BaTiO_3$-$BaZrO_3$ forms a complete series of solid solution, $Ba_2Ti_5O_{12}$ can incorporate about 13 mole% ZrO_2, $BaTi_3O_7$ only 2 mole%, $BaTi_4O_9$ 10 mole % and $Ba_2Ti_9O_{20}$ about 5 mole %. All unit cell dimensions are increased by Zr substitution. They have also reported that in the Ba_2 (Ti, Zr)$_5$ O_{12} X-ray diffraction pattern there was a splitting of some of the lines, showing that there is a deformation of the original unit cell. Continuous series of mixed crystals between $BaTiO_3$ and $SrTiO_3$ and between $SrTiO_3$ and $CaTiO_3$ exist. However, $BaTiO_3$ and $CaTiO_3$ don't form a continuous series. The Ca ions are not only substituted for Ba ions but also find other site in the crystal lattice (perhaps Ti sites). Ca ion can occupy Ti site [26], but this will be accompanied by a simultaneous formation of O^{2-} vacancies. DeVries and Roy [27] investigated the phase equilibria in the system $BaTiO_3$-$CaTiO_3$. They found a solubility gap between these two compounds up to the melting point (1600^{o}C). At 1400^{o}C, the maximum solubility is 18 weight % on both sides. The system $BaTiO_3$-$SrTiO_3$ was investigated by Basmajian and DeVries [27]. Here a complete series of solid solutions

of the two compounds exists. McQuarrie [29] investigated the crystallographic transitions in the ternary perovskite system (Ba, Sr, Ca) TiO_3. They have reported that the solubility gap between $BaTiO_3$-$CaTiO_3$ decreases with increase in $SrTiO_3$, but the crystal modifications are not considered in the work. Keeping this in view, solubility of $SrTiO_3$ and $CaTiO_3$ in $BaTiO_3$ in the presence of ZrO_2 was studied and their crystal structure ware also investigated in the present study.

The objective of this Chapter is to gain insight into the kinetics and mechanism of phase formation, reaction mechanism and room-temperature crystal structure of these compositions using metal oxide precursors. In the present study interdiffusion and phase formation of the studied compositions were investigated using loose powders.

4.2. Experimental Procedure

The compositions with general formula $Ba_{1-x}Sr_xTi_{1-y}Zr_yO_3$ (with x and/or y=0.0, 0.2, 0.4, 0.5, 0.6, 0.8, 1.0), $Ba_{1-x}Ca_x$ $(Ti_{0.6}Zr_{0.4})$ O_3 (with x =0.0, 0.1, 0.2, 0.4, 0.5) and Ba_{1-x} Mg_x $(Ti_{0.6}Zr_{0.4})$ O_3 (with x =0.03, 0.07 and 0.14) were synthesized through conventional solid state reaction route. The detailed procedures for sample preparations were explained in the Chapter 3. The particle size of starting raw materials was measured using Malvern Mastersizer. After proper mixing, the decomposition behavior of the raw mixture and pure Precursors were investigated using a NETZSCH Thermal Analyzer. To study the phase formation behavior, the compositions $(Ba_{0.5}Sr_{0.5})TiO_3$, $Ba_{0.5}Sr_{0.5}ZrO_3$, $Ba(Ti_{0.5}Zr_{0.5})O_3$ and $Sr(Ti_{0.5}Zr_{0.5})O_3$), were calcined at different temperature from 700 ^oC to 1600 ^oC for 1 hour in an alumina crucible at heating rate 3^OC per minute and then cooled in the furnace. The other compositions were calcined at 1300^0C for 4h, 1400^0C for 4h and finally 1600^0C for 1h with intermediate mixing and grinding between each firing. The calcined powders were characterized with respect to phase identification, phase quantity measurement, crystallite size determination and lattice parameter measurement etc., all by using Cu-K_α XRD (PW-1830, Philips, Netherlands). For quantitative estimation of phases, calcined powders were uniformly mixed and the resulting mixture was analyzed by XRD using a step size of 0.02^o, 2θ with 10 second/step. The relative weight fractions were quantified from the ratio of peak areas, according to the process described by S.Kumar and G.L.Messing [30]. On the basis of XRD line broadening at half maxima, crystallite sizes of the phases were estimated using the Scherrer equation [31], as $\mathbf{t=k\lambda/\beta_{1/2}\ Cos\ \theta_p}$, where **t**; linear particle size, k; 0.89, θ_p; peak position and $\beta_{1/2}$; half peak width.

4.3. Result and Discussion

This section describes the results obtained from the study on different compositions and their phase formation behavior.

4.3.1. Particle Size and Thermal Analysis of Raw Powders

The particle size analysis shows that the raw powders contains particles of different size and are: $BaCO_3$ [D(v,0.1)=0.25 μm, D(v,0.5)=2.09 μm, D(v,0.9)=13.20 μm], $SrCO_3$ [D(v,0.1)=0.48 μm, D(v,0.5)=13.13 μm, D(v,0.9)=14.63 μm], $CaCO_3$ [D(v,0.1)=0.29 μm, D(v,0.5)=3.86 μm, D(v,0.9)=8.70 μm], TiO_2 [D(v,0.1)=0.27 μm, D(v,0.5)=0.35 μm, D(v,0.9)=0.48 μm] and ZrO_2 [D(v,0.1)=0.42 μm, D(v,0.5)=10.27 μm, D(v,0.9)=15.48 μm], where D is the mean diameter of particles and v is the volume percent of the particle present in the materials.

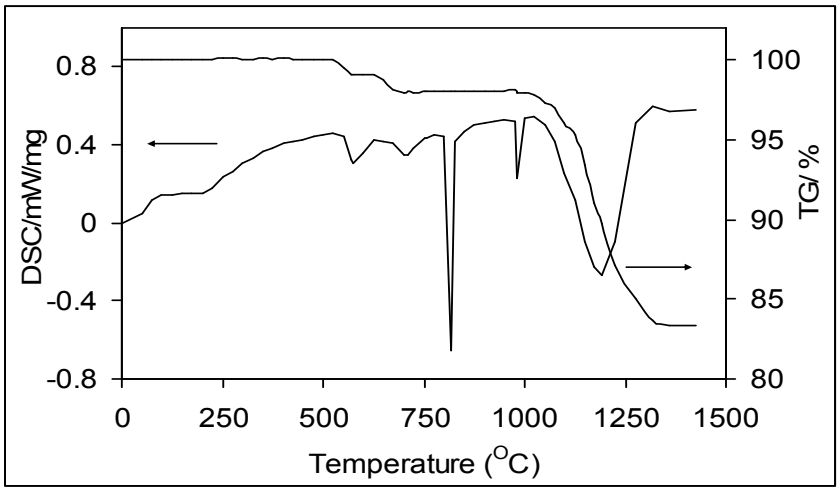

Figure 4.1 TGA and DSC curves in air for the $BaCO_3$ raw powder.

Fig. 4.1 and Fig. 4.2 show the TG/DSC of the raw powder $BaCO_3$ and $SrCO_3$ respectively. Fig. 4.1 shows five endothermic peaks. The small endothermic peaks at 570 ^{O}C and 710^{O} C correspond to ~0.95% and ~1.10% wt loss of the powder. As previously mentioned, $BaCO_3$ raw material has finer particle fractions D(v,0.1)=0.25 μm. These fractions decompose at lower temperature. These weight losses may be attributed to the decomposition of very fine $BaCO_3$ particles present in the powder.

The two sharp endothermic peaks at 814.7^{O}C and 986 ^{O}C are due to the polymorphic transformations of $BaCO_3$ as there is no weight loss found at that temperature. The sharp peak at 814.7^{O}C is due to the polymorphic transformations of

the rhombohedral $BaCO_3$ to hexagonal $BaCO_3$ (gamma --- Beta) structure (this peaks theoretically occurs at 806 C) [32]. The sharp peak at 986 ^{O}C is due to the structural transformation from hexagonal to cubic $BaCO_3$ (beta ---alpha) [33]. The huge endothermic peak at 1187^{0}C corresponding to 18% wt loss and it is due to the major decomposition of $BaCO_3$. Fig. 4.2 shows two endothermic peaks at 934^{O}C and 1110^{O}C. The sharp endothermic peaks at 934 ^{O}C corresponds to polymorphic transformation from orthorhombic $SrCO_3$ (space group Pmcn) to the rhombohedral $SrCO_3$ (space group R-3m) [34], as there is no wt loss found at that temperature. The huge endothermic peak at 1110 ^{O}C corresponding to ~28.72% wt loss is due to the major decomposition of the $SrCO_3$ powder.

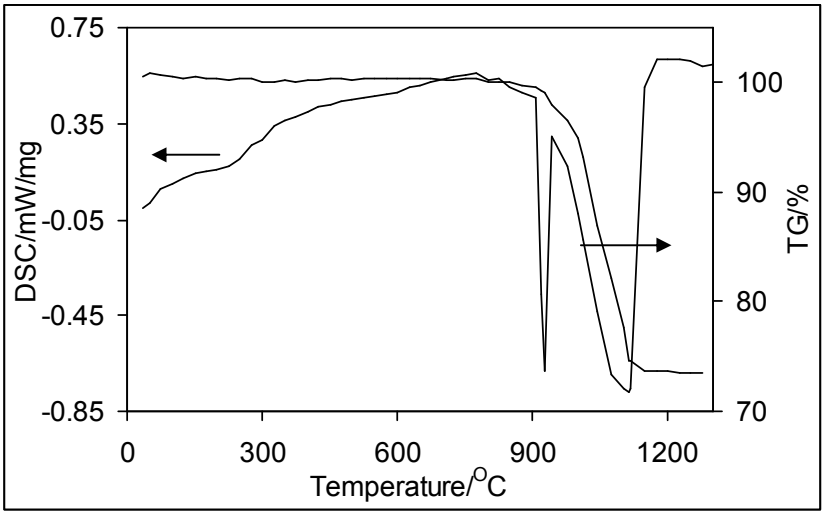

Figure 4.2 TGA and DSC curves in air for the $SrCO_3$ raw powder.

4.3.2 Thermal Analysis of Precursors

Fig.4.3 shows DSC-TG tracing of $Ba_{0.5}Sr_{0.5}TiO_3$ precursor. TG graph shows a continuous wt loss of 17.69% from about 700 ^{O}C to 1275 ^{O}C. The graph shows four endothermic peaks at 718 ^{O}C, 806.7 ^{O}C, 928^{o}C and 1156 ^{O}C. The small peak at 718 ^{O}C corresponds to ~0.8 % wt loss of the precursor as earlier. This weight loss may be attributed to the decomposition of very fine $BaCO_3$ particles present in the precursor. As there was no weight loss found under the peak at 806.7^{O}C, it corresponds to polymorphic transformations of rhombohedral to hexagonal (gamma -- Beta) structure of $BaCO_3$ (this peak theoretically occurs at 806 ^{O}C) [32]. The hexagonal to cubic $BaCO_3$ (beta --alpha) transformation peak which occurs at 986 ^{O}C [32, 33], is not observed in the precursor. Both the peaks were prominent in case of pure $BaCO_3$. The

endothermic peak at 928^{o}C is due to the polymorphic transformation of $SrCO_3$ from the orthorhombic space group (Pmcn) to the rhombohedral space group (R-3m) [34]. The huge 1156 ^{O}C endothermic peak corresponds to the major decomposition of both $BaCO_3$ and $SrCO_3$ in the precursor. However, in pure $BaCO_3$ that peak occurs at about 1130^{0}C and in pure $SrCO_3$ that peak occurs at about 1187^{O}C. This is one overlapping decomposition peak which occurs in between the decomposition temperature of $BaCO_3$ and $SrCO_3$, which is the decomposition peak of both the carbonate present in the precursor.

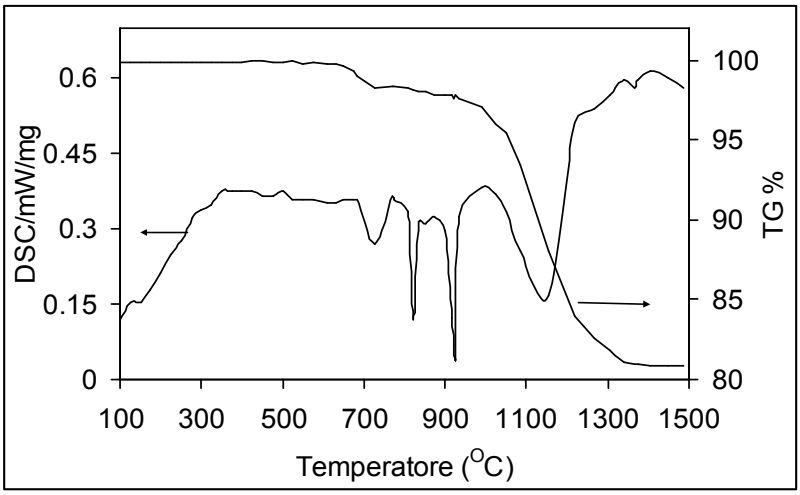

Figure 4.3. TGA and DSC curves in air for the $BaCO_3$, $SrCO_3$ and TiO_2 powder mixture.

Fig. 4.4 shows DSC-TG tracing of $Ba_{0.5}Sr_{0.5}ZrO_3$ precursor. TG graph shows a continuous wt loss ~ 15.79% from about 875^{O}C to 1200 ^{O}C. The graph shows four endothermic peaks at 600 ^{O}C, 850.7 ^{O}C, 950 ^{O}C and 1150 ^{O}C. The small peak at 600 ^{O}C corresponds to ~0.8 % wt loss of the precursor. As stated earlier $BaCO_3$ raw material has finer particle fraction D (v, 0.1)=0.25 μm, so this weight loss may be attributed to the decomposition of very fine $BaCO_3$ particles present in the precursor. As there was no weight loss found under the peak at 850.7, it corresponds to polymorphic transformations of $BaCO_3$ from rhombohedral to hexagonal (gamma -- Beta) structure [32]. The hexagonal to cubic (beta --alpha) transformation peak, which occurs at 986 ^{O}C [32, 33], is not observed in the precursor. Both the peaks were prominent in case of pure $BaCO_3$ (Fig. 4.1). The endothermic peak at 928^{O}C due to the polymorphic transformation of $SrCO_3$ from the orthorhombic space group (Pmcn) to the rhombohedra space group (R-3m) [34] is not observed due to the earlier decomposition reaction of the precursor. The huge 1140 ^{O}C endothermic peak corresponds to the major decomposition of both $BaCO_3$ and $SrCO_3$ in the precursor. However, in pure $BaCO_3$

that peak occurs at about 1187^{O}C and in pure $SrCO_3$ it peak occurs at about 1130^{o}C. Similar overlapping was also observed (Fig.4.3) in case of BST precursor.

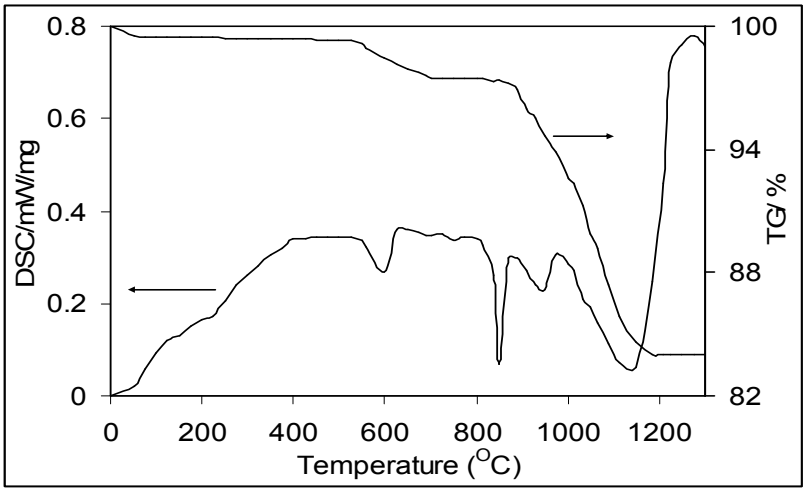

Figure 4.4 TGA and DSC curves in air for the $BaCO_3$, $SrCO_3$ and ZrO_2 powder mixture.

Fig. 4.5 shows DSC-TG tracing of $BaTi_{0.5}Zr_{0.5}O_3$ precursor. TG graph shows a continuous wt loss from about 500^{o}C. There are two small DSC peaks at 556^{O}C and 728^{O}C, corresponding ~1.4% and ~0.8% wt loss of the precursor respectively. These weight losses may be attributed to the decomposition of very fine $BaCO_3$ particles present in the precursor. As stated previously, these fractions decompose at lower temperature in presence of TiO_2. A sharp endothermic peak at 810^{o}C corresponds to the polymorphic transformation of witherite to α-$BaCO_3$ [32]. The 979^{O}C huge endothermic peak corresponds to the major decomposition of $BaCO_3$ in the precursor. However, in pure $BaCO_3$ that peak occurs at about 1187^{O}C. This indicates that $BaCO_3$, which is present in the precursor, decomposes at much lower temperature due to the presence of acidic TiO_2 in the mixture [35].

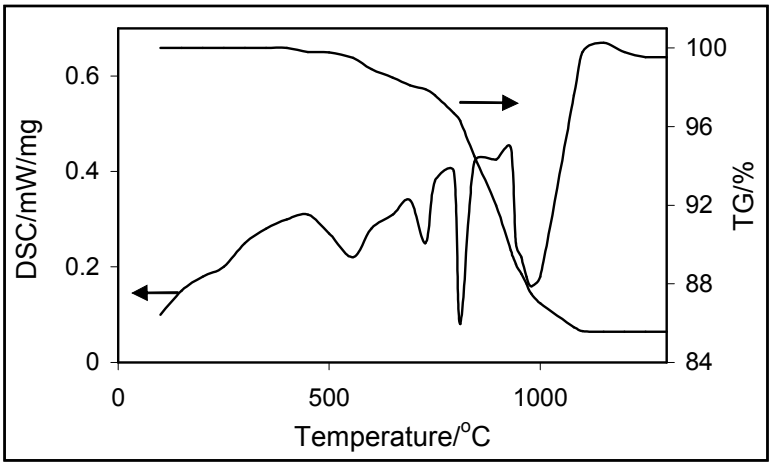

Figure 4.5 TGA and DSC curves in air for the $BaCO_3$, TiO_2 and ZrO_2 powder mixture.

Fig. 4.6 shows a differential scanning calorimetric and thermo gravimetric (DSC-TG) tracing of the $SrTi_{0.5}Zr_{0.5}O_3$ precursor. The TG graph shows a continuous wt loss from about 875^oC to 1,100^oC. The DSC graph shows two endothermic peaks at 928^oC and 1,066^oC, respectively. The peak at 928^oC is due to the polymorphic transformation of $SrCO_3$, as stated earlier. The 1066^oC endothermic peak corresponds to the major decomposition reaction of $SrCO_3$ in the precursor. However, in pure $SrCO_3$ decomposition, that peak occurs at about 1,130^oC. This indicates that $SrCO_3$ in the precursor reacts at relatively lower temperature as per; $SrCO_3+TiO_2=SrTiO_3+CO_2$, which is due to the presence of acidic TiO_2 in the mixture [35].

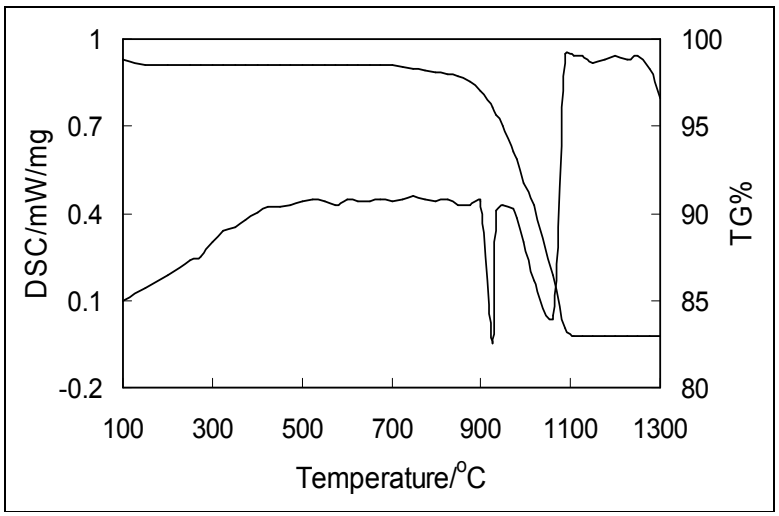

Figure 4.6 TGA and DSC curves in air for the $SrCO_3$, TiO_2 and ZrO_2 powder mixture.

4.3.3. Phase Formation Mechanism and Kinetics.

4.3.3.1. On the Phase Formation of $Ba_{0.5}Sr_{0.5}TiO_3$

Fig. 4.7 shows XRD pattern of $Ba_{0.5}Sr_{0.5}TiO_3$ raw precursor powder and powder calcined at different temperatures for 1 hour. It shows that BT and ST form in the system separately and then coherently with BST formation. Slow step scanning XRD analysis reveals that BT starts forming from 700 ^OC and ST starts forming from 800 ^OC. Formation of BaO or other phases like Ba_2TiO_4 or $BaTi_3O_7$, has not been observed within the detection limit of XRD. Here BT is directly formed through the reaction $BaCO_3 + TiO_2=BaTiO_3+CO_2$ (g).

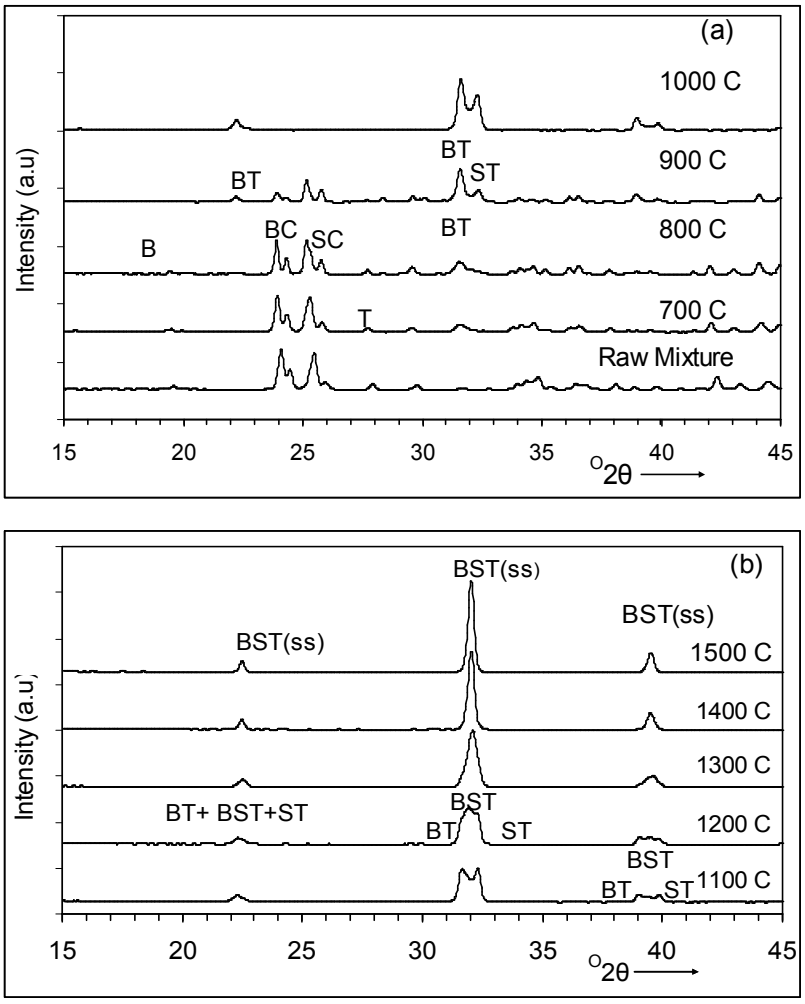

Figure 4.7 XRD patterns of raw mixture and calcined precursor powder for 1 h (a) Raw mixture at 700,800,900 and 1000 ^{O}C; (b) at 1100, 1200,1300,1400 and 1500 ^{O}C; with notations BC=$BaCO_3$, SC= $SrCO_3$,BT=$BaTiO_3$, ST=$SrTiO_3$, BST(ss)=$Ba_{0.5}Sr_{0.5}TiO_3$.

The intermediate phases like Sr_2TiO_4 and $SrTi_3O_7$ were observed in the samples calcined at 1000 ^{O}C for 1h and at 1,100 ^{O}C for 1h, with the presence of both Ti and Zr [38]. But in the present case, these phases were not observed, may be due to the presence of more acidic TiO_2 than ZrO_2 in the system, and ST is directly formed through the reaction $SrCO_3$ +TiO_2=$SrTiO_3$+CO_2(g).

The XRD patterns also suggest that the rate of formation of $SrTiO_3$ is lower than the formation of $BaTio_3$, which may be due to the (i) presence of more stable Sr than Ba in the system, and/or (ii) high average particle size of Sr than Ba. BST (ss) starts forming from 900^{O}C coherently with both BT and ST. Variation of their phase content with calcinations temperature is shown in the Fig. 4.8. As 1000^{O}C/1hour and 1,100^{O}C/1hour samples show maximum integrated intensity of BT and ST phases,

respectively, these quantities at that temperature were considered 100%. The quantity of BT is always higher than that of ST at temperatures up to 1,000 ^{O}C; but after 1000 ^{O}C, the quantity of BT decreases more quickly than ST and the quantity of BST (ss) increases rapidly. These observations indicate that $BaTiO_3$ forms easily in the system through solid-state reaction between $BaCO_3$ and TiO_2 and the rate of ST formation is relatively slower.

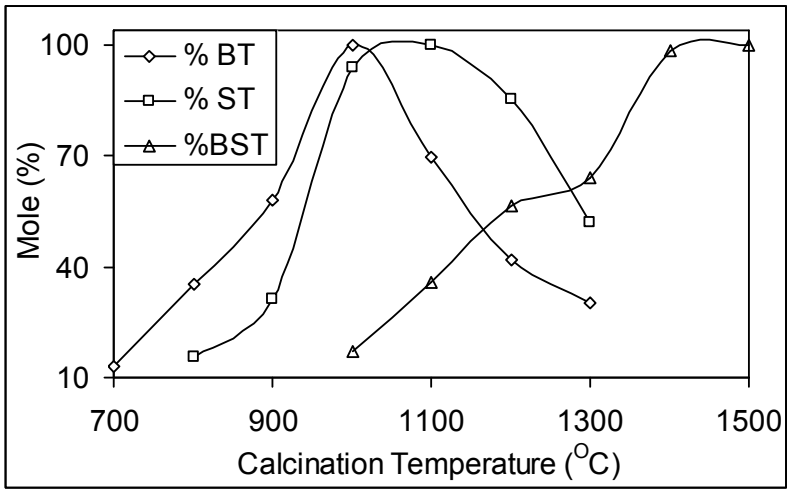

Figure 4.8 Non-isothermal transformation kinetics of precursor in static air.

However, quantity of BT increases slowly near the temperature 900^{o}C, which may be due to the decrease in the finer fraction of $BaCO_3$ and TiO_2 reactants, as they are used to form BT in the lower temperature range. Above 1300^{o}C, BST (ss) increases rapidly due to inter-diffusion between BT and ST.

To check the phase formation kinetics, concentrations of the phases were used to measure the activation energy for their formation using the following relationship [39]:

$$[1- [(1-X_B)^{1/3}]^2 = 2Kt/R^2 \quad (4.1)$$

where $2K/R^2$ is essentially a reaction rate constant, X_B is the volume fraction reacted at time 't'.

The same expression is used through out the study on the phase formation and reaction mechanism of different compositions. Here Log (K/R^2) vs. 1/T plot represents Arrhenius expression and activation energy for the phase formation can be derived from the slope of the plot.

Fig. 4.9 shows temperature dependency of their phase formation reaction. They show Arrhenius type of linear temperature dependency. Activation energy measured from slope shows that BT formation requires less activation energy (40.41 kcal/mol)

than that of ST formation (58.867 kcal/mol). Activation energy required for formation of BT and ST in the present system is higher than that reported else where [38, 40]. Here higher activation energy required may be due to simultaneous formation of BT, ST in the temperature range $800^{O}C$ to $1000^{O}C$ and BT, ST with BST(ss) at the temperature $1000^{O}C$. Phases were formed in this system through solid state interdiffusion between different particles. Interdiffusion takes place with different ions limiting the speed of diffusion. Activation energy results shows that phase formation reaction may be limited by the diffusion of Ba for BT and Sr for ST formation respectively. In this case Ti and O are assumed to be immobile because their concentrations are spatially invariant. Since $SrCO_3$ particles are relatively higher than $BaCO_3$, $SrTiO_3$ diffusion requires more activation energy to form perovskite phase.

BST solid solution formation requires less activation energy (43.41 kcal/mol) in the temperature range $1,000^{O}C$ to $1,200^{O}C$ but requires relatively high activation energy (76.999 kcal/mol) in the temperature range $1,300^{O}C$ to $1,500^{0}O$. The activation energy in the temperature range $1,200^{O}C$ to $1,300^{O}C$ is not calculated due to temporary slow down in the formation kinetics. The activation energy for formation of BST (ss) in the lower temperature range is close to the activation energy of BT formation. The study also indicates that solid solution formation takes place by the diffusion of BT into ST lattice, as BT decays more rapidly than ST at higher temperature. Also, XRD analysis indicates that solid -solution formation takes place by the diffusion of BT into ST lattice. As the peaks of ST are shifting towards lower angle with increase in calcinations temperature from $800^{O}C$ to $1,000^{O}C$, indicating increase in unit cell volume (Table 4.1) due to the incorporation of bigger Ba^{2+} ions, whereas, lattice parameter of BT remains constant in the said temperature range (Table 4.1), indicating no diffusion of Sr^{2+} in to BT lattice. At the temperatures above $1,100^{O}C$, the peaks of BT shift towards higher angle and lattice parameter of BT decreases (Table 4.1), indicating the incorporation of Sr^{2+} into $BaTiO_3$.

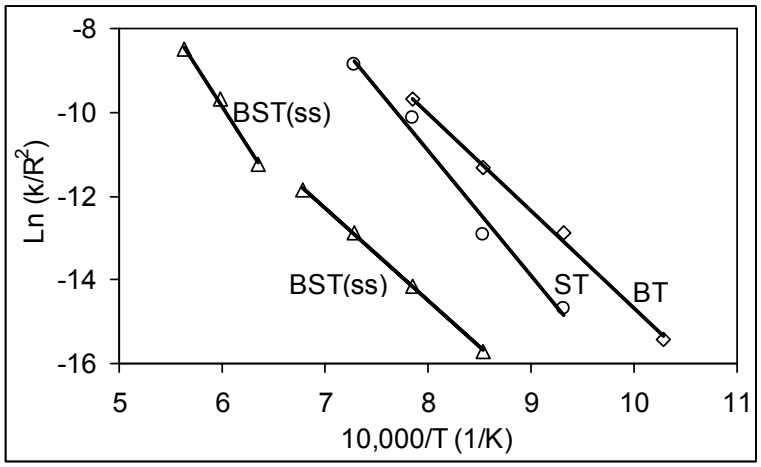

Figure 4.9 Arrhenius dependence of reaction rate on calcination temperature for the transformation of precursor to $BaTiO_3$ (◊) and $SrTiO_3$ (o) and then to $Ba_{0.5}Sr_{0.5}TiO_3$ solid solution (Δ).

The room temperature lattice parameters of three different phases at different temperatures along with their X-ray crystallite size are shown in Table 4.1. Lattice parameters of phases were calculated considering the cubic structure for BT (as per JCPDs card No 79-2263), structure for ST (as per JCPDs card No.84-0444) and also the cubic structure for BST (as per JCPDs card No.39-1395.). Lattice parameter of BST (ss), found in the present study (a_0= 3.952Å) is similar to that reported (a_0= 3.947 Å) in JCPDs card No.39-1395).

Previously we have indicated that initially the solid-solution formation takes place by the diffusion of BT into ST lattice and at higher temperature both the diffusions (i.e ST into BT and BT in to ST) take place. The XRD peaks of BST (ss), which forms in between [110] peak of BT and [110] peak of ST, (Figure 4.7(b)) was indexed as [110] reflections of cubic BST (ss) phase. A similar coherent interfaces between $BaZrO_3$ and $Ba(Ti_{0.5}Zr_{0.5})O_3$ lattices and $SrZrO_3$ with $Sr(Ti_{0.5}Zr_{0.5})O_3$ were also reported by the present author [37,38].This mechanism also suggests that the morphology of BST (ss) should be controlled by the morphology of ST and BT phase formed in the intermediate stage. Table 4.1 also shows the XRD crystallite sizes of BT, ST and BST (ss) at different temperatures. Crystallite size of BT is relatively higher than ST, which again indicates the easy formation of BT in the system.

Table 4.1: Lattice parameter 'a_0' in Å and XRD-crystallite size in nm of BT, ST and BST (ss) in the samples calcined at different temperatures.

Calcination Temp.(°C)	$BaTiO_3$		$SrTiO_3$		BST (ss)	
	a_0 (Å)	Crystallite Size(nm)	a_0 (Å)	Crystallite Size(nm)	a_0 (Å)	Crystallite Size (nm)
700	4.0065(8)	44.171				
800	4.0065(8)	43.762	3.9150(4)	23.776		
900	4.0066(3)	43.132	3.9196(9)	35.608		
1000	4.0065(2)	42.146	3.9238(9)	40.824	3.9850(7)	24.7205
1100	3.9978(7)	48.659	3.9169(7)	50.464	3.9802(4)	25.2730
1200	3.9962(4)	50.045	3.9202(7)	47.123	3.9756(4)	26.7247
1300	3.9949(6)	30.245	3.9301(4)	50.259	3.9433(4)	33.1065
1400	--------	-------	--------	--------	3.9532(4)	40.3569
1500	--------	-------	--------	--------	3.9529(4)	49.0520

Note. The numbers in the parentheses are the estimated standard deviations.

4.3.3.2. On the Phase Formation of $Ba_{0.5}Sr_{0.5}ZrO_3$

Fig. 4.10 shows XRD patterns of $Ba_{0.5}Sr_{0.5}ZrO_3$ raw precursor powder and powder calcined at different temperature for 1 hour. It shows that BZ and SZ form in the system initially and BSZ forms in the system coherently with SZ. Slow-step scanning XRD analysis reveals that BZ and SZ starts forming from 700 ^{O}C. Formation of BaO or other phases like Ba_2ZrO_4 or Sr_2ZrO_4, has not been observed within the detection limit of XRD. Here BZ is directly formed through the reaction $BaCO_3 + ZrO_2 = BaZrO_3 + CO_2$ (g). The intermediate Sr-rich phases like Sr_2ZrO_4 and $SrZr_3O_7$ were observed in the samples calcined at 1,000^{O}C for 1h and at 1,100 ^{O}C for 1h, with the presence of both Ti and Zr [38]. But in the present case these phases were not observed may be due to formation of SZ directly through the reaction $SrCO_3 + ZrO_2 = SrZrO_3 + CO_2$(g). The XRD patterns also suggest that the rate of formation of $SrZrO_3$ is lower than that of the formation of $BaZrO_3$, which may be due to the (i) presence of more stable Sr than Ba in the system, and/or (ii) high average particle size of $SrCO_3$ than $BaCO_3$. BSZ (ss) starts forming from 900^{O}C.

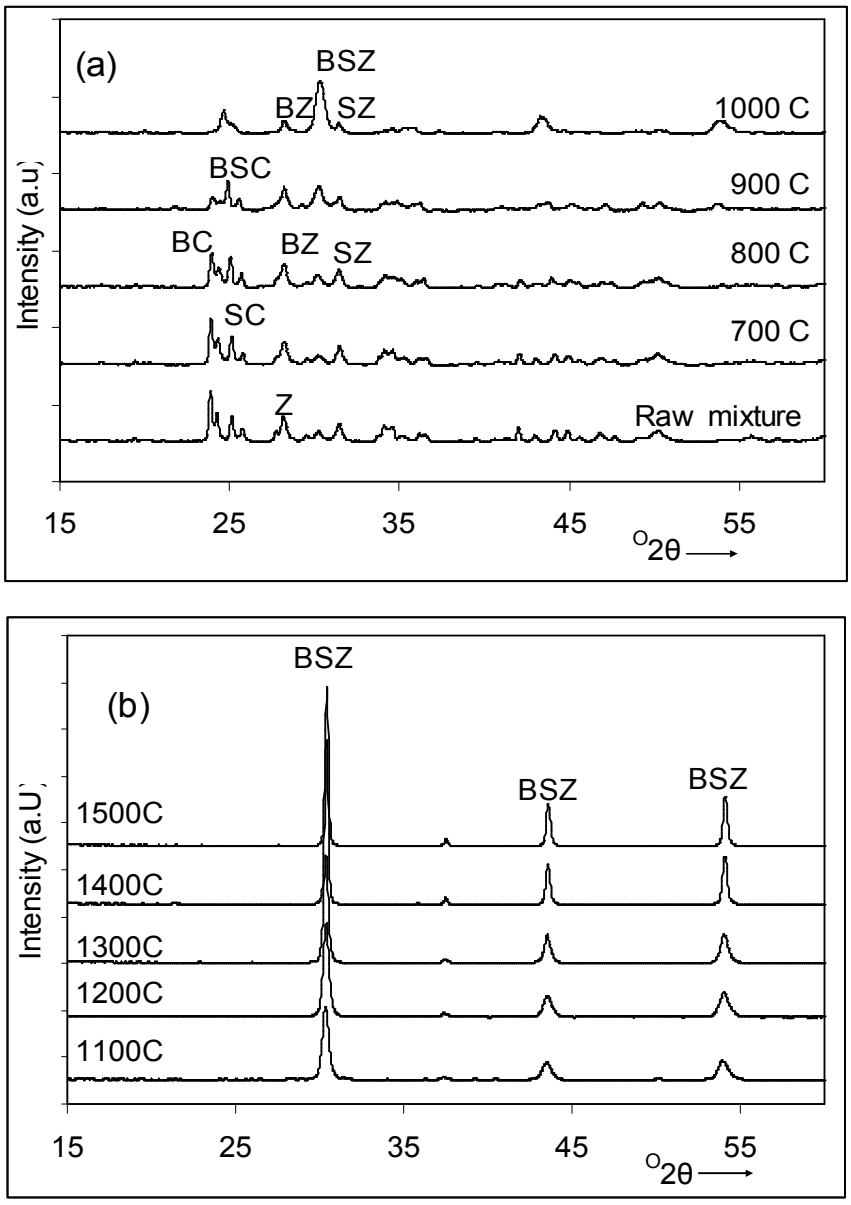

Figure 4.10 XRD patterns of raw mixture and calcined precursor powder for 1 h (a) Raw mixture, 700,800,900 and 1000 ^{O}C; (b) at 1100, 1200,1300,1400 and 1500 ^{O}C; with notations BC=$BaCO_3$, SC= $SrCO_3$, BZ=$BaZrO_3$, Z=ZrO_2, SZ=$SrZrO_3$, BSZ=$Ba_{0.5}Sr_{0.5}ZrO_3$.

Variation of their phase content with calcination temperature is shown in the Fig. 4.11. As 900 ^{O}C/1hour sample shows maximum integrated intensity of BZ and SZ phases respectively, these quantities at that temperature were considered 100%. The quantity of BZ is always higher than that of SZ at any temperature up to 1,000 ^{O}C; but after 1,000 ^{O}C, the quantity of BZ decreases more quickly than SZ and the quantity of BSZ (ss) increases rapidly. These observations indicate that BZ forms easily in the

system through solid-state reaction between $BaCO_3$ and ZrO_2 and the rate of SZ formation is relatively slower. Above 1,000^oC, BSZ (ss) increases rapidly due to inter-diffusion between BZ and SZ.

To check the phase formation kinetics, concentrations of the phases were used to measure the activation energy for their formation using the same relation (equ. 4.1) as used earlier for BST (ss) formation as per [39].

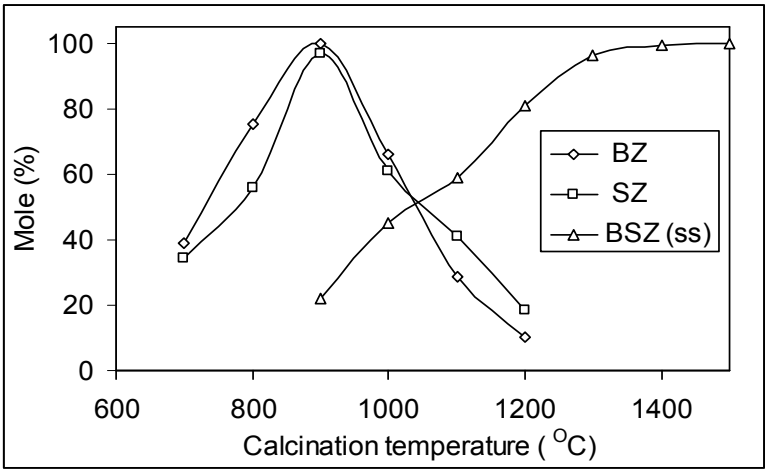

Figure 4.11 Non-isothermal transformation kinetics of precursor in static air.

Fig. 4.12 shows temperature dependency of their phase formation reactions. They show Arrhenius type linear temperature dependency. Activation energy measured from the slope shows that BZ formation requires activation energy (~58.069 kcal/mol) which is about same as that for SZ activation energy (~60.78 kcal/mol).The activation energies of BZ and SZ are near about the same value, indicating the simultaneous formation of both the phases. These activation energies are in the same range as that reported by Alberto Ubaldini [40]. Phases were formed in this system through solid state interdiffusion between different particles. Interdiffusion takes place with different ions limiting the speed of diffusion. Activation energy results indicate that the phase formations may be limited by diffusion of Ba and Sr for the formation of BSZ(ss). In the present case, Zr and O are assumed to be immobile because their concentrations are spatially invariant, when compared for the two perovskite structure. BSZ (ss) formation requires a little higher activation energy (97.43 kcal/mol) as compared to the other two phases.

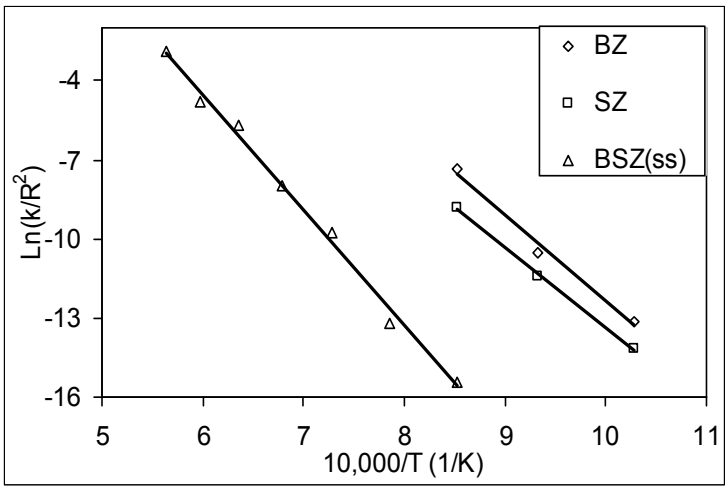

Figure 4.12 Arrhenius dependence of reaction rate on calcination temperature for the transformation of precursor to $BaZrO_3$ (◊) and $SrZrO_3$ (o) and then to $Ba_{0.5}Sr_{0.5}ZrO_3$ solid solution (Δ).

Table 4.2 and Table 4.3 show the lattice parameters of three different phases at different temperatures along with their X-ray crystallite size. Lattice parameters of phases were calculated considering the cubic structure for BZ, orthorhombic structure for both SZ and BSZ (ss) as per [41, 42]. Lattice parameters of the phases were very much similar to those reported by Kennedy *et al* [32]. Previously, it was indicated that the solid solution formation takes place by the diffusion of BZ into SZ lattice, as BZ decays more rapidly than SZ. It can be seen that the crystallite size of BZ and SZ are more or less comparable, which indicates that BT and ST form simultaneously in the temperature range 700 to 900^{O}C. At $1,000^{O}$C the crystallite size of both BZ and SZ decreases, but in the meanwhile, BSZ (ss) starts forming in the interface. At 1000^{O}C, the BSZ (ss) shows higher cell volume may be due to the disordered mixed phase structure. It can be noticed in the XRD pattern the same composition shows higher FWHM. This peak broadening arises in a number of ways including compositional inhomogeneity and hysteresis near the phase transition. The associated broadening at that temperature might be related to phase transition hysteresis. As indicated in Fig. 3.10, the BZ and SZ phases decrease rapidly above $1,100^{O}$C, so their lattice parameters and crystallite sizes could not be found at the temperatures $1,100^{O}$C and 1200^{O}C within the detection limit of XRD. With increase in temperature the cell volume become almost stable and lattice parameters are in good agreement with Kennedy *et al* [41]. The XRD peak of BSZ (ss), which grows between [110] peak of BZ and [200] peak of SZ (Fig.2 a) was indexed as [020], [112] reflection of orthorhombic phase. Such clear

splitting is not observed by XRD, which could be best observed using high resolution synchrotron diffraction measurements [41]. If the solid solution grows on BZ lattice, one would expect that peak is composed of [110], [101] reflections of orthorhombic structure. But the present investigation shows that the peak was for [020], [112] reflection of orthorhombic phase. That indicates that the solid solution formed coherently with [200] plain of orthorhombic structure. Similar coherent interface between $BaZrO_3$ and $Ba(Ti_{0.6}Zr_{0.4})O_3$ lattices and between $SrZrO_3$ and $SrTi_{0.5}Zr_{0.5}O_3$ were also reported by the present author [37,38].

Table 4.2: Lattice parameters in Å and XRD-crystallite size in nm of BZ and SZ in the samples calcined at different temperatures.

Calcination	$BaZrO_3$		$SrZrO_3$			
Temp.(°C)	a_0 (Å)	Crystallite Size (nm)	a_0 (Å)	b_0 (Å)	c_0 (Å)	Crystallite Size(nm)
700	4.2790(7)	13.838	5.5691(4)	8.0166(1)	5.1046(4)	13.7141
800	4.2673(6)	15.080	5.7034(8)	8.0124(7)	5.1011(4)	15.5211
900	4.1853(2)	21.727	5.8178(7)	8.2038(7)	5.7938(7)	20.8716
1000	4.1803(2)	14.750	5.6817(9)	7.9895(4)	5.1015(3)	19.2116
1100	…….	……	…….	……	…….	……

Note. The numbers in the parentheses are the estimated standard deviations.

Table 4.3: Lattice parameters in Å, cell volume in $Å^3$ and XRD-crystallite size in nm of BSZ (ss) phase in the samples calcined at different temperatures.

Calcination	$Ba_{0.5}Sr_{0.5}ZrO_3$				
Temp.(°C)	a_0 (Å)	b_0 (Å)	c_0 (Å)	Cell Volume ($Å^3$)	Crystallite Size (nm)
1000	5.8934(9)	8.3760(8)	5.8690(7)	289.71	15.0054
1100	5.8911(6)	8.3545(8)	5.8717(3)	288.99	17.0540
1200	5.8739(7)	8.3731(5)	5.8860(4)	288.49	23.6604
1300	5.8776(8)	8.2825(7)	5.8873(1)	286.60	31.0875
1400	5.8724(6)	8.3058(9)	5.8781(4)	286.70	60.8115
1500	5.8715(4)	8.2842(4)	5.8809(8)	286.05	74.8650

Note. The numbers in the parentheses are the estimated standard deviations.

4.3.3.3. On the Phase Formation of $BaTi_{0.5}Zr_{0.5}O_3$

Fig. 4.13 shows XRD pattern of Ba $(Ti_{0.5}Zr_{0.5})$ O_3 precursor powder calcined at different temperatures for 1 hour. It shows that BT and BZ form separately in the system and then BTZ(ss) forms by inter-diffusion between BT-BZ. Slow-step scanning XRD analysis reveals that $BaTiO_3$ starts forming from 700°C and $BaZrO_3$ from 800°C.

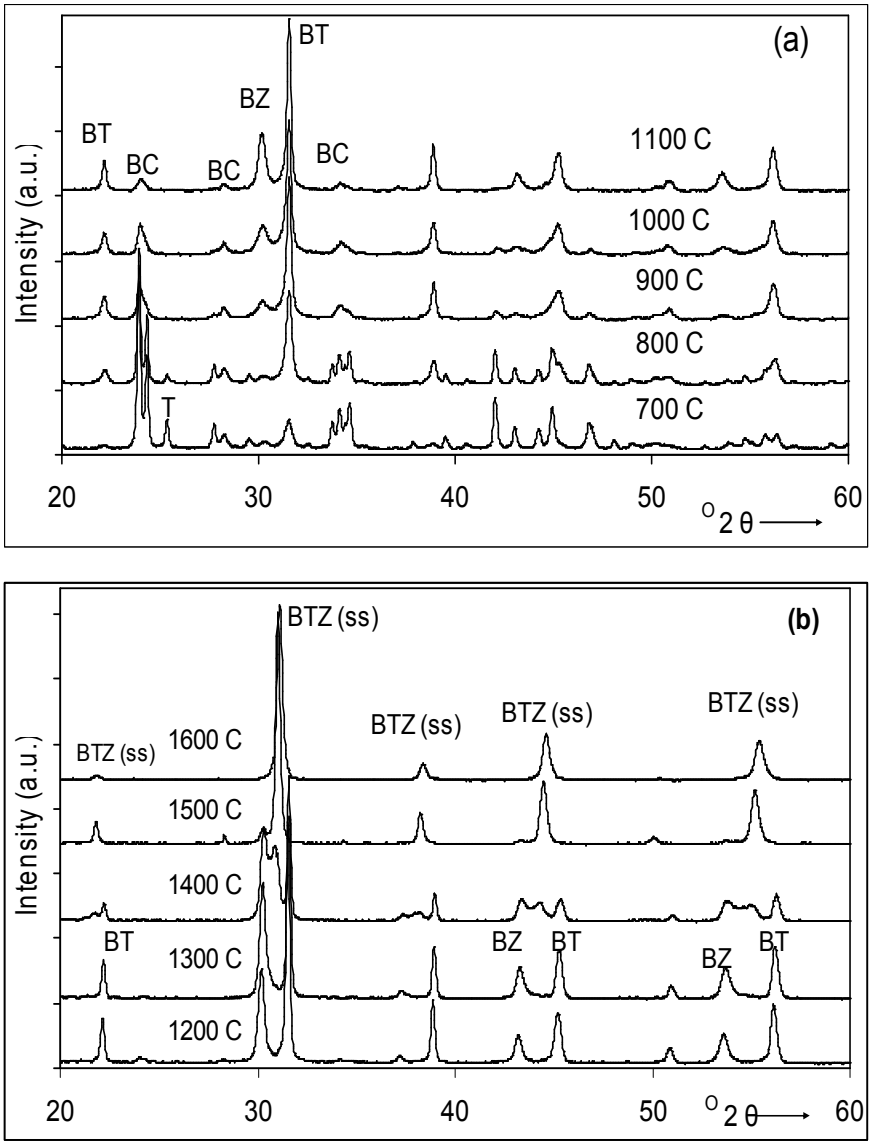

Figure 4.13 XRD patterns of calcined precursor powder for 1 hour (a) at 700°, 800°, 900°, 1000° and 1100°C; (b) at 1200°, 1300°, 1400°, 1500° and 1600°C; with notations: BT=$BaTiO_3$, BZ= $BaZrO_3$, BC=$BaCO_3$, BTZ(ss)= $Ba(Ti_{0.5}Zr_{0.5})O_3$ and T=TiO_2

Formation of intermediate BaO or other phases, like Ba_2ZrO_4, Ba_2TiO_4 or $BaTi_3O_7$, has not been observed within the detection limit of XRD. Consequently, BT and BZ are formed directly due to the reaction:

$$BaCO_3(s)+ZrO_2(s)+TiO_2(s)= BaTiO_3(s)+BaZrO_3(s)+CO_2\,(g)$$

The XRD patterns also suggest that the rate of $BaZrO_3$ formation is lower than that of $BaTiO_3$, which may be due to the (i) high average particle size of ZrO_2 (10.27 μm) than TiO_2 (0.35 μm), and/or (ii) higher ionic radius of Zr^{+4} (0.72 Å) than that of Ti^{+4} (0.61 Å). BTZ(ss) starts forming from 1,300°C. Variation of their phase content with calcinations temperature is shown in Fig. 4.14. The quantity of BT is always higher than the quantity of BZ at any temperature up-to 1200°C. But after 1,300°C, quantity of BT decreases quicker than BZ and the quantity of BTZ(ss) increases rapidly. These observations indicate that $BaTiO_3$ forms easily in the system through solid-state reaction between $BaCO_3$ and TiO_2, and the rate of BZ formation is relatively slower. However, quantity of BT increases slowly in the temperature range 900°C to 1100°C, which may be due to the decrease in the finer fraction of $BaCO_3$ and TiO_2 reactants, as they are used to form BT in the lower temperature range. These phase formations may be considered to follow a diminishing-core model. Diminishing cores are TiO_2 and ZrO_2. Above 1300°C, BTZ(ss) increases rapidly due to inter-diffusion between BT and BZ. To check the phase formation kinetics, concentrations of the phases were used to measure the activation energy for their formation using the same relation as used earlier for BST (ss) and BSZ (ss) formation as per [39].

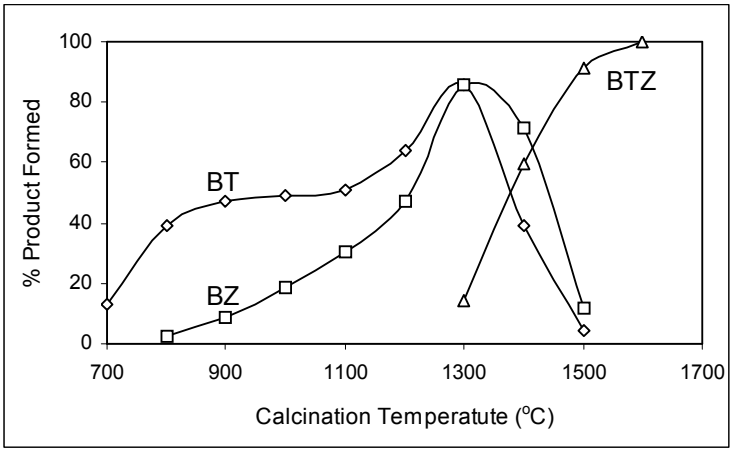

Figure 4. 14 Non-isothermal transformation kinetics $BaTi_{0.5}Zr_{0.5}O_3$ of precursor in static air.

Fig. 4.14 shows temperature dependency of their phase formation reactions. They show Arrhenius type of linear temperature dependency. Activation energy measured from the slope shows that BT formation requires less activation energy (32.65 kcal/mol and 34.3 kcal/mol in the temperature range 700° to 900°C and 1,100°C to

1,300^{o}C, respectively) than that of BZ formation (48.4 kcal/mol). BT-formation activation energy in the temperature range 900^{o}C to 1,100^{o}C, is not evaluated due to its temporary slow down in formation kinetics. Phases were formed in this system through solid-state interdiffusion between different particles. Interdiffusions take place with different ions limiting the speed of diffusion. Activation energy results show that phase formation reactions may be limited by the diffusion of Ti for BT and Zr for BZ formation, respectively. In this case, Ba and O are assumed to be immobile because their concentrations are spatially invariant. Since Zr^{+4} has higher ionic radius than Ti^{+4}, its diffusion requires higher energy than Ti^{+4} to form perovskite phase.

BTZ solid solution formation requires much high activation energy (133 kcal/mole), which is slightly higher than that (3.66 eV) reported by S.Gopalan and A.V.Virkar [42] for doped BT-BZ couples. In the present case, slight increase in activation energy may be due to the use of loose powders for reaction kinetics experiment as compared to sintered pellets and/or use of un-doped material. For BTZ (ss) formation reaction, the rate may be limited by the diffusion of Ba and/or O movement, which were proposed to be moveable during inter-diffusion experimental study in doped BT-BZ perovskites [42].

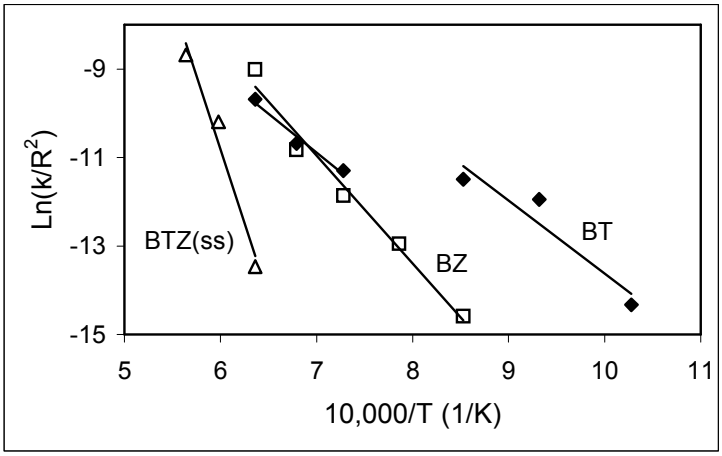

Figure 4.15 Arrhenius dependency of reaction rate on calcinations temperature for the transformation of precursor to $BaTiO_3$ (♦) and $BaZrO_3$ (□) and then to $BaTi_{0.5}Zr_{0.5}O_3$ solid solution (Δ).

The studies also indicate that solid-solution formation takes place by the diffusion of BT into BZ lattices, as BT decay more rapidly than BZ. Also from XRD data, it is found that [110] peak of BZ shifted to higher angle with calcinations temperature from 900^{o}C to 1,300^{o}C, indicating the decrease in unit cell volume (Table-4.4) due to the incorporation of smaller Ti^{+4} ions, whereas, lattice parameter of BT remains almost same in the said temperature range (Table-4.4), indicating there is no

diffusion of Zr^{+4} ion into BT lattices. Table 4.4 also shows that BTZ (ss) has higher lattice parameter at 1300°C than that at 1,600°C, indicating that initial solid solution is higher in Zr^{+4} ion content than the final equilibrium one. So it may be considered that solid solution grows on BZ lattices having a coherent interface with BZ crystal. Here the diminishing core is BZ. This mechanism also suggests that the morphology of BTZ (ss) should be controlled by the morphology of BZ phase formed in the intermediate stage. Table 4.4 also shows the XRD crystallite sizes of BZ, BT and BTZ (ss) at different calcinations temperatures. Crystallite size of BT is always much higher than that of BZ, which again shows the easy formation of BT in the system.

Table 4.4. Variation of lattice parameter a_0 and XRD crystallite size (within first bracket) of BT, BZ and BTZ-solid solution with calcinations temperature.

	Lattice parameter in Å (Crystallite size in nm)		
	900^0C	1300^0C	1600^0C
$BaTiO_3$	4.0094 (65.3)	4.0057 (232.4)	-----
$BaZrO_3$	4.1914 (39.1)	4.1696 (64.5)	-----
BTZ (ss)	-------	4.1216 (19.5)	4.0750 (180.2)

4.3.3.4. On the Phase Formation of $SrTi_{0.5}Zr_{0.5}O_3$

Fig. 4.16 shows the XRD pattern of the $Sr(Ti_{0.5}Zr_{0.5})O_3$ precursor powder calcined at different temperatures for one hour. It shows that ST and SZ form separately in the system and then STZ (ss) appears due to the inter-diffusion between ST and SZ. The 800°C/1hour sample shows the presence of $SrTiO_3$ in the calcined product. The $SrTiO_3$ is formed due to the decomposition reaction of the precursor. The decomposition reaction releases highly reactive SrO in the system and that immediately reacts with TiO_2 to form ST. That may be the reason, SrO was not detected by XRD. The SZ phase was identified only from 1000°C/1hour sample. Thus, the rate of formation of SZ was slower than ST in the system. That sample also shows the presence of two intermediate phases, Sr_2TiO_4 and $Sr_3Ti_2O_7$ along with $SrTiO_3$. The reason for the formation of Sr-rich intermediate phase may be due to the release of a huge amount of SrO in the system at that temperature range. At 1200°C, Sr_2TiO_4 and $Sr_3Ti_2O_7$ phases were not found due to their conversion into ST upon reacting with TiO_2 through Sr_2TiO_4 -to- $Sr_3Ti_2O_7$ -to- $SrTiO_3$ and then only ST and SZ phases were found.

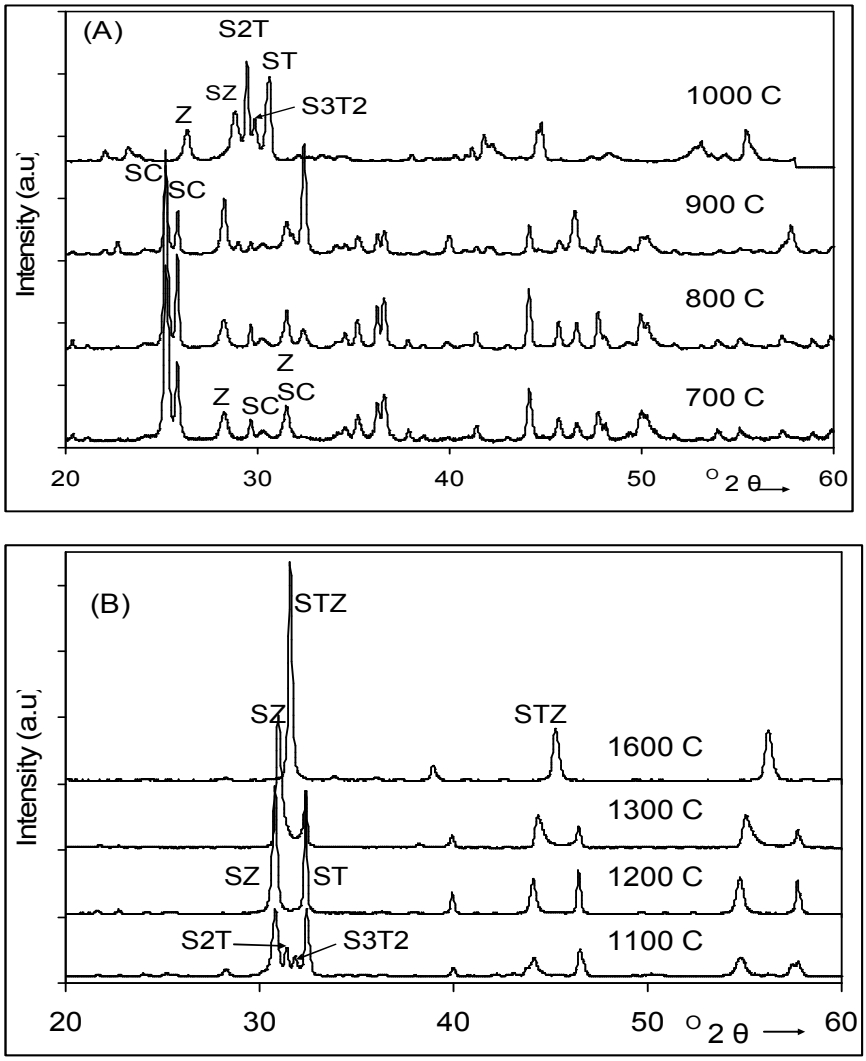

Figure 4.16 XRD pattern of calcined precursor powder for 1 hour at (A) 700^{o},800^{o},900^{o},1000^{o}C and (B) at 1100^{o}, 1200^{o}, 1500^{o} and 1600^{o}OC; with notation: ST=$SrTiO_3$, SZ=$SrZrO_3$, S2T=Sr_2TiO_4, S3T2=$Sr_3Ti_2O_7$, SC=$SrCO_3$, Z=ZrO_2, T=TiO_2 and STZ (ss)= $Sr(Ti_{0.5}Zr_{0.5})O_3$.

They started diffusing to form STZ (ss) in the temperature range $1,300^{o}$C to $1,350^{o}$C and STZ (ss) formation was complete in the range $1,550^{o}$C to $1,600^{o}$C. Intermediate phases like Sr_2ZrO_4 were not observed within the detection limit of XRD. ST and SZ were found to match best with PDF No. 05-0634 for ST and 70-0283 for SZ, respectively. However, no standard pattern is available for $Sr(Ti_{0.5}Zr_{0.5})O_3$ compound in PDF version-1998.

It is already indicated that the rate of $SrZrO_3$ formation is lower than that of $SrTiO_3$ formation. This may be due to the (i) less acidic nature of ZrO_2 than that of TiO_2, and/or (ii) high average particle size of ZrO_2 (10.27 μm) than TiO_2 (0.35 μm),

and/or (iii) higher ionic radius of Zr^{+4} (0.72 Å) than that of Ti^{+4} (0.61 Å). Variation of their phase content with calcinations temperature is shown in Fig. 4.16. As 1,300^{o}C/1hour sample shows maximum integrated intensities of ST and SZ phases, the quantities at that temperature were considered 100%. The quantity of ST apparently decreases at 1,000^{o}C due to the conversion of some fraction of that to Sr_2TiO_4 and $Sr_3Ti_2O_7$. The quantity of ST is higher than that of SZ up to 1,100^{o}C. After 1,300^{o}C, quantities of two phases are decreased due to their conversion into STZ (ss). But STZ (ss) was detectable only at 1,500^{o}C through slow step scanning. After 1,400^{o}C, quantity of ST decreases quicker than that of SZ, indicating that ST easily diffuses into SZ to form STZ (ss). After 1,500^{o}C, STZ (ss) increases rapidly.

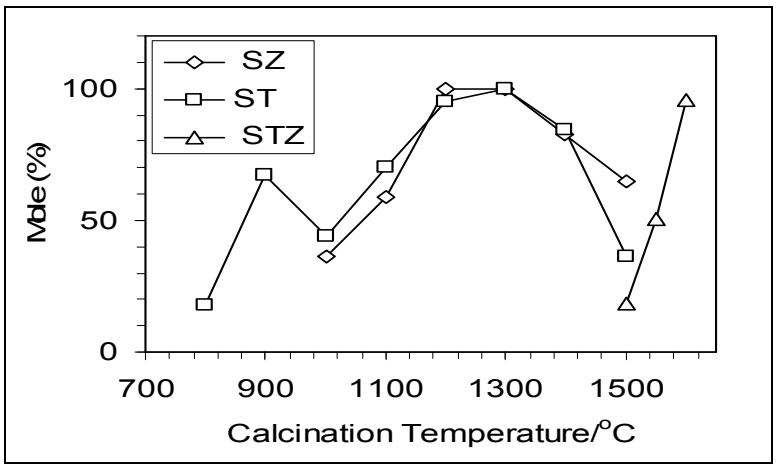

Figure 4.17 Non-isothermal transformation kinetics of precursor in static air.

To check the phase formation kinetics, concentrations of the phases were used to measure the activation energy for their formation using the same relation (Eq. 4.1) as used earlier for BST (ss), BSZ (ss) and BTZ (ss) formation as per [39].

Fig. 4.18 shows temperature dependency of their phase formation reactions. They show Arrhenius type of linear temperature dependency. The activation energy for the phase formation is measured from the slope, and it shows that ST formation requires less activation energy (47.27kcal/mol) than that of SZ formation (65.78kcal/mol) in the temperature range 1,000^{o}C to 1,300^{o}C. The activation energy found for SZ formation is in the same range of that found for BZ formation by Alberto Ubaldini *et al*. [40]. Phases were formed in this system through solid-state interdiffusion between different particles. Interdiffusions take place with different ions limiting the speed of diffusion. Activation energy results indicate that the phase formation reactions may be limited by the diffusion of Ti for ST and Zr for SZ formation, respectively. In the present case, Sr and O are assumed to be immobile because their concentrations are spatially invariant,

when compared for the two perovskite structures. Since Zr^{+4} has a larger ionic radius than Ti^{+4}, its diffusion requires a higher energy than Ti^{+4} to form perovskite phase.

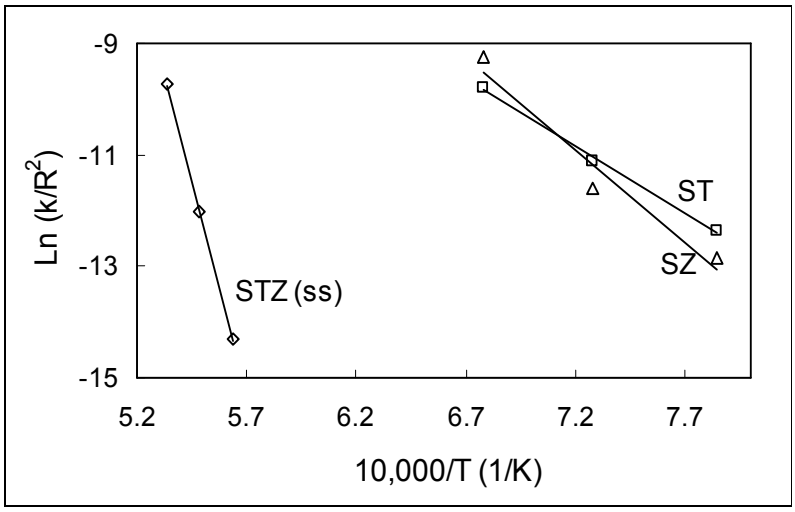

Figure 4.18 Arrhenius dependency of reaction rate on calcinations temperature for the formation of $SrTiO_3$ (□) and $SrZrO_3$ (Δ) and $SrTi_{0.5}Zr_{0.5}O_3$ solid solution (◊).

STZ solid solution formation requires much high activation energy (297.52 kcal/mole). In the present case, a high activation energy found may be due to the use of loose powders for reaction kinetics experiment as compared to sintered pellets and/or use of un-doped material. For STZ (ss) formation, the rate of reaction may be limited by the diffusion of Ti through the SZ structure because the activation energy for the process is very similar to that calculated by Lewis *et al.* for the Ti- vacancy migration in $BaTiO_3$ [43].

The room temperature lattice parameters of the three phases present in the samples calcined at different temperatures are shown in Table 4.5 along with their x-ray crystallite size. These parameters of phases were calculated considering cubic structure for ST, orthorhombic for SZ and tetragonal for STZ (ss) as per T.K.Y.Yong *et al*.[44]. For comparison only 'a_0' values are given in the Table 4.5. Lattice parameter of STZ (ss), found in the present study (a_0= 5.6688(6) Å, c_0= 8.0212(0) Å) is similar to that reported (a_0= 5.6650 Å, c_0= 8.011 Å) by [44]. Previously, we indicated that solid-solution formation takes place by the diffusion of ST into SZ lattices, as ST decomposes more rapidly than SZ.

Table 4.5 Lattice parameter 'a_0' in Å and XRD-crystallite size in nm of ST, SZ and STZ (ss) in the samples calcined at different temperatures.

Calcination Temp.(^oC)	$SrTiO_3$		$SrZrO_3$		STZ (ss)	
	a_0 (Å)	Crystallite Size (nm)	a_0 (Å)	Crystallite Size (nm)	a_0 (Å)	Crystallite Size (nm)
800	3.9107(8)					
900	3.9054(8)					
1000	3.8957(9)	42.47	5.8004(9)	17.48		
1100	3.9039(7)	54.83	5.8037(9)	30.75		
1200	3.9076(5)	164.01	5.8048(9)	39.57		
1300	3.9037(6)	171.72	5.7967(8)	45.18		
1400	3.9083(3)	217.31	5.7899(6)	53.37		
1500	3.9126(2)	411.57	5.7753(5)	67.39	5.6882(9)	14.49
1550	--------		-------		5.6755(9)	45.55
1600	--------		-------		5.6715(8)	59.0
1650	--------		-------		5.6688(6)	65.0

Note. The numbers in the parentheses are the estimated standard deviations.

Also it is found that lattice parameter of SZ decreases with increase in temperature from 1,100^{o}C to 1,400^{o}C (Table 4.5) due to the incorporation of smaller Ti^{+4} ions in SZ, whereas, lattice parameter of ST remains almost the same up to 1400^{o}C, indicating there is negligible diffusion of Zr^{+4} ion into ST structure. Some Zr^{+4} ion diffusion into ST structure may be expected at higher temperatures as 1,500^{o}C samples show slight increase in 'a_0' value of ST. Table 4.5 also shows that STZ (ss) has higher lattice parameter at 1,500^{o}C than that at 1,600^{o}C, indicating that initial solid solution is higher in Zr^{+4} ion content than the final equilibrium one. Thus, it may be considered that solid solution forms on SZ lattices having a coherent interface with SZ crystal, but not on the ST lattice The XRD peaks of STZ (ss) which forms in between [110] peak of ST and [200] peak of SZ (Fig. 4.15(b)) was indexed as overlapping [020], [112] reflections of tetragonal STZ (ss) phase. If solid solution forms on ST lattice, one would expect that peak to be composed of [110], [101] reflections of tetragonal structure. But the present investigation shows that the peak was for [020] reflection of tetragonal structure. That indicates that the solid solution is formed coherently with [200] plane of SZ. A similar coherent interface between $BaZrO_3$ and $Ba(Ti_{0.6}Zr_{0.4})O_3$ lattices was also found by the present author [37].This mechanism also suggests that the morphology of STZ (ss) should be controlled by the morphology of SZ phase formed in the intermediate stage. Table 4.5 also shows the XRD crystallite sizes of SZ, ST and STZ (ss) at different

temperatures. Crystallite size of ST is always much higher than that of SZ, which again indicates the easy formation of ST in the system.

4.4. Phase Formation of the Ba-Sr-Ti-Zr- Oxide System

4.4.1. Phase Formation of $Ba_{1-x}Sr_xTi_{0.5}Zr_{0.5}O_3$ Ceramics

Fig. 4.19 shows the room temperature XRD pattern of the $Ba_{1-x}Sr_xTi_{0.5}Zr_{0.5}O_3$ ceramics with different Sr (x) concentration. The XRD patterns were indexed and cell parameters were refined by using standard CCP-14 program "CHEKCELL" [45]. It is evident from the figure that all the peaks correspond to perovskite phase. The composition with x=0.0, i.e, $Ba(Ti_{0.5}Zr_{0.5})O_3$, was indexed in cubic system (space group Pm-3m) and the pattern was very similar to the standard PDF-2 card No. 36-0019 (for Cubic $BaTi_{0.75}Zr_{0.25}O_3$). It has been suggested that the solid solution $Ba(Ti_{1-x}Zr_x)O_3$ does not exist for x>0.42 [46]. However, in the present investigation the solid solution $Ba(Ti_{0.5}Zr_{0.5})O_3$ was found to exist as a single phase perovskite. The ceramic compositions were synthesized in the present study through successive calcinations and long time sintering etc. These processing may be responsible for the formation of a single phase solid solution of the same. With increase in Sr, the BSTZ system remains cubic upto 50 atom% substitution; only peaks were shifted towards higher angle yielding the decrease in lattice parameter due to the substitution of bigger Ba^{+2} (R=1.35 Å) by smaller Sr^{+2} (R = 1.13 Å) in the structure.

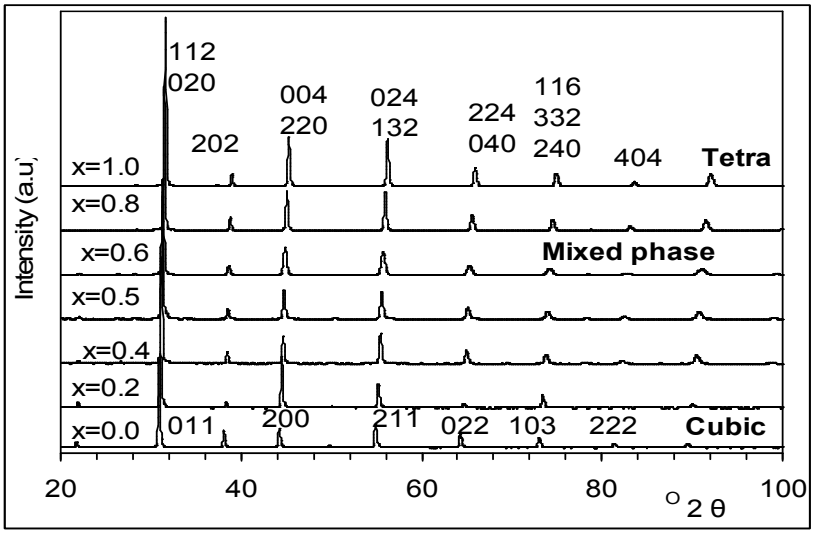

Figure 4.19 XRD pattern of $(Ba_{1-X}Sr_X)Ti_{0.5}Zr_{0.5}O_3$ ceramics with different Sr (x) content. Indexing (cubic) in x=0.0 is valid upto x=0.5 and those (Tetragonal) for x=1.0 upto x=0.06

The lattice parameters of different compositions are shown in Table 4.6. The pattern of composition x=0.6 appears to contain both the cubic and tetragonal phases. Because, (a) both cubic and tetragonal indexing were possible on the pattern (the lattice parameters for both the indexing are shown in Table 4.6) and (b) it shows relatively higher FWHM (Table 4.6) of its diffraction peaks. However, the patterns of x=0.8 and 1.0, were indexed in tetragonal system. The composition, x=1.0, i.e, $Sr(Ti_{0.5}Zr_{0.5})O_3$, is reported to be tetragonal [44,38] with space group I4/mcm. So upon Sr substitution in BTZ, the structure changes from Pm-3m cubic (Z=1) to I4/mcm tetragonal (Z=4) above x>0.6. The 100% relative intensity peak widths of all the compositions were compared (Table-4.6). Composition with x=0.6 show highest FWHM among all, mainly due to the presence of both cubic and tetragonal phases in it. The composition x=0.5 shows slightly higher FWHM, may be due to the presence of 50:50 ratio of $Ba(Ti_{0.5}Zr_{0.5})O_3$ and $Sr(Ti_{0.5}Zr_{0.5})O_3$ in the solid solution.

Table 4.6: Variation of crystal symmetry, lattice parameter, FWHM (100% relative intensity peak) and X-ray density of the $(Ba_{1-x}Sr_x)Ti_{0.5}Zr_{0.5}O_3$ compositions with different Sr (x) content.

Sr (x)	Symmetry	Lattice parameter(Å)	FWHM of I_{100} peak	X-ray Density (gm/cc)
0	Cubic	a_0 =4.101(02)	0.131	6.14
0.2	Cubic	a_0 =4.078(07)	0.116	5.99
0.4	Cubic	a_0 =4.065(02)	0.149	5.81
0.5	Cubic	a_0 =4.057(07)	0.167	5.72
0.6	Cubic + Tetragonal	a_0=4.042(06) and a_0 =5.717(15) c_0 =8.104(21)	0.263	5.66 5.64
0.8	Tetragonal	a_0 =5.694(06) c_0 =8.064(04)	0.140	5.46
1.0	Tetragonal	a_0=5.671(03) c_0 =8.023(06)	0.138	5.38

The calculated X-ray density was found to decrease with Sr substitution. As expected, the bulk density also decreases with the increase in Sr substitution. The apparent porosity was found to increase with the Sr substitution. This indicates that BTZ composition (x=0.0) is easy to sinter than $SrTi_{0.5}Zr_{0.5}O_3$ (STZ) ceramics, i.e. the

composition with x=1.0. The better sintering behavior of BTZ may also be revealed from its bigger grain size (Fig.6.1) in the sintered ceramics.

4.4.2. Phase Formation of $(Ba_{0.5}Sr_{0.5})(Ti_{1-x}Zr_x)O_3$ Ceramics

Fig. 4.20 shows the XRD pattern of $(Ba_{0.5}Sr_{0.5})(Ti_{1-x}Zr_x)O_3$ ceramics with different x value. The composition with x=0 was indexed in cubic system and was similar to PDF-2 card no. 39-1395 for the material $Ba_{0.5}Sr_{0.5}TiO_3$. The intermediate compositions from x=0.2 to 0.6, were also indexed in cubic system with space group symmetry *Pm3m*. The diffraction pattern of x=0.8 composition was analyzed to contain cubic and tetragonal *(I4/mcm)* phase mixture. The cubic phase of x=0.8 composition was very similar to the cubic phase of x=0.6 composition. This indicates that solid solution breaks around the composition x=0.8. The 80 atom% Zr substituted composition also suggests having superlattice structure due to the presence of two dissimilar structures [45].

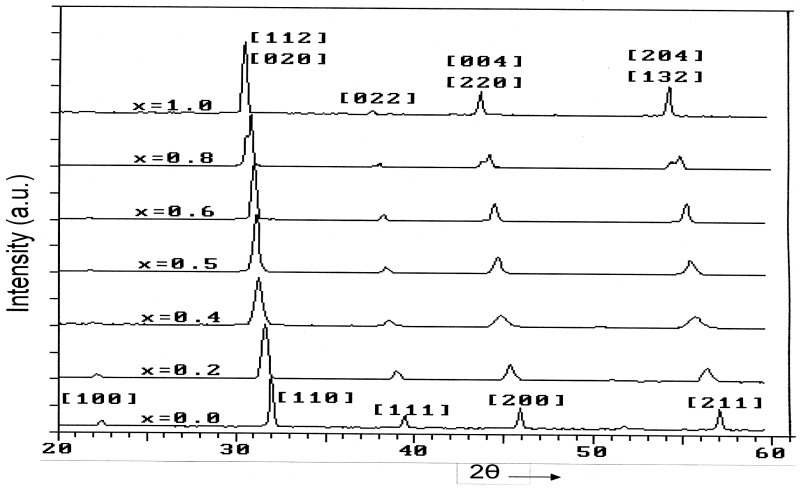

Figure. 4.20. XRD patterns of $(Ba_{0.5}Sr_{0.5})(Ti_{1-x}Zr_x)O_3$ ceramics with their representative value of x (Zr) in the composition.

It is reported by B.J.Kennedy, *et al* [41] that the end composition with x=1.0, i.e. $Ba_{0.5}Sr_{0.5}ZrO_3$, contains orthorhombic *Imma* symmetry. No standard XRD pattern is available in PDF-2 data file for barium strontium zirconate (x=1.0) material. These identifications revealed that the system ($Ba_{0.5}Sr_{0.5}TiO_3$) transforms from cubic to orthorhombic ($Ba_{0.5}Sr_{0.5}ZrO_3$) upon Zr substitution for Ti, through an intermediate tetragonal phase formation. In our case, the composition $Ba_{0.5}Sr_{0.5}Zr_{0.8}Ti_{0.2}O_3$ contains both tetragonal and orthorhombic phase. The details of structural information of the $Ba_{0.5}Sr_{0.5}ZrO_3$ composition are given in the Chapter 7 after Rietveld refinement. The

Fig.4.19 also shows that the substitution of Zr^{4+} for Ti^{4+} increases the d-spacing yielding the shift of diffraction peaks towards lower 2θ angle. This is the clear indication that Zr^{4+} is systematically dissolved in $Ba_{0.5}Sr_{0.5}TiO_3$ lattice upto 60 atom% substitutions. Lattice parameter increases due to the incorporation of bigger Zr^{4+} (0.087 nm) for smaller Ti^{4+} (0.068 nm). The lattice parameters of respective cubic, tetragonal and orthorhombic phases present in the samples are shown in the Table-4.7, along with the full width at half maxima (FWHM) of the 100% relative intensity (I_{100}) peak of the phases and their X-ray density. Compositions with x=0.2, 0.4 and 0.5 show comparatively higher FWHM (Table-4.7) than other samples. The peak broadening can arise in a number of ways including compositional inhomogeneity, hysteresis near the phase transition, presence of defects in the crystal lattice, presence of very fine particles, etc.

Table 4.7: The crystal symmetry, lattice parameter and FWHM of 100% relative intensity peak of the phases present in the $(Ba_{0.5}Sr_{0.5})(Ti_{1-x}Zr_x)O_3$ with different Zr (x) concentration.

Zr(x)	Symmetry	Lattice parameter	FWHM of I_{100} peak	X-ray Density (gm/cc)
0	Cubic*(Pm3m*)	a_0=3.9535(12)	0.114	5.596
0.2	Cubic	a_0=4.0046(41)	0.302	5.6107
0.4	Cubic	a_0=4.0485(40)	0.415	5.6471
0.5	Cubic	a_0 =4.057(07)	0.167	5.7194
0.6	Cubic	a_0=4.0822(11)	0.156	5.7199
0.8	Cubic	a_0=4.10976(17)	0.185	5.8128
	Tetragonal *(I4/mcm)*	a_0=5.8707(80) c_0= 8.1683(44)	0.219	5.7332
1.0	Orthorhombic (*Imma)*	a_0=5.86900(50) b_0=8.30590(71) c_0= 5.90058(36)	0.121	5.8122

The presence of very fine particles may be ruled out here because of the several heat treatments during processing. For example the composition x=0.2 shows a high FWHM, although it was allmost melted during high temperature calcinations. Here the associated broadening may be related to the formation of disordered cubic structure as reported for barium titanate zirconate (BZT) by A. Dixit *et al.*[47]. This disorderness (i.e., peak broadening) is maximum at x=0.4 composition.

4.5. Effect of Ca and Mg on $BaTi_{0.6}Zr_{0.4}O_3$ Ceramics

4.5.1. Effect of Ca on the Phase Formation of $BaTi_{0.6}Zr_{0.4}O_3$ Ceramics

Fig. 4.21 shows the XRD pattern of the $Ba_{1-x}Ca_xTi_{0.6}Zr_{0.4}O_3$ samples with different Ca (x) concentration. The compositions, x=0.0, and x=0.1, i.e., Ba $(Ti_{0.6}Zr_{0.4})O_3$ and $Ba_{0.9}Ca_{0.1}Ti_{0.6}Zr_{0.4}O_3$ were indexed in cubic symmetry with space group pm3m. The Ca-rich compositions (i.e., with $x \geq 0.2$) are indexed according to a mixture of orthorhombic $CaTiO_3$ and tetragonal $Ba_{0.9}Ca_{0.2}Ti_{0.6}Zr_{0.4}O_3$ phases. Recently, I. Levin *el al* [49] reported that solubility of CaO in $BaZrO_3$ increases from a few percent at 1,400^{o}C to about 30 % at 1,650^{o}C. But in the present study at 1,500^{O}C/ 4hr, the solubility of Ca, in Ba (TiZr) O_3 fails at around 20 atom %. The Zr^{4+} ion is chemically more stable than Ti^{4+} ion, which may be the one cause for breaking of solid solution [50]. The quantities of these phase present in the Ca rich compositions are discussed in the Chapter-5 by quantitative estimation of the phases using Rietveld refinement technique.

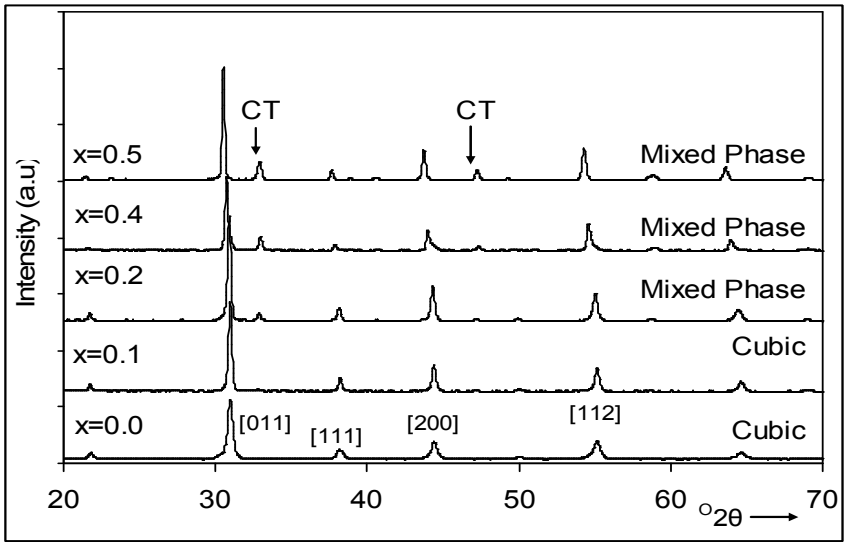

Figure. 4.21. XRD pattern of $(Ba_{1-X}Ca_X)$ $Ti_{0.6}Zr_{0.4}O_3$ ceramics with different Ca (x) content.

The lattice parameters of single phase compounds in the system are shown in the Table-4.8 along with the cell volume, x ray density and full width at half maxima (FWHM) of the 100% relative intensity (I_{100}) peak of the phases. The lattice parameters of other compositions (mixed phase) are given in the Chapter 5 after Rietveld refinement.

Table 4.8: Variation of crystal symmetry, lattice parameter, Cell volume and FWHM (100% relative intensity peak) with different Ca (x) concentration in the $(Ba_{1-X}Ca_X)$ $Ti_{0.6}Zr_{0.4}O_3$.

Ca (x)	Symmetry	Lattice parameter(Å)	Cell Volume ($Å^3$)	X-ray density (gm/cc)	FWHM of 100% RI peak
0	cubic	a_0 =4.0934	68.6566	6.0695	0.209
0.1	Tetragonal	a_0 = 4.061	66.973	5.8002	0.201
0.2	Mixed Phase				
0.4	Mixed Phase				
0.5	Mixed Phase				

4.5.2. Effect of Mg on the Phase Formation of $BaTi_{0.6}Zr_{0.4}O_3$ Ceramics

Fig. 4.22 shows the XRD pattern of the $Ba_{1-x}Mg_xTi_{0.6}Zr_{0.4}O_3$ samples with different Mg (x) concentration. The plot shows that the compositions are of single phase and were indexed in cubic system with space group pm3m. There is a slight shift of the peaks towards higher angle indicating the decrease in lattice parameter due to the substitution of Ba by smaller Mg. This observation indicates that Mg is systematically dissolved in BTZ ceramic within the studied composition range (x=0.14).

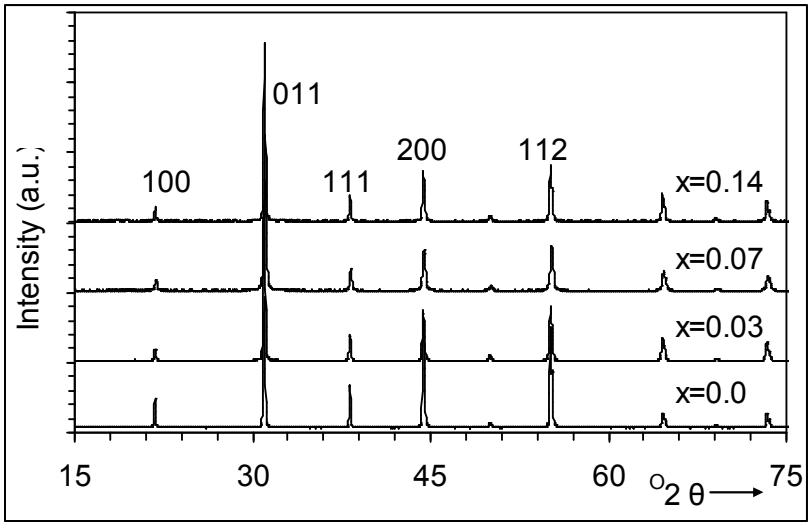

Figure. 4.22. XRD patterns of $(Ba_{1-X}Mg_X)$ $Ti_{0.6}$ $Zr_{0.4}O_3$ ceramics with different Mg(x) content.

Table 4.9: Variation of crystal symmetry, lattice parameter, cell volume and FWHM (100% relative intensity peak) with different Mg (x) concentration in the $(Ba_{1-X}Mg_X)Ti_{0.6}Zr_{0.4}O_3$.

Mg(x)	Symmetry	Lattice parameter(Å)	Cell Volume ($Å^3$)	X-ray density (gm/cc)	FWHM of 100% RI peak
0.0	cubic	a_0 =4.0934	68.6566	6.0695	0.209
0.03	cubic	a_0 =4.091	68.618	5.9721	0.160
0.07	cubic	a_0 =4.089	68.368	5.8717	0.163
0.14	cubic	a_0 =4.081	67.97	5.6687	0.144

Table 4.9 shows; there is decrease in cell volume with increase in Mg content due to the substitution of smaller Mg in place of Ba. The FWHM of 100% relative intensity peak of the compositions decreases with increase in Mg content. The reason may be due to the formation of more crystalline phase with increase in Mg, which has relatively lower melting temperature than Ba.

4.6. Summary and Conclusions

The formation kinetics of $BaTiO_3$-$SrTiO_3$ solid solution from mixture of $BaCO_3$, $SrCO_3$ and TiO_2 powders and the formation kinetics of $BaZrO_3$-$SrZrO_3$ solid solution from mixture of $BaCO_3$, $SrCO_3$ and ZrO_2 powders have been studied in air at 700-1500^{O}C using TGA/DSC and XRD. The formation kinetics of $BaTiO_3$-$BaZrO_3$ solid solution from mixture of $BaCO_3$, TiO_2 and ZrO_2 powders and the formation kinetics of $SrTiO_3$-$SrZrO_3$ solid solution from mixture of $SrCO_3$, TiO_2 and ZrO_2 powders have been studied in air at 700^o-1600^{o}C using TGA/DSC and XRD. Based on non-isothermal kinetic analysis and on crystal structure, the reaction mechanism can be described as follows;

1. During $Ba_{0.5}Sr_{0.5}TiO_3$ formation, initially $BaTiO_3$ and $SrTiO_3$ phases are formed through direct solid state reaction between $BaCO_3$, $SrCO_3$ and TiO_2 at lower temperature. The phases like Ba_2TiO_4, $BaTi_3O_7$, Sr_2TiO_4 or $SrTi_2O_7$ etc., have not been detected. $BaTiO_3$ formation requires less activation energy than $SrTiO_3$, which may be due to the difference in their ionic radius. The BST(ss) forms coherently with BT at lower temperature. During the second stage, at relatively higher temperature, BST solid solution is formed due to the diffusion of $BaTiO_3$ and $SrTiO_3$. Activation energy for this step is relatively higher.

2. During $Ba_{0.5}Sr_{0.5}ZrO_3$ formation, $BaZrO_3$ and $SrZrO_3$ phases are formed through direct solid state reaction between $BaCO_3$, $SrCO_3$ and ZrO_2 at lower temperature. The phases like Ba_2ZrO_4, $BaZr_3O_7$, Sr_2ZrO_4 or $SrZr_2O_7$ etc., have not been detected. $BaZrO_3$ formation requires less activation energy than $SrZrO_3$. During the second stage, at relatively higher temperature, BSZ solid solution is formed coherently at the [200] plane of SZ due to the diffusion of $BaZrO_3$ in to $SrZrO_3$. Solid solution was formed coherently with the crystal of $SrZrO_3$.
3. During phase formation of Ba $(Ti_{0.5}Zr_{0.5})O_3$, the BaTiO3 and $BaZrO_3$ phases are formed through direct solid-state reaction between $BaCO_3$ and TiO_2, ZrO_2, with latter two acting as diminishing cores. Formation of intermediate phases as Ba_2ZrO_4, Ba_2TiO_4 or $BaTi_3O_7$, etc has not been detected. $BaTiO_3$ formation activation energy, 34.3 kcal/mol, is lower than $BaZrO_3$ formation energy, 48.4 kcal/mol, which may be due to the difference in their ionic radius. During the second step, $BaTiO_3$-$BaZrO_3$ solid solution is formed mainly by the diffusion of $BaTiO_3$ into the $BaZrO_3$ lattice, where latter phase acts as diminishing core. Activation energy for this step is 133 kcal/mole, which may be due to the diffusion of Ba and/or O ions through solid solution interface.
4. $Sr(Ti_{0.5}Zr_{0.5})O_3$ solid solution was formed through solid state reaction from a mixture of $SrCO_3$, TiO_2 and ZrO_2, via the formation of $SrTiO_3$ and $SrZrO_3$ phases separately in the system and then inter-diffusion of $SrTiO_3$ into $SrZrO_3$ to form the solid solution. The rate of $SrTiO_3$ formation was higher than that of $SrZrO_3$ formation, apparently due to the higher ionic radius of Zr^{+4} ions. The activation energies of phase formations were 47.27, 65.78 and 297.52 Kcal/mol for SrTiO3, SrZrO3 and $Sr(Ti_{0.5}Zr_{0.5})O_3$ respectively and the formation reactions were limited by the diffusion of Sr ion for $SrTiO_3$, Zr ion for $SrZrO_3$ and Ti ions for $Sr(Ti_{0.5}Zr_{0.5})O_3$, etc. Solid solution was formed coherently with the crystal of $SrZrO_3$.
5. The solid solution system $Ba_{1-x}Sr_x$ $(Ti_{0.5}Zr_{0.5})O_3$ remains cubic up to $x<0.6$ and tetragonal in the range x = 0.6 to 1.0. Composition at x=0.6 contains mixed phase structure with broadened diffraction pattern.
6. The solid solution system $(Ba_{0.5}Sr_{0.5})(Ti_{1-x}Zr_x)O_3$ remains cubic up to $x\leq0.6$, the solid solution breaks around x=0.8 and $Ba_{0.5}Sr_{0.5}ZrO_3$ has tetragonal structure. Compositions with x=0.2, 0.4 and 0.5 have deformed cubic structure with broadened diffraction pattern, suggesting to show relaxor properties

7. The compositions, x=0.0, and x=0.1, i.e, $Ba(Ti_{0.6}Zr_{0.4})O_3$ and $Ba_{0.9}Ca_{0.1}Ti_{0.6}Zr_{0.4}O_3$ were indexed in cubic system with space group pm3m The compositions with x=0.2, 0.4 and 0.5 were indexed as mixture of both tetragonal (like $Ba_{0.9}Ca_{0.1}Ti_{0.6}Zr_{0.4}O_3$) symmetry with space group 14/mcm and orthorhombic $CaTiO_3$ symmetry with space group Pbnm, respectively.
8. The solid solution system $Ba_{1-x}Mg_x$ $(Ti_{0.6}Zr_{0.4})O_3$ remains cubic in the studied compositions. The peaks are only shifting towards higher angle, indicating decrease in lattice parameter due to the incorporation of smaller Mg in place of higher-radius Ba. This is a clear indication that the Mg is systematically dissolved in BTZ lattice in the studied composition range.

4.7. References

1. W.D.Kingery, H.K.Bowen and D.R.Uhlmann, "*Introduction to Ceramics*", Wiley, New York, (1976).
2. H.Iwahara, T.Yajuna, T.Habino, K.Ozaki and H.Suzuki, *Solis State Ionics*, **61**, 65-69 (1993).
3. K.Abe, and S.Komatsu, *J.Appl.Phys*. **77**, 6461 (1995).
4. H.D. Megaw, *Proc. Phys. Soc. London* **58**, 133(1946).
5. S. Kucheiko, J.W. Cho, H.J. Kim and H.J. Jung, *J. Am. Ceram. Soc*.**79,** 2739(1996).
6. J.H. Yang, C.K. Choo and W.K. Choo, *Ferroelectrics* **223,** 329(1999).
7. D.F.K.Hennings,B. Schreinemacher and H. Schreinemacher, *J. Eur Cera Soc*.**13**, 81(1994).
8. R. Lindstrom, *J.Phys.Chem.Solids*, **30**.401 (1969)
9. S.Gopalan and A.V.virker, *J.Am.Ceram. Soc*., **78** 993(1995).
10. L.B. Borovskii, K.P.Gurov, L.D. Marchukova and 1. L.B. Borovskii, K.P.Gurov, L.D. Marchukova and Yu.E.Ugaste, "*Interdiffusion Processes in Alloy*," Nauka, Moscow, Russia, (1986).
11. B.J. Kennedy, C.J. Howard and B.C. Chakoumkos, *Phys. Rev. B* **59** (6) (1999) 4023.
12. J.A.Pask and L.K.Templeton, *Kinetics of high temperature processes*. Edited by W.D. Kingery. MIT Press, Cambridge. MA, pp255-64 (1959).
13. A.Ubaldini, V.Buscaglia, C. Uliana, G.Costa and M.Ferretti, *J. Am. Cerm. Soc*., **86,** 19(2003).
14. J.M. Vieira and R.A. Brook, "*Lattice, Grain- boundary, surface and gas diffusion constant in Magnesium oxide*" pp 438-63, edited by W.B. Kingery, *Am.Ceram. Soc*, Columbus, OH, (1984).
15. P.F.Wastman and I.B. Cutler, *J. Am.Ceram. Soc*., **49**, 526 (1996).
16. G.V.Lewis and C.R.A. Catlaw, *Radiat Eff*, **73**. 307 (1983)
17. W.D.Rhodes and W.D Kingery *J. Am.Ceram. Soc*., **49**, 521-26 (1996).
18. R. Wernkke, *Philips Res. Rep*, **31,** 526 (1976)
19. S.Gopalan and A.V.virker, *J.Am.Ceram. Soc*., **82**, 2887(1999).
20. H.P.Butler, H.Jain, and D.M.Smyth, *J.Am.Ceram. Soc*., **74**, 772-76(1991)
21. B.J. Kennedy,C.J. Howard,G.J. Thorogood and J.R. Hester, *J. Solid State Chem*. **161,** 106(2002).
22. H.Yugami, F. Iguchi and H.Naito, *Solid State Ionics*, **136-137**, 203(2000).

23. H.M. Christen, L.A.Knauss and K.S.Harshavardhan, *Mat.Sc and Engg. B*, **56**, 200(1998).
24. T.K.Y.Wong, B.J.Kennedy, C.J.Howard, B.A.Hunter and T.Vogt, *J. Solid State Chemistry* **156**, 255(2001).
25. G.H. Jonker and W. Kwestroo, *Am. Cera.Soc***. 41**, 390(1958).
26. W.Kwestroo and H.A.M.Paping, *J.am Cera Soc*., **42**, 292-299, (1959).
27. R.C. DeVries and R.Roy, *J.Am.Cera.Soc*, **38**,142 (1955).
28. J.A.Basmajian and R.C.De Vries, *J.Am.Ceram.Soc*, **40**, 373 (1957).
29. Malcolm McQuarrie, *J.Am.Ceram. Soc*., **38**], 444 (1955).
30. S. Kumar and G.L. Messing, *J. Am. Cerm. Soc*. **77,** 2940(1994).
31. H. P. Klug and L. E. Alexander, *Crystallite Size Determination from Line Broadening*. (Wiley, New York,), p. 491 (1954).
32. *Perry's Chemical Engineers' Handbook*, 6th Edition, edited by Robert H. Perry, Don W. Green, and James O. Maloney (McGraw-Hill Book Company, New York,), p. 3-8 (1984).
33. D. Schultz, *Differentialthermoanalysis*, VBE Deutscher Verlag der Wisscnschaften, Berlin, (1971).
34. R. C. Evans, *An Introduction to Crystal Chemistry*, Cambridge University Press, Cambridge, UK, p.410 (1996).
35. M Stockenhuber, H Mayer, and J. A. Lercher, *J. Am. Cerm. Soc*. **76** 1185 (1993).
36. A.Erbil,Y.Kim and R.A.Gerhardt, *Phys.Rev.Lett*.**77**, 1628 (1996).
37. J.Bera and S.K.Rout, *Materials Letter* **59,** 135(2005).
38. J.Bera and S.K.Rout, *Materials Research Bulletin* **40**1187(2005).
39. Terry A. Ring, *Fundamentals of Ceramic Powder Processing and Synthesis*, Academic Press, Inc, pp 174 (1996).
40. A.Ubaldini, V.Buscaglia, C. Uliana, G.Costa and M.Ferretti, *J. Am. Cerm. Soc*., **86,** 19(2003).
41. B.J. Kennedy,C.J. Howard,G.J. Thorogood and J.R. Hester, *J. Solid State Chem*. **161,** 106(2002).
42. S.Gopalan and A.V.Virkir, *J. Am. Cerm. Soc*. **82,** 2887 (1999).
43. G.V.Lewis and C.R.A. Catlow, *Radiat. Eff.,* **73,** 307(1983).
44. T.K.Y.Wong, B.J.Kennedy, C.J.Howard, B.A.Hunter and T.Vogt, *J. Solid State Chemistry* **156**, 255(2001).
45. http:/www.ccp14.ac.uk/tutorial/lmgp/
46. Ph. Sciau, G. Calvarin and J. Ravez, *Solid State Comm*., **113,** 77-82 (2000).
47. A. Dixit, S.B. Majumdar, P.S. Diobal and A.S.Bhalla, *Thin Solid Films* **447-448** 284(2004).
48. J.A.Basmajian and R.C. DeVrie, *J.Am Ceram. Soc*., **40**, 373-76 (1957)
49. I. Levin, T.G.Amos, S.M.Bell, L. Faber, T.A.Vanderah, R.S.Roth and B.H.Toby, *J. Solid State Chem*. **175,** 170(2003).
50. T.B. Wu, C.M. Wu and M. L. Chen, *Appl. Phys.lett*. **69**, 2659(1996).

Chapter 5

RIETVELD REFINEMENT

5.1. Introduction

The work of structure determination goes on continuously since there is no dearth of unsolved structures. New substances are constantly being synthesized and the structures of many old ones are still unknown. In themselves crystal structures vary widely in complexity: the simplest can be solved in a few hours, while the more complex ones may require months or even years for their complete solution. Protein forms a notable example of latter kind; some protein structures are now known, but others still defy solution. Complex structure requires complex methods of solution, and structure determination. All we can do here is to consider some of the principles involved and how they can be applied to the solution of fairly simple structures. Moreover, we will confine our attention to the methods of determining structures from powder patterns alone, because such patterns are the kind most often encountered by the material physicist.

The wellknown basic principle of the crystal structure determination is that the crystal structure of a substance determines the diffraction pattern of the substance or, more specifically, that the shape and size of the unit cell determine the angular position of the diffraction lines, and the arrangement of the atom within the unit cell determines the relative intensities of the lines. Since structure determines the diffraction pattern, it should be possible to go in the other direction and deduce the structure from the pattern. It is possible, but not in any direct manner. Given a structure, we can calculate its diffraction pattern in a very straightforward way. But the reverse problem, that of directly calculating the structure from the observed pattern, has not yet been solved for the general case. The procedure adopted is essentially one of trial and error. If they agree in all detail, the assumed structure is correct; if not, the process is repeated as often as is necessary to find the correct solution. The problem is not unlike that of deciphering a code, and requires of the crystallographer the same quality possessed by a good cryptanalyst, namely, knowledge, perseverance, and not a little intuition.

Only when these three steps have been accomplished the structure determination is complete. The third step is generally the most difficult, and there are many structures which are known only incompletely, in the sense that the final step has not yet been

made. Nevertheless, knowledge of the shape and size of the unit cell, without any knowledge of atom positions, is in itself of very great value in many applications.

Rietveld method is a wellestablished technique for crystal structural refinement. Since the last few decades, there have seen great advances in our ability to extract detailed crystal structural information from powder diffraction data, e.g. to do systematic structure refinement using the Rietveld method. It was Rietveld who first worked out computer based analytical procedures [1,2] to make use of full information content of powder pattern and very importantly, widely, freely, put them in the public domain through his computer program. This chapter provides a general introductory account of what the method is and how it works.

In this technique, the things actually being refined are parameters in models for the structure and the instrumental effects on the diffraction pattern. In the Rietveld method the least squares refinements are carried out until the best fit is obtained between the entire observed powder diffraction pattern taken as a whole and the entire calculated patterns based on the simultaneously refined models for the crystal structure(s), diffraction optics effect, instrumental factors, and other specimen characteristics (e.g. lattice parameters) as may be desired and can be modeled [3]. A key feature is the feedback, during refinement, between improving knowledge of the structure and improving allocation of observed intensity to partially overlapping individual Bragg reflections.

This key feature is not present in other popular methods of structure refinement from powder data in which: (i) the assignment of all observed intensity to individual Bragg reflections, and (ii) subsequent structure refinement with so derived Bragg intensities is carried out as separate, non interacting procedures. The first procedure is appropriately called “pattern decomposition” and may be defined as a systematic procedure for decomposing a powder pattern into its component Bragg reflections without reference to a crystal structural model. The decomposition procedures in general use may be classified into two categories according to whether the lattice parameters are known and are used to fix the positions of the possible Bragg reflections. Such use of the lattice parameters goes a long way toward reducing the intensity assignment ambiguity to acceptable level.

5.2. Structure Evolution by X-ray Powder Diffraction

On the basis of an educated guess, a structure is assumed, its diffraction pattern calculated, and the calculated pattern compared with the observed one. If the two agree

in all details, the assumed structure is correct; if not, the process is repeated as often as is necessary to find the correct solution.

The determination of an unknown structure proceeds in three major steps:

1. The shape and size of the unit cell are deduced from the angular positions of the diffraction lines. An assumption is first made as to which of the seven crystal systems the unknown structure belongs to, and then, on the basis of this assumption, the correct Miller indices are assigned to each reflection. This step is called indexing the pattern and is possible only when the correct choice of crystal system has been made. Once this is done, the shape of the unit cell is known (from the crystal system), and its size is calculable from the positions and Miller indices of the diffraction lines.
2. The number of atoms per unit cell is then computed from the shape and size of the unit cell, the chemical composition of the specimen, and its measured density.
3. Finally, the positions of the atoms within the unit cell are deduced from the relative intensities of the diffraction lines.

Only when these three steps have been accomplished is the structure determination complete. The third step is generally the most difficult, and there are many structures which are known only incompletely, in the sense that this final step has not yet been made. Nevertheless, knowledge of the shape and size of the unit cell, without any knowledge of atom positions, is in itself of very great value in many applications.

The average metallurgist is rarely, if ever, called upon to determine an unknown crystal structure. If the structure is at all complex, its determination is a job for a specialist in x-ray crystallography, who can bring special techniques, both experimental and mathematical, to bear on the problem. The metallurgist should, however, know enough about structure determination to unravel any simple structures he may encounter and, what is more important, he must be able to index the powder patterns of substances of known structure, as this is a routine problem in almost all diffraction work. The procedures given above for indexing patterns are applicable whether the structure is known or not, but they are of course very much easier to apply if the structure is known beforehand.

There are several procedures for measurement of lattice parameters. The least square method provides more accurate information in comparison to others. “If a number of measurements are made of the same physical quantity and if these measurements are subject only to random errors, then the theory of least squares states

that the most probable value of the measured quantity is that *which makes the sum of the squares of the errors a minimum*".

In all cases, the best-fit sought is the best least squares fit to all thousands of y_i'*s* simultaneously. The quantity minimized in the least squares refinement is the residual, S_y:

$$S_y = \sum_i w_i (y_i - y_{ci})^2 \tag{5.1}$$

where $w_i = 1/y_i$,

y_i = observed (gross) intensity at the *i* th step,

y_{ci} = Calculated intensity at the *i* th step

and the sum is over all dada points.

A powder diffraction pattern of a crystalline material may be thought of as a collection of individual reflection profiles, each of which has a peak height, peak position, a breadth, tails which decay gradually with distance from the peak position, and an integrated area which is proportional to the Bragg intensity, I_K, where K stands for Miller indices, h,k,l, I_K is proportional to the square of the absolute value of the structure factor, $|F_K|^2$. In all powder diffraction patterns but those so simple that the Rietveld method is not needed in the first place, these profiles are not all resolved but partially overlap one another to a substantial degree.

It is a crucial feature of the Rietveld method that no effort is made in advance to allocate observed intensity to particular Bragg reflections or to resolve overlapped reflections. Consequently, a reasonably good starting model is needed. The method is a structure refinement method. It is not a structure solution method.

Typically, many Bragg reflections contribute to the intensity, y_i, observed at any arbitrarily chosen point, *i*, in the pattern. The calculated intensities y_{ci} are determined from $|F_K|^2$ values calculated from the structural model by summing of the calculated contributions from neighboring (i.e. within a specified range) Bragg reflections plus the background:

$$y_{ci} = s \sum_K L_K |F_K|^2 \phi(2\theta_i - 2\theta_K) P_K A + y_{bi} \tag{5.2}$$

where; S is the scale factor,

K represents the Miller indices, h k l, for a Bragg reflection,

L_K contains the Lorentz, polarization, and multipilicity factor,

Φ is the reflection profile function,

P_K is the preferred orientation function,

A is the absorption factor,

F_K is the structure factor for the K the Bragg reflection, and

y_{bi} is the background intensity at the i th step,

The effective absorption factor, A, differs with instrument geometry, It is usually taken to be a constant for the instrument geometry most used for X-ray diffractometers, that of a flat specimen with its surface maintained normal to the diffraction vector by a θ-2θ relationship between specimen rotation and detector rotation about the diffractometer axis. It does depend on angle for other geometries.

In a number of available computer programs for Rietveld method, the ratio of the intensities for the two X-ray K_α wavelengths (if used) is absorbed in the calculation of $|F_K|^2$, so that only a single scale factor is required.

The least squires minimization procedures lead to a set of normal equations involving derivatives of all of the calculated intensities, y_{ci}, with respect to each adjustable parameter and soluble by inversion of the normal matrix with element M_{jk} formally given by

$$M_{jk} = -\sum_i 2w_i \left[(y_i - y_{ci}) \frac{d^2 y_{ci}}{dx_j dx_k} - \left(\frac{dy_{ci}}{dx_j} \right) \left(\frac{dy_{ci}}{dx_k} \right) \right] \tag{5.3}$$

where the parameters x_j,x_k are the adjustable parameters. In the use of this algorithm, it is a common practice to approximate these matrix elements by deletion of the first term, that is $(y_i\text{-}y_{ci})$.

Thus, one is dealing with the creation and inversion of an m by m matrix, where m is the number of parameters being refined. Because the residual function is non linear, the solution must be found with an iterative procedure in which the shifts, Δx_k, are

$$\Delta x_x = \sum M_{jk}^{-1} \frac{ds_j}{dx_k} \tag{5.4}$$

The calculated shifts are applied to the initial parameters to produce a, supposedly, imposed model and the whole procedure is then repeated. Because the relationships between the adjustable parameters and the intensities are nonlinear, the starting model must be close to the correct model or the nonlinear least squares procedure will not lead to the global minimum. Rather, the procedure will either diverge or lead to a false minimum if the starting point is in its domain. This is true for all nonlinear least squares refinements, not just for Rietveld refinements. Selection of different least squares algorithms at different stages of refinement may alleviate the

false minimum problem in some cases. Another approach is to use multiple data sets of different kinds, e.g., X-ray and neutron, simultaneously or to use constraints. Other approaches can also help one to avoid false minima or, at least, to be properly suspicious that a minimum may not necessarily be the global minimum just because it is stable.

The model parameters that may be refined include not only atom positional, thermal, and sit-occupancy parameters but also parameters for the background, lattice, instrumental geometrical-optical features, specimen aberrations (e.g. specimen displacement and transparency), an amorphous component, and specimen reflection profile-broadening agents such as crystallite size and microstrain. In some cases, it is important to model extinction, as well. Although it is, in general, a much less severe problem with powders than with single crystals, extinction can be quite important in some powder specimen. Multiple phase may be refined simultaneously and comparative analysis of the separate overall scale factors for the phases offers what is probably the most reliable current method for doing quantitative phase analysis. Individual anisotropic thermal parameters have rarely been refined satisfactorily from ordinary laboratory X-ray powder diffraction data, but they have been with fixed wavelength neutron data and are refined almost routinely with TOF neutron powder diffraction data.

5.2.2. Microstructure Evolution by X-ray Powder Diffraction

Microstructure characterization of $(Ba_{0.5}Sr_{0.5})\ TiO_3$, $(Ba_{0.5}Sr_{0.5})ZrO_3$, $Ba_{0.5}(Ti_{0.5}Zr_{0.5})O_3$, $Sr_{0.5}\ (Ti0_{.5}Zr_{0.5})O_3$ and $Ba_{1-x}A_x\ (Ti_{0.6}Zr_{0.4})\ O_3$ samples (where A is Ca or Mg) has been made by employing the Rietveld's whole profile fitting method based on structure and microstructure refinement. The experimental profiles were fitted with most suitable pseudo-Voigt analytical function because it takes individual care for both the particle size and strain broadening of the experimental profiles.

For both the $K\alpha_1$ and $K\alpha_2$ profiles, the line broadening function B (2θ) and the symmetric part of instrumental function S (2θ) may be represented by the pseudo-Voigt function [4]:

$$pV(x) = \sum_{\alpha_a \alpha_2} I_{mt}\left[nC(x) + (1-\eta)G(x)\right] \tag{5.5}$$

where the Cauchyian component, $C(x) = (1 + x^2)^{-1}$ and the Gaussian component, $G(x) = \exp[-(\ln 2)x^2]$ with $x = (2\theta - 2\theta_0)/\mathrm{HWHM}$ (HWHM: half-width at half-maxima of the X-ray peaks) and $\mathrm{HWHM} = 1/2\mathrm{FWHM} = 1/2(U\tan^2\theta + V\tan\theta + W)^{1/2}$, where U, V

and W are coefficients of the quadratic polynomial, η the Gaussianity of X-ray profile, θ_0 the Bragg angle of $K\alpha_1$ peak and I_{nt} the scale factor.

The powder diffraction patterns were simulated providing all necessary structural information and some starting values of microstructural parameters of the individual phases with the help of the Rietveld software, the MAUD l.99 [5]. Initially, the positions of the peaks were corrected by successive refinements of zero-shift error. Considering the integrated intensity of the peaks as a function of structural parameters only, the Marquardt least-squares procedures were adopted for minimization of the difference between the observed and simulated powder diffraction patterns, and the minimization was carried out by using the reliability index parameter, R_{wp} (weighted residual error), and R_B (Bragg factor) defined as:

$$R_{wp} = \left[\frac{\sum_i w_i (y_{i(obs)} - y_{i(cal)})^2}{\sum_i w_i y_{i(obs)}^2} \right]^{1/2} \tag{5.6}$$

$$R_B = \frac{100 \sum_i \left| (y_{i(obs)} - y_{i(cal)}) \right|}{\sum_i y_{i(obs)}} \tag{5.7}$$

The goodness of fit (GoF) is established by comparing R_{wp} with the expected error, R_{exp}

$$R_{\exp} = \left[\frac{N - P}{\sum_i w_i y_{i(obs)}^2} \right]^{1/2} \tag{5.8}$$

where $y_{i(obs)}$ and $y_{i(cal)}$ are the experimental and calculated intensities, respectively, $w_i (1/ y_{i(obs)})$ *a*nd N are the weight and number of experimental observations, and P is the number of fitting parameters. This leads to the value of goodness of fit [6]:

$$GoF = \frac{\mathrm{R}_{wp}}{R_{\exp}} \tag{5.9}$$

Refinement continues till convergence is reached with the value of the quality factor, GoF very close to 1, which confirms the goodness of refinement.

5.2.3. Phase Quantity Analysis by X-ray Powder Diffraction

The Rietveld's method was successfully applied for determination of the quantitative phase abundances of the composite materials. There is a simple relationship between the individual scale factor determined, considering all refined structural parameters of individual phases of a multiphase sample, and the phase concentration

(volume/weight fraction) in the mixture. The weight fraction (W_i) for each phase was obtained from the refinement relation

$$w_i = \frac{S_j (ZMV)_i}{\sum_j S_j (ZMV)_j} \tag{5.10}$$

where i is the value of j for a particular phase among the N phases present, Sj the refined scale factor, Z the number of formula units per cell, M the atomic weight of the formula unit and V the volume of the unit cell [7,5]. The structure refinement along with size–strain broadening analysis was carried out simultaneously by adopting the standard procedure [5, 7].

5.2.4. Size-Strain Analysis by X-ray Powder Diffraction

The basic consideration of this method is the modeling of the diffraction profiles by an analytical function, which is a combination of Cauchyian, Gaussian, and asymmetry functions as well. It has been well established that the observed peak broadenings of the sample profiles are mainly due to the presence of small particle size and rms strain inside the particles. The particle size and strain broadening can be approximated better with Cauchian and Gaussian type functions, respectively [8,9]. Being a linear combination of a Cauchyian and Gaussian functions, the pV function is the most reliable peak-shape function and is being widely used in the Rietveld structure refinement software. The process of successive profile refinements is modulated with different structural and microstructural parameters of the simulated pattern to fit the experimental diffraction pattern. Profile refinement continues until convergence is reached in each case, with the value of the quality factor (GoF) approaching very close to 1.

5.3. Method of Analysis

In the present case, we have adopted the Rietveld's powder structure refinement analysis of X-ray powder diffraction data to obtain the refined structural parameters, such as atomic coordinates, occupancies, lattice parameters, thermal parameters, etc. and microstructural parameters, such as particle size and rms lattice strain, etc. The Rietveld software MAUD 1.99 [7] is used here for structural and microstructural parameter refinement. The program was developed to analyze diffraction spectra and obtain crystal structures, quantity and microstructure of phases along with the texture and residual stresses. It applied the RITA/RISTA method as developed by Wenk,

Matthies and Lutterotti [10] and Ferrari and Lutterotti [11]. The diffraction spectrum fitting is based on the so-called Rietveld method. Rietveld software MAUD is specially designed to refine simultaneously both the structural and microstructural parameters along with the texture and residual stresses through a least square method. The peak shape was assumed to be a pseudo-Voigt (*pV*) function with asymmetry. The background of each pattern was fitted by a polynomial function of degree four.

To simulate the theoretical X-ray powder diffraction pattern, the phases in the following considerations were made:

(i) $SrTiO_3$, and $BaZrO_3$ (Cubic), the space group was taken as *pm3m* with all atom in the general Wyckoff position.

(ii) $CaZrO_3$ (Orthorhombic), the space group is *Pcmn (#62)* with all atom in the general Wyckoff position.

(iii) $BaTi_{0.5}Zr_{0.5}O_3$ (Cubic), the space group was taken as *pm3m* with all atoms in the general Wyckoff position similar to cubic $BaZrO_3$.

(iv) $SrTi_{0.5}Zr_{0.5}O_3$ (Tetragonal), the space group was taken as *I4/mcm* with all atoms in the general Wyckoff position as suggested by B.J.Kennedy [12]

(v) $Ba_{0.5}Sr_{0.5}TiO_3$ (Cubic), the space group was taken as *pm3m* with all atoms in the general Wyckoff position similar to cubic $SrTiO_3$.

(vi) $Ba_{0.5}Sr_{0.5}ZrO_3$ (Orthorhombic), the space group was taken as *Imma* with all atoms in the general Wyckoff position as suggested by B.J. Kennedy [13]

(vii) $Ba_{1-x}Ca_xTi_{0.6}Zr_{0.4}O_3$ ($x \geq 0.2$) is the mixture of two phases. For $Ba_{1-x}Ca_xTi_{0.6}Zr_{0.4}O_3$ ($x<0.1$) the space group was taken as *Pm3m* with all atoms in the general Wyckoff position obtained $BaTi_{0.6}Zr_{0.4}O_3$ as the complete solid solution exists. For higher Ca content compositions the initial parameters were taken as suggested by I.Levin *et al.* for $Ba_{0.8}Ca_{0.2}$ ZrO_3 [14]. For $CaTiO_3$, the space group and Wyckoff positions were taken as available in the MAUD standard structure database

(viii) $Ba_{1-x}Mg_xTi_{0.6}Zr_{0.4}O_3$ ($x \leq 0.14$) (Cubic), the space group was taken as *pm3m* with all atoms in the general Wyckoff position similar to cubic $BaTi_{0.6}Zr_{0.4}O_3$ as observed in the present study.

The initial lattice structural parameter was calculated from the reflections and by correcting with CCP14 program “Checkcell”. The Wyckoff positions were taken from the Wyckoff’s series. Initially, the positions of the peaks were corrected by successive refinements of systematic errors taking into account the zero-shift error and sample

displacement error. The *U*, *V*, *W* parameters of instrumental broadening, instrumental asymmetry and Gaussianity of reflections were estimated for the present setting of the instrument using a specially prepared Si standard [15] and found to vary with scattering angle in different manners. However, during the refinement all these instrumental parameters were kept fixed for estimation of values of all these parameters solely for a sample under investigation. Because the peak broadening, asymmetry and change in Gaussianity is directly related to the content of lattice imperfections (small particle size, lattice strain, dislocations, stacking faults, etc.) inside the sample. By refining instrumental parameters (which is a usual practice for structure refinement by Rietveld's method) all this information regarding microstructure parameters of the sample would be lost. Structure and microstructure refinements were carried out simultaneously by refining scale factors, lattice parameters, occupancy factors, variable fractional atomic coordinates, particle size, rms lattice strain, preferred orientation factors, etc., of individual phases. Considering the integrated intensity of the peaks as a function of structure/microstructure parameters only, the Marquardt least squares procedures were adopted for minimization of the difference between the observed and simulated powder diffraction patterns. The minimization was carried out by using the reliability index parameter R_{wp} (weighted residual error), and R_B (Bragg factor) [16-18]. The goodness of fit (GoF) was established by comparing R_{wp} with the expected error, R_{exp} [16-18].

The Rietveld's method was successfully applied for determination of the quantitative phase abundances of the composite materials [19-20]. There is a simple relationship between the individual scale factor determined, considering all refined structural parameters of individual phases of a multiphase sample, and the phase concentration (volume/weight fraction) in the mixture. The structure refinement along with size–strain broadening analysis was carried out simultaneously by adopting the standard procedure [5]. The process of successive profile refinements modulates different structural and microstructural parameters of the simulated pattern to fit the experimental diffraction pattern. Refinement continues till convergence is reached with the value of the quality factor, GoF very close to 1, which confirms the goodness of refinement. Refined parameters included scale factor, background coefficient, profile coefficients, positional parameter and isotropic thermal displacement parameters. During the refinement fitting of both background and diffraction intensities were taken care by interactive method. Symmetry constraints on the thermal parameters in the

different space group were taken into account, but parameters could not be measured satisfactory within the detection limit of the present XRD data. This can be better monitored using high resolution synchrotron radiation or neutron diffraction data.

5.4. Experimental Setup and Conditions

Obviously, the powder data must be in digitized form in order to be used in today's computers. Hence the diffraction pattern is recorded in digitized form, i.e., as a numerical intensity value, y_i, at each of several thousand equal increments (steps), i, in the pattern. Depending on the method, the increments may be either in scattering angle, 2θ, or some energy parameter such as velocity (for time-of- flight neutron data) or wavelength (for X-ray data collected with an energy dispersive detector and an incident beam of white X radiation). For constant-wave data, the increments are usually steps in scattering angle and intensity y_i at each step i. The pattern is measured either directly with a quantum detector on diffractometer or indirectly with step scanning microdensitometry of film data. Rietveld refinement with X-ray diffraction data has been notably successful both with fixed wave length data and with TOF data. In Rietveld method, it does not matter what powder diffraction data are used for refinement. Typical step sizes range from 0.01 to 0.05^{O} 2θ for fixed wavelength X-ray data and a bit larger for fixed wave length neutron data.

In the present case for structural refinement, all of the powders mixtures (except Ca and Mg substituted samples) were calcined at $1{,}300^{0}$C for 4h, $1{,}400^{0}$C for 4h and finally $1{,}600^{0}$C for 1h with intermediate mixing and grinding between each firing. The samples with Ca and Mg substitution samples were calcined at $1{,}200^{0}$C for 4h, $1{,}350^{0}$C for 4h and finally $1{,}450^{0}$C for 1h. The resulting powders were ground by an agate mortar to avoid aglomorization, and considered for further study. After the above thermal treatment, all the phases in their respective compositions were stabilized. Structural and microstructural parameters were analyzed from the X-ray powder diffraction profile. Patterns were recorded using Cu - $K\alpha_1$ radiation from a highly stabilized and automated Philips (Netherlands) X-ray generator (PW 1830) operated at 35 kV and 30 mA. The generator is coupled with a Philips X-ray powder diffractometer consisting of a PW 3710 mpd controller, PW 1050/51 goniometer, and a proportional counter. For this experiment, 1^{O} divergence slit, 0.2 mm receiving slit, 1^{O} scatter slit and 5^{O} soller slit system were used. The step scan data of step size 0.02^{O} 2 theta and 5 sec, counting time per step were recorded and stored in a PC, coupled with the diffractomter.

5.5. Results and Discussion

5.5.1. Refinement of $BaTi_{0.5}Zr_{0.5}O_3$.

Structural refinements were carried out for the composition $BaTi_{0.5}Zr_{0.5}O_3$ using Rietveld structural refinement program MAUD 1.999 and the final output is drawn in the Fig. 5.1. Structural refinements were carried out taking the end member reference for the cubic (space group *Pm3m*) compound $BaZrO_3$. The initial parameters for the end member were taken from the reference [14]. The structural refinement showed that the composition $BaTi_{0.5}Zr_{0.5}O_3$ is cubic with space group Pm3m. The lattice parameter, crystallite size and rms strain were found to be 4.11731 (Å), 57.40 nm and 0.0008, respectively. The occupancy factors for the mixed Ti and Zr sites were fixed at the nominal composition. The Ti and Zr displacement parameters were constrained to be equal. The refinements produced satisfactory agreement factors R_{wp} (weighted residual error), R_p (Brag factor) and R_{exp} (expected error) for 5500 observations and 42 variables (Fig.5.1), which are given in the caption of the Fig. 5.1. Atomic thermal (displacement) parameters are x 100$Å^2$.

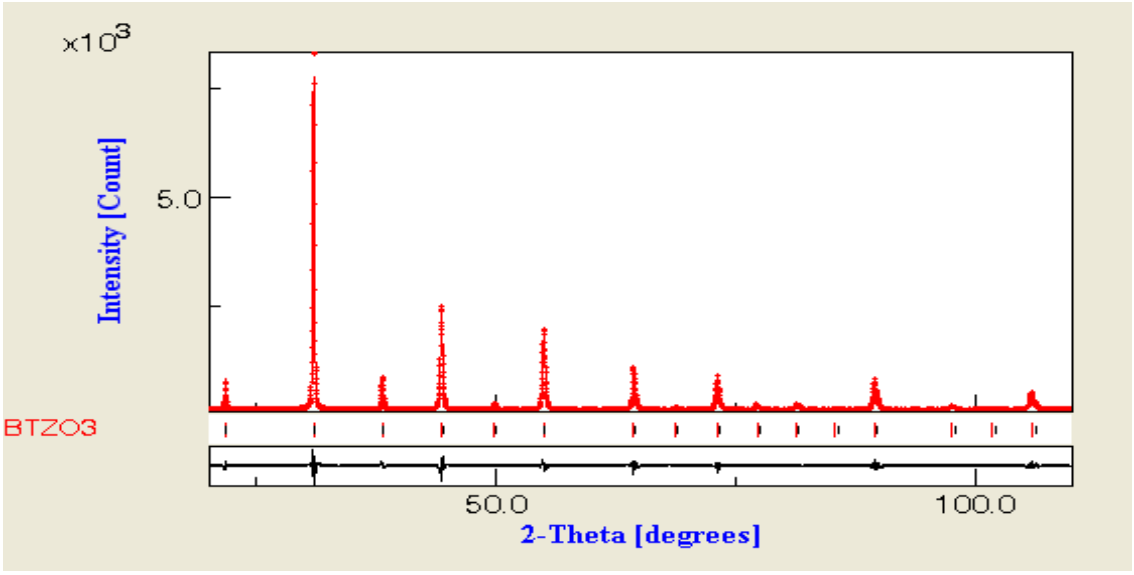

Figure 5.1 Observed (▪), calculated (—) and residual (lower) X -ray powder diffraction patterns of $BaTi_{0.5}Zr_{0.5}O_3$ composition revealed from Rietveld's powder structure refinement analysis. Peak positions of the phases are shown at the base line as small markers (l). R_{wp} (%) = 12.096081, R_p (%) = 9.412923, R_{exp} (%) = 8.68739 and Sigma= 1.3922173

Table 5.1: Final outcome of the structural feature of the $BaTi_{0.5}Zr_{0.5}O_3$ composition

Atom	x	y	z	ζ	N	β
Ba	0.0	0.0	0.0	1	1	1.1618
Ti	0.4997	0.4995	0.4998	0.5	0.5	1.1832
Zr	0.4999	0.4995	0.4997	0.5	0.5	1.1832
O(1)	0.0	0.4996	0.4999	1	3	0.7176

where ζ : Site occupancy, β : Isotropic thermal parameter,

and N : Atom Number per unit cell calculated from site occupancy

5.5.2. Refinement of $SrTi_{0.5}Zr_{0.5}O_3$.

Fig. 5.2 represents the final output after structural refinements for the composition $SrTi_{0.5}Zr_{0.5}O_3$. Structural refinements were carried out taking the positional parameter for end members $SrZrO_3$ as orthorhombic with space group Pbnm, and $SrTiO_3$ as cubic with space group Pm3m. Recently B.J. Kenedy *et al* [13] reported that orthorhombic symmetry with space group Pbnm transforms to a higher symmetry cubic symmetry with space group *Pm3m* with intermediate tetragonal structure with space group *I4/mcm*. As reported by B.J. Kennedy [13], in tetragonal stracture of $SrTi_{0.5}Zr_{0.5}O_3$ with space group *I4/mcm*, the Sr occupies the 4b site at (0, 0.5, 0.25) and the Ti and/or Zr on 4 c site at (0, 0, 0). There are also two types of oxygen atoms, O (1) on 4 a site (0,0,1/4) and O (2) on 8h site at (0.2840, x+0.5, 0). In our case successful refinement confirms that the structure of $SrTi_{0.5}Zr_{0.5}O_3$ is tetragonal with space group I4/mcm. The lattice parameter, crystallite size and rms strain were found to be a_0=5.67375 Å and c_0= 8.01273 Å, 49.66 nm and 0.0013 respectively. The refinements produced satisfactory agreement factors for 5500 observations and 42 variables (Fig.5.2), which are given in the caption of the Fig. 5.2.

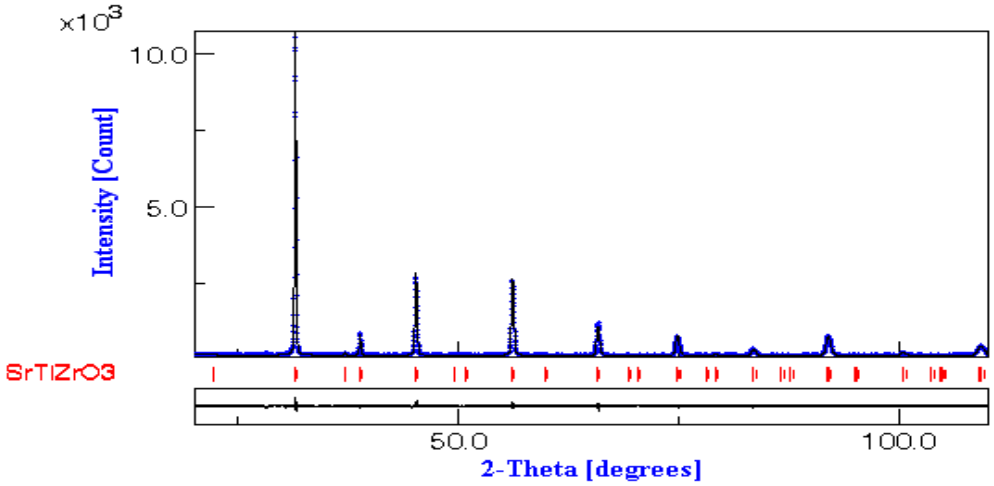

Figure 5.2 Observed (▪), calculated (—) and residual (lower) X -ray powder diffraction patterns of $SrTi_{0.5}Zr_{0.5}O_3$ composition revealed from Rietveld's powder structure refinement analysis. Peak positions of the phases are shown at the base line as small markers (l). R_{wp} (%) = 8.653015, R_p (%) = 6.1653423, R_{exp} (%) = 7.5683146, and Sigma = 1.1433213

The occupancy factors for the mixed Ti and Zr sites were fixed at the nominal composition. The Ti and Zr displacement parameters were constrained to be equal. Some of the positional features revealed from Rietveld's powder structure refinement analysis for the composition $SrTi_{0.5}Zr_{0.5}O_3$ are given in Table 5.2. Atomic thermal (displacement) parameters are x 100Å^2. ζ : Site occupancy and β : Atom Number per unit cell calculated from site occupancy.

Table 5.2.: Final outcome of the structural feature of the $SrTi_{0.5}Zr_{0.5}O_3$ composition

Atom	x	y	z	ζ	N	β
Sr	0.0	0.4995	0.2504	1.0	4	0.9973
Ti	0.0	0.0	0.0	0.5	2	0.5011
Zr	0.0	0.0	0.0	0.5	2	0.5011
O(1)	0.0	0.4996	0.2497	1	3	-0.2521
O(2)	0.2165	X+0.5	0	1	8	2.9499

5.5.3. Refinement of $Ba_{0.5}Sr_{0.5}TiO_3$

Fig. 5.3 represents the final output after structural refinements for the composition $Ba_{0.5}Sr_{0.5}TiO_3$. Structural refinements were carried out, initially taking the end member reference for the cubic (space group *Pm3m*) compound $SrTiO_3$. The

occupancy factors for the mixed Ba and Sr sites were fixed at the nominal composition. Initial atomic positional parameters for the composition $Ba_{0.5}Sr_{0.5}TiO_3$ were taken as: Ba/Sr 1a (0,0,0), Ti 1b (1/2,1/2,1/2) and O 3c (0,1/2,1/2). After refinement, the positional and isotopic thermal (displacement) parameters are (x 100Å^2) tabulated in the Table 6.3. The Ba and Sr displacement parameters were constrained to be equal. The refinements produced satisfactory agreement factors R_{wp} (weighted residual error), R_p (Brag factor) and R_{exp} (expected error) for 5,500 observations and 42 variables (Fig.5.3) which are given in the caption of the Fig. 6.3. The structural refinement showed that the composition $Ba_{0.5}Sr_{0.5}TiO_3$ is cubic with space group *Pm3m*. The lattice parameter, crystallite size and rms strain of the composition were found to be a_0=3.93526 Å, 58.54 nm and 0.0007, respectively.

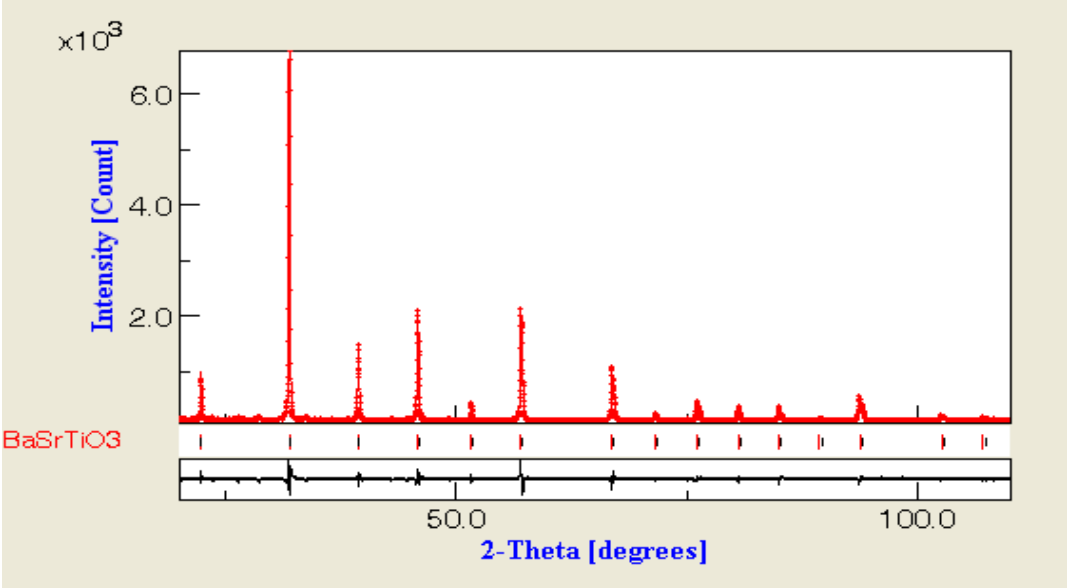

Figure 5.3 Observed (▪), calculated (—) and residual (lower) X -ray powder diffraction patterns of $Ba_{0.5}Sr_{0.5}TiO_3$ composition revealed from Rietveld's powder structure refinement analysis. Peak positions of the phases are shown at the base line as small markers (l). R_{wp} (%) = 11.831947, R_p (%) = 8.892393,R_{exp} (%) = 8.670418, and Sigma= 1.364634

Table 5.3.: Final outcome of the structural feature of the $Ba_{0.5}Sr_{0.5}TiO_3$ composition

Atom	x	y	z	ζ	N	β
Ba	0.0	0.0	0.0	0.5	0.5	0.4151
Sr	0.0	0.0	0.0	0.5	0.5	0.4151
Ti	0.5000	0.4999	0.5000	1	1	0.0126
O(1)	0.0	0.5000	0.4996	1	3	1.0615

5.5.4. Refinement of $Ba_{0.5}Sr_{0.5}ZrO_3$

From Fig. 6.19 (Chapter 4) there is a systematic shift of the peaks to the lower angle. One may expect that this is due to the difference in ionic radius of the tetravalent cations. It is also mentioned in Chapter 4, that the transformation occurs from cubic (g.s *Pm-3m*) to orthorhombic (s.g *Imma*) with an intermediate space group *I4/mcm*. This phase transformation occurs in the composition around 80 % of the Zr. These observations are also in good agreement with the observation of B.J.Kennedy [12, 13]. To study the detailed structural and microstructural parameters, the composition $BaSrZrO_3$ was studied using the Rietveld structural refinement program. The Wyckoff positions of orthorhombic symmetry with space group *Imma* were taken from the Wyckoff's series. The structural refinement confirms that the composition $Ba_{0.5}Sr_{0.5}ZrO_3$ presents orthorhombic symmetry with space group *Imma*. The occupancy factors for the mixed Ba and Sr sites were fixed at the nominal composition. The Ba and Sr displacement parameters were constrained to be equal.

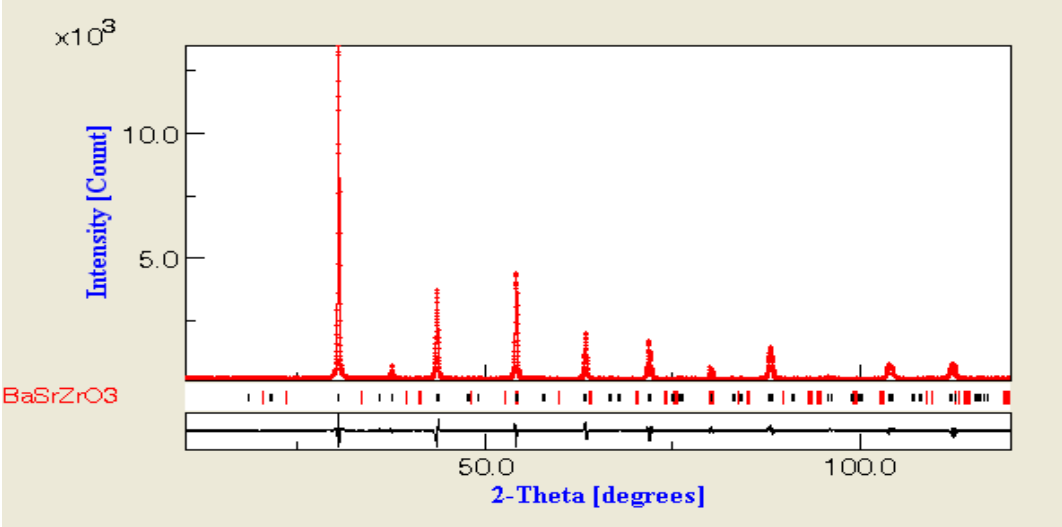

Figure 5.4. Observed (▪), calculated (—) and residual (lower) X -ray powder diffraction patterns of $Ba_{0.5}Sr_{0.5}ZrO_3$ composition revealed from Rietveld's powder structure refinement analysis. Peak positions of the phases are shown at the base line as small markers (l). R_{wp} (%) = 8.84, R_p (%) = 6.96, R_{exp} (%) = 6.06, and Sigma= 1.46

The refinements produced satisfactory agreement factors R_{wp} (weighted residual error), R_p (Brag factor) and R_{exp} (expected error) for 5500 observations and 42 variables (fig.5.3), which are given in the caption of the Fig. 5.3. The structural refinement showed that the composition $Ba_{0.5}Sr_{0.5}ZrO_3$ is Orthorhombic with space group *Imma*. The lattice parameters were a_0= 5.8857 Å, b_0=8.2941 Å and c_0=5.8896 Å. The

crystallite size and rms strain of the composition were found to be 66.73 nm and 0.0015, respectively. The refined positional parameters of the composition are given in the Table 5.4. Atomic thermal (displacement) parameters (β) are x 100Å^2. ζ; site occupancy and N; Atomic number per unit cell calculated from site occupancy.

Table 5.4.: Final outcome of the structural feature of the $Ba_{0.5}Sr_{0.5}ZrO_3$ composition

Atom	x	y	z	ζ	N	β
Ba	0.0	0.25	0.0118	0.5	2	0.125
Sr	0.0	0.25	0.0118	0.5	2	0.125
Zr	0.0	0.0	0.5	1	4	1.59
O(1)	0.0	0.25	0.5041	1	4	0.250
O(2)	0.25	-0.0774	0.25	1	8	3.002

From the structural and microstructural information of the end members of the previously mentioned BSTZ series, it can be concluded from the refinement that the cubic BTZ transforms to a lower symmetry tetragonal structure with the substitution of Sr in place of Ba. The appearance of the (121) and related reflections confirms the tetragonal structure of $SrTiZrO_3$. This structural transformation occurs may be due to the large difference in the size of the two divalent cations, suggesting the possibility of A-site cation ordering. The transition composition in this compositionally induced transition from *Pm-3m* to *I4/mcm* can be examined with the high resolution neutron or synchrotron diffraction data with large number compositions with slight variation in Ba and Sr content. In tetragonal phase, the angle of rotation of the oxygen octahedron $\{\varphi=\tan^{-1} 4u\}$ can be taken as the order parameter. Tilt angle decreases with transformation to higher symmetry and increases with transformation to lower symmetry. In the present transformation from tetragonal to cubic, this tilt angle $\varphi = 6.5$ for tetragonal $SrTiZrO_3$ whereas $\varphi = 0$ for cubic $BaTiZrO_3$.

It is also evidentfrom the refinement that the composition $BaSrTiO_3$ is transformed from cubic to orthorhombic symmetry with space group *Imma* with Zr substitution in place of Ti. This structural transformation occurs may be due to the large difference in the size of the two tetravalent cations, suggesting the possibility of B-site cation ordering. This compositionally induced transition from *Pm-3m* to *Imma* can be examined with the high resolution neutron or synchrotron diffraction data with large number of compositions with slight variation in Ti and Zr content.

5.5.5. Refinement of $Ba_{1-x}Ca_xTi_{0.6}Zr_{0.4}O_3$

Fig. 5.5 represents the final output after structural refinements for the composition $BaTi_{0.6}Zr_{0.4}O_3$. Structural refinements were carried out taking the positional parameter for the earlier refined (Fig 5.1) $BaTi_{0.5}Zr_{0.5}O_3$ composition with space group *Pm-3m*. Successful refinement confirms that all these compositions have cubic symmetry with space group *Pm-3m*. The refinements produced satisfactory agreement for 5500 observations and 42 variables. The observed R-factors and good ness of fit (GoF) (Sigma) of all these compositions are given the Table 5.5. Atomic thermal (displacement) parameters are x 100Å^2. The GoF for all the compositions shows in the range of 1.2 to 1.35. This indicates the good quality of the fitting of the experimental data with the theoretical one. The occupancy factors for the mixed Ti and Zr sites were fixed at the nominal composition. The Ti and Zr displacement parameters were constrained to be equal. After refinement, the final outputs of the positional parameter of the compositions are given in the captions of each figure.

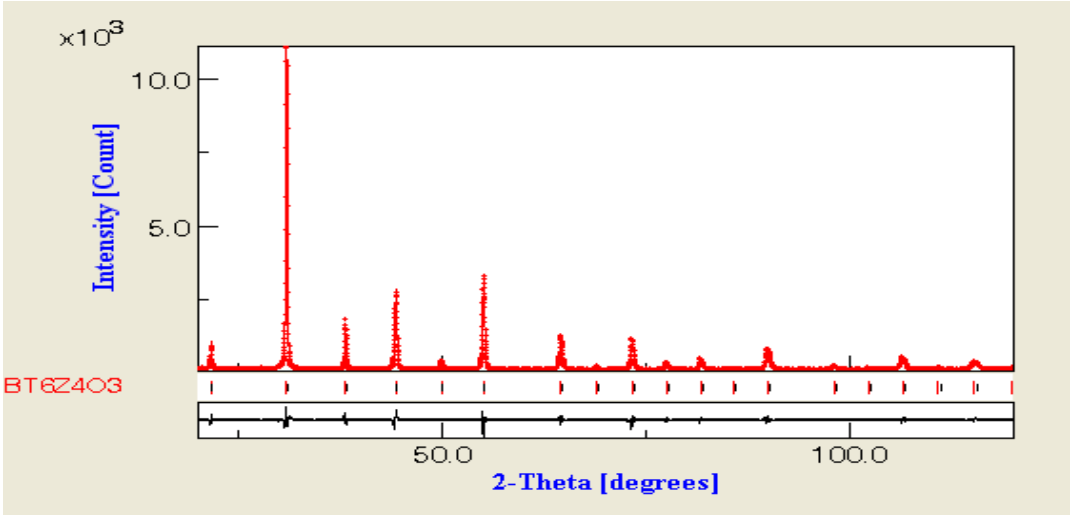

Figure 5.5 Observed (▪), calculated (—) and residual (lower) X -ray powder diffraction patterns of $BaTi_{0.6}Zr_{0.4}O_3$ composition revealed from Rietveld's powder structure refinement analysis. Peak positions of the phases are shown at the base line as small markers (l). Positional parameters for the compositions are: Ba at 1a (0,0,0), Ti at 1b (0.4998, 0.4999, 0.4998), Zr at 1b (0.5002, 0.4997, 0.4997) and O is at 3c (0, 0.5004, 0.4998).

Fig. 5.6 represents the final output after structural refinements for the composition $Ba_{0.9}Ca_{0.1}Ti_{0.6}Zr_{0.4}O_3$. Structural refinements were carried out initially taking the positional parameters of tetragonal $Ba_{0.8}Ca_{0.2}ZrO_3$ with space group *I4/mcm* [14] and cubic $BaTi_{0.6}Zr_{0.4}O_3$ with space group *Pm-3m,* as reported evidence from the

Fig. 5.5. Successful refinement confirms that the structure of $Ba_{0.9}Ca_{0.1}Ti_{0.6}Zr_{0.4}O_3$ is cubic at room temperature with space group *Pm-3m*. The refinements produced satisfactory agreement factors for 5500 observations and 42 variables, which are given in the caption of Fig. 5.6. The occupancy factors for the mixed Ti and Zr sites were fixed at the nominal composition. The Ti and Zr displacement parameters were constrained to be equal. Some of the structural and microstructural features revealed from Rietveld's powder structure refinement analysis for the composition $Ba_{0.9}Ca_{0.1}Ti_{0.6}Zr_{0.4}O_3$ are given in Table 5.5. The structure was confirmed as cubic having space group *Pm-3m* with atoms located at following positions: Ba and Ca occupies the 1a site at (0, 0, 0); Ti and/or Zr on 1b site at (0.5, 0.5, 0.5) and O (1) on 4 a site (0, 0.5, 0.5). Atomic thermal (displacement) parameters are x 100Å^2.

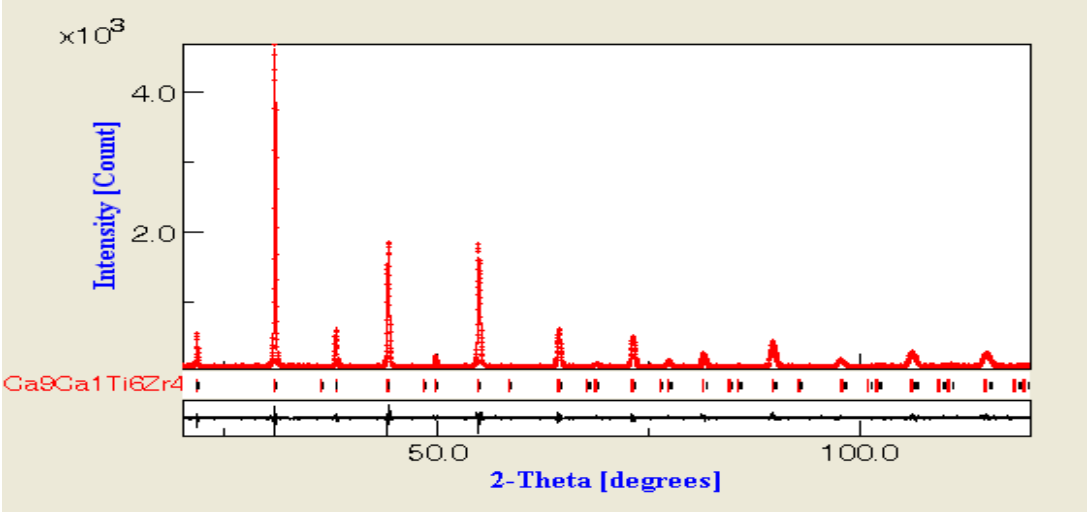

Figure 5.6 Observed (▪), calculated (—) and residual (lower) X -ray powder diffraction patterns of $Ba_{0.9}Ca_{0.1}Ti_{0.6}Zr_{0.4}O_3$ composition revealed from Rietveld's powder structure refinement analysis. Peak positions of the phases are shown at the base line as small markers (I). R_{wp}(%) = 11.601819, R_p(%)=8.97334,R_{exp}(%)=9.958377, and Sigma= 1.1650311.

Fig. 5.7 represents the final output after structural refinements for the composition $Ba_{0.8}Ca_{0.2}Ti_{0.6}Zr_{0.4}O_3$. The pattern shows a mixture of tetragonal $Ba_{0.8}Ca_{0.2}Ti_{0.6}Zr_{0.4}O_3$ and orthorhombic structure of $CaTiO_3$. Structural refinements were carried out initially taking the positional parameters of tetragonal $Ba_{0.2}Ca_{0.2}ZrO_3$ with space group *I4/mcm* [14] and orthorhombic structure of $CaTiO_3$, as available in the structural data base of the software used (MAUD). Successful refinement confirms that the composition of $Ba_{0.8}Ca_{0.2}Ti_{0.6}Zr_{0.4}O_3$ is a mixture of tetragonal $Ba_{0.8}Ca_{0.2}Ti_{0.6}Zr_{0.4}O_3$ with space group *I4/mcm* and orthorhombic $CaTiO_3$ with space group *Pbnm:cab,* and

the result are tabulated in the Table 5.5. The refined positional parameters of the $CaTiO_3$ in the composition $Ba_{0.8}Ca_{0.2}Ti_{0.6}Zr_{0.4}O_3$ are: Ca (1.002, 0.0279, 0.25), Ti (0.0.25.0), O1 (0.1478, 0.5483, 0.25) and O2 (0.7573, 0.285, 0.0419). The refinements produced satisfactory agreement factors R_{wp} (%) = 11.947288, R_p (%)=9.4384365,R_{exp} (%)=9.360648, and Sigma= 1.2763312 for 5000 observations and 42 variables (Fig.5.7). The occupancy factors for the mixed Ti and Zr sites were fixed at the nominal composition. De Varies and Roy [20] investigated the phase equilibria in the system $BaTiO_3$-$CaTiO_3$. They found a solubility gap between these two compounds up to the melting point (1600^{o}C). At 1400^{o}C, the maximum solubility is 18 weight % on both sides. I. Levin, *et al* [14] reported that the solubility of Ca in $BaZrO_3$ breaks around 30 atom % of Ca even heated at 1,650^{O}C. Here the results show that the solid solution breaks around 20 atom % of Ca in the compositions, heated at 1,500^{O}C. The reason may be due to the presence of more acidic TiO_2 in the mixture.

Fig. 5.8 represents the final output after structural refinements for the composition $Ba_{0.5}Ca_{0.5}Ti_{0.6}Zr_{0.4}O_3$. Again, the pattern shows a mixture of tetragonal $Ba_{0.9}Ca_{0.1}Ti_{0.6}Zr_{0.4}O_3$ and orthorhombic structure of $CaTiO_3$. Structural refinements were carried out initially taking the positional parameters as taken for the composition $Ba_{0.8}Ca_{0.2}Ti_{0.6}Zr_{0.4}O_3$. Successful refinement confirms that the composition of $Ba_{0.5}Ca_{0.5}Ti_{0.6}Zr_{0.4}O_3$ is a mixture of tetragonal $Ba_{0.8}Ca_{0.2}Ti_{0.6}Zr_{0.4}O_3$ with space group *I4/mcm* and orthorhombic $CaTiO_3$ with space group *Pbnm:cab,* and the result are tabulated in the Table 5.5. The refined positional parameters of the $CaTiO_3$ in the composition $Ba_{0.5}Ca_{0.5}Ti_{0.6}Zr_{0.4}O_3$ are: Ca (0.9821, 0.0328, 0.25), Ti (0.0.25.0), O1 (0.0162, 0.475, 0.25) and O2 (0.7969, 0.2398, -0.0445). The refinements produced satisfactory agreement factors for 5000 observations and 44 variables which are given in the caption of Fig.5.8.

The quantitative estimation of the different phases using Rietveld program MAUD, that shows there is increase in $CaTiO_3$-like phase with increase in Ca content in the mixture. The weight percents of the different phases are given in the Table 5.5. The result tabulated in the Table 5.5 shows that there is increase in crystallite size of tetragonal phase with increase in Ca content and increase in wt % and volume percent of orthorhombic $CaTiO_3$ phase.

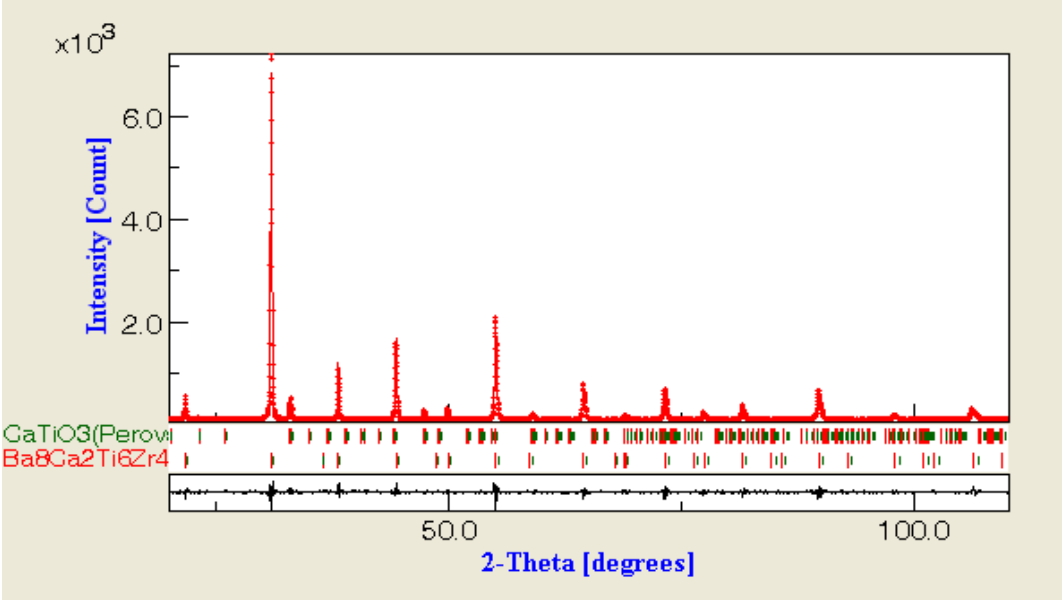

Figure 5.7 Observed (▪), calculated (—) and residual (lower) X -ray powder diffraction patterns of $Ba_{0.8}Ca_{0.2}Ti_{0.6}Zr_{0.4}O_3$ composition revealed from Rietveld's powder structure refinement analysis. Peak positions of the phases are shown at the base line as small markers (l). R_{wp} (%) = 11.947288, R_p (%)=9.4384365,R_{exp} (%)=9.360648, and Sigma= 1.2763312.

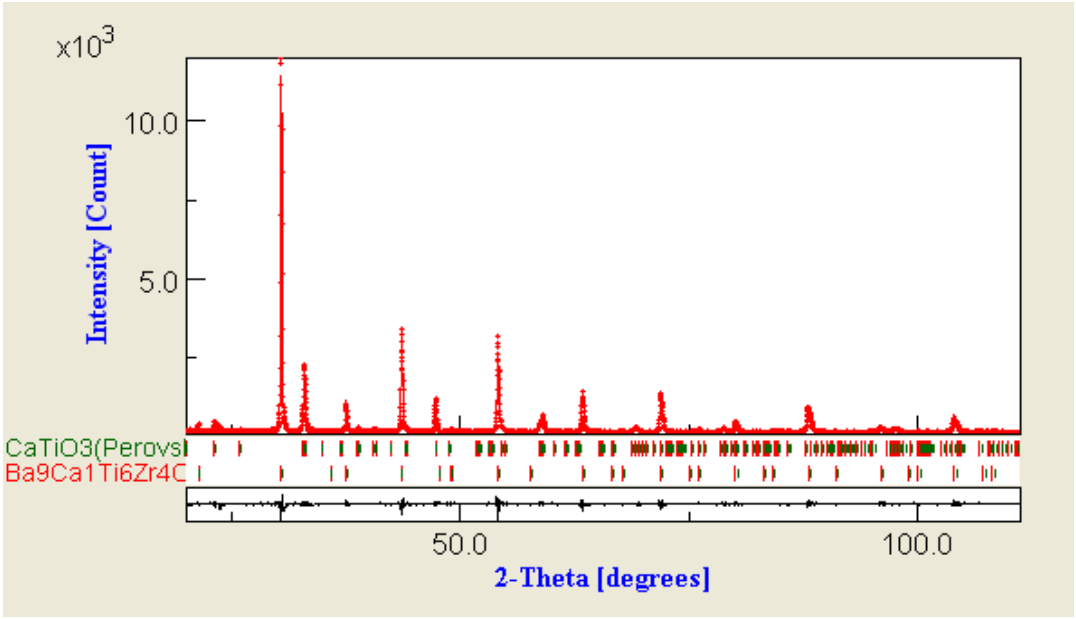

Figure 5.8. Observed (▪), calculated (—) and residual (lower) X -ray powder diffraction patterns of $Ba_{0.5}Ca_{0.5}Ti_{0.6}Zr_{0.4}O_3$ composition revealed from Rietveld's powder structure refinement analysis. Peak positions of the phases are shown at the base line as small markers (l). R_{wp} (%) = 10.051784, R_p (%)=7.546414,R_{exp} (%)=7.2008095, and Sigma= 1.3959241.

Table 5.5: Refined room temperature selected structural parameter of $Ba_{1-x}Ca_xTi_{0.6}Zr_{0.4}O_3$ using x-ray diffraction

Quantity	**$Ba_{1-x}Ca_xTi_{0.6}Zr_{0.4}O_3$**				**$CaTiO_3$**	
	X=0.0	X=0.1	X=0.2	X=0.5	X=0.2	X=0.5
a_0 (Å)	4.0921	4.061	5.7840	5.8587	5.4309	5.3986
b_0 (Å)	-----	----	8.1857	8.2843	5.4920	5.4523
c_0 (Å)	-----	-----	-----	-----	7.7149	7.667
S. grp	Pm-3m	Pm-3m	I4/mcm	I4/mcm	Pbnm:cba	Pbnm:cba
Cryst.size(nm)	72.51	159.1	163.33	142.06	93.15	165.23
Rms strain	0.001	0.0015	0.0011	0.00001	0.0012	0.0011
Density(gm/cc)	6.0712	5.8002	5.8318	5.6249	3.9858	4.001
wt %	100%	100%	85.98	61.50	14.02	38.49
Vol %	100%	100%	80.723	53.20	19.27	46.79
Ba (β_{iso})	0.5117	1.489	1.532	3.166	-----	-----
Ca (β_{iso})	-----	0.84	1.532	3.166	1.5429	2.1024
Ti (β_{iso})	0.512	0.869	3.665	0.4557	1.5532	1.6088
Zr (β_{iso})	0.512	0.869	3.665	0.4557	----	----
O(1) (β_{iso})	0.512	0.735	0.4621	2.586	0.5429	4.3721
O(2) (β_{iso})	-----	-----	0.59	2.4560	1.5429	-0.004
O(2) (x)	-----	-----	0.2399	0.2515	0.7573	0.7969

5.5.6. Refinement of $Ba_{1-x}Mg_xTi_{0.6}Zr_{0.4}O_3$

Final outputs after structural refinements for the composition $Ba_{0.97}Mg_{0.03}Ti_{0.6}Zr_{0.4}O_3$, $Ba_{0.93}Mg_{0.04}Ti_{0.6}Zr_{0.4}O_3$, $Ba_{0.86}Mg_{0.14}Ti_{0.6}Zr_{0.4}O_3$ are represented in the Fig 5.9, 5.10, and 5.11 respectively. Structural refinements were carried out taking the positional parameter for the earlier refined (Fig 5.5) $BaTi_{0.6}Zr_{0.4}O_3$ composition with space group Pm-3m. Successful refinement confirms that all these compositions remain cubic symmetry with space group *Pm-3m*. There is only a decrease in lattice parameter which is observed due to the substitution of lower radii Mg in place of Ba. The refinements produced satisfactory agreement for 5500 observations and 43 variables. The observed R-factors and good-ness of fit (GoF) (Sigma) of all these compositions are given in the Table 5.6. The GoF for all the compositions lie in the range of 1.2 to 1.5. This indicates the good quality of the fitting

of the experimental data with the theoretical one. The occupancy factors for the mixed Ti and Zr sites were fixed at the nominal composition. The Ti and Zr displacement parameters were constrained to be equal. Refined parameters included scale factor, background coefficient, profile coefficients, and anisotropic thermal (displacement) parameters. Some of the structural and microstructural features revealed from Rietveld's powder structure refinement analysis for these compositions are given in table 5.6. Atomic thermal (displacement) parameters are x 100Å^2.Initially the atom positional parameters for the compositions were taken as: Ba/Mg at 1a (0,0,0), Ti/Zr at 1b (1/2,1/2,1/2) and O is at 3c (0,1/2,1/2). After refinement a small change occurs to these parameters. The refined positional parameters of different atoms in the different composition were given in the captions of respective figures As previously mentioned, the symmetry constraints on the thermal parameters in the *Pm3m* space group are as follows: for Ba, Sr, Ti and Zr $U_{11}=U_{22}=U_{33}$, $U_{12}=U_{13}=U_{23}=0$, for O $U_{22}=U_{33}$, $U_{12}=U_{13}=U_{23}=0$. In the refinement, these conditions are also taken care, but values of these parameters were not reliable. The exact values of these anisotropic thermal parameters could be best monitored using high resolution synchrotron radiation or neutron diffraction.

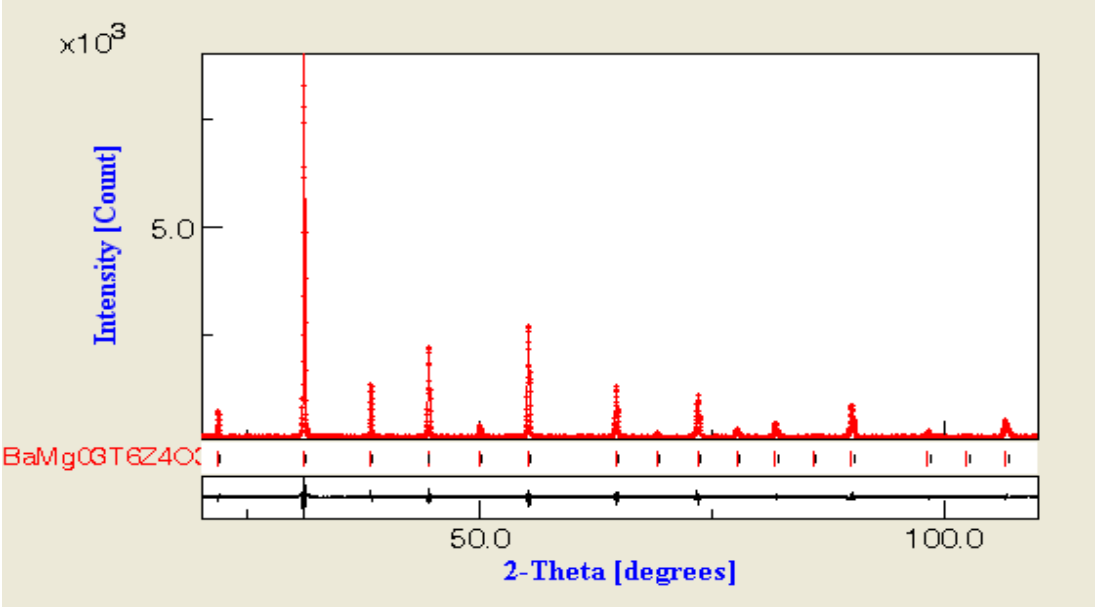

Figure 5.9 Observed (▪), calculated (—) and difference X -ray powder diffraction patterns of $Ba_{0.97}Mg_{0.03}Ti_{0.6}Zr_{0.4}O_3$ composition revealed from Rietveld's powder structure refinement analysis. Positional parameters for the compositions are: Ba/Mg at 1a (0,0,0), Ti at 1b (0.4999, 0.4998, 0.4996), Zr at 1b (0.5002, 0.4991, 0.4996) and O is at 3c (0, 0.50012, 0.4999).

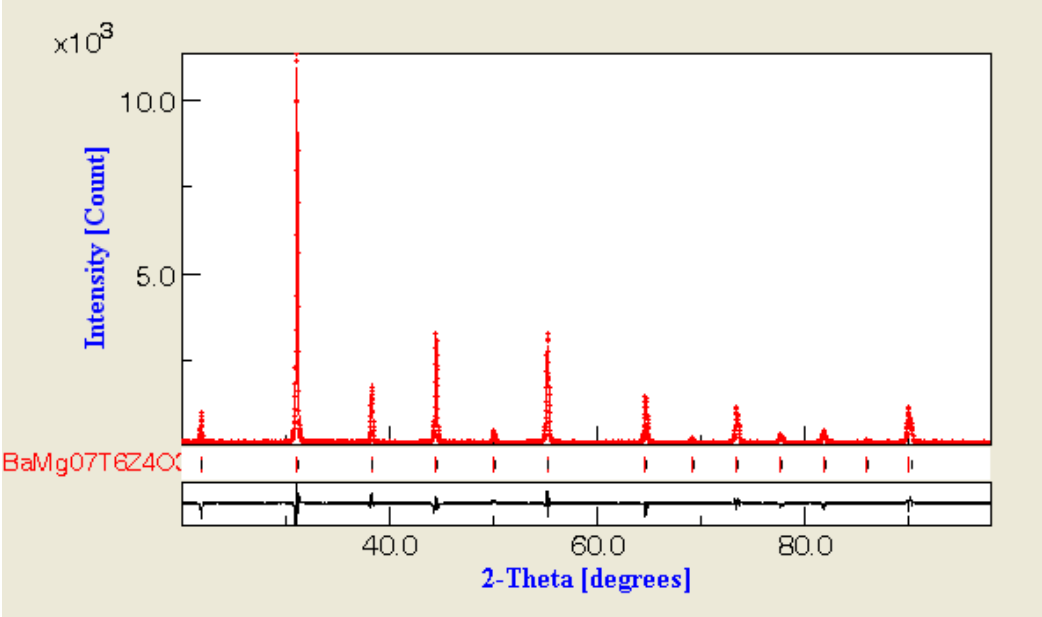

Figure 5.10. Observed (▪), calculated (—) and difference in X-ray powder diffraction patterns of $Ba_{0.93}Mg_{0.07}Ti_{0.6}Zr_{0.4}O_3$ composition revealed from Rietveld's powder structure refinement analysis. Positional parameters for the compositions are: Ba/Mg at 1a (0,0,0), Ti at 1b (0.4995, 0.5, 0.49994), Zr at 1b (0.5002, 0.4998, 0.4999) and O is at 3c (0, 0.5001, 0.5003).

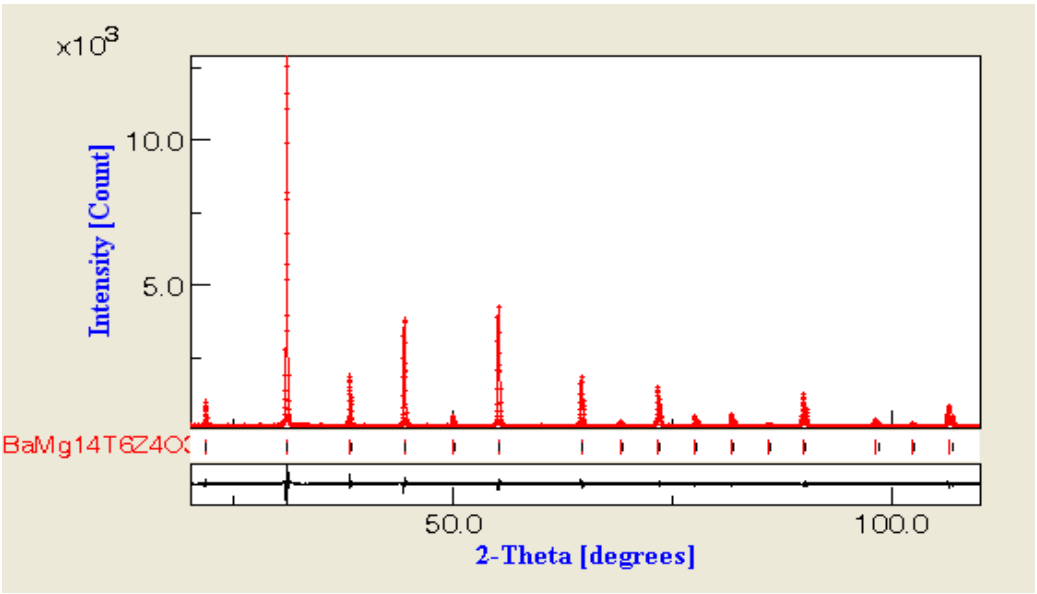

Figure 5.11. Observed (▪), calculated (—) and difference in X- ray powder diffraction patterns of $Ba_{0.86}Mg_{0.14}Ti_{0.6}Zr_{0.4}O_3$ composition revealed from Rietveld's powder structure refinement analysis. Peak positions of the phases are shown at the base line as small markers (l). Positional parameters for the compositions are: Ba/Mg at 1a (0,0,0), Ti at 1b (0.5, 0.4998, 0.4999), Zr at 1b (0.5005, 0.4996, 0.4999) and O is at 3c (0, 0.5001, 0.5006).

Table 5.6: Refined room temperature selected structural parameter of $Ba_{1-x}Mg_xTi_{0.6}Zr_{0.4}O_3$ (space group *pm-3m*) using x-ray diffraction

Quantity	X=0.0	X=0.03	X=0.07	X=0.14
a_0 (Å)	4.0921	4.0959	4.0939	4.0967
Cryst. size (nm)	44.915	66.018	64.069	79.569
rms strain	0.0015	0.00074	0.0011	0.0008
Density (gm/cc)	6.0712	5.972	5.8717	5.6687
Ba (β_{iso})	0.5117	0.4734	0.61	1.247
Mg (β_{iso})	-----	0.473	0.618	1.247
Ti (β_{iso})	0.512	0.86	0.700	1.486
Zr (β_{iso})	0.512	0.76	0.88414	1.486
O (β_{iso})	0.512	0.61	0.78	2.48
R_{wp} (%)	10.1632	12.603	11.76	10.7408
R_p (%)	7.6520	9.742	9.076	8.1486
R_{exp} (%)	6.9455	9.208	8.977	7.9108
GoF	1.4633	1.36	1.31	1.3577

5.6. Conclusions

From the above study, it can be concluded that $BaTi_{0.5}Zr_{0.5}O_3$ has cubic symmetry with space group *Pm-3m*, which transforms to a lower symmetry tetragonal structure having space group *I4/mcm* with the substitution of Sr in place of Ba. Cubic structure of $Ba_{0.5}Sr_{0.5}TiO_3$ having space group *Pm-3m* transforms to lower symmetry orthorhombic and tetragonal phases. The composition $BaTi_{0.6}Zr_{0.4}O_3$ was cubic structure having space group Pm-3m. When Sr was substituted in place of Ba upto 50 atom % in the above compositions, the structure remained cubic with space group unchanged. When 10 atom % of Ca is substituted in place of Ba in the composition, the structure remains cubic. When the Ca concentration becomes 20 atom %, the solubility of Ca in $BaTi_{0.6}Zr_{0.4}O_3$ breaks and orthorhombic phase of $CaTiO_3$ develops along with tetragonal structure of $Ba_{0.8}Ca_{0.2}Ti_{0.6}Zr_{0.4}O_3$. With further increase in Ca, the concentration of $CaTiO_3$ increases, but the $Ba_{0.8}Ca_{0.2}Ti_{0.6}Zr_{0.4}O_3$ remains tetragonal having space group I4/mcm. The study predicts that there is a likely chance of increase of T_c with substitution of Ca in $BaTi_{0.6}Zr_{0.4}O_3$ system. When Mg is substituted in place of Ba, in

the said composition the structure remains cubic. Only the lattice parameter decreases due to the substitution of lower radii Mg in place of Ba.

5.7. References

1. H.M.Rietveld, *Acta Crystallogr*, **22**, 151-152 (1967).
2. H.M.Rietveld, *J.Appl. Crystallogr*, **2**, 65-71 (1969).
3. R.A.Young, *The Rietveld Method*, Oxford Unv. Press (1995).
4. R.A.Yang and B.D. Wiles, *J. Appl.Cryst*. **15**, 430 (1982).
5. L.Lutterotti, P.Scardi, P.Maistrelli, *J.Appl. Crystallogr*. **25**, 459 (1992)
6. R.A.Yang, *The Rietveld Method*, IUCr, Oxford, pp-1-38, 1996.
7. http://www.*ing.unitn.it/~maud/*.
8. S.Enzo, G.Fagherazzi, A.Benedetti and S.Polizzi. *J. Apl.Crystallogr*. **21**, 536, (1988)
9. B.E.Warren, *X-ray diffraction*, Addition-Wesley, Reading, MA, Chapter 13 (1969).
10. H.-R. Wenk, S. Matthies and L. Lutterotti, *Mater. Sci. Forum*, **157-162**, 473-480, (1994).
11. M. Ferrari and L. Lutterotti, *J. Appl. Phys*., **76** (11), 7246-55, 1994.
12. T.K.Y. Wong, B.J. Kennedy, C.J. Howard, B.A. Hunter and T.Vogt, *J.Solid State Chemistry* **156**, 255-263 (2001).
13. B.J. Kennedy, C.J. Howard, G.J.Thorogood and J.R.Hester, *J.Solid State Chemistry* **161**, 106-112 (2001).
14. I.Levin, T.G. Amos, S.M.bell, L. Farber, T.a. Vanderah, R.S. Roth and B.H.Toby, *J.Solid State Chemistry* **175,** 170-181 (2003).
15. J.M.G. Van Berkum, *Ph.D thesis*, Delft University of Technology, The Netherlands, (1994).
16. H.Pal, A.Chanda and M.De, *J.Alloys Compd,* **278**,209 (1998).
17. S.Bid and S.K.Pradhan, *J.Appl. Crystallogr*. **35**, 517(2002).
18. P.Bose, S.K.Shee, S.K.Pradhan and M. De, *Mater.Eng* (Italy) **12**, 353 (2001).
19. H.Dutta, S.K.Manik and S.K.Pradhan, *J.Appl Crystallogr*. **36,** 260 (2003).
20. R.C. De Vries and R.Roy, *J. Am.Cera.Soc*., **38**,142-146 (1955).

Chapter 6

STOICHIOMETRIC STUDY BY ENERGY DISPERSIVE X-RAY FLUORESCENCE (EDXRF) SPECTROMETRY

6.1. Introduction

X-ray fluorescence (XRF) spectrometry provides a non-destructive analytical method capable of analyzing solids from a few parts per million to near 100% for a wide range of elements. This versatile technique is ideally suited for the analysis of rocks, soils, dust, contaminated land samples, mineral concentration and products, archaeological artifacts, synthetic materials and metals. The nondestructive nature of the technique allows long term storage of samples, which can then be re-analyzed any number of times for additional elements as necessary. This approach, therefore, avoids problems of re-sampling and digestion of separate aliquots.

Since 1960s, XRF spectrometers has been fully automated and today's state of art machines are compact, self-contained analytical units, capable of running unattended for several days, with flexibility of rapid transition from one analytical program to another. One of the more recent designs has been the use of end window X-ray tubes, which reduces the coupling distance between the sample and the tube, and this, together with upgraded detection system, enhances the sensitivity of the spectrometers.

6.2. Sample Preparation

Sample preparation is an important procedure in XRF analysis, and this starts with the initial sample selection and subsequent preparation (i.e. crushing and milling of consolidated materials), with the final product being a fine grained (ideally <63 micro-meter) powder. The ideal sample to be presented to the X-ray beam is flat, homogeneous and infinitely thick with respect to the X-ray. It should be capable of with standing a vacuum, though this constraint can easily be overcome by the use of helium atmosphere in the spectrometer. There are many methods for preparing bulk materials; two basic types are most suitable for the types of samples under discussion here.

I. Fused beads, where the sample is mixed with a suitable flux, which is then fused into glass and either cast or pressed into a disc.

II. Pressed powder pellets, where the sample powder, with or without a binder is compressed to produce a solid tablet of powder.

Provided the correct flux is used, the fusion method provides the simplest method for obtaining an ideal sample. The pressed powder method can also provide a suitable sample, but there can be concerns about homogeneity. In general terms, this can mean problems concerning particle size effect and chemical/mineralogical homogeneity. For most XRF applications, the fusion bead method provides a superior solution, with heterogeneity problems minimized, and with the right matrix corrections, consistent and reliable results are easily achieved. However, in certain situations (e.g.mineral exploration) a number of issues arise whereby the pressed powder pellet method is to be preferred. Some of these issues include:

a) Preparation of fusion beads is relatively slow compared to pellet making and the equipment required is more expensive. Fusion is normally undertaken Pt-Au crucibles, although cheaper alternatives can be used.

b) Depending on the analytical problem (i.e., sample composition), it may be necessary to vary the flux mixes. Consequently, where large numbers of samples are to be analysed, this may not produce an economic solution.

c) Production of fusion beads inevitably involves the dilution of the original sample, with a corresponding decrease in detection limits or, in some case, to achieve the desirable limits, counting times may have to be significantly increased.

In commercial setting, all these factors can significantly increase the costs and increased analytical times. Given these factors, it may be desirable on a job-by job basis to select pressed powder pellets as the analytical medium, since this may affect the cost for a commercial contract and/or yield lower limits of detection for the selected trace elements.

There are numerous methodologies and recipes for preparing pressed powder pellets. Many materials, such as coal, many soils and shales, waxes and some synthetic materials will form stable pellets without the addition of a binder. For routine preparation, however, a binder is necessary to produce a coherent and semi resistant pellet, which can be handled during loading and XRF analysis. Commonly employed binders include ethyl and methyl cellulose, starch, Moviol (Hoechst, Inc) and polyvinyl binders. In some applications, large volumes of binders have been used, which act as dilutents. Again this dilution procedure has the effect of raising the lower limit of

detection, and it does not remove grain size effects. In the case of low-level trace element work, this approach is not advised. In our case, pressed powder pellets method is used for purity study of the compositions by XRF spectrometry.

500 mg of the dried powder sample was crushed and mixed with 500 mg of high purity cellulose powder in 1:1 ratio by weight. The mixture was then crushed thoroughly so as to get a homogenized powder mixture. The corresponding mixture was then pressed in a KBr press to make pellets of size 25 mm diameters.

6.3. Quantitative Analysis

To a first approximation, the intensity of any given line is proportional to concentration, but modified by a combination of absorption and enhancement effects, which are, in turn, a function of the composition of the sample and the primary spectrum from the X-ray tube. Quantitative analysis involves choosing a calibration strategy that can accommodate or attempt to eliminate these effects, and most methods attempt to achieve a simple linear relationship between the measured spectral line intensity and concentration. There is a very wide range of methods available [1], two of which are particularly suitable for the analysis of most natural and synthetic materials.

The (major) elements that make up the bulk of a rock are normally determined using fused beads; this produces homogeneous samples for analysis, and a significant dilution of the original rock powder which, in turn, minimizes the absorption and enhancement effect. This is most effective when fusion is achived together with a heavy absorber (usually La_2O_3) as part of the fusion mixture [2]. Calibration is achieved either by simple straight-line methods, or by multi element measurement approaches. The software that comes with modern instruments contains algorithms for the latter, though there are many variations, some of which are not suitable for wide range in composition. The most “all embracing” model published in 1984 by Rousseau [3] is not always supported.

The (minor) trace elements are generally determined using pressed powder pellets to minimize the dilution of the sample. With only a few exceptions, the spectral lines used for trace element analysis lie at shorter wave lengths (higher energy) than those of the associated major elements. And the dominant problem to be overcome is that of absorption. The simplest, and probably the most effective, approach to correcting for absorption makes use of the fact that the intensity of the background, and of the coherent and incoherent scattered lines of the anode element, vary systematically with the mass absorption of the sample matrix. Measurement of this scattered radiation,

usually that of the Compton K_α for most anodes, thus provides an absorption correction factor. There are several ways in which scattered correction can be applied; most involve ratioing the scatter measurement on a standard at a wavelength shorter than the lines of the elements to be measured [4]. This model works well, though problem can arise with higher trace element concentrations (1,000s ppm) when the ratio relationship may break down with increasing wavelength. While these methods work well with most rocks and related materials, for heavily mineralized samples a different approach might be needed. For these samples internal standard and double dilution techniques [1] are recommended. In our case, the latter is preferred and the results are shown in Table 1 and Table2.

6.4. Experimental Setup

The elemental analysis of the samples was carried out by EDXRF. The EDXRF system at the Institute of Physics, Bhubaneswar, incorporates a low power (50 watt) tungsten anode, air cooled X-ray tube as an excitation source with tri-axial geometry. The X-ray tube was operated at 30 kV and 0.6 mA. The X-rays from the X-ray tube irradiated on a Mo secondary exciter were used to excite the characteristics K X-rays of secondary exciter which, in turn, used to excite the characteristics X-rays of elements present in samples. The X-rays from the sample were detected by a Si (Li) X-ray detector (without X-ray absorber) and the signals were processed by an amplifier. The system was calibrated by using an Am^{241} X-ray source.

6.5. Data Acquisition and Analysis

The data acquisition and analysis of X-ray spectra was done by using a PC based multi channel analyser. The photo-peak areas in each spectrum were evaluated using the computer program AXIL supplied by International Atomic Energy Agency (IAEA), Australia. K-characteristic X-rays of molybdenum were used to excite the elements present in all the samples. Matrix effects were taken into account by recording spectra from the sample and the standard.

6.6. Results and Discussion

Fig. 6.1 shows the EDXRF spectrum of BTZ ceramics. From the spectrum, it was found that Ba, Ti and Zr, were present in the BTZ synthesized sample in pure form. None other elements are present except these elements. The elemental concentrations of the elements are depicted in Table.1. Since, Mo was used as a secondary exciter in the analysis of the sample, so Ba-K_α was not detected whose K_α and K_β energy falls after Molybdenum K_α.

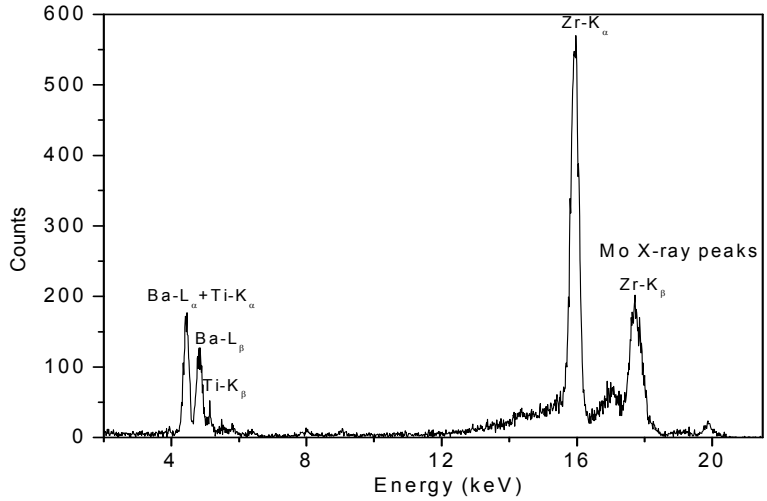

Figure 6.1. EDXRF spectrum of $BaTi_{0.5}Zr_{0.5}O_3$ ceramics

The peak at 4.43 keV corresponding to the Ba-L_α line which theoretically occurs at 4.47 keV, and the peak at 4.835 keV corresponding to Ba-L_β line which also theoretically occurs at 4.83 keV, were prominent in this spectrum. The peaks at 4.55 keV and at 4.95 keV are due to the transition of Ti- K_α and Ti- K_β line, respectively. Similarly, the peak at 17.70 keV corresponds to the transition of Zr- K_α. Since Mo is used as the secondary exciter in the EDXRF system, so, Mo peak is present in the spectra. As Zr- K_β energy is close to Mo- K_α energy; hence, these two peaks are overlapping.

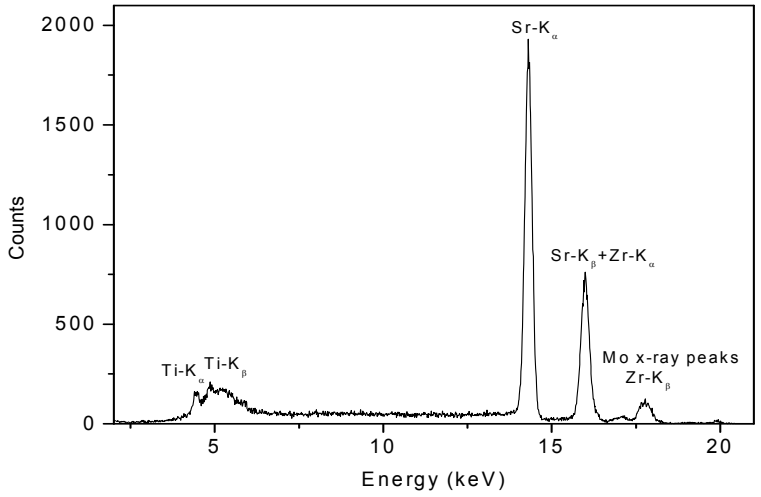

Figure 6.2. EDXRF spectrum of $SrTi_{0.5}Zr_{0.5}O_3$ ceramics

Fig. 6.2 shows the EDXRF spectrum of STZ ceramics. The figure shows the presence of the emission peaks of Sr, Ti and Zr without evidence of any other trace element peak. It was found that K_α and K_β lines of Ti, Sr and Zr, were present in the STZ synthesized sample in pure form. None other contaminants are present except these elements. The elemental concentrations of the elements are depicted in Table.6.1. The peak at ~15.9 keV is the overlapping emission peak of Sr- K_β and Zr- K_α lines. These lines were not separated as theoretically their emission energy is very close to each other (15.83 keV for Sr - K_β and 15.77 for Zr-K_α). The emission line of Zr- K_β is overlapped with the Mo-K_α line due to close spacing of their energy level.

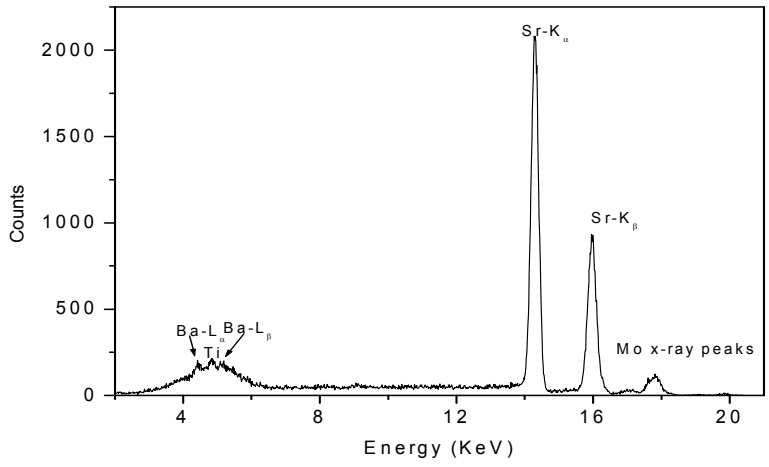

Figure 6.3. EDXRF spectrum of $Ba_{0.5}Sr_{0.5}TiO_3$ ceramics

Fig. 6.3 shows the EDXRF spectrum of BST ceramics. From the spectrum, it was found that Ba, Sr and Ti were present in the synthesized BST sample in pure form. None other elements are present except these elements. The elemental concentrations of the elements are depicted in Table 6.2. Since, Mo was used as a secondary exciter in the analysis of the sample, so Ba-K_α was not detected, whose K_α and K_β energy falls after Molybdenum K_α. Rather, the Ba-L_α and Ba-L_β lines are prominent in this spectrum. The Sr- K_β and Sr- K_α lines were prominent in the composition at 14.2 and 15.85 keV, respectively. The peaks at 4.55 keV and at 4.95 keV are due to the transition of Ti- K_α and Ti- K_β line, respectively. The peak for Ti is observed along with Ba L_α and Ba L_β line, making the peaks overlapping and undistinguishable as their emission energies were very close to each other.

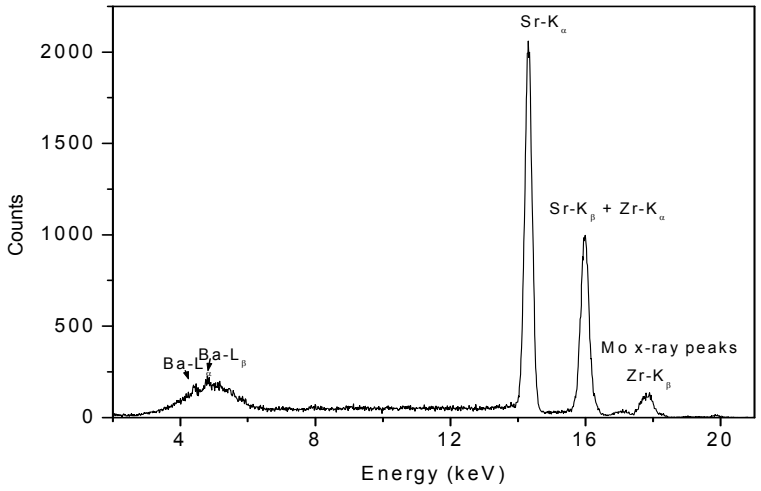

Figure 6.4. EDXRF spectrum of $Ba_{0.5}Sr_{0.5}ZrO_3$ceramics

Fig. 6.4 shows the EDXRF spectrum of BSZ ceramics. From the spectrum, it was found that Ba, Sr and Zr were present in the synthesized BSZ sample in pure form. None other elements are present except these elements. The concentrations of these elements are depicted in Table 6.2. Since, Mo was used as a secondary exciter in the analysis of the sample, Ba-K_α and Ba- K_β were not detected as the K_α and K_β energy falls after Molybdenum K_α. Rather, the Ba-L_α and Ba-L_β lines are prominent in this spectrum. The Sr- K_α lines were prominent in the composition at 14.2 keV and the peak at 15.85 keV is due to the overlapping peak of Sr- K_β and Zr- K_α. The Zr- K_β peak is overlapped with the Mo peak in the spectrum as their energies were very close to each other. The elemental concentrations of the samples are given in Table 6.1 and Table 6.2. The estimated standard deviation is with in 1-3 %.

Table.6.1: Concentration (in ppm by weight) of various elements present in the samples

Compound	Ti	Sr	Zr	Ba
$BaTi_{0.5}Z_{0.5}O_3$	5021	----	4984	9942
$Ba_{0.8}Sr_{0.2}Ti_{0.5}Zr_{0.5}O_3$	10104	1941	10059	7937
$Ba_{0.6}Sr_{0.4}Ti_{0.5}Zr_{0.5}O_3$	10082	4101	9927	5892
$Ba_{0.5}Sr_{0.5}Ti_{0.5}Zr_{0.5}O_3$	9896	5058	10027	5025
$Ba_{0.4}Sr_{0.6}Ti_{0.5}Zr_{0.5}O_3$	9971	5962	9945	4060
$Ba_{0.2}Sr_{0.8}Ti_{0.5}Zr_{0.5}O_3$	9926	7994	10121	2016
$SrTi_{0.5}Zr_{0.5}O_3$	5053	9927	4959	----

Table.6.2: Concentration (in ppm by weight) of various elements present in the samples

Compound	Ti	Sr	Zr	Ba
$Ba_{0.5}Sr_{0.5}TiO_3$	9907	4941	----	5056
$Ba_{0.5}Sr_{0.5}Ti_{0.8}Zr_{0.2}O_3$	7876	5038	2090	5089
$Ba_{0.5}Sr_{0.5}Ti_{0.6}Zr_{0.4}O_3$	6256	5177	4181	5332
$Ba_{0.5}Sr_{0.5}Ti_{0.5}Zr_{0.5}O_3$	4948	5058	5013	5025
$Ba_{0.5}Sr_{0.5}Ti_{0.4}Zr_{0.6}O_3$	3899	4905	5915	4921
$Ba_{0.5}Sr_{0.5}Ti_{0.2}Zr_{0.8}O_3$	2064	4812	7931	4756
$Ba_{0.5}Sr_{0.5}ZrO_3$	----	4987	9880	5011

6.7. Conclusions

XRF is now a well-established analytical tool for the analysis of specimens of geological interest and synthetic materials for elemental and concentration analysis. EDXRF is rapid, efficient, multi-elemental, non-destructive in nature and sensitive to all elements from Na to U. This can provide precise analysis for a wide spectrum of elements at much reduced lower limits of detection; typically most elements can now be analysed at sub-ppm level. Another recent advance, resulting from spectrometer redesigns, is the ability now to analyse light elements such as B, C, N and Be, which are important in the assessment of synthetic materials. All of these advances suggest that the XRF spectrometry will retain its importance as an analytical tool and allow development into new areas as defined by the user. In our study with EDXRF, we conclude that the

synthesized materials are in pure form without evidence of spectral line of any trace element. Quantitative analysis shows that the concentrations of the elements in the compositions are in similar proportion, as taken during synthesis and the results are within the permissible range of deviation.

6.8. References

[1]. R.Tertian and F.Claisse, "*Principles of Quantitative X-ray Fluorescence Analysis*". Heyden & son, London, ISBN 0-85501-709-0 (1982)

[2]. K. Norrish and J.T.Hutton, "*An accurate X-ray spectrographic method for the analysis of a wide range of geological samples*", *Geochim. Cosmochim. Acta* **33**, 431 (1969).

[3]. P.K. Harvey, " Fundamental algorithm between concentration and intensity in XRF analysis: 1-Theory, 2- practical application" *X-ray Spectrom*. **13**, 115-125 (1984).

[4]. P.K.Harvey, "Automated X-ray Flurorescence in Geochemical Exploration", in X-ray Fluorescence Analysis in the Geological Sciences. Advances in Methodology, Ed by T.S. Ahmedali, Short Course Vol.7. Geological association of Canada, Montreal, pp.221-257 (1989).

Chapter 7

MICROSTRUCTURE AND DIELECTRIC STUDY

7.1. Introduction

$BaTiO_3$ was first found to be the lead-free perovskite ferroelectric material [1], and it has a large electromechanical coupling factor. $BaTiO_3$ (BT) is known to form a complete solid solution with $BaZrO_3$ (BZ) (i.e. BZT solid solution). Solid solution compositions in $BaTiO_3$ (BT)-$BaZrO_3$ (BZ) or BTZ-system have been established as one of the most important compositions for dielectrics in multilayer ceramic capacitors [2] due to their high permittivity, and are highly promising materials for dynamic random access memory (DRAM) [2]. Moreover, BZT ceramics have seen renewed research interest due to their high strain level, minimal hysteresis, very stable, high insulating characteristic against voltage and good piezoelectric properties, for single crystals as well as for multi-crystalline ceramics [3-5] due to which the materials are ideal for MEMS devices. It has been reported [6] that at ~15 atom % Zr substitution, the three transition temperatures of $BaTiO_3$, rhombohedra to orthorhombic, orthorhombic to tetragonal and tetragonal to cubic, merge near room temperature and the doped material exhibits enhanced dielectric constant. With further increase in Zr contents beyond 15 atoms %, a diffuse dielectric anomaly in the ceramic has been observed with the decrease in the transition temperature [7] and the material showed typical relaxor–like behavior in the range 25-42 atom % Zr substitution [8].

Most of the literature for the system Ba $(Ti_{1-x}Zr_x)$ O_3 is restricted upto the value of x ~0.4 [9-11]. That is the reason, 50 atom% Zr (x=0.5) substituted composition Ba $(Ti_{0.5}Zr_{0.5})O_3$ has been investigated in the present work. $SrTiO_3$ also forms complete solid solution with $BaTiO_3$ and that (BST) material is also a popular composition for DRAM application [12]. The solid solutions of BZT and BST, i.e., Ba/Sr titanate-zirconate are reported to have improved tunability and low temperature coefficient of dielectric constant [13-15]. In these circumstances, room temperature dielectric behavior, microstructure and a.c. conduction characteristics effect of Sr substitution in Ba $(Ti_{0.5}Zr_{0.5})O_3$ have been studied.

At the other end, the Barium Strontium Titanate (BST) has been considered to be an important material for tunable microwave devices such as microwave tunable phase shifters, tunable filters, and high-Q resonators for radar and communication

applications, as well as dynamic random access memory (DRAM) applications because of its high dielectric constant, large electric field tunability, relatively low dielectric loss and variable Curie temperature from 30 to 400K, depending on the composition of Barium [16-20]. For optimal performance of the tunable devices, it is important to grow materials with high dielectric tunability, low dielectric losses, low voltage hysteresis, and low temperature dependence of the dielectric permittivity in the operation frequency and temperature range of the device. To improve the material performance for the use of tunable devices, many efforts have been made, such as doping, fabrication of composite and even multilayered structure, etc. The recent work [21] suggests that $Ba_{1-x}Sr_xTiO_3$ thin films with x=0.5-0.6 are preferred for use at room temperature tunable circuit components. For example, H.M. Cristen *et al* [22] found a strong bias voltage tunability and very low hysteresis in the composition $Ba_{0.5}Sr_{0.5}TiO_3$. Considering all these, the composition $Ba_{0.5}Sr_{0.5}TiO_3$ has been selected as a base material in the present study to investigate the effect of Zr^{4+} substitution for Ti^{4+} in the material. Among the several isovalent substitutions in $BaTiO_3$, other than Sr which are also able to shift the T_c below room temperature, Zr is of interest because a different character of dielectric response with respect to the paraelectric to ferroelectric phase transition can be achieved by the Zr substitution due to the disparate distortions of oxygen octahedral in the perovskite lattice [23]. Moreover, Zr^{4+} ion is chemically more stable than Ti^{4+} and has larger ionic size to expand the perovskite lattice. Therefore, the conduction by electron hopping between Ti^{4+} and Ti^{3+}, if any, would be depressed by the substitution of Ti with Zr [5]. Another motivation behind Zr substitution is that the substitution of Ti^{4+} with Zr^{4+} ions in barium titanate can reduce the dielectric loss or leakage current in the material [5]. The BST thin films often have high current emission at low electric field [24]. Therefore, new types of dielectrics with high dielectric constant and low stable leakage current need to be developed. It is expected that Zr-doped $Ba_{0.5}Sr_{0.5}TiO_3$ ceramics should have further improved dielectric losses. A high dielectric constant and low leakage current of $(Ba_{0.65}Sr_{0.35})(Ti_{0.65}Zr_{0.35})O_3$ thin film has been reported [25] and proposed as a promising material for DRAM applications. A similar type of compositionally-graded multilayer $(Ba_{0.8}Sr_{0.2})$ $(Ti_{1-x}Zr_x)$ O_3 films has shown an improved dielectric property and tunability [20]. However, no literature are available on bulk ceramic of $(Ba_{0.5}Sr_{0.5})(Ti_{1-x}Zr_x)O_3$ composition. In this Chapter, a study concerning the microstructure, room temperature dielectric properties and conduction characteristics of bulk $(Ba_{0.5}Sr_{0.5})(Ti_{1-x}Zr_x)O_3$ ceramics is reported.

Dixit *et al* [26] have reported a relaxor behavior with diffused phase transition at T_c= *-113* ^{O}C, which has maximum dielectric constant (~650) at 1 kHz, in Ba $(Ti_{0.6}Zr_{0.4})O_3$ thin film, which are very attractive for sensor and actuator applications. Byun *et al* [25] reported that the composition $(Ba_{0.65}Sr_{0.35})$ $(Ti_{0.65}Zr_{0.35})$ O_3 shows a dielectric constant about 2,700 at room temperature and transition temperature nearly -30 ^{O}C. Apart from these studies, many recent literatures like [27, 28] reported Ba $(Ti_{1-x}Zr_x)O_3$ $(0.27\leq x \geq 0.42)$ as relaxor dielectric. But almost all the studies report their relaxor nature at relatively low temperature. Research works are now in progress to obtain such lead-free ceramics, which could be relaxors at temperatures close to room temperature. Therefore, it attracts our attention to study the composition Ba $(Ti_{0.6}Zr_{0.4})$ O_3 and to shift the T_C towards room temperature.

As previously mentioned, Ba $(Ti_{0.6}Zr_{0.4})$ O_3 ceramic has a cubic paraelectric structure, which shows a high dielectric constant, comparable to BST ceramic with Curie temperature below the room temperature, and the transition from ferroelectric to paraelectric is of second order relaxor type. When lower radii Ca/Mg replaces Ba in the Ba $(Ti_{0.6}Zr_{0.4})$ O_3 perovskite structure, there is decrease in lattice parameter leading to lowering of dipole moment and causing a decrease in permittivity. But, the Ca/Mg ions are too small to occupy the centre of 12 coordinated sites. On the other hand, they may take 12 co-ordination sites with eight near neighbors and four more distant ones [29]. That modification supposes a possible displacement of Ca/Mg ion out of the oxygen dodecahedron centre able to induce a dipolar moment whose occurrence should lead to increase of T_C. This is the motivation behind the Ca and Mg substitution in Ba $(Ti_{0.6}Zr_{0.4})$ O_3 composition.

7.2. Experimental Procedure

Microstructures of the sintered pellets were studied using optical microscope connected with a PC. For electrical measurement, thin silver electrodes were printed on to opposite faces of the ceramic disk by screen printing technique. For organic removal, printed disks were kept on an alumina plate and fried at 700^0C, 15 minutes. This procedure was repeated twice for better electroding. Room temperature dielectric measurements were carried out over the range 10 Hz to 13 MHz using HP-4192A LF Impedance Analyzer through a calibrated Agilent 16451B dielectric test fixture. The temperature dependency of dielectric measurement was carried out with a self-designed programmable temperature controlled oven with a heating rate of 0.5°C min^{-1}. While heating, the dielectric data were taken within 4 or 5 degree interval and found to be

reproducible. Dielectric measurements were carried out using pure sinusoidal wave. The Impedance Analyzer was connected with a PC for data acquisition. Conductivity of the samples was calculated using capacitance and tan δ values measured at different frequencies. The detailed experimental procedures are explained in the Chapter 3.

7.3. Results and Discussions

7.3.1. Composition Dependency Dielectric Study

7.3.1.1. Effect of Sr on $Ba_{1-x}Sr_x(Ti_{0.5}Zr_{0.5})O_3$ Ceramics.

Fig. 7.1 shows the effect of Sr (x) on Microstructure of $Ba_{1-x}Sr_x(Ti_{0.5}Zr_{0.5})O_3$ ceramics. There is a decrease in average grain size with the increase in Sr (x) content. The average grain size of $Ba_{1-x}Sr_x(Ti_{0.5}Zr_{0.5})O_3$ ceramics are given in the Table 7.1. The decreasing grain size with increasing Sr content may be attributed to lower grain growth rates from the slower diffusion of Sr^{2+} ion, which is more stable than the Ba^{2+} ion. Crystallization may be initiated earlier with lower Sr contents, resulting in a larger grain size for the same heat treatment. $BaO\text{-}TiO_2$ phase diagram [30] has lowest liguidus temperature at $1{,}317^0C$, whereas $SrO\text{-}TiO_2$ phase diagram [31] shows $1{,}440^0C$, which is nearly 100^OC higher than the previous one. So Ba-rich compositions are easy to sinter, whereas the Sr-rich compositions still require higher temperature for comparable grain growth. One could expect, as Sr has lower ionic radius, that it can easily substitute Ba and hence will result in higher grain size. But it is not the case. As the Sr has higher melting point ($1{,}041\ ^OC$) than that of Ba ($1{,}002^OC$), it may be another reason for lower grain growth in the above-mentioned thermal treatment with increase in Sr concentration.

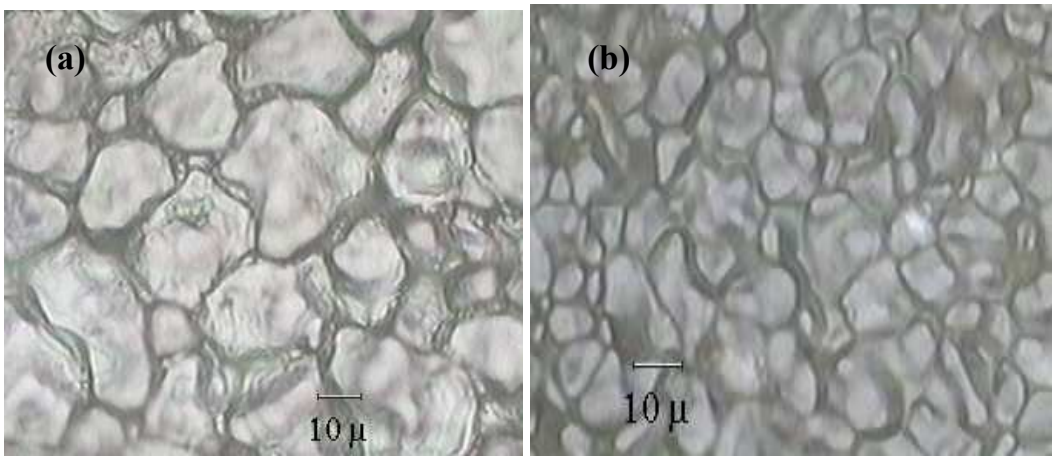

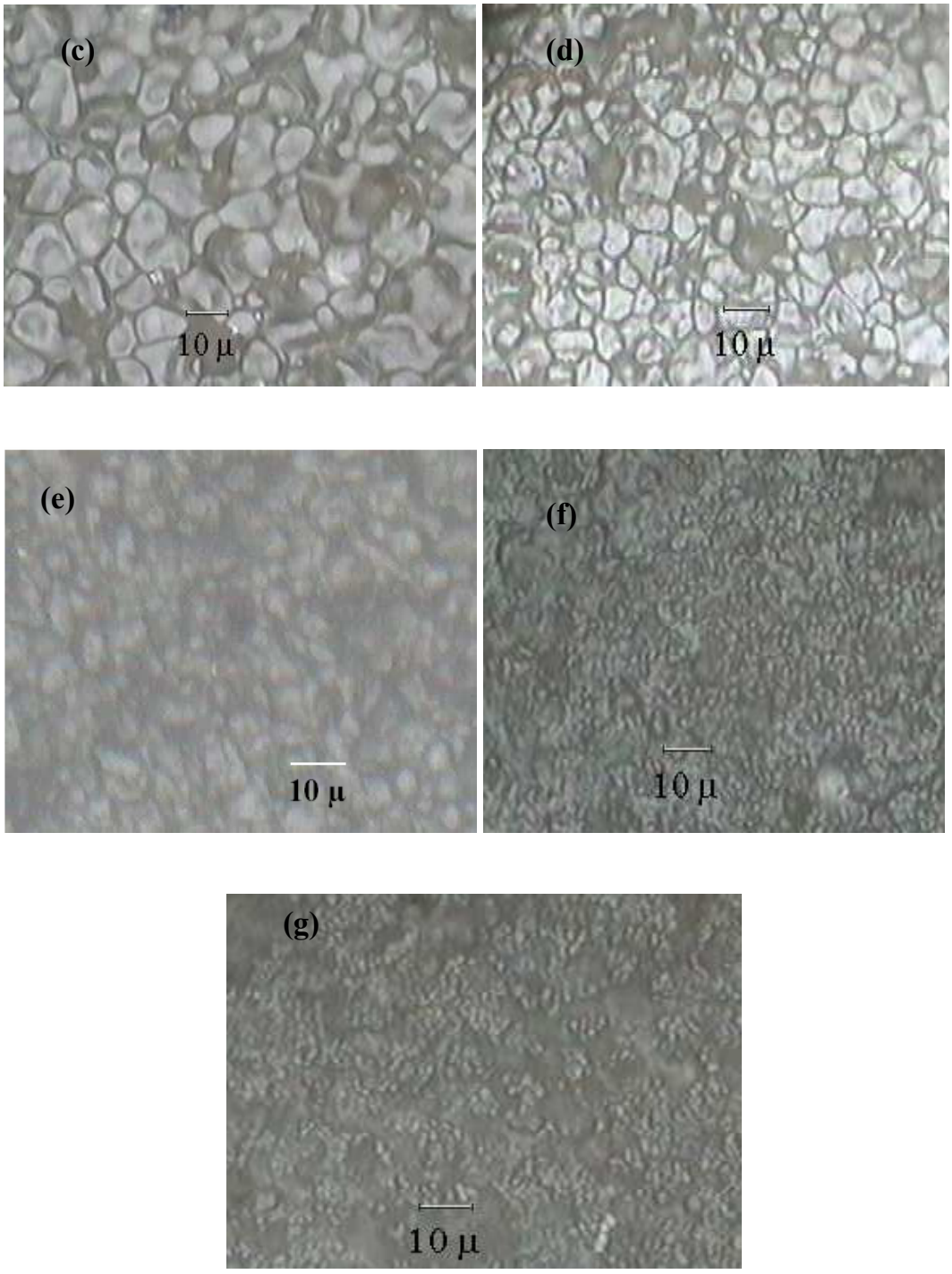

Figure 7.1 Microstructure of $Ba_{1-x}Sr_x(Ti_{0.5}Zr_{0.5})O_3$ ceramics, (a) x=0.0, (b) x=0.2, (c) x=0.4, (d) x=0.5, (e) x=0.6, (f) x=0.8 and (g) x=1.0.

Table 7.1 Variation of crystal symmetry, grain size, X-ray density, bulk density and percentage porosity with different Sr (x) concentration in the $(Ba_{1-X}Sr_X)\ Ti_{0.5}Zr_{0.5}O_3$.

Sr (x)	Symmetry	Grain size (μm)	X-ray Density (gm/cc)	Bulk Density (gm/cc)	Apparent Porosity (%)
0	cubic	17.5	6.14	5.75	2.0
0.2	cubic	11.7	5.99	5.65	2.5
0.4	cubic	10.2	5.81	5.35	3.1
0.5	cubic	7.3	5.72	5.20	3.4
0.6	Mixed Phase	5.4	5.66 5.64	4.92	4.2
0.8	Tetragonal	2.5	5.46	4.78	4.7
1.0	Tetragonal	2.2	5.38	4.44	7.2

Fig. 7. 2 shows the variation of bulk density and percentage true porosity with different Sr (x) concentration in $Ba_{1-x}Sr_x(Ti_{0.5}Zr_{0.5})O_3$. There is a systematic decrease in bulk density with increase in Sr content. This may be due to the substitution of lower density Sr (2.6 g/cc) than Ba (3.5 g/cc) in the system.

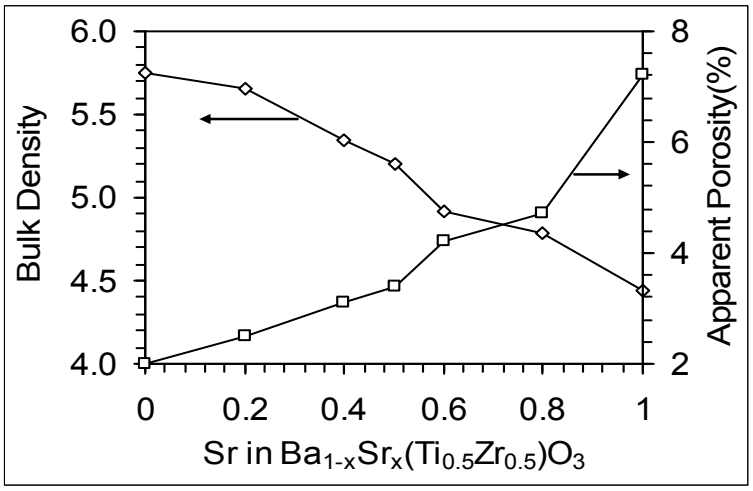

Figure 7.2 Effects of Sr (x) content on bulk density and true porosity of $Ba_{1-x}Sr_x$ $(Ti_{0.5}Zr_{0.5})\ O_3$ ceramics.

As the samples were having different porosity, to compare their room temperature electrical properties experimental data were corrected as per the following relation.

$$Actual(\varepsilon') = \frac{\text{Experimental}(\varepsilon')}{(1 - TruePorosity)} \tag{7.1}$$

Fig.7.3 shows the frequency dependency of dielectric constant of $Ba_{1-x}Sr_xTi_{0.5}Zr_{0.5}O_3$ compositions. The BSTZ composition with x=0.0, shows the highest dielectric constant. The dielectric constant decreases with Sr substitution, yielding the lowest dielectric constant in x=1.0 composition. The dielectric constants of all the compositions were very stable in the frequency range 1 kHz to about 7 MHz. In general, dielectric constant decreases with the increase in Sr substitution due to; (i) the decrease in concentration of high permittivity material BTZ, and (ii) due to the decrease in polarizability of the atoms in the structure. When a lower radius Sr replaces higher radius Ba in the structure, there is a decrease in lattice parameter, yielding the lowering of dipole moment in cubic perovskite. The permittivity of Sr-rich compositions could be increased from the present study by increasing their density and grain size in the sintered dielectrics, but it will not be more than that of its counterpart Ba-rich compositions.

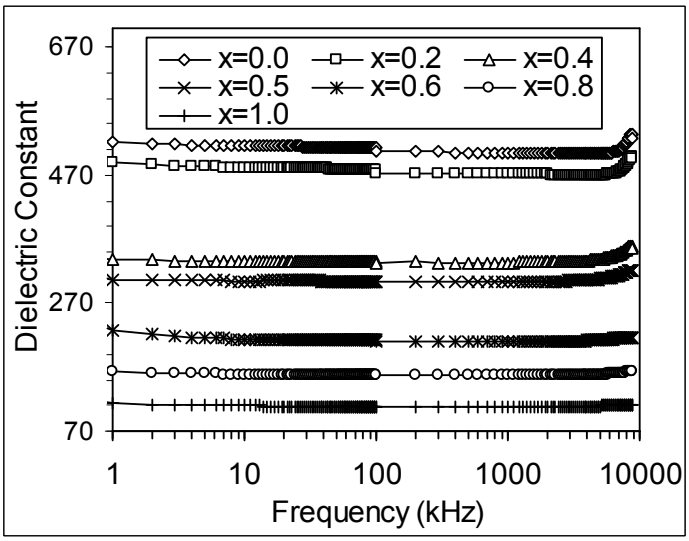

Figure 7. 3 Frequency dependency of dielectric constant of different $Ba_{1-x}Sr_x$ $(Ti_{0.5}Zr_{0.5})$ O_3 compositions.

Fig. 7. 4 shows the frequency dependency of the dielectric loss of the samples. In general, tan δ decreases with Sr-substitution. At very low frequency, high dielectric loss is observed due to presence of all type of polarization including space charge polarization. That also quickly decreases upto about 10 kHz due to the space charge polarization losses. The loss was found to decrease nominally with the increase in Sr substitution. This may be primarily attributed to the decrease in dielectric constant with

Sr substitution. In general high permittivity materials possess higher losses. Other reason may be the effect of increased Sr-content. It is known that Q-factor of BST ceramics increases with the increase in Sr-content [32]. The loss is stable as well as fairly low (<0.6%) for all the compositions in the frequency range 100 KHz to about 5 MHz. Below 100 kHz, the loss was progressively higher with the decrease in frequency, mainly due to the space charge polarization phenomena. The dispersion of loss at higher frequency (≥5 MHz) is due to some extrinsic loss phenomena [33]. At high frequency, a dielectric loss peak is observed. Several possible causes exist for such dispersion including the hypothesis of the influence of the contact resistance between the probe and electrode, presence of barrier layer between the insulating materials and the electrode surface, resonance due to high dielectric constant or leaky grain boundary. Similar frequency dispersion behavior was also reported for other ferroelectric materials prepared by other techniques also [34, 35,]. This is to note that the frequency dependency of permittivity shows almost stable behavior and dielectric losses are very low for all compositions in bulk ceramics in the frequency range 100 kHz to 5 MHz. The materials are suitable for low loss application in the said frequency range.

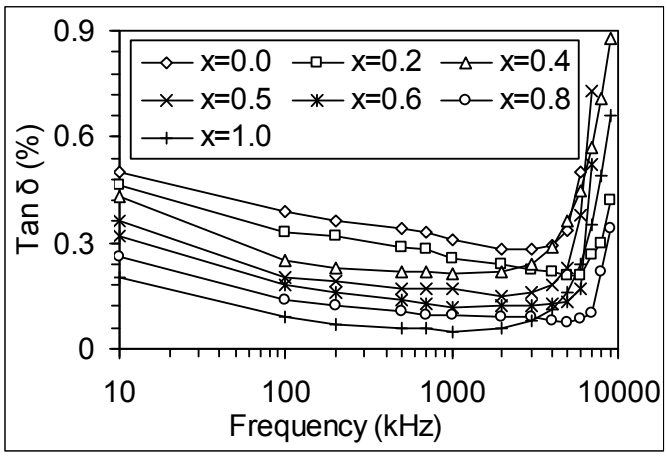

Figure 7. 4 Frequency dependency of dielectric loss of different $Ba_{1-x}Sr_x (Ti_{0.5}Zr_{0.5}) O_3$ compositions.

For thorough analysis of the electrical properties, conductivity (σ) of the samples were calculated using the formula

$$\sigma = 2\pi f d\, C \tan \delta / A. \qquad (7.2)$$

where; f is the operating frequency, d is the thickness of the dielectrics, tan δ is the dielectric loss, C is the capacitance and A is the area of the electrode.

The variation of ac conductivity with Sr content in the composition system is plotted in the Fig. 7.5. The conductivity was found to decrease with increase in Sr

concentration as well as increase in frequency. The decrease in conductivity may be primarily due to the decrease in tan δ loss with Sr substitution as stated earlier. Also, that decrease may be partly due to the decrease in grain size and hence increase in grain boundary areas/resistance with Sr substitution. Grain boundary areas are highly resistive in oxide ceramics. Smaller grain sized ceramics have larger grain boundary areas, i.e., in case of smaller grain, no of grain boundary per unit thickness is more than that of bigger grain size and hence smaller grained ceramics have higher resistivity than bigger grain sized ceramics (Fig 7.1). As suggested by R K Astala [36], impurities and defects are considered to have largest effect in ST ceramics. i.e., higher the defect higher will be the conductivity. Here, as Sr addition reduces the defect in the ceramic, that may be another reason for decrease in conductivity with substitution.

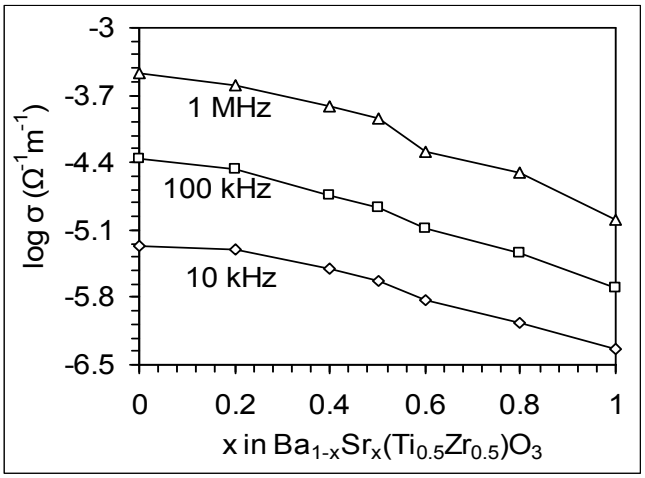

Figure 7. 5 Variation of AC conductivity with Sr (x) content in $Ba_{1-x}Sr_x$ $(Ti_{0.5}Zr_{0.5})O_3$ ceramics.

7.3.1.2. Effect of Zr on $(Ba_{0.5}Sr_{0.5})$ $Ti_{1-x}Zr_xO_3$ Ceramics

Fig.7.6 shows the effect of Zr (x) on microstructure of $(Ba_{0.5}Sr_{0.5})Ti_{1-x}Zr_xO_{3-}$ ceramics. There is a decrease in average grain size with the increase in Zr (x) content. The decreasing grain size with increasing Zr content may be attributed to lower grain growth rates from the more slow diffusion of Zr^{4+} ion, which has a bigger ionic radius than Ti^{4+}. Crystallization may be initiated earlier with lower Zr contents, resulting in a larger grain size for the same heat treatment. The decrease in grain size in Zr may also imply that the existence of Zr in BTZ ceramic makes the initiation of crystallization harder to occur.

From the Table 7.2, the x-ray density of the compositions is found to increase with Zr content, which may be due to the higher density of Zr (5.85g/cc) than that of Ti (4.5g/cc). But the experimental bulk density is found to decrease with Zr content. The reason may be due to increase of more stable and bigger Zr^{4+} ion than Ti^{4+}, which reduces the initiation of grain growth (Fig. 7.6) at the experimental sintering temperature as well as density. As there is a large difference between their melting temperatures, a large difference in grain size is observed. Again, due to this high melting temperature difference, a large difference in density and porosity between the two end compositions of the series is also observed.

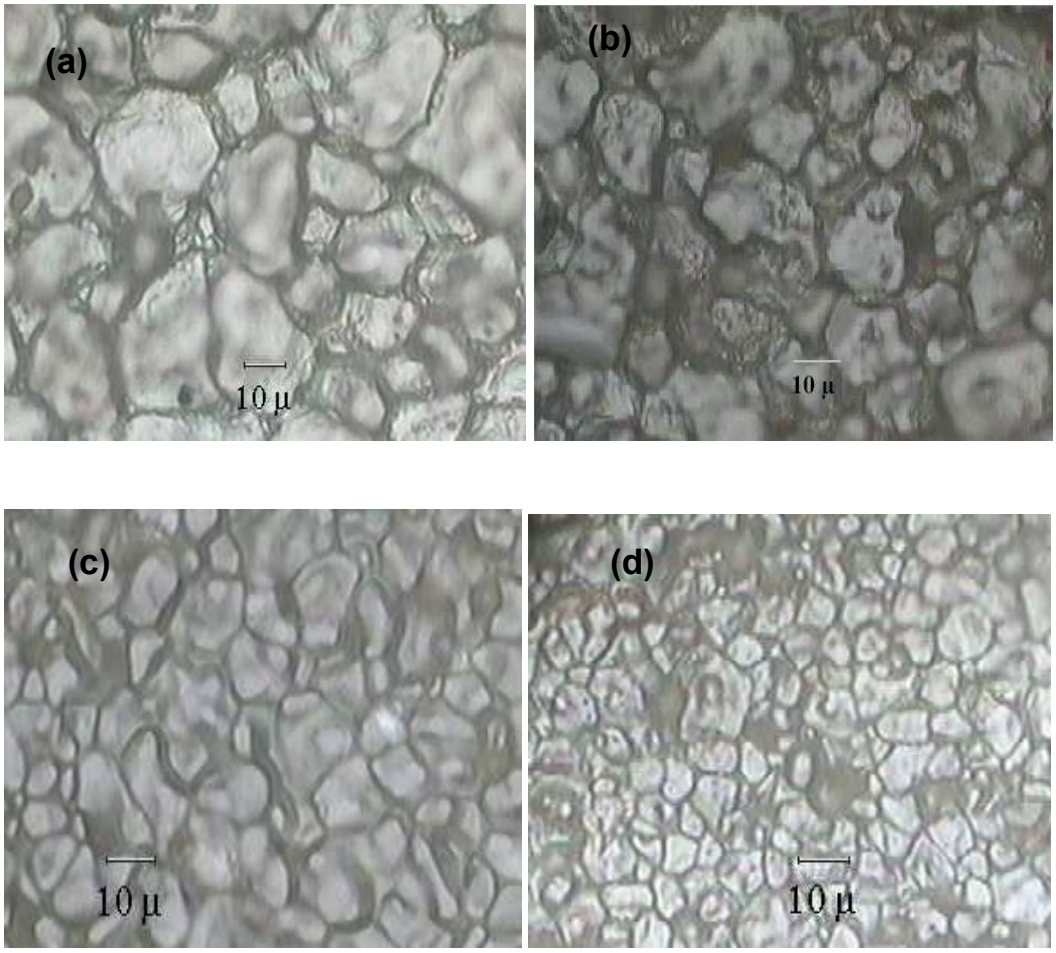

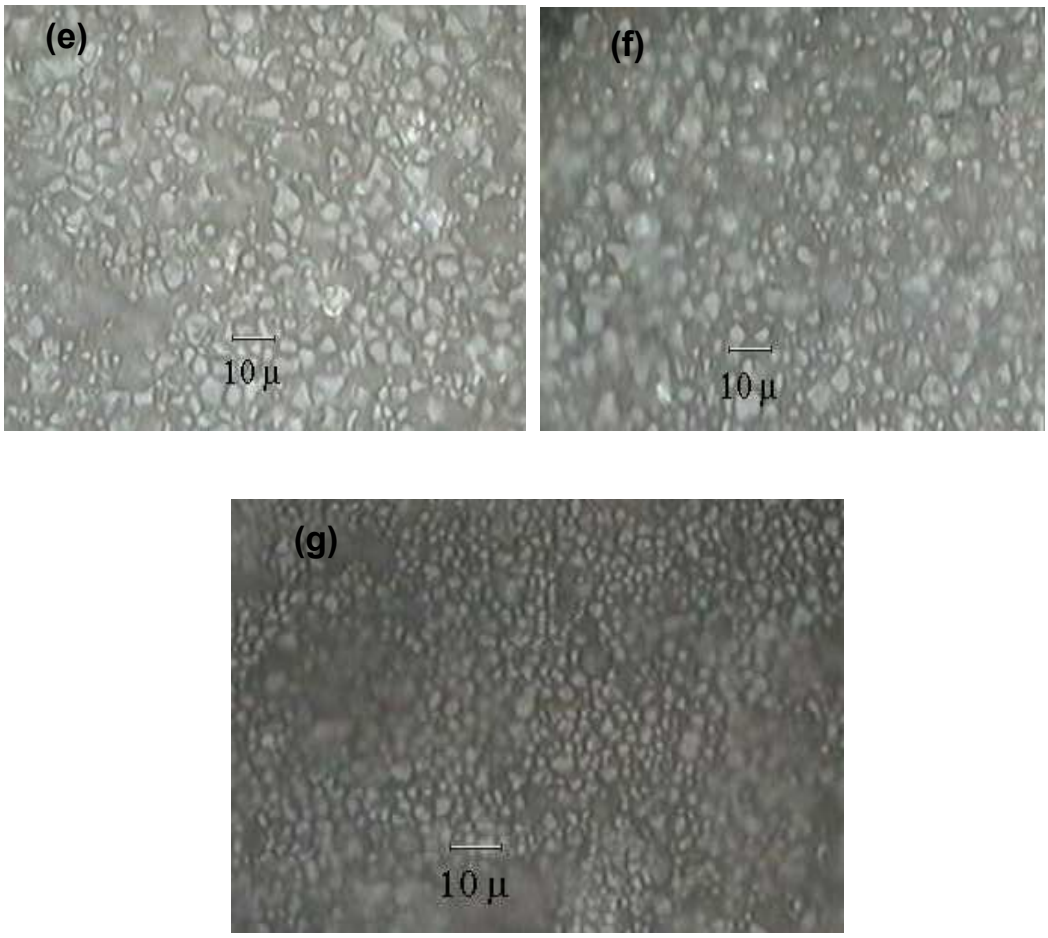

Figure 7.6. Microstructure of $(Ba_{0.5}Sr_{0.5})Ti_{1-x}Zr_xO_3$ ceramics, (a) x=0.0, (b) x=0.2, (c) x=0.4, (d) x=0.5, (e) x=0.6, (f) x=0.8 and (g) x=1.0.

Table 7.2: Variation of crystal symmetry, Grain size, x ray density, bulk density, apparent porosity and true porosity with different Zr (x) concentration in the $(Ba_{0.5}Sr_{0.5})Ti_{1-x}Zr_xO_3$.

Zr (x)	Symmetry	Grain size (μm)	X-ray Density (gm/cc)	Bulk Density (gm/cc)	Apparent Porosity (%)
0	cubic	21.1	5.596	5.35	2.0
0.2	cubic	19.8	5.6107	5.41	1.0
0.4	cubic	11.6	5.6471	5.21	3.8
0.5	cubic	7.3	5.7194	4.81	9.8
0.6	cubic	5.1	5.7199	4.76	9.9
0.8	Cubic (*pm3m*) + Tetragonal *(I4/mcm)*	4.8	5.8128 5.7332	4.6	14.0
1.0	Orthorhombic (*Imma)*	2.5	5.8122	4.75	11.1

Fig. 7.7 shows the variation of bulk density and true porosity with Zr (x) content in $(Ba_{0.5}Sr_{0.5})(Ti1_{-x}Zr_x)O_3$. There is an average decrease in bulk density with increase in Zr content. But the composition with x=0.2 shows the highest density and lowest porosity in the system. This may be due to the presence of lowest eutectic composition of the system around that composition. There is a decrease in density from x≥0.5 composition due to the presence of progressively higher amount of Zr in the system.

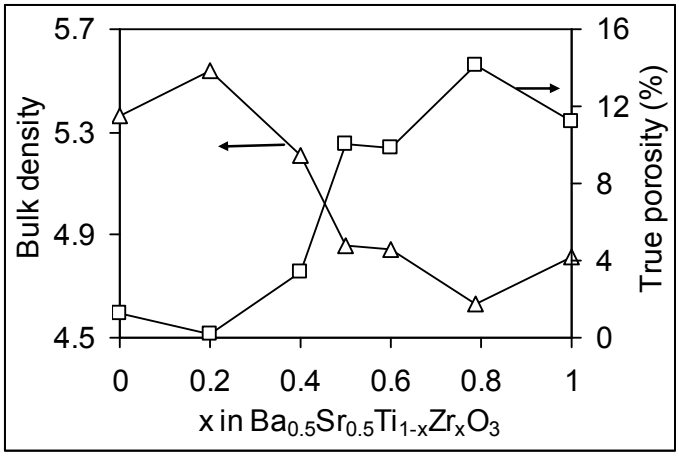

Figure 7.7 Bulk density and true porosity of the $(Ba_{0.5}Sr_{0.5})Ti_{1-x}Zr_xO_3$ samples with different concentration of Zr(x).

The change in permittivity with frequency of $(Ba_{0.5}Sr_{0.5})(Ti_{1-x}Zr_x)O_3$ is plotted in the Fig. 7.8 after considering the above correction (as per Equation 7.1) for different compositions. The permittivity (ε) decreases with the increase in Zr substitution due to the (i) decrease in concentration of high permittivity BST material and (ii) due to the decrease in polarizability of the atoms in the structure. For all the compositions, dielectric constant decreases nominally upto about 10-50 kHz. This is mainly due to the decrease in the space charge polarization contribution. Permittivities are stable in the frequency range 100 kHz to about 3 MHz for compositions upto x=0.4 and stable beyond 10 MHz for compositions with 'x' from 0.5 to 1.0. So it may be concluded that the materials with high Zr content are suitable for high frequency application compared to BST. At low frequency a high value of dielectric constant is observed and that decreases with increase in frequency. As a guide to the forthcoming discussion, let us remember the simple Debye formula giving the complex permittivity related to free dipoles oscillating in an alternating field given as

$$\varepsilon^* = \varepsilon' - j\varepsilon'' = \varepsilon_\infty + \frac{(\varepsilon_s - \varepsilon_\infty)}{1 + j\omega\tau} \tag{7.3}$$

The dielectric constant (real part of ε*) is given by

$$\varepsilon' = \varepsilon_\infty + \frac{(\varepsilon_s - \varepsilon_\infty)}{1 + (\omega\tau)^2} \tag{7.4}$$

where τ is the characteristic relaxation time of the process. At very low frequencies *($\omega << 1/\tau$),* dipoles follow the field and we have $\varepsilon' \approx \varepsilon_s$ (value of dielectric constant at quasistatic field). As the frequency increases *($\omega < 1/\tau$),* dipoles begin to "lag" behind the field and ε' slightly decreases. When frequency reaches characteristic frequencies *($\omega = 1/\tau$),* dielectric constant drops (relaxation process). At very high frequencies *($\omega >> 1/\tau$),* dipoles can no longer follow the field and $\varepsilon' \approx \varepsilon_\infty$.

Fig. 7.9 shows the frequency dependency of the dielectric loss in the material. The high losses at lower frequency range are due to space charge polarization losses. This can also be explained in consequence of excitation of localized, hardly reorientable polarizations and conduction mechanism [37]. It is observed that the compositions with x=0.0 to 0.4 show low loss in the range ~100 kHz to 6-7 MHz, which may be primarily due to their higher density. However, the compositions with x=0.5 to 1.0 have low losses in the higher frequency range ~3 MHz to 13 MHz.

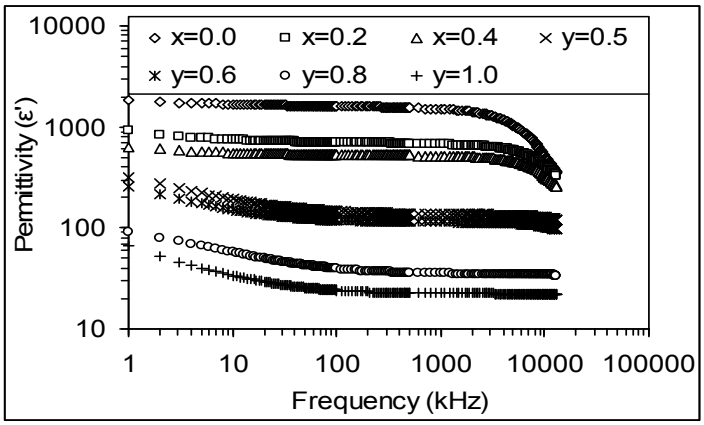

Figure 7.8 Frequency dependency of permittivity for $(Ba_{0.5}Sr_{0.5})(Ti_{1-x}Zr_x)O_3$ with different x-values.

That is high-frequency loss decreases with Zr substitution. It is interesting to note that a dispersion of loss occurs around 7 to 10 MHz range and that dispersion seems to decrease with the increase in Zr content. Several possible causes exist for such dispersion at high frequencies including the hypothesis of the influence of the contact resistance between the probe and electrode, presence of barrier layer between the insulating materials and the electrode surface, resonance due to high dielectric constant or leaky grain boundary. Similar frequency dispersion behavior was also reported for

other ferroelectric materials prepared by other techniques also [34, 35,]. One source may be the extrinsic resonance behavior [35]. Decrease in dispersion with Zr substitution may be considered to be due to the decrease in defects (vacancy, mobile ions or leaky grain boundary [33], etc.). The dispersion in the compositions with x=0.0, 0.2 and 0.4 is higher than for the others. These three samples also show (Fig. 7.8) decrease in permittivity after 3-5 MHz frequency. That may be due to the inability of some of the polarization processes to respond to the faster polarity reversals of the field, such that the net contribution of polarization to the dielectric constant is reduced and the loss is increased. These effects are more prominent in the formulations having large ionic polarization. The a.c conductivity of the compositions at different frequencies was calculated by using Equation 7.2. The variation of conductivity of $(Ba_{0.5}Sr_{0.5})$ $(Ti_{1-x}Zr_x)O_3$ compositions with Zr content is plotted in the Fig. 7.10.

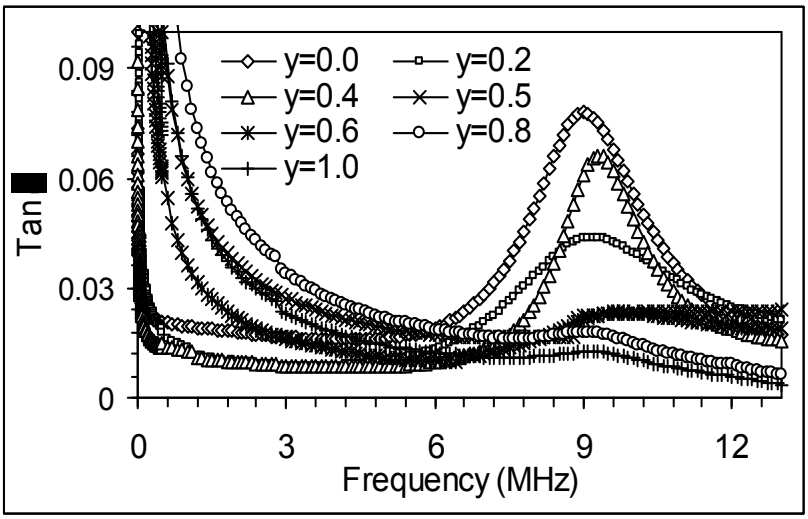

Figure 7.9 Frequency dependency of dielectric loss (tan δ) for different $(Ba_{0.5}Sr_{0.5})$ $(Ti_{1-x}Zr_x)O_3$ compositions.

It shows that the conductivity of BST decreases rapidly with Zr substitution for Ti. It has been established [38] that introduction of Zr^{+4} ions in $BaTiO_3$ lattice occurs in three steps; firstly filling Ba^{+2} vacancies, secondly solid solution formation in between BT and BZ, and thirdly occupying interstitial site in BT lattice. So minimum conductivity of composition with x=0.2, may be due to the filling of Ba^{+2} vacancies by the Zr^{+4} ions and associated reduction in Ba^{+2} induced conductivity. The end composition BSZ has lower conductivity than other end member BST, which may be due to the presence of more stable Zr^{+4} ions in BSZ than Ti^{+4} ions in BST. The conductivity of BST is highest due to both the A-site vacancy as well as the conductivity by electron hopping between Ti^{+4} and Ti^{+3} [23].

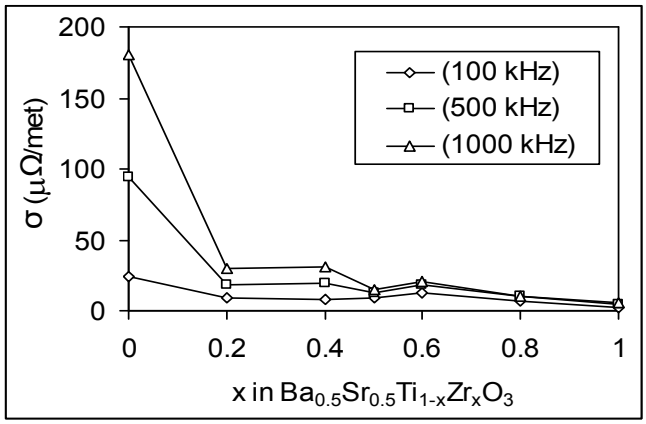

Figure 7.10 The dielectric conductivity of different $(Ba_{0.5}Sr_{0.5})(Ti_{1-x}Zr_x)O_3$ compositions.

7.3.1.3. Effect of Ca on $(Ba_{1-x}Ca_x)Ti_{0.6}Zr_{0.4}O_3$ Ceramics

Fig. 7.11 shows the microstructure of $Ba_{1-x}Ca_xTi_{0.6}Zr_{0.4}O_3$ ceramics. There is a decrease in average grain size with the increase in Ca (x) content.

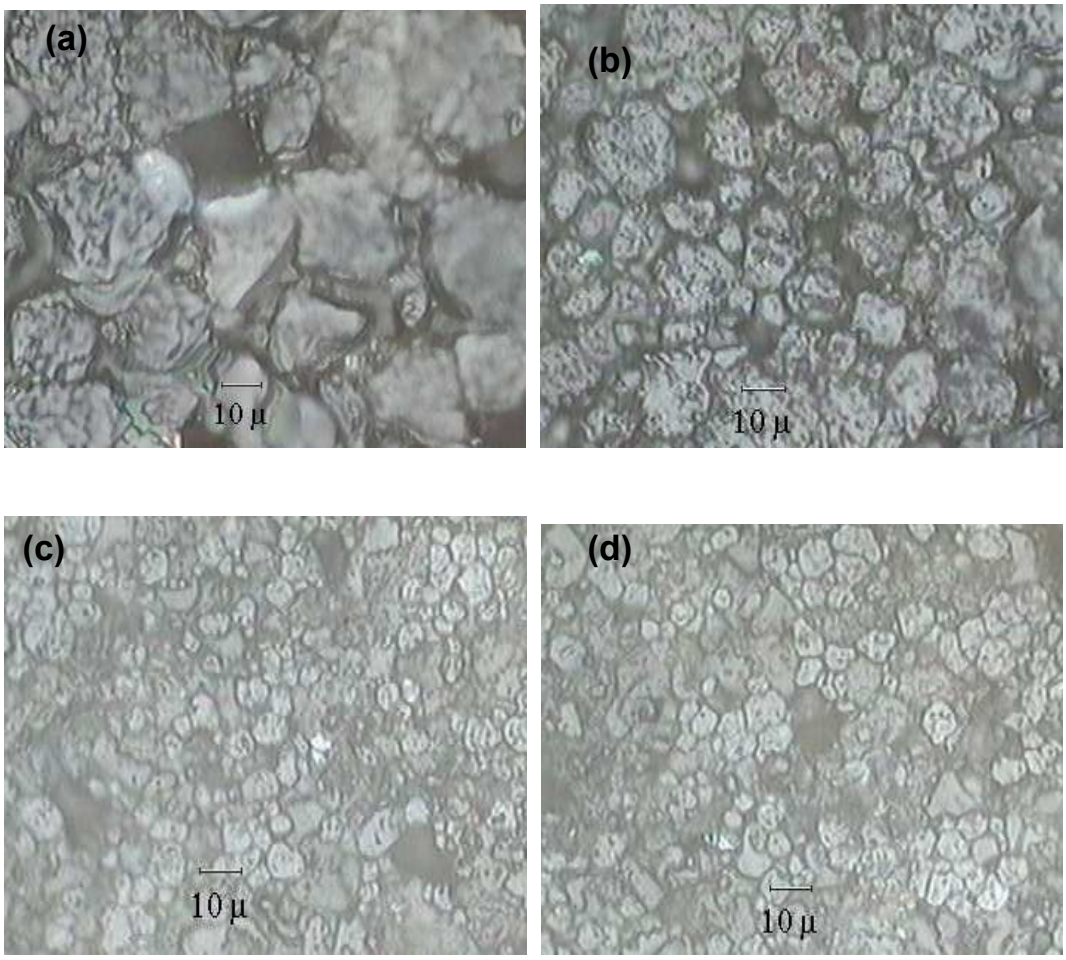

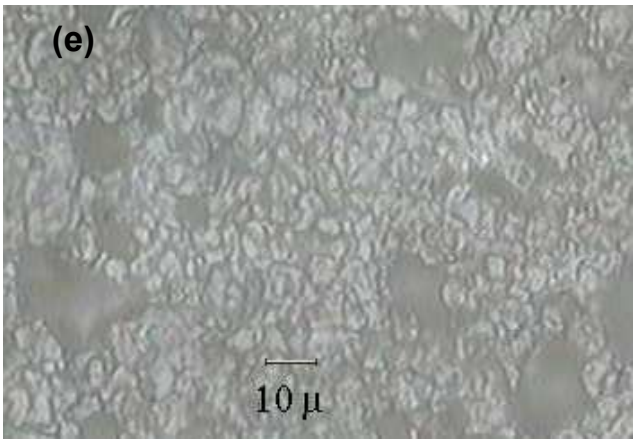

Figure 7.11 Microstructure of $Ba_{1-x}Ca_xTi_{0.6}Zr_{0.4}O_3$ ceramics, (a) x=0.0, (b) x=0.1, (c) x=0.2, (d) x=0.4, (e) x=0.5,

Table 7.3: Variation of crystal symmetry, grain size, x ray density, bulk density, apparent porosity and true porosity with different Ca (x) concentration in the $Ba_{1-x}Ca_xTi_{0.6}Zr_{0.4}O_3$.

Ca (x)	Symmetry	Grain size (µm)	X-ray Density (gm/cc)	Bulk Density (gm/cc)	Apparent Porosity (%)
0	cubic	22.2	6.0695	5.0036	5.86
0.1	Tetragonal	15.2	5.8322	4.92	3.0
0.2	Mixed Phase	9.2	----	5.14	2.7
0.4	Mixed Phase	8.7	----	4.55	8.8
0.5	Mixed Phase	4.5	----	4.47	10.6

Fig. 7.12 shows the variation of bulk density and percentage true porosity with Ca content in $Ba_{1-x}Ca_xTi_{0.6}Zr_{0.4}O_3$. There is an average increase in bulk density and decrease in porosity with increase in Ca content.

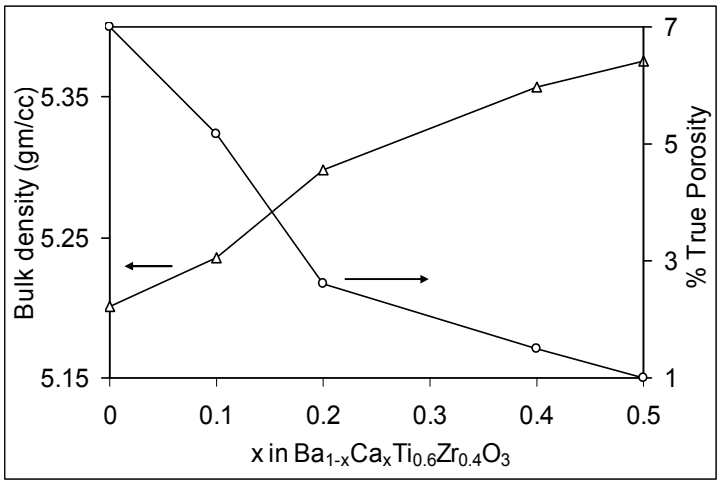

Figure 7.12 The variation of bulk density and percentage true porosity with Ca(x) concentration in $Ba_{1-x}Ca_xTi_{0.6}Zr_{0.4}O_3$.

Fig. 7.13 shows the frequency dependency of the permittivity of $Ba_{1-x}Ca_xTi_{0.6}Zr_{0.4}O_3$ compositions. As the samples were having different porosities their experimental permittivity were normalized with respect to porosity by multiplying with {1/(1-True porosity)} and are presented in the Fig. 7.13.

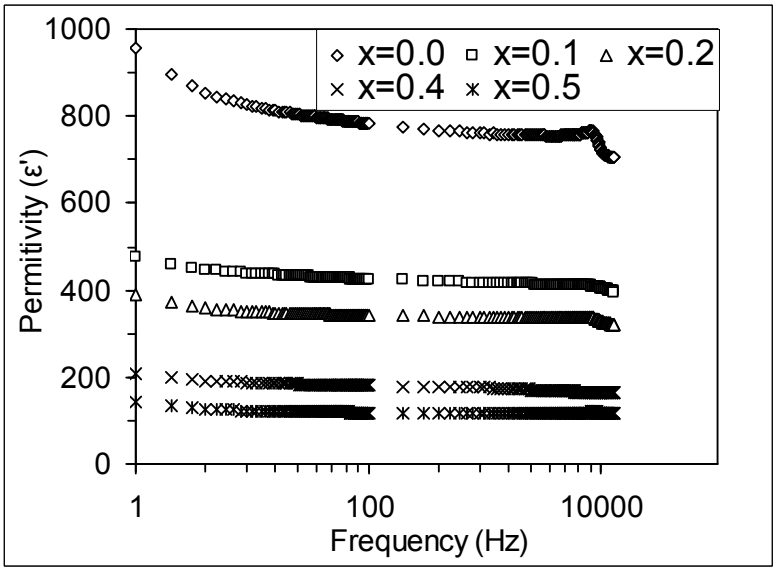

Figure 7.13 Frequency dependency of permittivity of $Ba_{1-x}Ca_xTi_{0.6}Zr_{0.4}O_3$ compositions

Permittivity (ε) decreases with the increase in Ca substitution due to (i) when Ba is substituted by Ca, the dipole moment decreases, as the atomic radius of Ca is too small in comparison to Ba, (ii) decrease in concentration of high permittivity material BTZ and (iii) due to the decrease in grain size leading to the decrease in polarizability of the atoms in the structure. When lower radii Ca replaces Ba in the structure, there is

decrease in lattice parameter leading to lowering in dipole moment causing a decrease in permittivity.

Fig. 7.14 shows the frequency dependency of the dielectric loss of the samples. At middle frequency range, all the samples show a dielectric loss within two percent, which indicates the good quality of the samples. In general, tan δ decreases with Ca-substitution. At very low frequency, high dielectric loss is observed due to presence of all types of polarization including space charge polarization. That also quickly decreases up to about 10 kHz due to the space charge polarization losses. This high loss can be explained on the basis of Maxwell –Wagner polarisation mechanism as was done by D. O'Neill *et al*. [37]. At high frequency, a dielectric loss peak is observed. As mentioned earlier, several possible causes exist for such dispersion including the hypothesis of the influence of the contact resistance between the probe and electrode, and resonance due to high dielectric constant. Similar frequency dispersion behavior was also reported for other ferroelectric materials [34, 35]. This behavior is verified by changing the electrod area.

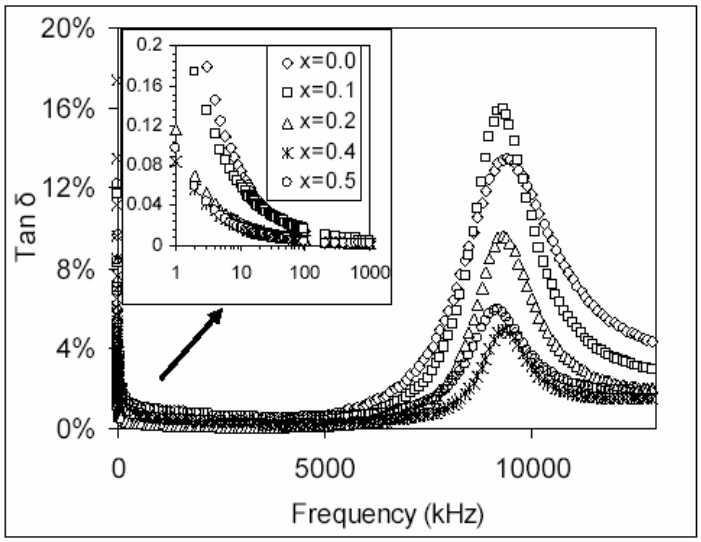

Figure 7.14 Frequency dependency of dielectric loss of $(Ba_{1-x}Ca_x)$ $Ti_{0.6}Zr_{0.4}O_3$ compositions. The low frequency region is shown as an inset in log frequency scale.

The a.c conductivity of the different compositions at three different frequencies is calculated using the relation 7.2. The variation of conductivity with Ca content in the ceramic is plotted in the Fig. 7.15. The decrease in conductivity may be primarily due to the decrease in tan δ loss with Ca substitution, as stated earlier.

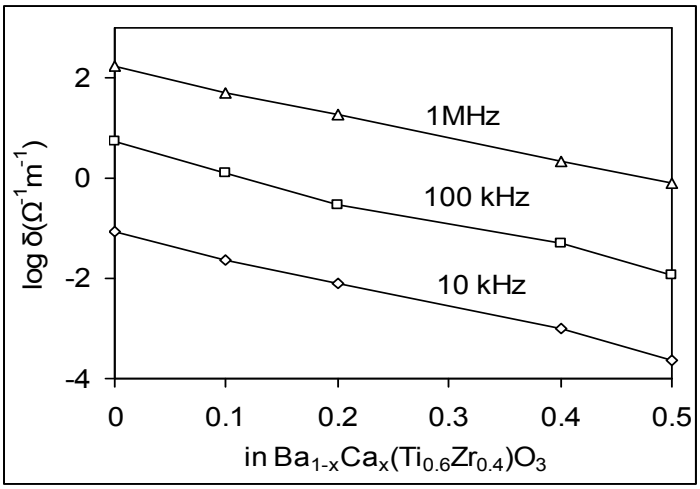

Figure 7.15. Conductivity of the $Ba_{1-x}Ca_xTi_{0.6}Zr_{0.4}O_3$ samples with different concentration of Ca(x).

Also that decrease may be partly due to the decrease in grain size and hence increase in grain boundary areas/resistance with Ca substitution. Grain boundary areas are highly resistive in oxide ceramics. Smaller grain sized ceramics have larger grain boundary areas, i.e., in case of smaller grain, no. of grain boundary per unit thickness is more than that of bigger grain size and hence smaller-grained ceramics have higher resistivity than bigger grain sized ceramics. As suggested by R K Astala [36], impurities and defects are considered to have largest effect in ST ceramics, i.e., higher the defect higher will be the conductivity. Here, as Ca addition reduces the defect in the ceramic, that may be another reason of decrease in conductivity with substitution.

7.3.1.4. Effect of Mg on $(Ba_{1-x}Mg_x)Ti_{0.6}Zr_{0.4}O_3$ Ceramics

Fig. 7.16 shows the microstructure of $Ba_{1-x}Mg_xTi_{0.6}Zr_{0.4}O_3$ ceramics. There is a decrease in average grain size with the increase in Mg (x) content. The Table 7.4 shows that there is a decrease in apparent porosity. This may be due to the decrease in melting temperature of the oxides with increase in Mg content. The binary phase diagram [39] containing MgO and BaO or SrO or BaO shows that there is systematic decrease in melting temperature with increase in Mg content up to 40 mol%. Again, the same type of behavior in the phase diagram [40.41] containing MgO with TiO_2 or ZrO_2 is also observed. Here, in the similar way, the decrease in porosity may be interpreted.

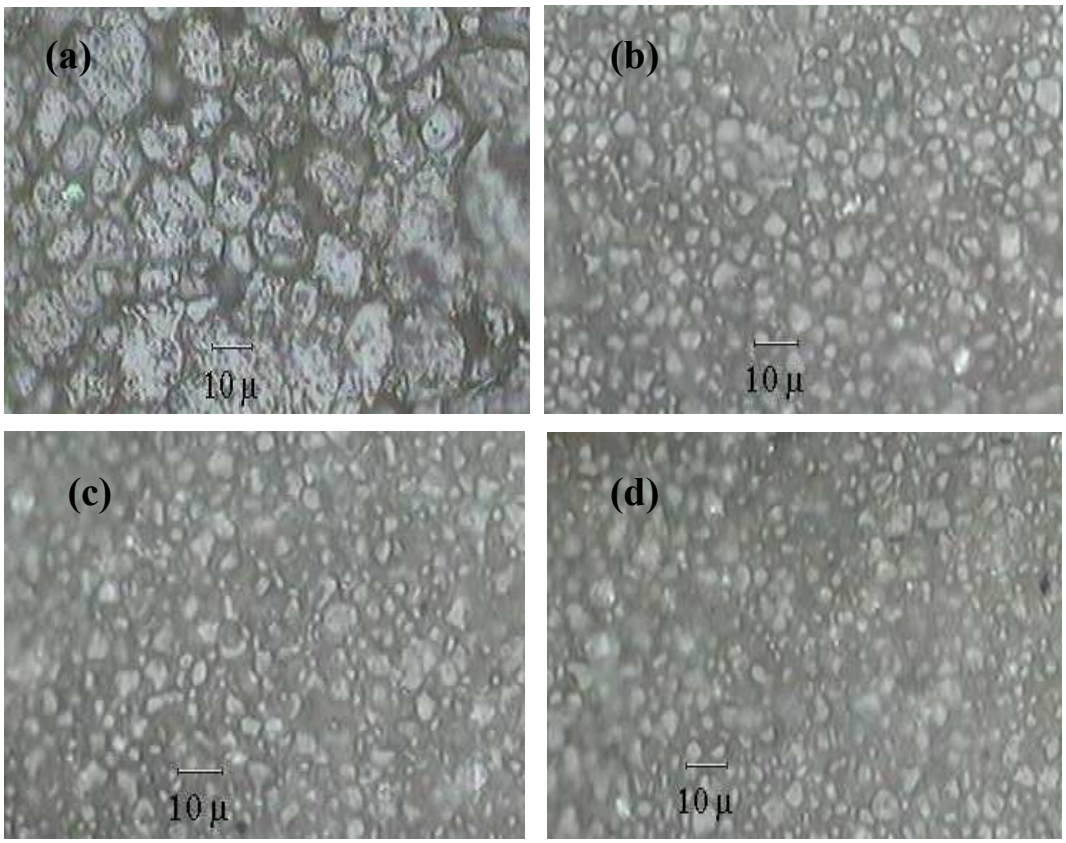

Figure 7.16 Microstructure of $Ba_{1-x}Mg_xTi_{0.6}Zr_{0.4}O_3$ ceramics, (a) x=0.0,(b) x=0.03,(c) x=0.07,(d) x=0.14.

Table 7.4: Variation of crystal symmetry, Grain size, x ray density, bulk density, apparent porosity and true porosity with different Mg (x) concentration in the $Ba_{1-x}Mg_xTi_{0.6}Zr_{0.4}O_3$.

Mg (x)	Symmetry	Grain size (µm)	X-ray Density (g/cc)	Bulk Density (g/cc)	Apparent Porosity (%)
0	cubic	22.2	6.0695	5.0036	5.86
0.03	cubic	3.9	5.9721	5.673	1.8
0.07	cubic	3.6	5.8717	5.573	1.5
0.14	cubic	3.1	5.6687	5.716	1.1

Fig. 7.17 shows the frequency dependency of the permittivity of $Ba_{1-x}Mg_xTi_{0.6}Zr_{0.4}O_3$ compositions. The composition with x=0.0, shows the highest dielectric constant. The dielectric constant decreases with Mg substitution. The dielectric constant of all the compositions was very stable in the frequency range 1 kHz to about 6 MHz. In general

dielectric constant decreases with the increase in Mg substitution due to; (i) the decrease in concentration of high permittivity material BTZ, and (ii) due to the decrease in polarizability of the atoms in the structure. When a lower-radii Mg replaces higher-radii Ba in the structure, there is a decrease in lattice parameter, yielding the lowering of dipole moment in cubic perovskite.

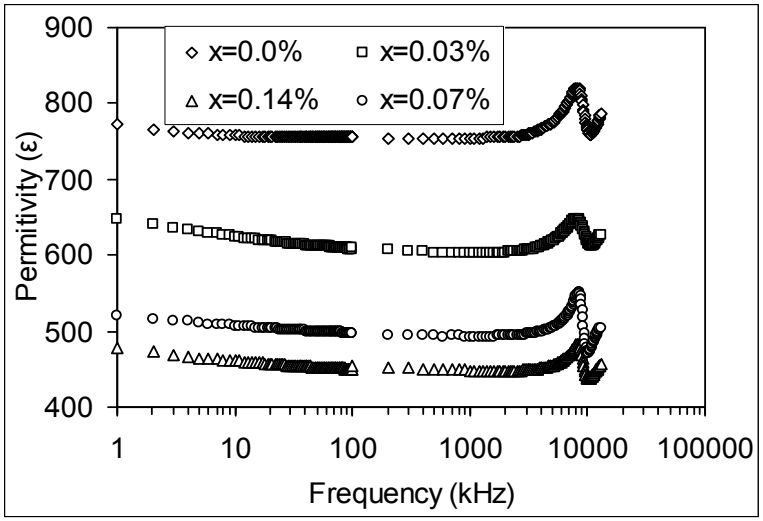

Figure 7.17. Frequency dependency of permittivity of $Ba_{1-x}Mg_xTi_{0.6}Zr_{0.4}O_3$ compositions

Fig. 7.18 shows the frequency dependency of the dielectric loss of the samples. In general tan δ decreases with Mg-substitution. At very low frequency, high dielectric loss is observed due to presence of all type of polarization including space charge polarization. That also quickly decreases up to about 10 kHz due to the space charge polarization losses. The loss was found to decrease nominally with the increase in Mg substitution.

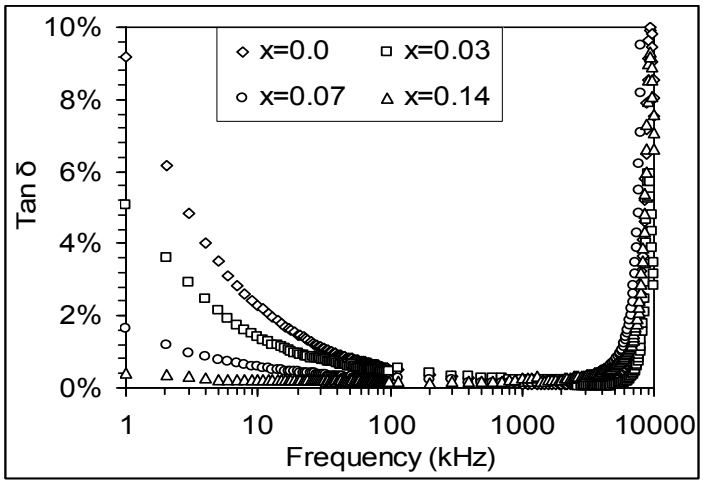

Figure 7.18. Frequency dependency of dielectric loss of $(Ba_{1-x}Mg_x)Ti0_{.6}Zr_{0.4}O_3$ compositions

At high frequency, a dielectric loss peak is observed. Several possible causes exist for such dispersion including the hypothesis of the influence of the contact resistance between the probe and electrode, presence of barrier layer between the insulating materials and the electrode surface, and resonance due to high dielectric constant or leaky grain boundary. Similar frequency dispersion behavior was also reported for other ferroelectric materials prepared by other techniques also [34, 35,]. This is to note that the frequency dependency of permittivity shows almost stable behavior and dielectric losses are very low for all compositions in bulk ceramics in the frequency range 100 kHz to 6 MHz. The materials are suitable for low loss application in the said frequency range.

7.3.2. Temperature Dependency Dielectric Study

7.3.2.1. The Composition $BaTi_{0.6}Zr_{0.4}O_3$

Fig. 7.19 and Fig. 7.20 show the temperature dependency of the dielectric constant and dielectric loss of bulk ceramics at different frequency respectively. The Fig. 7.19 shows, that the value of ε increases gradually to a maximum value (ε_m) with increase in temperature up to the transition temperature and then decreases smoothly, indicating a phase transition. The maximum of dielectric permittivity, ε_m and the corresponding temperature maximum T_m, depend upon the measurement frequency.

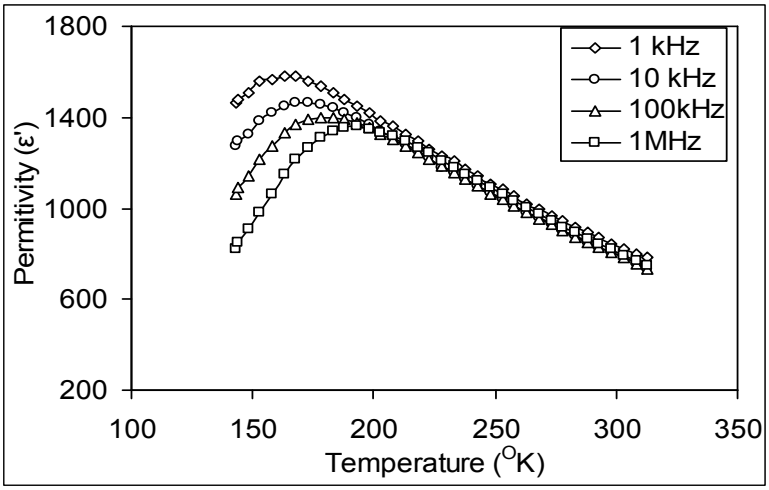

Figure 7.19. Temperature dependency of ε' for $BaTi_{0.6}Zr_{0.4}O_3$ at various frequencies

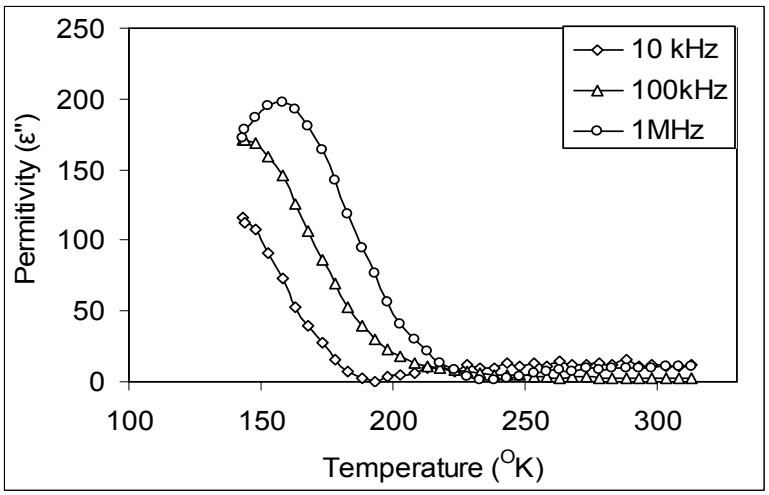

Figure 7.20. Temperature dependency of ε'' for $BaTi_{0.6}Zr_{0.4}O_3$ at various frequencies

The magnitude of dielectric constant decreases with increase in frequency and the maximum is shifting to higher temperature. As shown in Fig. 7.20, the dielectric loss values of the ferroelectric phase were reduced substantially at room temperature in the paraelectric phase (above T_m). The imaginary part of the spectrum (Fig. 7.20) shows that there is an increase in dielectric loss peak temperature with increase in frequency. This indicates that the dielectric polarization is of relaxation type in nature such as dipolar glasses. In analogy with spin glasses, such a behavior of the dynamic susceptibility in disordered ferroelectric is supposed to be concerned with the existence of the broad spectrum of relaxation times. It is generally considered that the Debye model is based on the assumption of a single relaxation time. The model fails because of the existence of a distribution of relaxation times. Such a distribution of relaxation time implies that the local environment seen by individual dipoles differs from site to site. This is a reasonable assumption in amorphous materials. As a rule [42], this relaxation occurs in disorder ionic structures, particular, in solid solutions. Within the Curie range of temperature, dielectric permittivity achieves very high value and displays very large dispersion, which is reminiscent of that found for orientational glasses [43]. Qualitatively, the strongly-broadened dielectric peak indicates that the phase transition is of a diffuse type near the transition temperature (T_m), which is caused by the inhomogeneous distribution of the Zr ion on Ti site and mechanical stress in the grain [44]. The observed lower temperature (below T_m) frequency dispersion may also have some contribution from the space charge effect. An increase in the value of ε" at lower frequency region may be due to the increase in ionic conductivity resulting from the disordering of mobile cations in the oxygen octahedral skeleton [45].

7.3.2.1. a. Diffuse Phase Transition Behaviors

A diffuse phase transition (DFT) is generally characterized by broadening in dielectric constant versus temperature curve. i.e the transition temperature is nor sharply defined. This DFT is not only observed in relaxors but may be realized in normal dielectrics under certain special circumstances.

A relatively large separation (in temperature) between the maximum of the real (dielectric constant) and imaginary (dielectric loss) part of the dielectric spectrum, a deviation from Curie-Weiss law in the vicinity of T_m, and frequency dispersion of both ε' and $\tan\delta$ (dielectric loss) in transition region implies a frequency dependency of T_m. It is known that the dielectric permittivity of a normal ferroelectric above the Curie temperature follows the Curie-Weiss law described by

$$\varepsilon' = C \big/ (T - T_0), \ (T > T_C) \tag{7.3}$$

where T_0 is the Curie-Weiss temperature and C is the Curie-Weiss constant. Fig. 7.21 shows the plot of inverse dielectric constant versus temperature at different frequency. A deviation from Curie Weiss law can be seen in all representative frequency. The parameters obtained from the fitting are listed in the Table 7.5. The parameter ΔT_m, which describes the degree of the deviation from the Curie Weiss law, is defined as

$$\Delta T_m = T_{cw} - T_m, \tag{7.4}$$

Where T_{cw} denotes the temperature from which the permittivity starts to deviate from the Curie Weiss law and T_m represents the temperature of the dielectric maximum. The Curie temperature was determined from the graph by extrapolation of the reciprocal of dielectric constant of the paraelectric region. The parameters obtained after fitting are also given in the Table 7.5.

A modified Curie-Weiss law has been proposed to describe the diffuseness of a phase transition,

$$\frac{1}{\varepsilon'} - \frac{1}{\varepsilon_m} = (T - T_m)^{\gamma} / C' \tag{7.5}$$

where γ and C' are assumed to be constant. The parameter γ gives information on the character of the phase transition; for $\gamma=1$, a normal Curie Weiss law is obtained, for $\gamma=2$, it reduces to the quadratic dependency which describes a complete diffuse phase transition. The plot of $Log\ (1/\varepsilon' - 1/\varepsilon_m)$ vs $Log\ (T - T_m)$ at 100 kHz is shown in the Fig. 7.22. A linear relationship is observed. The slope of the fitting curve is used to determine the value of parameter γ. In the present composition, the value of γ is found to be 1.66 at 100 kHz. The value of the γ shows that the material is highly disordered.

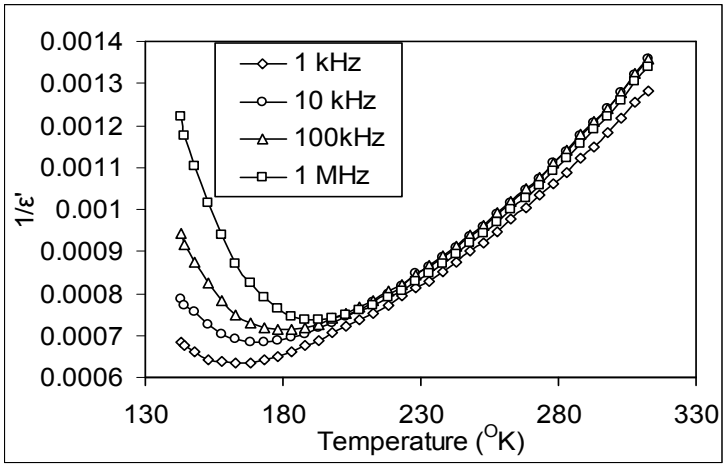

Figure 7.21. Temperature dependency of 1/ε' for $BaTi_{0.6}Zr_{0.4}O_3$ at various frequencies

The broadened dielectric maximum (in *ε'* vs *temperature* curve) and its deviation from Curie–Weiss law are the main characteristics of a diffuse phase transition of the material. The diffuse phase transition and deviation from Curie-Weiss type law may be assumed to be due to disordering. The broadness in ε' vs. temperature curve is one of the most important characteristics of the disordered perovskite structure with diffuse phase transition. The broadness or diffusiveness occurs mainly due to compositional fluctuation and structural disordering in the arrangement of cation in one or more crystallographic sites of the structure. This suggests a microscopic heterogeneity in the compound with different local Curie points. The nature of the variation of dielectric constant and non-polar space group suggests that the material may have ferroelectric phase transition.

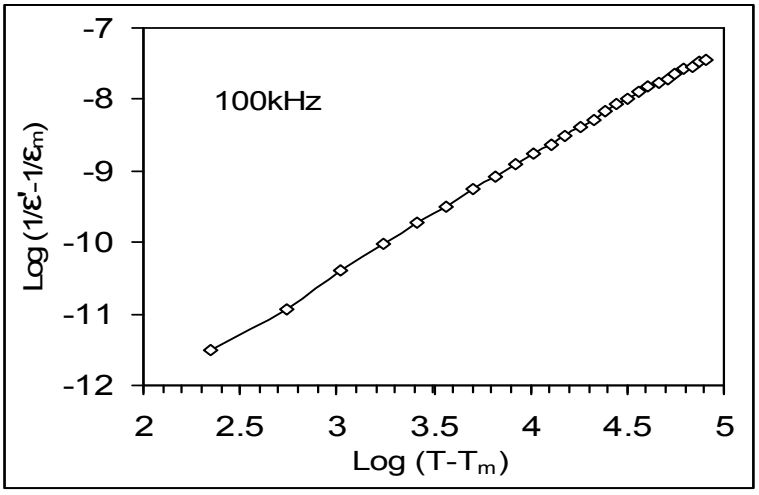

Figure 7.22. Log $(1/\varepsilon'-1/\varepsilon_m)$ vs Log $(T-T_m)$ for $BaTi_{0.6}Zr_{0.4}O_3$ at 100 kHz

Table 7.5: Parameters obtained from temperature dependency dielectric study (fig. 7.22) on the composition $BaTi_{0.6}Zr_{0.4}O_3$ at corresponding measured frequencies.

Frequency	T_m (K)	T_0 (K)	C (10^5K)	ΔT_m	ε_m	T_{cw}
1kHz	163.5	189.41	1.666	88.81	1598.7	252.3
10kHz	170.91	195.57	1.665	80.14	1473.5	252.7
100kHz	179.97	198.1	1.665	78.66	1415.3	257.8
1 MHz	192.713	211.60	1.665	74.89	1370.4	267.6

7.3.2.1. b. Vogel-Fulcher Relationship

The plot of *Log* (ν) vs. T_m is shown in Fig.7.23. The non-linear nature indicates that the data cannot be fitted with a simple Debye equation. In order to analyze the relaxation features of the ceramic, the experimental curves were fitted using the Vogel-Fulcher formula [46, 47],

$$\nu = \nu_0 \exp\left[\frac{-E_a}{k_B (T_m - T_f)}\right] \tag{7.6}$$

where ν_0 is the attempt frequency, E_a is the measure of average activation energy, and k_B is the Boltzmann constant, and T_f is the freezing temperature. T_f is regarded as the temperature where the dynamic reorientation of the dipolar cluster polarization can no longer be thermally activated. The fitting curve is shown in Fig. 7.23. The fitting parameters are E_a =0.1020 eV, T_f =106K, and ν_0 =8.5X10^{11}Hz. The close agreement of the data with the *V~F* relationship suggests that the relaxor behavior in the system is analogous to that of a dipolar glass with polarisation fluctuations above a static freezing temperature. The activation energy and pre-exponential factor are both consistent with thermally activated polarisation fluctuations. The empirical relaxation strength describing the frequency dispersion of T_m is defined as

$$\Delta T_{res} = T_{m\,(1M\,Hz)} - T_{m(10\,kHz)}, \tag{7.7}$$

where ΔT_{res} was derived from the dielectric measurement of the ceramics. The values of ΔT_{res} is found to be 20.14 for the composition.

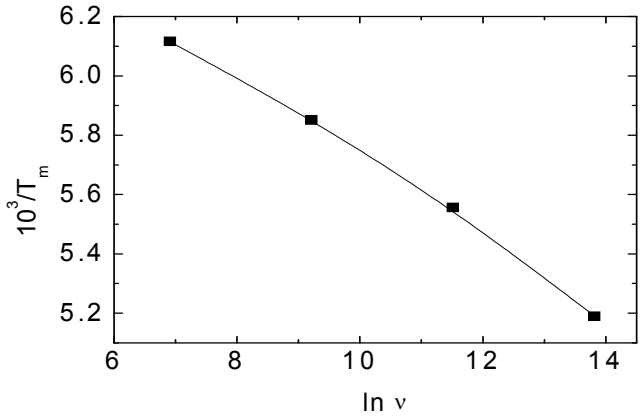

Figure 7.23. $1/T_m$ as function of the measured frequency of $BaTi_{0.6}Zr_{0.4}O_3$. The solid circles are the experimental points and the line is to the Vogel-Fulcher relationship.

The relaxor behavior, as observed in this ceramic, can be induced by many factors such as microscopic compositions fluctuation, the merging of micropolar regions in to macropolar regions, or a coupling of order parameter and local disorder mode through the local strain [48-50]. Vugmeister and Glinichuk reported that the randomly distributed electrical field or strain field in a mixed oxide system was the main reason leading to the relaxor behavior [51]. In the solid solution of $BaTi_{0.6}Zr_{0.4}O_3$, Ba ions occupy the A sites of the ABO_3 perovskite structure. Zr and Ti ions occupy the B site, and the ionic radius of Zr^{4+}(0.98Å) is larger than that of Ti^{4+}(0.72Å), therefore an inhomogeneous distribution results at the B site of the structure and induces a mechanical stress in the grain. Stress was introduced into the lattice during cooling after sintering process, which is due to the transition from a cubic to rhombohedral phase below the Curie temperature [52]. On the other hand, it is known that $BaZrO_3$ shows non ferroelectric (cubic paraelectric phase) behavior at all temperatures because, the Zr ion locates at the central equilibrium position of the $BaZrO_3$ lattice. In this case, the macrodomain in $BaTiO_3$ could be divided into the microdomains, which probably cause the relaxor behavior.

7.3.2.2. The Composition $Ba_{0.9}Ca_{0.1}Ti_{0.6}Zr_{0.4}O_3$

Fig. 7.24 and 7.25 show the temperature dependency of the dielectric constant and dielectric loss of bulk $Ba_{0.9}Ca_{0.1}Ti_{0.6}Zr_{0.4}O_3$ ceramics respectively at different frequency. The nature of the plot shows a typical relaxor behavior. The nature of the

material can be interpreted as described in section 7.3.2.1 and the parameters obtained from the plot are tabulated in the Table 7.7.

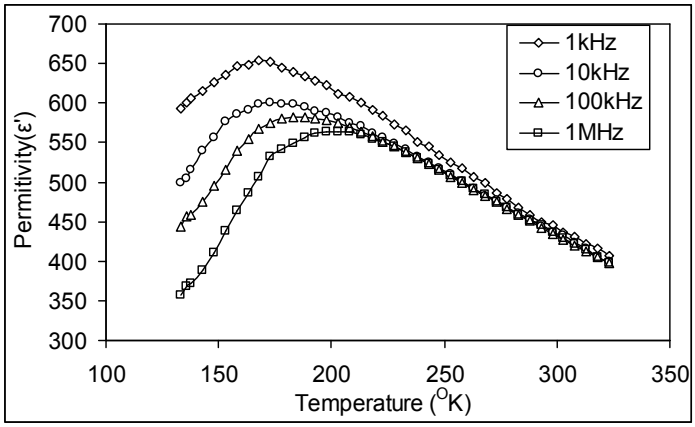

Figure 7.24. Temperature dependency of ε' for $Ba_{0.9}Ca_{0.1}Ti_{0.6}Zr_{0.4}O_3$ at various frequencies

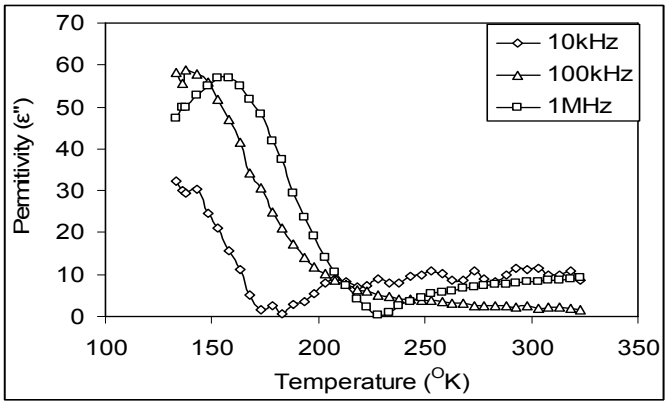

Figure 7.25. Temperature dependency of ε'' for $Ba_{0.9}Ca_{0.1}Ti_{0.6}Zr_{0.4}O_3$ at various frequencies.

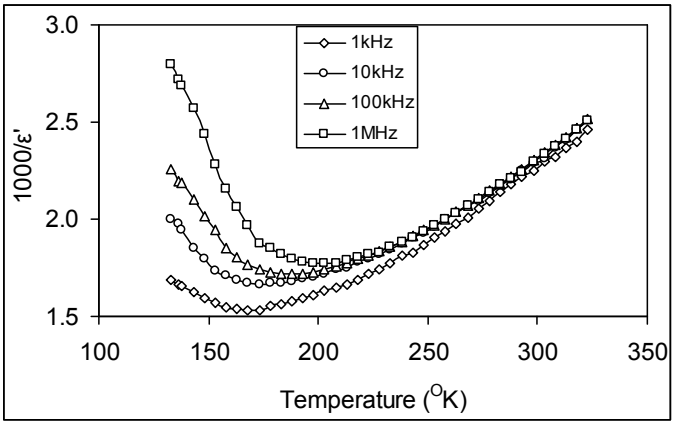

Figure 7.26. Temperature dependency of 1/ε' for $Ba_{0.9}Ca_{0.1}Ti_{0.6}Zr_{0.4}O_3$ at various frequencies.

The Fig. 7.26 shows temperature dependency of *1/ε'* for $Ba_{0.9}Ca_{0.1}Ti_{0.6}Zr_{0.4}O_3$ at various frequencies, which shows a deviation from the Curie Weiss law. The parameters obtained (T_m, T_C and T_{wc}) from the plot are given in the Table 7.6.

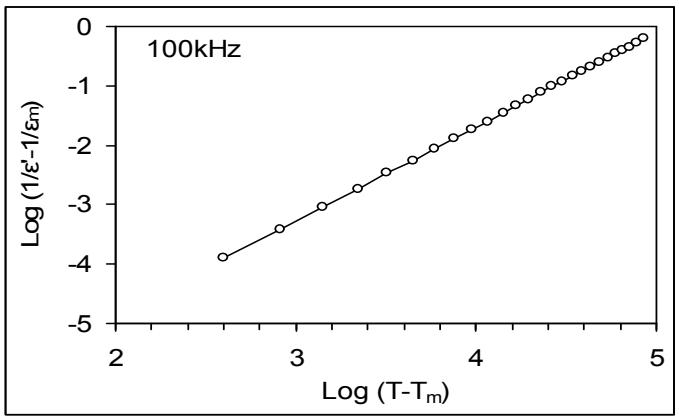

Figure 7.27. Log ($1/\varepsilon'-1/\varepsilon_m$) vs Log ($T-T_m$) for $Ba_{0.9}Ca_{0.1}Ti_{0.6}Zr_{0.4}O_3$ at 100 kHz

The plot of *Log (1/ε'-1/ε_m)* as a function of *Log (T-T_m)* is shown in the Fig. 7.27. The slope of the fitted curve is used to determine the value of γ, which gives the information on the diffusivity of the material. In the present composition, the value of γ is found to be 1.50 at 100 kHz which again confirms the nature of the diffuse phase transition.

Table 7.6: Parameters obtained from temperature dependency dielectric study on the composition $Ba_{0.9}Ca_{0.1}Ti_{0.6}Zr_{0.4}O_3$ at corresponding measured frequencies.

Frequency	T_m (K)	T_0 (K)	C (10^5K)	ΔT_m	ε_m	T_{cw}
1kHz	167.47	186.6	1.45	79.64	657.44	247.11
10kHz	173.35	198	1.42	75.85	604.35	249.20
100kHz	184.602	205.6	1.42	69.548	584.65	254.15
1 MHz	198.79	214	1.42	68.73	572.21	267.52

The plot of transition temperature as function of Log (frequency) is shown in the fig. 7.28. The data could not be fitted with simple Debye relation and is fitted with V~F relation (Eq. 7.6). The solid circles are the experimental data points and the line is the fitted curve. The parameters obtained from the fitting are: E_a =0.0461 eV, T_f= 130 K, and ν_0=2.51X10^9 Hz. The empirical relaxation strength (ΔT_{res}) describing the frequency dispersion of T_m is found to be 25.44 using the relation 7.7.

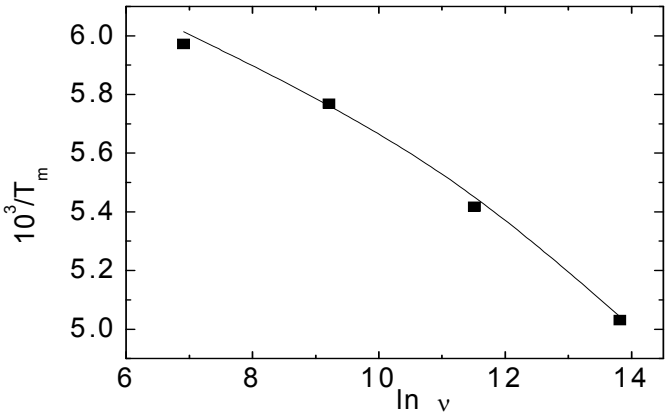

Figure 7.28. $1/T_m$ as function of the measured frequency of $Ba_{0.9}Ca_{0.1}Ti_{0.6}Zr_{0.4}O_3$. The solid circles are the experimental points and the line is to the Vogel-Fulcher relationship.

From the Table 7.6, it can be noticed that there is an increase in transition temperature with Ca substitution in $BaTi_{0.6}Zr_{0.4}O_3$ ceramic (Table 7.5). When Ca is substituted in 12 coordination site, it traps with eight nearest neighbors Oxygen and four more distant ones. That modification supposes a possible displacement of Ca^{2+} out of the oxygen dodecahedron centre able to induce a dipolar moment whose occurrence should lead to increase in transition temperature [53]. The observed transition temperature is less than that observed by Ph. Sciau *et.al.* [54] in Ca substituted Ba (Ti/Zr) O_3 is due to the presence of higher amount of Zr in the system. The parameter which describes the degree of deviation, i.e., ΔT_m, decreases slightly, indicating decrease in relaxor nature.

7.3.2.3. The composition $Ba_{0.93}Mg_{0.07}Ti_{0.6}Zr_{0.4}O_3$

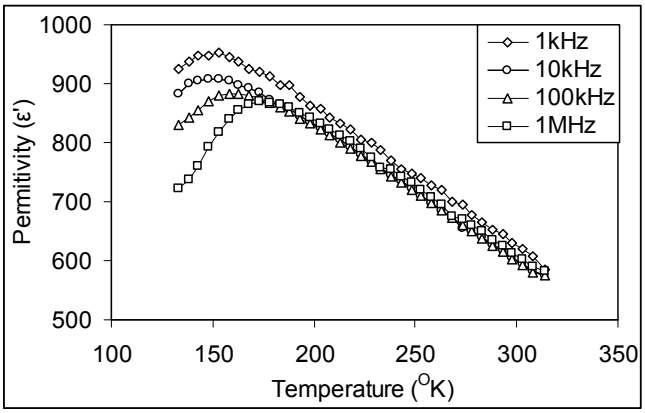

Figure 7.29. Temperature dependency of ε' for $Ba_{0.9}Mg_{0.07}Ti_{0.6}Zr_{0.4}O_3$ at various frequencies.

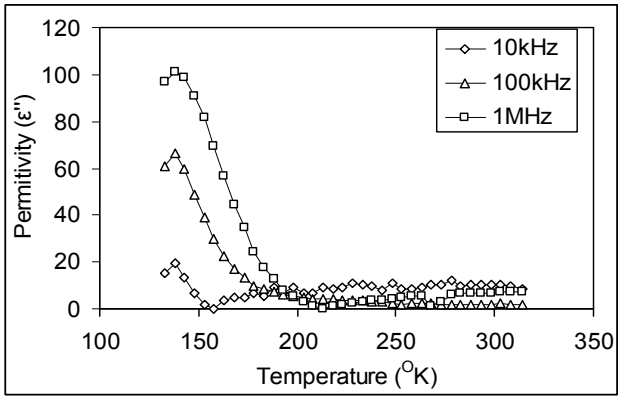

Figure 7.30. Temperature dependency of ε'' for $Ba_{0.9}Mg_{0.07}Ti_{0.6}Zr_{0.4}O_3$ at various frequencies.

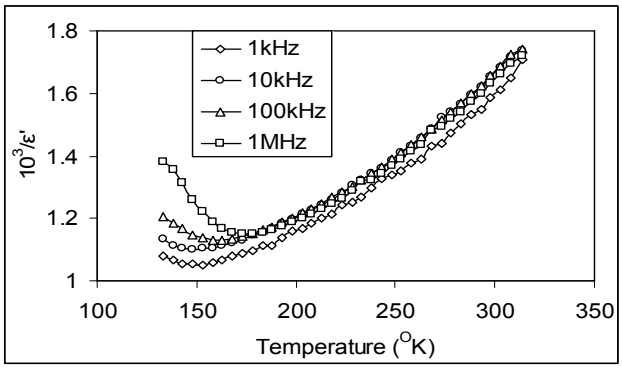

Figure 7.31. Temperature dependency of 1/ε' for $Ba_{0.9}Mg_{0.07}Ti_{0.6}Zr_{0.4}O_3$ at various frequencies.

Fig. 7.29 and Fig. 7.30 show the temperature dependency of the dielectric constant and dielectric loss of bulk $Ba_{0.9}Mg_{0.07}Ti_{0.6}Zr_{0.4}O_3$ ceramics respectively at different frequencies. The nature of the plot shows a typical relaxor behavior. The dielectric constant and loss tangent exhibit strong frequency dependency below Curie region. The nature of the material can be interpreted as described in Section 7.3.2.1 and the parameters obtained from the plot are tabulated in the table 7.7.

The thermal variation of 1/ε' is plotted in the Fig. 7.31. The plot clearly indicates the deviation from Curie-Weiss law. The parameters T_m, T_O and T_{wc} obtained from the plot are shown in the Table 7.7.

The plot of *Log* $(1/\varepsilon'-1/\varepsilon_m)$ as a function of *Log* $(T-T_m)$ is shown in the Fig. 7.32. The diffuseness parameter γ is found to be 1.46 at 100 kHz which again confirms the nature of the diffuse phase transition.

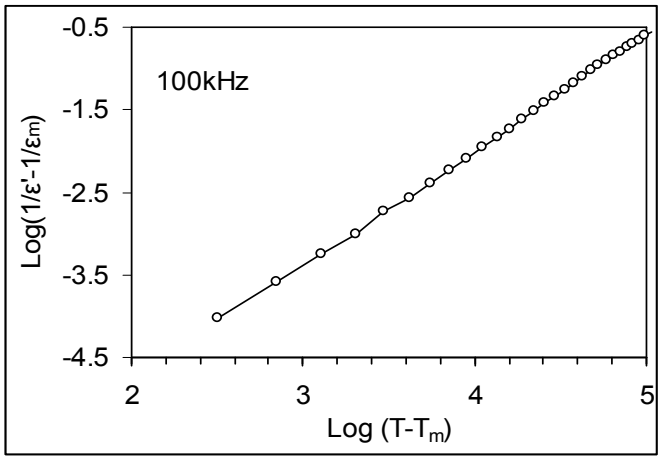

Figure 7.32. Log ($1/\varepsilon'-1/\varepsilon_m$) vs Log ($T-T_m$) for $Ba_{0.9}Mg_{0.07}Ti_{0.6}Zr_{0.4}O_3$at 100 kHz

The plot of dependency of transition temperature as function of Log (frequency) is shown in the Fig. 7.33. The darkened circles are the experimental points and the solid line is the fitted curve using the *V~F* relation given in the Equation 7.6. The parameters obtained from the fitting are: E_a =0.014 eV, T_f= 132 K, and ν_0=5.4X10^7 Hz. The empirical relaxation strength (ΔT_{res}) describing the frequency dispersion of T_m is found to be 22 using the relation 7.7.

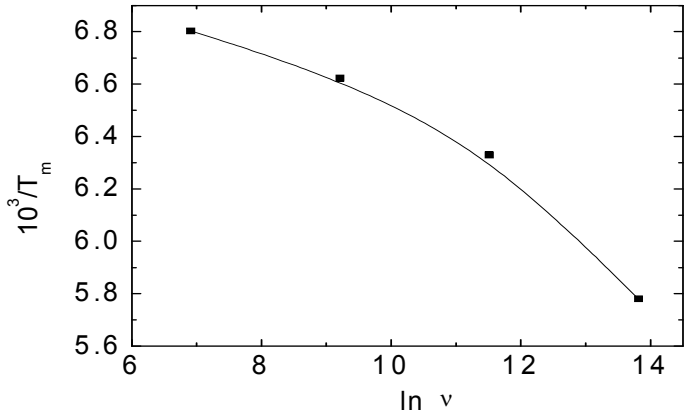

Figure 7.33. $1/T_m$ as function of the measured frequency of $Ba_{0.9}Mg_{0.07}Ti_{0.6}Zr_{0.4}O_3$. The solid circles are the experimental points and the line is to the Vogel-Fulcher relationship.

Table 7.7 Parameters obtained from temperature dependency dielectric study on the composition $Ba_{0.9}Mg_{0.07}Ti_{0.6}Zr_{0.4}O_3$ at corresponding measured frequencies.

Frequency	T_m (K)	T_0 (K)	$C(10^5K)$	ΔT_m	ε_m	T_{cw}
1kHz	143	175.513	2.5	104.8	957.42	250.8
10kHz	151	169.73	2.5	96.73	914.50	261.73
100kHz	158	174.55	2.5	97.53	889.08	255.53
1 MHz	173	188.3	2.5	83.8	871.95	256.80

7.3.2.4. The Composition $Ba_{0.86}Mg_{0.14}Ti_{0.6}Zr_{0.4}O_3$

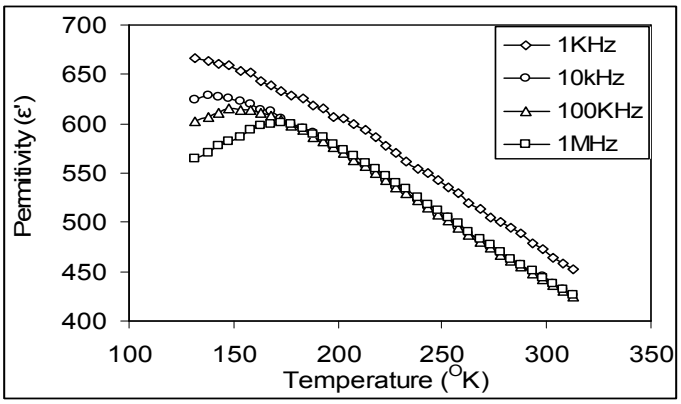

Figure 7. 34. Temperature dependency of ε' for $Ba_{0.86}Mg_{0.14}Ti_{0.6}Zr_{0.4}O_3$ at various frequencies.

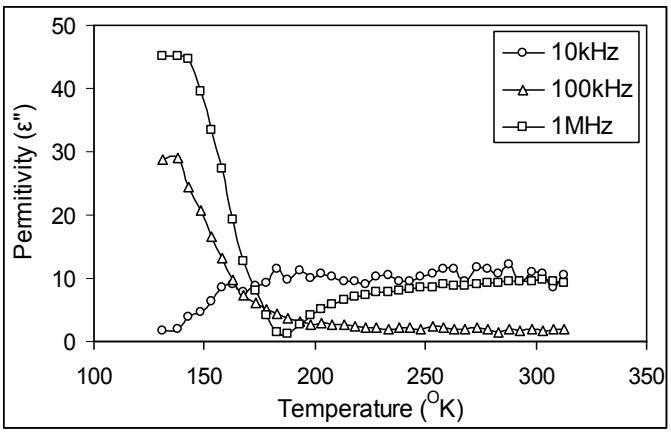

Figure 7.35. Temperature dependency of ε'' for $Ba_{0.86}Mg_{0.14}Ti_{0.6}Zr_{0.4}O_3$ at various frequencies.

Fig. 7.34 and Fig. 7.35 show the temperature dependency of the dielectric constant and dielectric loss of bulk $Ba_{0.86}Mg_{0.14}Ti_{0.6}Zr_{0.4}O_3$ ceramics respectively at

different frequencies. The nature of the plot shows a typical relaxor behavior. The parameters obtained from the plot are tabulated in the Table 7.8.

The thermal variation of *1/ε'* is plotted in the Fig. 7.36. The figure clearly deviates from Curie Weiss law with 0.14 atom % of Mg substitution in $BaTi_{0.6}Zr_{0.4}O_3$ ceramic. The parameters T_m, T_O and T_{wc} obtained from the plot is depicted in the Table 7.8.

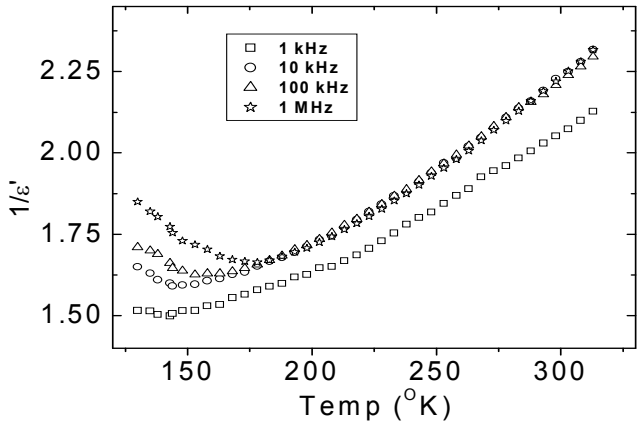

Figure 7.36. Temperature dependency of 1/ε' for $Ba_{0.86}Mg_{0.14}Ti_{0.6}Zr_{0.4}O_3$ at various frequencies.

The plot of *Log (1/ε'-1/ε$_m$)* as a function of *Log (T-T$_m$)* is shown in the Fig. 7.37. The diffuseness parameter γ is found to be 1.96 at 100 kHz which again confirms the nature of the diffuse phase transition.

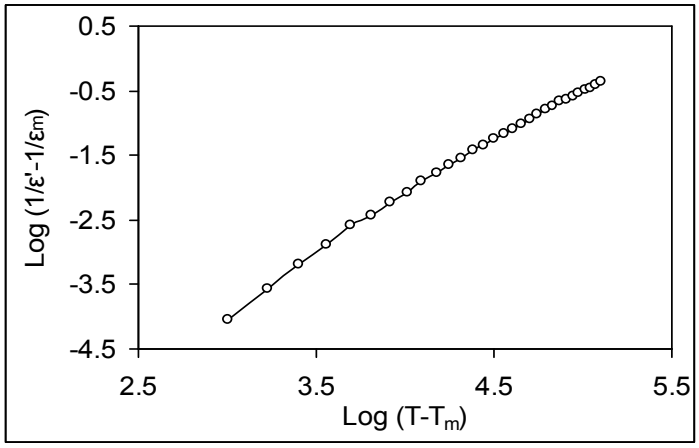

Figure 7.37. Log (1/ε'-1/ε$_m$) Vs Log (T-T$_m$) for of $Ba_{0.86}Mg_{0.14}Ti_{0.6}Zr_{0.4}O_3$ at 100 kHz

The plot of dependency of transition temperature as a function of Log (frequency) is shown in the Fig. 7.38. The darkened circles are the experimental points

and the solid line is the fitted curve using the *V~F* relation given in the Eq. 7.6. The parameters obtained from the fitting are: E_a =0.02 eV, T_f= 108 K, and ν_0 =5.35X10^7 Hz. The empirical relaxation strength (ΔT_{res}) describing the frequency dispersion of T_m is found to be 28.83 using the relation 7.7.

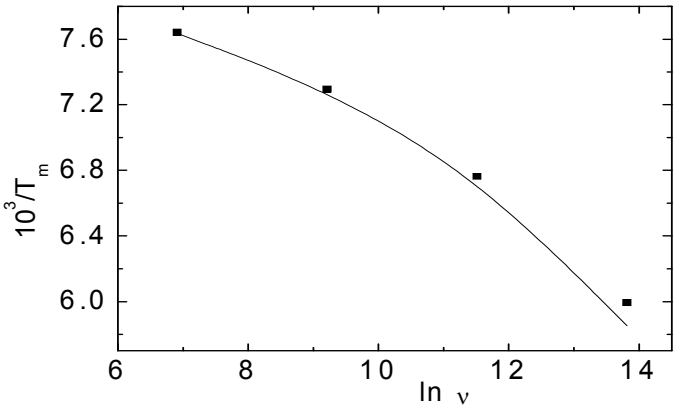

Figure 7.38. $1/T_m$ as function of the measured frequency of $Ba_{0.86}Mg_{0.14}Ti_{0.6}Zr_{0.4}O_3$. The solid circles are the experimental points and the line is to the Vogel-Fulcher relationship.

Table 7.8 Parameters obtained from temperature dependency dielectric study on the composition $Ba_{0.86}Mg_{0.14}Ti_{0.6}Zr_{0.4}O_3$ at corresponding measured frequencies.

Frequency	T_m (K)	T_0 (K)	C (10^5K)	ΔT_m	ε_m	T_{cw}
1kHz	131	151.226	2.0	117.07	670.62	248.07
10kHz	137.08	146.53	2.0	116.62	631.18	253.7
100kHz	147.87	170.87	2.0	107.84	618.45	255.71
1 MHz	165.91	187.8	2.0	93.65	604.18	259.56

From the Tables 7.5, 7.7 and 7.8 it can be noticed that there is decrease in transition temperature with Mg substitution in $BaTi_{0.6}Zr_{0.4}O_3$ ceramic. Mg is small enough to occupy the 12 coordination sites of the ABO_3 perovskite. But when it takes the 12 coordination sites (i.e., the A site), A-site ion and the oxygen ion of ABO_3 perovskite structure become stronger because the radius of the Ba^{2+} ion is larger than that of the Mg^{2+} ion: the bonding force Ti-O(Mg), therefore, becomes weaker than Ti-O(Ba) bond. The weakening of the Ti-O bond leads to a weaker distortion of the octahedron and brings about a decrease in Curie temperature [55]. It is reported [56] that as the grain

size decreases, the maximum dielectric constant and transition temperature decrease. This may be the region of decrease of transition temperature and dielectric constant with increase in Mg content. The effect of grain size originates from the higher surface tension in smaller grains [57], which acts in the same manner as hydrostatic pressure, thus decreasing the Curie point [58]. In addition, the force experienced by the atoms and ions in the vicinity of, or far from, the surface of grain, are not similar. These considerations suggest that a quadraticity gradient may exist between the surface and the bulk of grains [59]. For smaller grain sizes however, the superficial layers of the grains represent a significant fraction and may dominate the structural and the dielectric measurement.

7.4. Conclusions

It may be concluded that;

1. The compositions ($Ba_{1-x}Sr_xTi_{0.5}Zr_{0.5}O_3$) show decreased densification and grain growth with the increase in Sr substitution.
2. Composition with x=0.0 ($BaTi_{0.5}Zr_{0.5}O_3$) shows highest permittivity in the system. The permittivity and dielectric loss decrease with the increase in Sr substitution.
3. The permittivity and loss are found to be stable and loss is less than 0.6 % in the frequency range 100 kHz to about 5 MHz for all the compositions.
4. AC conductivity in the ceramics decreases with Sr-substitution due to the decrease in loss as well as grain size and increase with increase in frequency.
5. The compositions show a good densification around x=0.2 in the system ($Ba_{1-x}Sr_xTi_{0.5}Zr_{0.5}O_3$), suggesting a low melting eutectic near that composition in the four component system.
6. The compositions ($Ba_{0.5}Sr_{0.5}TiO_3$) show decreased densification and grain growth with the increase in Zr substitution.
7. Permittivity, dielectric loss and AC conductivity decrease with Zr-substitution in $Ba_{0.5}Sr_{0.5}TiO_3$ ceramic due to the decrease in charge defects by the substitution.
8. There is a decrease in density due to the substitution of more stable Zr in place of Ti.
9. Decrease in dielectric permittivity may be due to the decrease in grain size.
10. Dielectric loss peak at about 9.5 MHz is due to extrinsic resonances loss.

11. The effect of Ca and Mg on the composition $BaTi_{0.6}Zr_{0.4}O_3$ has been studied in details.
12. The microstructure shows that there is a decrease in grain size with the substitution. The rate of decrease in grain size is observed with the substitution of Ca and Mg.
13. The experimental density calculated by the water immersion technique shows there is an increase in density with Ca and Mg substitution in the experimental sintering temperature.
14. The room temperature dielectric study shows that there is a decrease in permittivity and dielectric loss with the substitution, which may be due to the decrease in grain size, as mentioned earlier.
15. The temperature dependency dielectric study on the composition $BaTi_{0.6}Zr_{0.4}O_3$, $Ba_{0.9}Ca_{0.1}Ti_{0.6}Zr_{0.4}O_3$, $Ba_{0.93}Mg_{0.07}Ti_{0.6}Zr_{0.4}O_3$ and $Ba_{0.86}Mg_{0.14}Ti_{0.6}Zr_{0.4}O_3$ was carried out in the temperature range 130 ^{O}K to 333 ^{O}K.
16. The compositions show a diffuse phase transition having its Curie range of temperature much below the room temperature.
17. The Ca-containing composition shows that there is a shift of transition temperature towards room temperature, but the Mg containing compositions shows shift of transition temperature further below.
18. A clear deviation from Curie-Weiss law is observed for all the compositions, and degrees of deviations were also calculated and found to increase with both Ca and Mg content.
19. To study the diffuseness the data were fitted with a modified Curie-Weiss law and it was found that the degree diffuseness decreases with Ca substitution, but increases with Mg substitution.
20. In order to analyze the relaxation feature, the strength of relaxation were also calculated and found to increase with Ca and Mg substitution.
21. The experimental curves were fitted with Vogel-Fulcher formula and the experimental data were found to be in good agreement with the theoretical fitting.

7.5. References

1. E. Wainer and A.N.Solomon, Elec. Report **8,** 127 (1942).
2. D.F.K. Hennings, B. Schreinemacher and H. Schreinemacher, *J. European Ceramic Society* **13,** 81-88 (1994).
3. J. Ravez and A.Simon, *Eur J. Solid State Inorg Chem*, **34**, 1199 (1997).

4. Y. Zhi, R.Gue and A.S. Bhala, *J. Appl. Phys*. **88**, 410-415 (2000).
5. T. B.Wu, C.M Wu and M.L. Chen, *J.Appl. Phys. Lett*. **69**, 2659 (1996).
6. D. Henning, A. Schnell, and G Simon, *J Am. Ceram Soc*, **65**, 539 (1982).
7. Z .Yu, R. Guo and A.S. Bhalla, *J.Appl. Phys*, **88**, 410 (2000).
8. Z. Yu, C. Ang, R. Guo and A.S. Bhalla, *Appl. Phys. Lett*, **81**, 1285 (2002).
9. F.M.Pontes, M.T.Escote, C.C.Escudeiro, E.R. Leite, L.Longo, A.J.Chiquito, P.S.Pizani and J.A.Varela, *J.Appl. Phys*, **96**, 4386-4391, (2004).
10. X.G.Tang, K-H. Chew and H.L.W. Chan, *Acta Materialia*, **52**, 5177-5183 (2004).
11. C. Hofer, R. Meyer, U. Bottger and R. Waser, *J Euro. Cera. Soc*., **24**, 1473 (2004).
12. K. Abe and S. Komatsu, *J.appl. Phys*, **77**, 6461 (1995).
13. S.G. Lu, X. H. Zhu, C. L. Mak, K. H. Wong, H. L. W. Chan, and C. L. Choy, *Appl Phys Lett*. **82**, 2877 (2003).
14. X. H. Zhu, N. Chong, H. Lai-Wah Chan, C. L. Mak, K. H. Wong, Z.G. Liu, and N. B. Ming, *Appl Phys Lett* **80**, 3376 (2002).
15. C. Wang, B. L. Cheng, S. Y. wang, H. B. Lu, Y. L. Zhou, Z. H. Chen and G. Z. Yang, *Appl Phys Lett*, **84**, 765 (2004).
16. A.T. Findikoglu, Q. X Jia, X.D. Wu, G.J. Chen, T. Venkatesan, and D.W Reagor, *Appl.Phy. Lett*.**68** (5) 1651(1996).
17. O.G. Vendik, and S.P.Zubko, *J. Appl. Phys***. 88**, 5343(2000).
18. U. Syamaprasad, R.K.Galgali and B.C. Mohanty, *Mater. Lett*. **7,** 197-200(1988).
19. A.T. Findikoglu, R. Camassa, G.Lythe and Q.X.Jia, *Appl.Phy. Lett*. **80,** 3391(1996).
20. C. Wang, B.L. Cheng, S.Y.Wang, H.B.Lu, Y.L.Zhou, Z.N.Chen and G.Z.Yang, *Appl. Phys.lett*. **84**, 765-767(2004).
21. W.J. Kim, H.D. Wu, W. Chang, S.B. Qadri, J.M. Pond, S.W. Kirchoefer, B.D. Chrisey, J.S. Horwitz, *J. Appl. Phys*, **88**, 5448 (2000).
22. H.M.Cristen, L.A. Knauss and K.S. Harshavardhan, *Materials Science and Engineering B* **56**, 200-203 (1998).
23. J.N.Lin and T.B.Wu, *J.Appl.Phys*. **68**, 985 (1990)
24. K. Numata, Y. Fukuda, K. Aoki and A. Nishimura, *Jap. J. Appl. Phys*. **34** 5245-5249 (1995).
25. J-D Byun, J-II Yoon, S. Nahm and J-C Kim, *Materials Research Bulletin* **35** 1755-1761(2000).
26. A. Dixit, S.B. Majumder, R.S. Katiyar and A.S. Bhalla, *Appl. Phys. Lett*, **82**, 2679 (2003).
27. U. Weber, G.Greuel, U. Boettger, S.Weber, D.Hennings and R.Waser, *J.Am.Ceram.Soc*., **84**, 759-66 (2001).
28. A. Kerfah, K. Taibi, A.G. Laidoudi, A. Simon, J. Ravez, *Materials Letter*, **42**,189-193 (2000).
29. J.Ravez and A.Simon, *Eur. J. Solis State Inorg. Chem*. **34** (1997) 1199. And T.Mitsui, W.B. Westphal, *Phys. Rev*. **124**, 1354 (1961).
30. D.E.Rase and Rustum Roy, *J. Am. Ceram. Soc*., **38**, 111(1955).
31. Miroslawa Drys and Wlodzimier Trzebiatowski, *Roczniki Chem*., **31**,492 (1957).
32. A. Ioachim, *et al*., *J. Optoelectron. Adv. Mater*. **5** 1389 (2003).
33. L.I. Maissel and R. Glang, *Handbook of Thin Film Technology*, McGraw-Hill, New York, (Chapter 16) (1970).
34. C.H.Lu and C.Y. Wen *Mater.Lett*. **38,** 278(1999).
35. S.H.Kim, D.J.Kim, J.I.M.C.E. Kim and A.I.Kingon, *J.Sol.gel.Sci. Technol*. **16**, 57(1999).

36. R. K. Astala and P. D. Bristowe, *Modelling Simul. Mater. Sci Eng* **12**, 79 (2004).
37. D. O'Neill, R.M.Bowman and J.M.Gregg, *Appl. Phys.Lett*., **77**, 1520-1522 (2000)
38. F.M. Pontes, E. Longo, E.R. Leite and J.A. Varela, *Thin Solid Films* **386,** 91(2001).
39. H.V. Wartenberg and E.Prophet, Part V, *Z.anorg.u.allgem.Chem*.,**208**, 378 (1932).
40. L.W.Coughanour and V.A.DeProsse, *J.Research Natl Bur Standards*, **51,** 87, R.P 2435 (1953).
41. Pol Duwez, Francis Odell and Frnk H.Brown, Jr., *J.Am.Ceram Soc*., **35**,109 (1952).
42. M.E.Lines and A.M. Glass, *Principles and applications of ferroelectrics and Related Materials*, Clarendon, Oxford, p.287 (1979).
43. U.T.Hochli, K.Knorr, and A.Loidl, *Adv.Phys*. **39**.405 (1990).
44. U. Weber, G. Greuel, U.Boettger et al., *J. Am. Ceram Soc*., **84**, 759 (2001).
45. B. Beleckas, J.Grigas and S.Stefanovich, *Litovskii Fizicheskii Sbornik*, **29**, 202 (1989).
46. H.T. Martirena and J.C. Burfoot, *Feroelectrics*, **7**, 151, (1974).
47. K.Uchino and S.Nomura, *Feroelectric Lett Sect*, **44**, 55(1982).
48. L.E Cross, *Feroelectrics,* **151**, 305, (1994).
49. L.E.Cross, *Feroelectrics*, **76**, 241, (1987).
50. D.Viehland, M.Wuttig and L.E.Cross, *Feroelectrics*, **120,** 71,(1991)
51. B.E. Vugmeister and M.D. Glinichuk, *Rev.Mod.Phys*., **62**, 993,(1990)
52. D.Henning, A.Schnell and G.Simon, *J. Am. Ceram Soc*., **65**, 539, (1982).
53. K.Aliouane, M.Hamadene, A.Guehria-Laidoudi, A.Simon and J.Ravez, *J.Fluorine Chemistry*, **105**, 71-76, (2000).
54. Ph. Sciau, G.Calvarin and J.Ravez, *Solid State Communication*, **113**, 77-82(2000)
55. J. Ravez, *Feroelectricity in solid state chemistry. C.R. Acad. Sci. Paris, Serie lic, Chimie/Chemistry*, **3,** 267-283, (2000).
56. X.G.Tang, K-H. Chew and H.L.W. Chan, *Solid State Communications*, **131**,163-168 (2004).
57. K.Uchono, E.Sadanaga and T.Hirose, *J.Am. Ceram.Soc*. **72**, 1955(1989).
58. G.A.Samara, *Phys.Rev*. **151**, 378 (1966).
59. S.Malbe, J.C.Mutin and J.C.Niepce, *EPDIC IV*, Chester, UK, July (1995).

Chapter – 8

THEORETICAL MODELS ON RELAXORS: A REVIEW

8.1. Introductions

Perovskite-like ferroelectric relaxors attract considerable interest owing to rich diversity of their physical properties and possible applications in various technological schemes. These relaxors possess very large dielectric constants, attractive for capacitors, exceptionally large electrostrictive coefficients, important for actuators and micropositioners, and large electro-optic constants, useful for information storage, shutters and optical modulators [1, 2].

The main features of relaxors are connected with their structural (compositional) inhomogeneity or disorder and with the presence of polar nanodomains in nonpolar matrix. The structural investigations and physical property studies reveal three peculiar temperatures: T_d, T_m and T_c. At temperature above T_d, so called the Burns temperature, the mixed compounds A ($B^{'}B^{''}$) O_3 have the cubic perovskite structure in which the B position is occupied by the approximately randomly distributed B' and B'' ions. On cooling below T_d small polar nanodomains appear, whose interactions and growth can trigger a transition into a glassy or ordered phase. If the domains become large enough, the sample will undergo a cooperative ferroelectric phase transition at T_c. On the other hand, if the nanodomains grow but do not become large enough, they will ultimately exhibit a dynamic slowing down of their fluctuations below T_m, which is the temperature of the dielectric permittivity maximum, leading to an isotropic relaxor state with random orientation of polar domains [2].

Relaxor ferroelectrics or relaxors exhibit many properties similar to those of spin or dipolar glasses. Relaxor behavior in normally ferroelectric materials results from compositionally inherent, disorder or frustration [1].This behavior has been observed and studied most extensively in disordered ABO_3 perovskite ferroelectric. Three essential ingredients of relaxor ferroelectric are the existence of lattice disorder, evidence of the existence of polar nanodomains at temperatures much higher than T_m and the existence of domains as islands in a highly polarisable host lattice.

To close similarity, spin glasses are magnetic systems in which the interactions among the magnetic moments are both random and frustrated because of structural

disorder. A common feature of these systems, and the one that makes them such an interesting object of study, is that they exhibit a freezing of magnetic moments in random directions at an apparently sharp temperature T_f [3].

8.2. Spin Glass Ising Models

8.2.1. Introduction

It can be said that the theory of spin glasses started in 1975 with a paper by Edwards and Anderson [4] attempting to explain the observed cusp in the susceptibility of dilute magnetic alloys. The cusp was puzzling because it strongly suggested a magnetic phase-transition in the alloy, but no long-range magnetic order was seen in these so called spin glass alloys. Edwards and Anderson explained this as follows. The localized magnetic moments of impurities – to be called spins henceforth – interact with each other through Ruderman-Kittel- Kasuya-Yosida (RKKY) interaction [5] mediated by the conduction electrons of the non-magnetic host metal. The RKKY interactions between a pair of spins oscillate in sign as the separation between the spins is varied. In a spin glass alloy, impurities are fixed (quenched) in various random positions in the host lattice. Because of the random positions of spins and the oscillatory nature of RKKY interaction, there are just as many ferro-magnetic pair interactions amongst spins as there are anti-ferromagnetic [6]. This makes it impossible for the system to settle into any overall ferromagnetic or antiferromagnetic state even at zero temperature. However, there is a preferred orientation into which each spin settles as temperature goes to zero. This preferred orientation varies randomly from spin to spin. Edward and Anderson showed that at critical temperature, the spin transition temperature T_{sg}, a finite fraction of spins spontaneously settled into their respective preferred directions. This gives rise to a singularity, a cusp, in the susceptibility. As temperature drops further, more and more spins freeze into their preferred directions. Because the preferred directions are completely random, there is no visible long range order in the spins. However, it was suggested that the quantity $q = \left\langle \overline{S}_t \right\rangle^2$ may serve as an order parameter for the spin glass transition, where the angular brackets denote the thermal average of spin S_i at site i, and the bar denotes configurational average over all impurity sites. The quantity q is called the Edwards-Anderson parameter [4].

8.2.2. Theory of Spin Glass Ising Model

Because there are similarities between spin glasses and relaxor ferroelectric and because of the wealth of available knowledge both from experimental and theoretical angles in the former, one can deal with the relaxor behavior in analogy with the spin glasses. This section attempts to model the problem of relaxor ferroelectric in analogy with Ising model description of spin glasses.

Under the most commonly studied Ising model of spin glas, consisting of N Ising spins $S_i = \pm 1$, i = 1, 2, …, N ,in the presence of an externally applied magnetic field H, the Hamiltonian for the model becomes,[7]

$$H_H = -\frac{1}{2}\sum_{i,j} J_{ij}\ \ S_i.S_j - H\sum_i S_i \tag{8.1}$$

Here each spin S_i interacts with every other spins S_j, with exchange transition J_{ij}.
In term of Pouli spin matrices

$$H_H = -\frac{1}{2}\sum_{i<j} \vec{J}\left(\left|\vec{R}_i - \vec{R}_j\right|\right)\sigma_i\sigma_j - H\sum_i \sigma_i \tag{8.2}$$

$$\text{where } \frac{1}{2}g\beta H_m = H \tag{8.3}$$

H_m being magnetic field strength.
Under the assumptions of one dimensional nearest neighbour interaction

$$H_H = -J\sum_n \sigma_n\sigma_{n+1} - H\sum_n \sigma_n \tag{8.4}$$

Because the relaxors are materials with random site lattice disorder, it is natural to resort to models that investigate the role of random fields. In ABO_3 relaxors, the dipolar nanodomains formed by chemical substitutions create random electric fields in the host lattices.

For an Ising spin model with infinite ranged interactions with statistically independent site field, one considers a collection of spin s=±1 located at lattice sites i,j and interacting in such a away that the total energy ,or Hamiltonian , is

$$H_H = -J\sum_{i\neq j} S_iS_j - \sum_i \sigma_n \tag{8.5}$$

Here the interaction J is a constant that incorporates all electronic properties in a phenomenological way, and $\langle ij \rangle$ designates nearest- neighbor pairs. Although in Eq 8.5, the quantities S_{ij} are called “spins” the model is by no. means restricted to magnetism. This model can describe any solid state system that has a transition with a doubly degenerate ordered state, and contains frozen impurities or point defects that break the symmetry and cannot move on the relevant time scale. The important feature of reloxor

is the presence of compositional and structural disorder, which breaks translation symmetry and produces random dipolar nanodomains.

For relaxor as consisting of Ising like dipoles in a regular lattice with randomly disturbed exchange energy parameters, the Hamiltonian is simplified to

$$H_H = \sum_{i \neq j} J_{ij} S_i S_j + \frac{E\bar{\mu}\sum \bar{\mu}_i \cos\theta_i}{\bar{\mu}} S_i \tag{8.6}$$

where J_{ij} is assumed to have a Gaussian distribution with zero mean field value. μ_i is the magnitude of the dipole moment of the *i-th* polar nano domains, θ_i is the angle between the external field *E*, and i-th dipole moment and $\bar{\mu}$ is the maximum projection of the dipole moments on the main axis.

Our aim is to find the free energy of this model as a function of temperature T, magnetic field *H*, and variance of random interactions σ.

Defining partition function Z and introducing 2x2 matrices as under

$$Z = \sum_{\sigma_1=\pm1} \sum_{\sigma_2=\pm1} ..... \sum_{\sigma_N=\pm1} e^{H_H(\sigma_1.....\sigma_n)/k_{BT}} \tag{8.7}$$

$$(V_1)_{\sigma_i\sigma_j} = \exp\left(k_1 \sigma_i \sigma_j\right) \tag{8.8}$$

$$(V_2)_{\sigma_i\sigma_j} = \exp\left(H'\sigma_i\right)\delta_{\sigma_i\sigma_j}$$

where $k_1 = J/K_B T$, $H' = H/K_B T$

One can get the Free energy per spin

$$F = \frac{-k_{BT}}{N} \log Z = -k_{BT} \log \lambda_1 \tag{8.9}$$

where $$\lambda_1 = e^{k_1} \cosh H' + \sqrt{e^{2k_1} \sinh^2 H' + e^{-2k_1}} \tag{8.10}$$

From the free energy one can calculate the magnetization $M = -\frac{\partial F}{\partial H_m}$ which, in turn, helps us to calculate magnetic susceptibility $\chi = \frac{\partial M}{\partial H_m}$. It is easy to see that the magnetic susceptibility approaches infinity for $H_m=0$ as T approaches to 0 if K is positive, corresponding to ferromagnetic transition.

Sherrington and Kirkpatrick [8] developed an infinite range model for spin glass which related the temperature dependence of the susceptibility below T_f to the onset of a local (spin glass) order parameter as

$$\chi = \frac{C[1-q(T)]}{T-\theta[1-q(T)]}, \tag{8.11}$$

where q is the local order parameter, which has been considered as Edward-Anderson spin glass order parameter and χ is the susceptibility (in magnetic system) in analogy with permittivity (in dielectric system). This relationship has been previously used by Nagata *et al*. [9] to extract a spin glass order parameter from the static susceptibility, where C and θ were determined by Curie Weiss analysis at high temperature. Deviation from Curie Weiss behavior was not observed in these measurements and *q* extrapolated to zero near T_f. Subsequent work has revealed strong deviations. Calculation by Binder [10] using Ising model with Gaussian distribution of correlation lengths between neighboring moments has indicated that q does not go to zero at T_f but tails to zero at much higher temperatures suggestive of Curie Weiss deviation about T_f. The deviation from Curie-Weiss behavior in spin glasses has been interpreted to mean that, on a local scale, strong magnetic correlations develop far above T_f. The ideal (non-interacting) super paramagnet is known to exhibit Curie Weiss behavior for finite measurement frequencies. The local polar regions in relaxors are believed to be homogeneous and of nanometer size, i.e superparaelectric. However, it has been recently shown [11] that the characteristic dielectric response of relaxor ferroelectrics can be determined by the competition between a nonequilibrium dipole spin glass freezing and a critical change of the relaxation time spectrum. Such a glasslike freezing of cluster dynamic could be characterized by the nonequilibrium spin glass order parameter*, q (T),* describing the fraction of cluster effectively frozen at time *t.*

8.3. Spherical Random Bond – Random Field (SRBRF) Model

8.3.1. Introduction

Since the discovery of relaxor ferroelectrics more than 50 years ago, a number of concepts have been introduced to account for their unusual physical behavior: diffuse phase transition, superparaelectric and dipolar glass models, random-field frustrated ferroelectric, and reorienting polar clusters. In spite of intensive investigations, the nature of the diffuse phase transition [12] in relaxors has remained the subject of some controversy. For example, it has been suggested some time ago that relaxors could be described as a dipolar glass due to the orientation of large superparaelectric clusters [13-16]. The existence of nanometer sized polar domains in lead-magnesium-niobate (PMN) has in fact been demonstrated by X-ray and neutron scattering experiments [17, 18]. In particular, the Nb NMR line shape and the associated probability distribution of

local polarization in PMN were shown to remain Gaussian at all temperatures. This is incompatible with the assumption of a fixed-length order parameter field typically made in dipolar glasses. Rather, in a relaxor the order parameter field is described as a continuous vector field of variable length, which is associated with the dipole moment of reorientable polar clusters, and is subject to a global spherical constraint on the square of the total polarization. Thus a relaxor corresponds to a new type of dipolar glass, namely, the spherical vector glass.

The purpose of the present Chapter is to derive the basic ideas of the SRBRF model in a concise way and calculate the predicted temperature and electric field dependencies of some crucial physical properties, such as the nonlinear dielectric response and probability distribution of local polarization. The SRBRF model may be regarded as the simplest generic model of relaxor ferroelectrics. Since the random interactions or bonds between polar clusters are by assumption infinitely ranged with a Gaussian distribution, and local random fields are similarly Gaussian and uncorrelated, this will lead to a mean field type theory analogous to the case of spin and dipolar glasses [19, 20].

8.3.2. Theory of SRBRF Model

We will consider $PbMg_{1/3}Nb_{2/3}O_3$ (PMN) as a representative relaxor ferroelectric system. On the mesoscopic level, PMN is a structurally inhomogenous material consisting of Nb-rich regions or polar clusters embedded in a quasiregular array of chemically ordered 1:1 regions or chemical clusters. The polar clusters have typically the size of a few nanometers and are reorientable, and are thus responsible for the observed dielectric behavior. In contrast, the chemical clusters are essentially static and act as sources of random electric fields.

We will, therefore, adopt the physical picture of interacting polar clusters and assume that there are n_i Nb type unit cells in a cluster C_i, where i=1,2,…..N. and N is the total no of reorientable clusters. Each polar cluster C_i consists of a number of pseudocubic unit cells containing either Nb or Mg ions. Here i = 1, 2, …, N and N denotes the total number of polar clusters. If $\vec{u}_k(il)$ is the displacement of the kth ion in the lth cell in C_i from its ideal perovskite cubic position and e_k(il) its charge, then the dipole moment of the cell is

$$\vec{m}(il) = \sum_k e_k(il)\vec{u}_k(il) \tag{8.12}$$

It has been argued that the dominant contribution to $\vec{m}(il)$ is due to the displacements of the Nb^{5+} and PB^{2+} ions, so that Eq. (1) can be simplified to

$$\vec{m}(il) = \frac{3}{2} e_0 \left[\vec{u}_{Nb}(il) - \vec{u}_{Pb}(il)\right] + ..., \tag{8.13}$$

where e_0 is the unit charge and the dots represent the contributions of the remaining terms. Since Mg and Pb ions have the same charge, the contribution of an Mg-type cell is much smaller and only Nb-type cells are relevant. Let n_i represent the number of Nb cells in cluster C_i. The dipole moment of C_i can then written as

$$\vec{M}_i = \sum_i \vec{m}(il) \cong n_i \vec{m}_0(i), \tag{8.14}$$

assuming that dipole moment $\vec{m}(il)$ is the same for each Nb cell in C_i, and can thus be replaced by $\vec{m}_0(i) = (3/2) e_0 \left[\vec{u}_{Nb}(i) - \vec{u}_{Pb}(i)\right]$

Let us now introduce a dimensionless order parameter field, which is proportional to $\vec{M}_i$ and thus scales with the number of Nb ions n_i

$$\vec{S}_i = \left(\frac{3}{\left[n^2\right]_{av}}\right)^{1/2} \frac{\vec{M}_i}{m_0(i)}, \tag{8.15}$$

Here $\left[n^2\right]_{av} = (1/N)\Sigma_i n_i^2$. It is easily verified that the order parameter field then satisfies the closure relation

There are n_i Nb-type unit cells in a cluster C_i, where i = 1,2,…,N and N is the total number of reorientable clusters. The main contribution to the dipole moment $m_0(i)$ of the lth cell in C_i is due to the relative displacements of the Nb^{5+} and Pb^{2+} ions from their pseudocubic positions [14,18]. The cluster dipole moment is thus $M_i = n_i m_0(i)$.

Introducing $S_i = \{[m_0(i)^2]_{av}/3\}^{-1/2} M_i/n_i$ as a dimensionless order parameter field, where $[m_0(i)^2]_{av} = (1/N) \sum_I m_0(i)^2$, we find that its components satisfy the closure relation

$$\sum_{i=1}^{N} S_i^2 = 3N \tag{8.16}$$

The model has two order parameters, the polarisation P and glass order parameter q.The Edwards-Anderson order parameter, the polarisation, is given by

$$P_\mu^{EA} = \frac{1}{N} \sum_{i=1}^{N} \left\langle S_{i\mu} \right\rangle = \left[\left\langle S_{i\mu} \right\rangle \right]_{av}; \qquad (\mu = x, y, z) \tag{8.17}$$

and the glass order parameter is

$$q_{\mu}^{EA} = \frac{1}{N}\sum_{i=1}^{N}\left\langle S_{i\mu}\right\rangle^{2} = \left[\left\langle S_{i\mu}\right\rangle^{2}\right]_{av}; \qquad (\mu = x, y, z) \tag{8.18}$$

This, together with the existence of randomly competing ferroelectric (FE) and antiferroelectric (AFE) interactions, leads to the SRBRF model Hamiltonian for relaxor ferroelectric as under

$$H_{s} = -\frac{1}{2}\sum J_{ij}\vec{S}_{i}.\vec{S}_{j} - \sum_{i}\vec{h}.\vec{S}_{i} - g\vec{E}.\sum_{i}\vec{S}_{i} \tag{8.19}$$

where $\vec{S}_i$ –dipole moment of the i -th polar cluster, J_{ij} –random inter cluster interactions (J_0/N –mean value, $(J)^2$/N –variance), $\vec{E}$ –external electric field, $\vec{h}_i$ –random fields (0 –mean value, $\left[h_{i\mu}h_{iv}\right]_{av}^{c} = \delta_{ij}\delta_{\mu v}\Delta$). Equilibrium values of polarization $P = N^{-1}\sum_i \left\langle S_i\right\rangle$ and the order parameter of glass $q = N^{-1}\sum_i \left\langle S_i^2\right\rangle$ are determined from the condition of the free energy minimum.

For $J_0 < (J^2 + \Delta)^{1/2}$, long-range order cannot exist and the system is in a spherical glass phase (P = 0, q ≠ 0) at all temperatures. If Δ = 0, a transition from a high-temperature paraelectric to glass phase occurs at $T_m = J/k$. For Δ ≠ 0 and $\Delta << J^2$ the sharp transition disappears, but the nonlinear susceptibility shows a maximum at $kT_m \approx (J^2 + \Delta)^{1/2}$.

For $J_0 > (J^2 + \Delta)^{1/2}$, long-range order is possible and a phase transition to an inhomogenous ferroelectric phase (P ≠ 0, q ≠ 0) occurs below the critical temperature

$$kT_c = J_0\left[1 - \Delta/\left(J_0^2 - J^2\right)\right]. \tag{8.20}$$

The average energy is calculated in a standard manner by applying the replica trick and imposing the spherical constraint. Introducing the familiar replica indices α = 1,2,….n and a Lagrange multiplier Z to enforce the speherical condition, one can write down the expression for the free energy F as

$$\beta F = \lim_{n\to 0}\frac{1}{n}\left\{\int_{-\infty}^{+\infty}\left[\prod_{i\mu\alpha} dS_{i\mu}^{\alpha}\right]\int_{c-i\infty}^{c+\infty}\frac{dz}{2\pi i}\exp\left[-z\sum_{\alpha}\left(\sum_{i\mu}\left(S_{i\mu}^{\alpha}\right)^2 - 3N\right)\right]\right.$$
$$\left.\times\exp\left[\beta\sum_{\alpha}\left(\frac{1}{2}\sum_{ij\mu}J_{ij}S_{i\mu}^{\alpha}S_{j\mu}^{\alpha} + \sum_{i\mu}h_{i\mu}S_{i\mu}^{\alpha} + g\sum_{i\mu}E_{\mu}S_{i\mu}^{\alpha}\right)\right] - 1\right\}. \tag{8.21}$$

where β is 1/kT

The knowledge of free energy per spin helps us to find polarization and dielectric susceptibility, in the same line with magnetization and magnetic susceptibility, respectively, as that of Ising spin model for spin glasses.

For isotropic system, spontaneous polarisation below T_c is given by,

$$P^2 = \left[1-\left(\frac{J}{J_0}\right)^2\right]\left[1-\left(\frac{T}{J_0}\right)-\frac{\Delta}{J^2}\right] \tag{8.22}$$

and the Edward-Anderson glass order parameter q_{EA} is given by

$$q_{EA} = 1 - T/j_0$$

J_0 and J being the uncoupled interaction parameter and $\Delta = | J_0^2 - J^2 |$

Normally the strong pseudospin-lattice coupling always occurs in dipolar glasses. To account for the pressure-induced FE-R crossover, it is necessary to include the pseudospin lattice coupling interaction. The nanodomains are dispersed in a deformable lattice, the total Hamiltonian now becomes [4]

$$H = H_S + H_L + H_{SL} \tag{8.23}$$

where H_L and H_{SL} are the lattice (phonon) contribution and pseudospin polar phonon, respectively. The lattice coupling modifies the uncoupled interaction parameters J_0 and J to J_0^* and J^*[7]

Lattice coupling modifies the uncoupled interaction parameters J_0 and J of the SRBRF model as follows:

$$J_0^* = J_0 + \sum_p \frac{\left|\vec{\gamma}_{0p}\right|}{\omega_{0p}^2} - \frac{1}{N}\sum_{\bar{k}p} \frac{\left|\vec{\gamma}_{\bar{k}p}\right|^2}{\omega_{\bar{k}p}^2} \tag{8.24}$$

and

$$\left(J^*\right)^2 = J^2 + \frac{1}{N}\sum_{\bar{k}}\left[\sum_p \frac{\left|\vec{\gamma}_{\bar{k}p}\right|^2}{\omega_{\bar{k}p}^2}\right] - \left[\frac{1}{N}\sum_{\bar{k}p} \frac{\left|\vec{\gamma}_{\bar{k}p}\right|^2}{\omega_{\bar{k}p}^2}\right] \tag{8.25}$$

where ω_0 is the $\bar{k} = 0$ optic phonon frequency.

As for the uncoupled SRBRF model, two limiting cases are of interest.

Case (i): $J_0^* < [(J^*)^2 + \Delta]^{1/2}$. Here long-range order cannot exist, and the system goes into a dipolar glass state with non-zero order parameter $q\ (T)$. If $\Delta = 0$, a transition from the high PE state to a dipolar glass (relaxor) phase occurs at $T_f \equiv T_0 = J^*/k$. for $\Delta \neq 0$ and

$\Delta << (J^*)^2$, the transition, which corresponds to the maximum in the nonlinear susceptibility, occurs at

$$T_f \approx \left[\left(J^*\right)^2 + \Delta\right]^{1/2} \tag{8.26}$$

Case (ii): $J_0^* > [(J^*)^2+\Delta]^{1/2}$. In this case, long- range order is possible. The phase transition to an inhomogeneous ferroelectric state occurs below transition temperature T_c given by

$$kT_c = J_0^*\left[1 - \frac{\Delta}{(j_0^*) - (j^*)^2}\right] \tag{8.27}$$

The average probability distribution of local polarization $\overrightarrow{p_i} = \left\langle \overrightarrow{S_i} \right\rangle$ is defined as

$$W(p) = \frac{1}{N}\sum_i \delta\left(p - \overrightarrow{p_i}\right) \tag{8.28}$$

8.3.2.1. Nonlinear Dielectric Response

A straight forward way to discriminate between a ferroelectric state broken up into nanodomains under the constraint of quenched random fields or a (dipolar) glass state is to check the temperature dependency of the nonlinear dielectric response.

In a system with average cubic symmetry, the phenomenological relation between the applied electric field E_μ (μ = 1, 2, 3) and polarization P_μ can be written, assuming small amplitudes, as a power series

$$P_1 = x_1 E_1 - x_{122} E_1\left(E_2^2 + E_3^2\right) - x_{111} E_1^3 + \ldots \tag{8.31}$$

The inverse relation is formally

$$E_1 = a_1 P_1 + a_{122} P_1\left(P_2^2 + P_3^2\right) + a_3 P_1^3 + \ldots \tag{8.32}$$

where $a_1 = \frac{1}{\chi_1}$, $a_{122} = \frac{\chi_{122}}{\chi_1^4}$, and $a_3 = \frac{\chi_{111}}{\chi_1^4}$.

According to the scaling theory one has for a ferroelectric in zero electric field

$$a_3^{FE} \propto (T - T_C)^{\gamma - 2\overline{\beta}}.$$

For a system with cubic symmetry in d=3 spatial dimensionalities, one has $\gamma - 2\overline{\beta} > 0$, where the mean value is $\gamma - 2\overline{\beta} = 0$. For a random field frustrated ferroelectric, a_3 thus decreases on approaching T_C from above. For a dipolar glass, on the other hand, χ_1 remains finite at T_f, whereas $\chi_3 \propto (T - T_f)^{-\gamma_3}$ with $\gamma_3 = 1$. Thus the nonlinear

coefficient $a_3^{DG} \propto (T - T_f)^{-\gamma_3}$ should in contrast to the ferroelectric case–increase with decreasing T on approaching T_f.

For relaxors described by SRBF model with $\tilde{\Delta} \neq 0$ one finds for E $\rightarrow$0.

$$\chi_3 = \frac{\beta\chi_1^2(J_0\chi_1 + 1)}{[1 - \beta^2 J^2(1-q)(1-3q-2\tilde{\Delta})][1 - \beta J_0(1-q)]} \tag{8.33}$$

where the linear susceptibility is given by

$$\chi_1 = \frac{\beta(1-q)}{1 - \beta J_0(1-q)} \tag{8.34}$$

8.3.2.2. Heat Capacity and Thermal Expansion Studies of Relaxors

Magnetic, dielectric, optical, and electric properties of these materials are studied extensively. Thermal properties, especially heat capacity and its behavior in a wide temperature range, were studied casually. Nevertheless, thermal parameters of relaxors may be important in the developing and refining models of the phenomena in questions. Calorimetric studies have some advantages since this method makes possible to detect and type of heat capacity anomalies, which are associated with electric as well as the elastic and other subsystems.

This section aims to study the heat capacity and thermal dilatation behavior of a leadfree relaxor material. The SRBRF Hamiltonian, as proposed earlier, is

$$H = -\frac{1}{2}\sum_{ij} J_{ij}\vec{S}_i\vec{S}_j - \sum_i \vec{h}_i\vec{S}_i - g\vec{E}\sum_i \vec{S}_i,$$

where $\vec{S}_i$ –dipole moment of the i -th polar cluster, J_{ij} –random intercluster interactions (J_0/N –mean value, $(J)^2$/N –variance), $\vec{E}$ –external electric field, $\vec{h}_i$ –random fields (0 –mean value, $\left[h_{i\mu}h_{iv}\right]_{av}^{c} = \delta_{ij}\delta_{\mu v}\Delta$). Equilibrium values of polarization $P = N^{-1}\sum_i \langle S_i \rangle$ and the order parameter of glass $q = N^{-1}\sum_i \langle S_i^2 \rangle$ are determined from the condition of the free energy minimum.

For $J_0 < (J^2 + \Delta)^{1/2}$ long-range order cannot exist and the system is in a spherical glass phase $(P = 0,\ q \neq 0)$ at all temperatures. If $\Delta = 0$, a transition from a high-temperature paraelectric to glass phase occurs at $T_m = J/k$. For $\Delta \neq 0$ and $\Delta << J^2$ the sharp transition disappears, but the nonlinear susceptibility shows a maximum at $kT_m \approx (J^2 + \Delta)^{1/2}$. For $J_0 < (J^2 + \Delta)^{1/2}$ long-range order is possible and a phase transition to an

inhomogenous ferroelectric phase *(P ≠ 0, q ≠ 0)* occurs below the critical temperature $T_c = J_0\left[1 - \Delta/\left(J_0^2 - J^2\right)\right]/k$.

The experimental results of M.V.Gorev *et. al* on anomalies of heat capacity and entropy change for leadfree materials are much smaller than for lead containing relaxors such as PMN and PET. The obtained results are in good agreement with the data of structural studies and with the SRBRF model. This strengthens the validity of the model.

8.4. Conclusions

In the nutt shell this chapter is devoted to throw some light in understanding the physical concept of relaxor ferroelectricity theoretically. Ther close analogy between relaxor ferroelectricity and magnetic spin glass system and the wealth of theoretical models in the later is prime cause of motivation.

To start with a well known Ising model for spin glass system is reviewed till to reach the expression for frwee energy per spin. Magnetisation and magnetic susceptibility can be calculated from the same.

With the understanding that the concept of spin is no more restricted to magnetic system rather to any solid state system containing the frozen impurities and point defects that break the symmetry. Ther relaxor behaviour in ferroelectric is one such attempt.

In spite of several attempts, the nature of diffused phase transition in relaxor ferroelectric has still remained in a controversial stage. Experimental evidence in them showed incompatibility with the assumptions of fixed length ordered paramenter as proposed in dipolar glasses rather in a relaxor the order paramenter field is described as a continious vector field of variable length. Thus a relaxor coreresponds to a new type of di-polar galass namely spherical vector glass. To account for, the SRBRF model is proposed. Section 8.3.2 presents a condensed review of the same.

With the introduction of two Edwards-Anderson order parameter p and q the SRBRF Hamiltonian is proposed. Using replica trick the average free energy per spin may be derived in a standard manner. The knowledge of free energy per spin helps us to find polarization and dielectric susceptibility, in same line with magnetization and magnetic susceptibility respectively as that of Ising spin model for spin glasses.

To account for strong pseudospin –lattice interaction and pressure induced FE-R crossover a modified Hamiltonian is proposed. The static SRBRF is exactly solvable by the replica method and predicts the existence of two phases, namely, the spherical glass (SG) phase without long-range order and the long range ordered polarized ferroelectric (FE) phase. The reviewed models are best suited for explaining nonlinear dielectric response and heal capacity and thermal expansion studies.

8.5. References

1. Yuhuan Xu, Ferroelectric Materials and their applications, 1st Ed. Elsevier, Amsterdam, (1991)
2. K.H.Yoon and H.R Lee, *J.Am.Cram.Soc*. **83**, 2693(2000).
3. L.E.Cross, *Ferroelectrics* **76**, 241(1987).
4. S.F.Edwards and P.W.anderson, J. Phys., F **5**, 965 (1975)
5. *Current trends in magnetism*, Ed. N.S.Satya Murthy and L.Madhav Rao, Indian Physics Association, pp 411 (1981)
6. G.A.Smolenskii and V.A.Isupov, *Dokl.Akad.Nauk SSSR* **97**, 653 (1954).
7. R.Pirk and R.Blink, *Phys. Rev.B* **60**, 13470 (1999).
8. D.Sherrington and S.Kirkpatrick, *Phys.Rev. Lett*. **35**, 1972 (1975)
9. S.Nagata, P. Keesom, and H.Harrison, *Phys.Rev. B* **19**, 1533 (1079)
10. K.Binder*, Festkorperprobleme*, **17**, 55 (1977)
11. B.E.Vugmeister and H.Rabitz*, Phys. Rev.B* **57**, 7581 (1998).
12. L.E.cross, *Ferroelectrics* **151**, 305 (1994)
13. D.Viehland, S.J.Jang, L.E. Cross, and M. Wuttig, *J. Appl. Phys*. **68,** 2916 (1990)
14. A.K.Tagantsev and A.E. Glazounov, *J. Korean Phys.Soc*. **32**, S951 (1998)
15. K. Bider and A.P. Young, *Rev. Mod.Phys*. **58**, 801 (1986).
16. B.E. Vugmeister and H. Rabitz, *Phys. Rev. B* **57**, 7581 (1998)
17. K.H.Fischer and J.A.Hertz, *Spin Glasses*, Cambridge University Press, Cambridge, (1991).
18. R.Pirc, B. Tadic and R.Blinc, *Phys.Rev.B* **36**, 8607 (1987)
19. R.Pirc and R.Blink, *Phys.Rev.B* **60**, 13470 (1999)
20. C.Boulesteix, F. Varnier, A. Llebaria and E. Husson, *J.Solid State Chem.* **108**, 141 (1994).

Chapter 9

MAJOR CONCLUSIONS AND FUTURE WORK

9.1 Conclusions

High permittivity barium titanate zirconate (BTZ) is often used for dielectrics in commercial multilayer ceramic capacitors, actuators applications, and is a highly promising material for dynamic random access memory (DRAM), and microelectromechanical system (MEMS) applications due to its very stable, high insulating characteristic against voltage. Especially (BTZ) system is promising for environmental friendly applications.

Different solid solutions in the system have been synthesized via solid state reaction route. Detailed phase formation behaviors of the solid solutions were investigated through; (i) phase identification, (ii) phase quantity determination, (iii) change in lattice parameters and crystallite sises, (iv) evolution of phase formation kinetics and reaction mechanism, and (v) structure and microstructure evolution by Rietveld refinement method.

During the formation of Barium Titanate Zirconate solid solution, in the first step $BaTiO_3$ (BT), $BaZrO_3$ (BZ) forms separately in the system. Formation of BT requires less activation energy (34.3 kcal/mol) than the formation of BZ (48.4 kcal/mol). In the second step, $BaTiO_3$-$BaZrO_3$ solid solution is formed mainly by the diffusion of $BaTiO_3$ into the $BaZrO_3$ lattice without any evidence of other intermediate phase formation. Activation energy for this step is 133 kcal/mole, which may be due to the diffusion of Ba and/or O ions through solid solution interface. In the formation of $Sr(Ti_{0.5}Zr_{0.5})O_3$ solid solution, $SrTiO_3$ (ST) and $SrZrO_3$ (SZ) phases form separately in the system and then $SrTiO_3$ diffuses into $SrZrO_3$ to form the solid solution. The rate of $SrTiO_3$ formation was higher than $SrZrO_3$ formation, apparently due to the higher ionic radius of Zr^{+4} ions. The activation energies of phase formations were 47.27, 65.78 and 297.52 kcal/mol for $SrTiO_3$, $SrZrO_3$ and $Sr(Ti_{0.5}Zr_{0.5})O_3$ respectively, and the formation reactions were limited by the diffusion of Sr ion for $SrTiO_3$, Zr ion for $SrZrO_3$ and Ti ions for $Sr(Ti_{0.5}Zr_{0.5})O_3$, etc. Solid solution was formed coherently with the crystal of $SrZrO_3$. Similarly during formation of $Ba_{0.5}Sr_{0.5}TiO_3$ (BST) and $Ba_{0.5}Sr_{0.5}ZrO_3$, BT and BZ form more easily than ST and SZ. The solid solution grows

coherently with ST lattice for formation of BST. During the formation of BSZ (ss), the activation energies required for BZ, SZ and BSZ (ss) are 58.069 kcal/mol, 60.78 kcal/mol and 97.43 kcal/mol, respectively. The solid solution formed coherently with SZ by the diffusion of Ba ion into SZ lattice. In general, the study on reaction mechanism concludes that; titanates form more easily in the system than zirconates. Then titanate inter-diffuses into zirconate, where latter phase acts as diminishing core

Coming to the Rietveld structural refinement on the four component system, the solid solution system $Ba_{1-x}Sr_x(Ti_{0.5}Zr_{0.5})O_3$ remains cubic up to $x<0.6$ and becomes tetragonal in the range $x>0.6$ to $x=1.0$. Composition with $x=0.6$ contains both the cubic and tetragonal phases. The compositions show decreased densification and grain growth with the increase in Sr substitution. The solid solution system $(Ba_{0.5}Sr_{0.5})(Ti_{1-x}Zr_x)O_3$ remains cubic up to $x\leq0.6$ and the solid solution breaks around $x=0.8$ with the formation of second phase of tetragonal type. The compositions show a good densification around $x=0.2$, suggesting a low melting eutectic near that composition in the four component system. Compositions with $x=0.8$ contains both the cubic and tetragonal phases and suggest to have a super-lattice structure due to the presence of two dissimilar structures. The $Ba_{0.5}Sr_{0.5}ZrO_3$ has orthorhombic structure.

Solubility of Ca and Mg with $BaTi_{0.6}Zr_{0.4}O_3$ was also studied by Rietveld method. The Study concludes that, Mg forms complete solid solution with $BaTi_{0.6}Zr_{0.4}O_3$ in the studied composition range and the structure remains cubic at room temperature. But solubility of Ca with $BaTi_{0.6}Zr_{0.4}O_3$ breaks at around 20 atom % of Ca. The composition $Ba_{0.9}C_{0.1}Ti_{0.6}Zr_{0.4}O_3$ remains cubic. With increase in Ca content, a different phase, orthorhombic $CaTiO_3$, grows along with tetragonal $Ba_{0.8}C_{0.2}Ti_{0.6}Zr_{0.4}O_3$.

Detailed composition dependency microstructure and dielectric behavior of the different solid solution in the system has been studied. Temperature dependency dielectric behaviors of some of the selected compositions have been studied.

The solid solution system $Ba_{1-x}Sr_x(Ti_{0.5}Zr_{0.5})O_3$ shows decreased densification and grain growth with the increase in Sr substitution. Composition with $x=0.0$ (BTZ) shows highest permittivity in the system. The permittivity and dielectric loss decrease with the increase in Sr substitution. The permittivity and dielectric loss are found to be stable, and the loss is less than 0.6 % in the frequency range 100 kHz to about 5 MHz for all the compositions. AC conductivity in the ceramics decreases with Sr-substitution due to the decrease in loss as well as grain size. The solid solution system $(Ba_{0.5}Sr_{0.5})(Ti_{1-x}Zr_x)O_3$ show decreased densification and grain growth with the increase in Zr

substitution. Permittivity, dielectric loss and AC conductivity decrease with Zr-substitution due to the decrease in charge defects by the substitution. The effect of Ca and Mg on the composition $BaTi_{0.6}Zr_{0.4}O_3$ has been studied in details. Similar dielectric behavior and microstructure are observed with the addition of Ca and Mg at room temperature.

The temperature dependency dielectric study on the composition $BaTi_{0.6}Zr_{0.4}O_3$, $Ba_{0.9}Ca_{0.1}Ti_{0.6}Zr_{0.4}O_3$, $Ba_{0.93}Mg_{0.07}Ti_{0.6}Zr_{0.4}O_3$ and $Ba_{0.86}Mg_{0.14}Ti_{0.6}Zr_{0.4}O_3$ was carried out in the temperature range 130 ^{O}K to 333 ^{O}K. The compositions show a diffuse phase transition having its Curie range of temperature much below the room temperature. The Ca-containing composition shows that there is a shift of transition temperature towards room temperature but the Mg containing compositions shows shift of transition temperature further below. A clear deviation from Curie-Weiss law is observed for all the compositions and degrees of deviations were also calculated. To study the diffuseness, the data were fitted with a modified Curie-Weiss law, and it was found that the degree diffuseness decreases with Ca substitution, but increases with Mg substitution. In order to analyze the relaxation feature, the experimental curves were fitted with Vogel-Fulcher formula and the experimental data were found to be in good agreement with the theoretical fitting.

To get into the realm of physics, relaxor ferroelectric is treated as a close analogy with Ising model of Spin glass system. Further extension of Ising model to spherical random bond–random field model is discussed. Both the models are extensively reviewed and presented towards end of the thesis.

9.2. Future Work

Complex oxides with perovskite-like structure, such as $(Ba/Sr)TiO_3$, $Ba(Ti/Zr)O_3$, are attractive candidates for use in wireless communications and are potential candidates for cell capacitors in giga-bit DRAM, FeRAM, MLCC, Microwave tunable applications, etc., due to their high dielectric constant, near –zero temperature coefficient of the resonant frequency and low dielectric loss tangent [1-5].

This thesis systematically represents some of their synthesis, phase formation behavior, structural transformation and dielectric properties in bulk ceramics, which is a very important document for science and technology. It is not possible to incorporate all the different types of characterization on the studied ceramics in one thesis document. Moreover, within the presently available laboratory facility, a more detailed study on

the ceramic is not possible. So, future programs of further study have been proposed in this section.

Structural changes in the system have been investigated by using normal XRD. The transforms of room temperature cubic structure of BST and BTZ to lower symmetry tetragonal structure is observed and confirmed by Rietveld refinement. The lower symmetry structures are also characterized by splitting of reflections. Such splitting and detailed information about the anisotropic thermal parameters can be best observed using high resolution synchrotron diffraction measurement. The temperature dependency of phase transformation may be well studied by temperature controlled XRD system. These are beyond the scope of our laboratory.

It is also well known and recently reported [6], which in normal ferroelectrics, dielectric constant increases with decrease in particle size upto nanometric scale. X.G.Tang. *et al*. [7], have studied the effect of grain size on dielectric and tunabilities properties of sol gel derived BTZ ceramic and observed that diffusivity increases with decrease in grain size. They also observed relaxor behavior in fined-grained samples, instead of coarse grained samples. In the present situation, nanocrystaline single-phase materials may be synthesized by different chemical and mechanical route. Their structural, dielectric and optical properties may be studied. Thin films may be prepared by different techniques like; sol gel, PLD, and RF magnetron sputtering. Electromechanical properties may be investigated for MEMS and NEMS applications. One of the most convenient ways for checking the polydispersive nature of dielectric relaxation is through complex Argand plan plots. The impedance spectroscopy may be used to study the grain and grain boundary effect of the nano-crystalline relaxor ferroelectric and dispersive nature may be studied. To explain the relaxor behavior, several theoretical models [8-12] have been proposed by many research groups. None of them has gained complete acceptance, although it has been widely accepted that nanoscale polar, ordered regions dispersed in a disordered matrix are responsible for the properties of RFE. Nature of their extraordinary properties has not yet been understood completely, and they are still the subject of intensive research. In the Chapter 8 we have presented a brief review on some theoretical models of lead based (heterovalent substation) relaxor. In future these theories may be used to study the physics of these lead free relaxors presented in this thesis.

Apart from the dielectric polarisation study, the spectroscopic study like, nuclear magnetic resonance (NMR), RBS and Raman scattering are some appropriate techniques to study the dynamics of structure by analyzing the characteristic modes

associated to nanoregions in relaxors. Because the local symmetry of nanoregions is different from that of the global symmetry, they govern different selection rules in different spectroscopic analysis. By examining the detailed composition dependence of the characteristic vibrational bands, it is possible to study the dynamics of the nanoregions. The detailed piezoelectric behavior may also be studied on all compositions.

All the ideas proposed above to study the lead free ferroelectric relaxors are very important to have a detailed insight into the physics and chemistry of the materials. But none of the above proposed experimental facility is available in the present laboratory.

9.3. References

1. M.M Watt, *Integrated Ferroelectrics*, **26**, 163-186 (1999)
2. H.J.Cho, S.Oh, C.S.Kang, C.S.Hwang, B.T.Lee, K.H.Lee, H.Horii, S.I.Lee and M.Y.lee, *Appl.Phys.Lett*. **71**, 3221 (1997).
3. S.Hoffmann and R. Waser, *Integrated Ferroelectrics* **17,**141 (1997).
4. T.B.Wu, C.M Wu and M.L.Chen, *Appl.Phys.Lett*. **69**, 2659 (1996).
5. D.Hennings, A.schnell and G.Simon, *J. Am. Ceram.Soc*. **65**, 539(1982).
6. S.K.S. Parashar, R.N.P. Choudhary and B.S. Murty, *Materials Science and Engineering B* **110**, 58–63 (2004).
7. X.G.Tang, J.Wang, X.X.Wang and H.L.W.Chan, *Solis State Communication* **131** 163-168 (2004).
8. G.A. Smolenskii, *J. Phys. Soc. Jpn* **28**, 26 (1970).
9. N. Setter and L.E. Cross, *J. Appl. Phys*. **51**, 4356 (1980).
10. X. Yao, Z.L. Chen and L.E. Cross, *J. Appl. Phys*. **54**, 3399(1984).
11. D. Viehland, S.J. Jang, L.E. Cross and M. Wuttig, *J. Appl. Phys*. **68**, 2916 (1990).
12. V. Westphal, W. Kleemann and M.D. Glinchuk, *Phys. Rev. Lett*. **68**, 2916 (1992).